FINAL TECHNICAL REPORT
Reporting Period: October 1, 2010 to June, 2015
Date of Report: June 30, 2015

Award Number:	DE-FE0005717
Project Title:	Development of Self-Powered Wireless-Ready High Temperature Electrochemical Sensors for In-Situ Corrosion Monitoring for Boiler Tubes in Next Generation Coal-based Power Systems
Project Period:	October 1, 2010 to June 30, 2015
Recipient Organization:	West Virginia University
Partners:	Western Research Institute Special Metals International Lead Zinc Research Organization
Principal Investigator:	Xingbo Liu, (304) 293-3339, Xingbo.Liu@mail.wvu.edu

---

July 2016

Abstract

The key innovation of this project is the synergy of the high temperature sensor technology based on the science of electrochemical measurement and state-of-the-art wireless communication technology. A novel self-powered wireless high temperature electrochemical sensor system has been developed for coal-fired boilers used for power generation. An initial prototype of the in-situ sensor demonstrated the capability of the wireless communication system in the laboratory and in a pilot plant (Industrial USC Boiler Setting) environment to acquire electrochemical potential and current signals during the corrosion process. Uniform and localized under-coal ash deposit corrosion behavior of Inconel 740 superalloy has been studied at different simulated coal ash hot corrosion environments using the developed sensor. Two typical potential noise patterns were found to correlate with the oxidation and sulfidation stages in the hot coal ash corrosion process. Two characteristic current noise patterns indicate the extent of the corrosion. There was a good correlation between the responses of electrochemical test data and the results from corroded surface analysis. Wireless electrochemical potential and current noise signals from a simulated coal ash hot corrosion process were concurrently transmitted and recorded. The results from the performance evaluation of the sensor confirm a high accuracy in the thermodynamic and kinetic response represented by the electrochemical noise and impedance test data.

List of Acronyms

A-USC	Advanced-Ultrasupercritial
CE	counter electrode
CPE	constant phase element
CTF	Combustion Test Facility
EDX	energy-dispersive X-ray microanalysis
EIS	electrochemical impedance spectroscopy
EN	electrochemical noise
ESP	electrostatic precipitator
FFT	fast fourier transform
FRA	Frequency Response Analyzer
HT	high temperature
JFET	junction gate field-effect transistor
LUDC	localized under-coal ash deposit corrosion
m.p.	melting point
MEM	Maximum Entropy Method
NETL	U.S. Department of Energy, National Energy Technology Laboratory
OCP	open circuit potential
PDP	potentiodynamic polarization
PSDs	power spectral densities
RE	reference electrode
SDA	spray dry absorber
SEM	Scanning electron microscopy
TC	Thermocouple
TEG	thermoelectric Generator
TEG	thermoelectric generator
USC	ultrasupercritical
WE	working electrode
WRI	Western Regional Institution
WVU	West Virginia University
XRD	X-ray diffraction

Table of Contents

List of Figures

List of Tables

1.0 Executive Summary

Objectives: The primary objectives of this project were to develop in-situ corrosion monitoring sensors for fireside corrosion of ultrasupercritical (USC) boiler tubes by coal ash, based on WVU's patent pending technology on high temperature electrochemical characterization devices and development of thermal-electric based energy harvesting and telecommunication devices for the self-powered wireless ready sensor system.

Project description: The research plan included: (1) extension of the technology developed on monitoring hardware corrosion in liquid metal baths, on which a patent is pending, to develop high temperature (HT) electrochemical sensors to monitor corrosion of the USC boiler tubes; (2) constructing electrochemical models of the corrosion system to develop predictive capabilities relevant to materials corrosion real-life performance; (3) development of thermal-electric based energy harvesting and telecommunication devices for the self-powered wireless ready sensor system; and (4) testing the sensor systems in industrial USC boiler settings.

Accomplishment to date: Real time hot corrosion monitoring is still a challenging issue in coal-based power generation systems. It is not easy to achieve reliable and repeatable data such as quantitative relations between corrosion progress and data readings. The research team developed and demonstrated an application of a new high temperature electrochemical sensor system with a reliable reference electrode to provide a clearer picture of the corrosion degradation. The hot corrosion behavior of a Ni-based superalloy was studied in the presence of a synthetic coal ash and a synthetic flue gas containing sulfur dioxide, using our proposed high temperature electrochemical sensor. Our newly developed high temperature electrochemical sensor was applied to study the effect of SO_2 in flue gas on thin film coal ash corrosion of Inconel 740 superalloy at 750 C. The response of electrochemical noise (EN), electrochemical impedance spectroscopy (EIS), and potentiodynamic polarization (PDP) test data from the sensor is compared with the results from a weight loss test. There is a good correlation between the electrochemical data and the actual degradation processes. The current noise analysis in time and frequency domains for the quantitative determination of hot corrosion rate in service was also identified. The data show that corrosion resistance of the alloy was significantly reduced at 750C and the highest tendency of TiS formation in the internal sulfidation stage led to accelerated intergranular and intragranular corrosion. In the meantime, in combination with our high temperature electrochemical sensor, we applied wireless communication and an energy harvesting thermoelectric Generator (TEG).This self-powered sensor demonstrates the successful wireless transmission of both corrosion potential and corrosion current signals to a simulated control room environment.

After the development and testing our new electrochemical corrosion sensor in the WVU research labs, the project team successfully carried out twice *In-situ Corrosion Monitoring testing in industrial USC boiler setting* at the Western Research Institute combustion testing facility with real USC environments**.** We have continuously tested the corrosion sensor in WRI for more than a week for each test without any major problems. The tests were stopped due to scheduled maintenance of the combustion facility. Our testing results are consistent with results obtained in WVU labs, and showed the effectiveness and potential of

the application of the WVU corrosion sensor in monitoring corrosion progress of boiler tubes in USC power plants.

Potential Impact: Real-time corrosion monitoring will reduce the number of forced outages and the avoidance of unplanned events in ultra-supercritical boilers. This research is also cross-cutting to other applications where corrosion in high temperature processes is a concern such as steel, aluminum, and metal casting. In all cases an increase in equipment reliability and a reduction in scrap or reworked material would be expected.

Major Participants: West Virginia University; Western Research Institute; Special Metals Corporation, as well as International Lead Zinc Research Organization, which co-invented the high temperature electrochemical characterization system with WVU.

2.0 Results and Discussion

Task 1: Project Management

Task 1.1 Project Management Plan

The project management plan was submitted within 30 days after the award and the principle investigator kept in communication with the project officer at NETL with any changes or deviations from the agreed upon plan. All quarterly reports were submitted within a timely manner and the PI tracked project tasks against the project timeline and the project management plan to ensure that milestones were being met. All project tasks and milestones have been completed.

Subtask 1.2 Project Communications

The principle investigator kept in communication with the project officer at NETL about the status of the project, any issues regarding the project, and concerns about the timeline. The PI also gave tours throughout the project to the project officer and other NETL researchers to keep them up to date on the status of the project and the laboratory testing. The PI also kept in communication with his co-PIs at WVU and at Western Research Institute.

Task 2: Development of High Temperature Corrosion Sensor

Subtask Task 2.1 Design and Construction of Corrosion Sensor

Experimental Methods

Ag/AgCl/β-Al_2O_3 Reference Electrode for High Temperature Corrosion Sensor

High temperature corrosion is the accelerated oxidation of materials at elevated temperatures induced by a thin film of fused salt deposit. Because of its high thermodynamic stability in the mutual presence of sodium and sulfur impurities in an oxidizing gas, Na_2SO_4 is often found to be the dominant salt in the deposit. The corrosive oxyanion-fused salts are usually ionically conducting electrolytes that exhibit an acid/base chemistry, so that high temperature corrosion must occur by an electrochemical mechanism that may involve fluxing of the protective oxides. To quantify an acid/base scale, the solubilities for various metal oxides in fused Na_2SO_4 can be measured with the aid of high temperature reference electrodes. Thus, a long-term stable reference electrode needs to be developed first as a key component of a high temperature corrosion sensor. A high temperature solid state Ag/AgCl/β-Al_2O_3 reference electrode was first fabricated and evaluated. Figure 1 shows a reference schematic of the reference electrode.

The detailed processes for the fabrication of reference electrode are described as following. The silver electrode was prepared by polishing a silver wire with sand paper and subsequently performing anode polarization at constant current density of 2 mA cm^{-2} in 1 M HCl for 10 min. Thus, a silver wire deposited

with a thin film of silver chloride can be used as a silver electrode. β-alumina powder (molar ratio of Na_2O:Al_2O_3=1:11) was fabricated by a conventional solid-state reaction method. Then, the pure β-alumina powder was pressed into pellets under 18,000 lb of pressure and sintered at 1550 ℃. One open end of an alumina tube as enclosure was sealed with the above β-alumina pellet using different pastes (ZrO_2 or Al_2O_3). The enclosure with a closed end was filled with a salt mixture of 45 wt% NaCl, 45 wt% KCl and 10 wt% AgCl, which had been dried at 400 ℃ for 24 h in air. The tube was then heated to melt the contained salt mixture, and the silver electrode was inserted into the molten salt. Two electrodes were needed to perform potential stability measurements since current must flow in a complete circuit. Thus, Pt wire was used as counter electrode and as-prepared reference electrode was used as working electrode. The open circuit potential (OCP) was recorded as the function of time. Its potential stability measurement was performed in the external electrolyte solution (45 wt.% Na_2SO_4, 45 wt.% K_2SO_4 and 10 wt.% NaCl) at 800 ˚C by using a Solartron Model 1287A Potentiostat/Galvanostat.

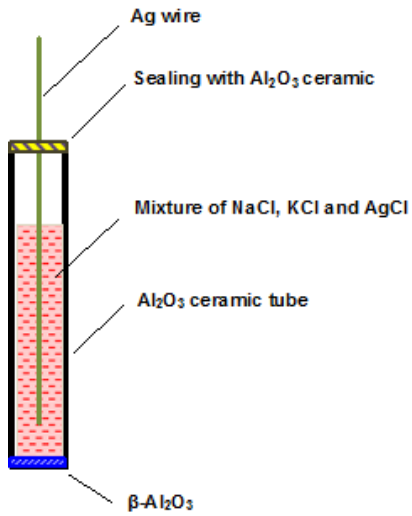

Figure 1: Schematic diagram of as-prepared Ag/AgCl/β-Al_2O_3 reference electrode

Ag/Ag^+/fused-silica Reference Electrode for High Temperature Corrosion Sensor

Since β-Al_2O_3 is not a suitable electrolyte for a reference electrode involving Ag^+ ions, fused-silica was chosen as an ion conducting membrane of the Ag/Ag^+ electrode. The sealed fused-silica structure was prepared by first sealing one end of a fused-silica (GE 214) tube in the hydrogen–oxygen gas flame. While still in the flame, a positive air pressure was blown into the closed end which then expanded into a capsule whose size, shape and wall thickness were controlled by the blowing operation. After cooling, the fused-silica tube was ready to receive the Ag/Ag^+ electrode that consisted of a silver electrode and the internal electrolyte. After being manually polished with different grades of sand paper for cleaning, a tungsten wire (0.2 mm in diameter) with a length longer than the tube was inserted rapidly into the heat-softened end of a silver rod (2.0 mm in diameter). The tube was then filled with a mixture of sulphate salt (10 mol% Ag_2SO_4+90 mol% Na_2SO_4) which had been dried at 400 ˚C in air for two days. The tube was then heated to melt the contained salt mixture, and the inner Ag electrode was inserted into the molten salt. Several minutes later, the whole electrode was cooled slowly to room temperature. After cleaning and drying, the

open end of the tube was connected to a rotary vacuum pump. The hydrogen–oxygen flame was used to seal the construction at a position around the tungsten wire, as shown in Figure 2.

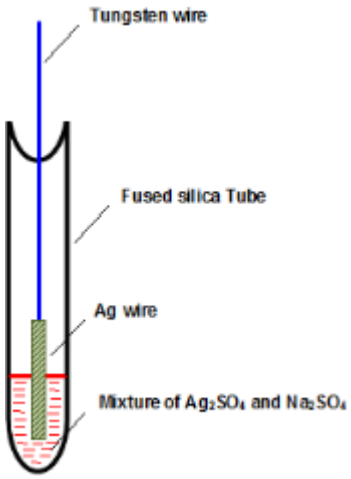

Figure 2: Schematic diagram of the sealed Ag/Ag+/fused-silica reference electrode

Preliminary High Temperature Corrosion Sensor Design for Lab-Scale Corrosion Testing

Our proposed sensor was based on a four-electrode system (two identical working electrodes (WE1 and WE2), one reference electrode (RE) and one counter electrode (CE)). The schematic design of the sensor is shown in Figure 3a. The working electrode was constructed of Nickle-based super alloys. In this study, Ag/Ag^+/fused-quartz reference electrode was chosen. The platinum wire was used as a counter electrode. A photograph showing the dimensions of the sensor components is presented in Figure 3b. The sensor was specially designed to utilize the response of several electrochemical measurements from a single electrochemical sensor.

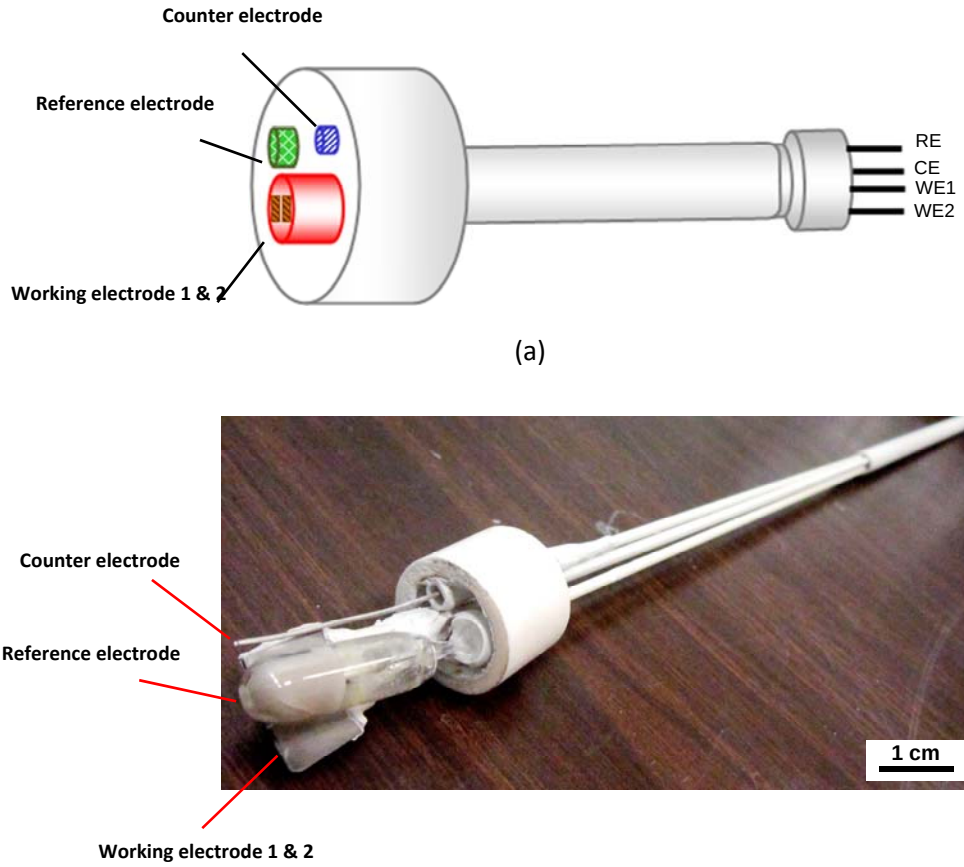

Figure 3: (a) Schematic design of our proposed high temperature corrosion sensor, and (b) photograph showing the dimensions of the sensor components

Modifications of Corrosion Sensor Design with Ag/Ag$^+$/mullite reference electrode

Modifications were made to an existing design of self-powered wireless high temperature electrochemical sensor. It was specially designed for concurrent measurements of potential noise and current noise signals from a single sensor. The new sensor was based on a five-electrode system (three identical working electrodes (WE1, WE2 and WE3), one reference electrode (RE) and one counter electrode (CE)). The corrosion potential of the coupled WE1 and WE2 of the sensor was measured against the Ag/Ag$^+$/mullite reference electrode. Schematic diagram of the sealed Ag/Ag$^+$/mullite reference electrode and the modified sensor design is shown in Figure 4a & Figure 4b.

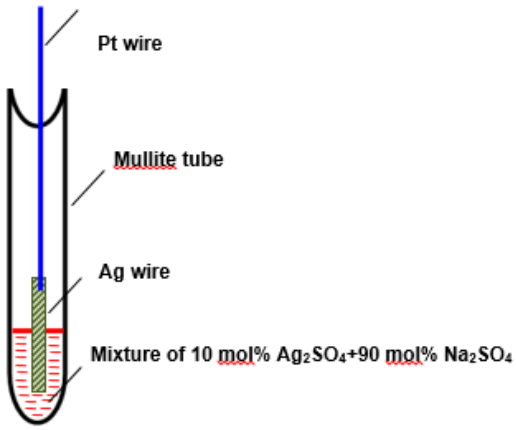

(a)

(b)

Figure 4: Schematic diagram of (a) the sealed Ag/Ag+/mullite reference electrode, and (b) the modified sensor design

Results and Discussions

April to June 2011

Ag/AgCl/β-Al_2O_3 Reference Electrode for High Temperature Corrosion Sensor

Time dependency of the potential of the electrode is given in Figure 5 and the sudden drops in the potential were observed. In the chloride molten salt at 800 °C, it would be difficult to avoid the dissolution of AgCl ((melting point (m.p.) = 455 °C). On the other hand, evaporation of the chloride melt at high temperatures (but below the boiling point) is common place, which can change the composition of the AgCl containing electrolyte, and hence the potential of the reference electrode. Therefore, a completely sealed structure is a preferred solution. Moreover, inspection of the β-Al_2O_3 tube after the test showed that the part contacting the reference melt become dark in color, indicating that the electrode had degraded β-Al_2O_3 which has an ideal composition of $Na_2O.11Al_2O_3$, attains its conductivity by diffusion of Na^+ ions between loosely packed spinel blocks. It is well known that the Na^+ ions in Na-β-Al_2O_3 can be easily exchanged with many other ions, including the Ag^+.

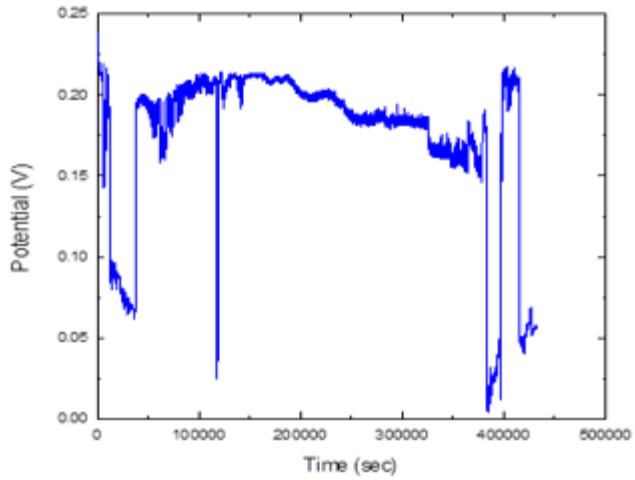

Figure 5: Time dependency of the potential of Ag/AgCl/β-Al2O3 reference electrode in sulphate/chloride melt at 800 ˚C

July to September 2011

Ag/Ag$^+$/fused-silica Reference Electrode for High Temperature Corrosion Sensor

The potential stability of the Ag/Ag$^+$/fused-silica reference electrode was investigated relative to the Pt wire working electrode in the synthetic coal ash mixture at 800 °C for 5 days. The mixture consisted of reagent-grade 29.25 wt.% SiO_2, 29.25 wt.% Al_2O_3, 29.25 wt.% Fe_2O_3, 5.625 wt.% Na_2SO_4, 5.625 wt.% K_2SO_4 and 1 wt.% NaCl. The fused-silica electrode was satisfactory in giving consistent potential readings along with long term stability (Figure 6). The potential was stable to within ± 10 mV after 6 h.

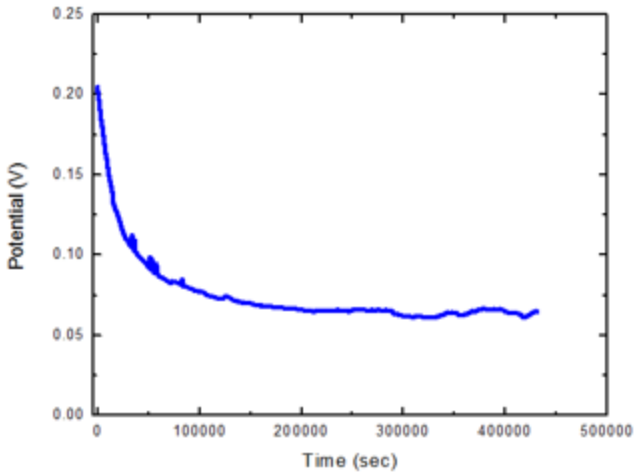

Figure 6: Time dependency of the potential of Ag/Ag+/fused-silica reference electrode in synthesis coal ash mixture at 800 ˚C

January to March 2012

Microstructure Analysis of IN740-1 Alloy

The Inconel 740 Ni-based superalloy which is currently being evaluated for use as tubing and piping for steam boiler application at Advanced-Ultrasupercritial (A-USC) steam conditions, was chosen to test its hot corrosion resistance. It was obtained from U.S. Department of Energy, National Energy Technology Laboratory (NETL) and it has the following chemical composition (in wt.%): Ni-49.45, Cr-24.67, Fe-0.62, Co-19.98, Mo-0.50, Nb-1.47, Al-1.23, Mn-0.3, Ti-1.23, Si-0.29. Prior to testing the alloy was given the following sequence of heat treatment: 1150 °C for 4 h followed by air cooling; 1120 °C for 1 h followed by air cooling; 850 °C for 16 h followed by air cooling. The alloy was then cut into samples of 10 mm×10 mm×2 mm in dimension for electrochemical tests and weight loss measurement. As shown in Figure 7a and Figure 7b, intermetallic phases occur intergranularly as well as intragranularly in 740 alloy. EDX analysis shows that the Ni_3Ti-based phase and (Ti, Nb)C were the major the intermetallic phases (Figure 7c). It should be noted that γ′ is the major strengthening phase in the Inconel 740 alloy but it is beyond the resolution for the SEM used in this research to be observable.

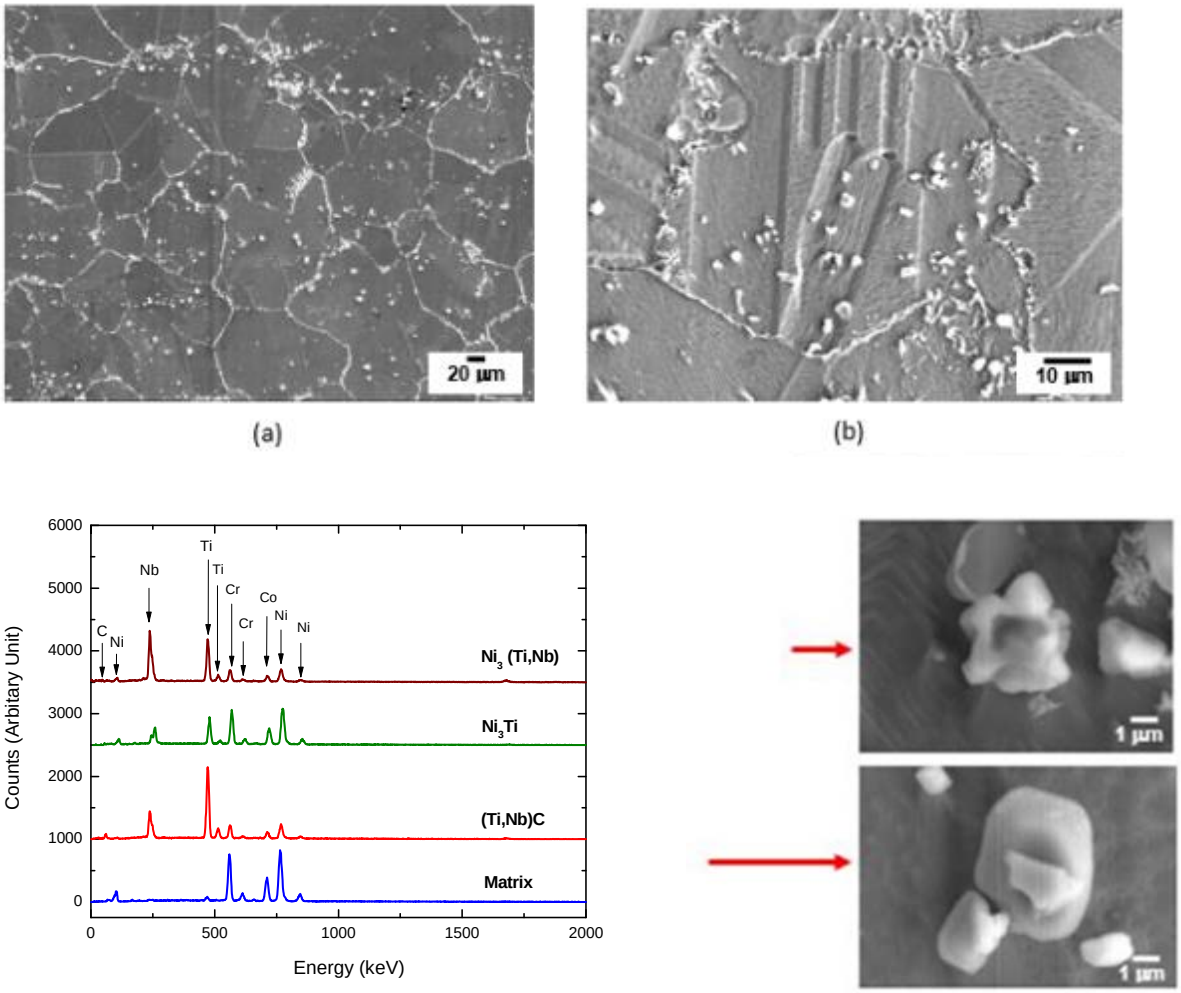

(c)

Figure 7: (a) SEM micrograph showing the microstructure of IN740-1 alloy, (b) closed-up of (a), and (c) Ni3Ti-based phase and (Ti, Nb) C in the microstructure with their EDX peaks

Conclusions

The concepts of high temperature reference electrode have been applied to investigate the hot corrosion of Ni based superalloy in synthetic coal ash environments. Due to the wholly sealed construction, the Ag/Ag^+/fused-quartz as well as the Ag/Ag^+/mullite reference electrodes are stable and re-usable in the same or similar electrolyte systems.

Subtask 2.2 In-situ Corrosion Monitoring Validation

Experimental Methods

Construction of Coal Ash Exposure Custom-Designed Unit

Construction of coal ash exposure custom-designed unit for lab-scale corrosion experiments has been completed in WVU (Figure 8a). There are three main systems in coal ash corrosion laboratory test configuration (Figure 8b):

1. Synthesis combustion gas exposure system,
2. High temperature corrosion system using tube furnace, and
3. Electrochemical measurement system

The electrochemical test data were analyzed using Metrohm Autolab PGSTAT302N with the Nova data acquisition system.

In-situ Monitoring of Coal Ash Hot Corrosion Using High Temperature Electrochemical Sensor

This research work demonstrates an application of a new high temperature electrochemical sensor system with a reliable reference electrode to provide a clearer picture of the corrosion degradation. The hot corrosion behavior of a Ni-based superalloy was studied in the presence of a synthetic coal ash and a synthetic flue gas containing sulphur dioxide using our proposed high temperature electrochemical sensor.

Electrochemical noise (EN), electrochemical impedance spectroscopy (EIS) and potentiodynamic polarization (PDP) measurements were used to study the corrosion behavior of a new Ni-based superalloy, inconel alloy 740 in a thin coal ash film environment. The EIS measurement was performed after measuring the open circuit potential for one hour between 1 Hz and 1×10^6 Hz with FRA system. The amplitude of the input sine signal was 10 mV and the interval of one EIS measurement was about 15 min. Simultaneous measurements of potential noise and current noise were conducted for 24 h. The EIS and EN measurements were carried out alternately during an exposure time of 123 h. PDP was measured with a scan rate of 0.5 mV s^{-1} after 123 h. The coal ash mixture consisted of reagent-grade 29.25 wt.% SiO_2, 29.25 wt.% Al_2O_3, 29.25 wt.% Fe_2O_3, 5.625 wt.% Na_2SO_4, 5.625 wt.% K_2SO_4 and 1 wt.% NaCl. The synthetic flue gas was composed of (in vol.%): 15 CO_2, 4 O_2 and 1 SO_2 and 80 N_2. The flow rate of the pre-mixed flue

gas was 150 ml min^{-1} and the operation temperature was 800 °C. The electrochemical test data were analyzed using the Metrohm Autolab/PGSTAT302N with the Nova data acquisition system.

(a)

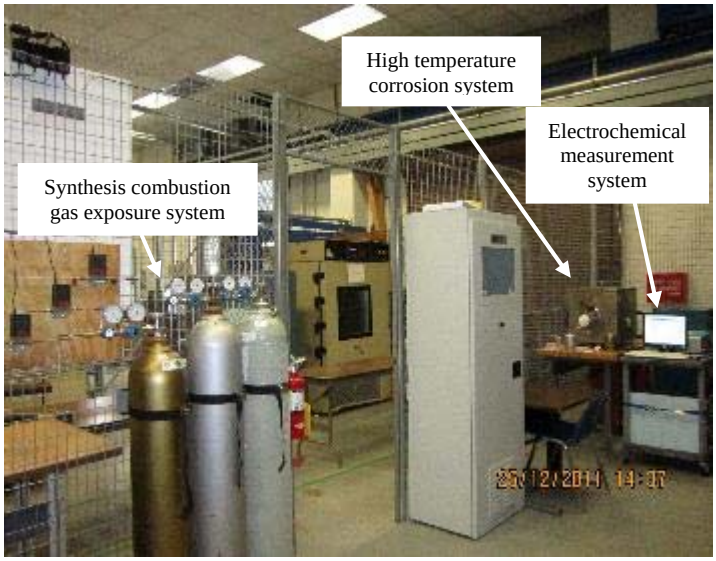

(b)

Figure 8: (a) Coal ash exposure custom-designed unit, and (b) Laboratory test configuration

Results and Discussions

January to March 2012

In-situ Monitoring of Coal Ash Hot Corrosion Using High Temperature Electrochemical Sensor

The EN is the most suitable technique for monitoring corrosion processes in-situ and its special advantage includes the possibility to detect and analyze the early stages of the localized corrosion process as well as corrosion rates. Typical time series plots of electrochemical noise test data are shown in Figure 9. The corrosion initiation stage was characterized by gradual potential shifting towards a more positive direction. The potential of the alloy shifted nearly 300 mV (from 100 mV to 400 mV vs Ag/Ag^{+}) (Figure 9a). The corresponding graph of current noise showed sudden spikes and the positive current density values decreased significantly (Figure 9b). The positive current density values indicate the preferential dissolution of one electrode only. The results suggest that recrystallization occurs of the protective oxide layer on the alloy surface. The recrystallization process near the surface can facilitate the inward movement of oxygen through a large number of grain boundaries, and then the inward-diffusing oxygen reacts with Al in the alloy to form Al_2O_3. Areas are protected in which the recrystallization process is more rapid than the initiation of corrosion. The potential values were stable after a longer exposure time (Figure 9a) and the corrosion propagated with negative (galvanic) current density values Figure 9b). Noise resistance has been shown to act as a useful indicator of the corrosion rate and data treatment in the time domain (R_n) and the frequency domain (R_{sn}) enabling the corrosion rate calculation. The noise resistance data processing included trend removal of the signal by minimum square linear fitting using the fast Fourier transform (FFT). The comparison of R_n and R_{sn} values is shown in Figure 9c. The values of R_{sn} and R_{sn} differ significantly even though they are based on the same original data. This result confirmed with other researcher's result. In the case of corrosion systems which are poorly stationary, misleading results can be produced with either fast fourier transform (FFT) or Maximum Entropy (MEM) method. It could be one of the reasons that R_{sn} is more sensitive to change in an unstable hot corrosion conditions than R_n. The localization index proved to be an indicator for the type of corrosion observed. It can be calculated as the ratio between the standard deviation of the measured current, σ_i and the root mean squared value of the current, I_{rms}. The values of this indicator can be between 0 and 1. A value close to 0 is observed for systems in which the measured current values show only small deviation with respect to the average current value. On the other hand, the localization index will be close to 1 when the individual current values are significantly deviating from the average current value. The results showed that the alloy is liable to suffer localized corrosion during 123 h (Figure 9d).

The EIS measurement can identify controlling mechanisms such as charge transfer or diffusion, and the solution resistances. The impedance spectra for the thin coal ash film corrosion of the alloy were similar during the initiation and propagation stages of corrosion, and are composed of a very small depressed semicircle at high frequency and a line at low frequency (Figure 10a). These typical features of an impedance spectrum suggested that the overall corrosion could be controlled by the diffusion of oxidants in the melts. The impedance was highly resistive after 123 h exposure. The impedance spectra upon repassivation indicate a double time-constant behaviour, suggesting the presence of both passive and

active areas in the pit. The impedance is essentially resistive in nature for the occurrence of an actively corroding pit on a passive surface. The PDP over a wide range of potential generates more information about localized corrosion susceptibility than just the corrosion rate (Figure 10b). The Tafel slope, β_a and β_c, for the anodic and cathodic reactions occurring at the open circuit were obtained from the linear extrapolation of the anodic and cathodic regions of the polarization curve. The values of polarization resistance (R_p), corrosion potential (E_{corr}), the corrosion current density (i_{corr}), and the corrosion rate are also summarized in Table 1.

Metallographic examination of the cross-sectional corroded surface showed significant localized pitting attack beneath the oxide scale (Figure 11). There are three different layers at the top of the cross sectional alloy surface. These layers can be identified from its corresponding elements mapping. The first top layer is the continuous Cr_2O_3 layer, the layer containing Ni-Al phase is the second layer, and followed by the layer containing Ni-Ti intermetallics (Figure 11a). Ni-Al phase could act as an Al-reservoir and the Ni-Al phase beneath the alloy surface could provide the Al to repair the Al_2O_3 scale during the recrystallization process. Formation of porous Cr_2O_3 can be the favourable condition for the initiation of hot corrosion. After 123 h exposure to hot corrosion, the internal pitting propagated at the Ni-Ti intermetallics sites inside and along the grain boundary as a consequence of inward-diffusing oxygen and sulphur (Figure 11b). It is evident that the alloy suffers serious hot corrosion with a deep corrosion affected zone (>50 μm) after 123 h.

Generally, Stern-Geary equation is used to convert noise resistance data in mass loss. However, this equation assumes that uniform corrosion is occurring and the corrosion reactions are activation controlled. For a diffusion-controlled hot corrosion process, the Stern-Geary constant (B) can vary significantly from system to system and it is therefore questionable to estimate the corrosion current density using B. This is another issue to address for the quantitative determination of corrosion rates in service, which is under investigation by the research team.

Conclusions

In summary, the concept of a high temperature reference electrode was applied to investigate the hot corrosion of Ni based superalloy in a synthetic coal ash environment. Due to the wholly sealed construction, the Ag/Ag^+/fused-quartz reference electrode is stable and re-usable in the same or similar electrolyte systems. The identical reference electrodes nominally deviate the potential value of ~400 mV with respect to the Ag/Ag^+/fused-quartz reference electrode. No visible damages to the electrode's outer tube were seen after continuously testing for 10 days. The preliminary results suggest that the proposed high temperature corrosion sensor can detect the hot corrosion process and corrosion rate via different electrochemical techniques. Future work will be focused on validation results with real time USC boiler systems, corrosion model development and testing sensor reliability and sensitivity for in-situ corrosion monitoring application.

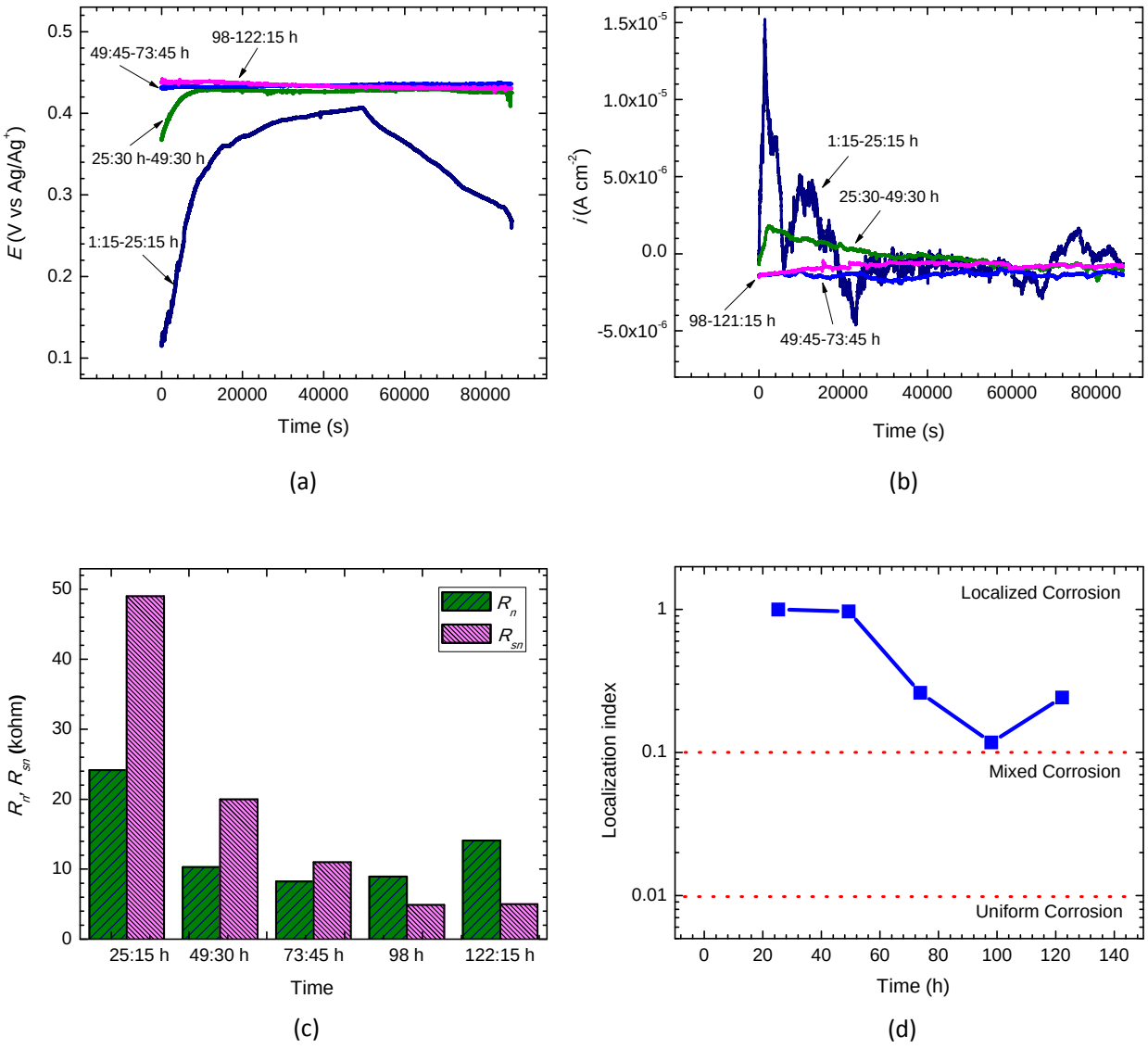

Figure 9: Time series of the electrochemical noise test data: (a) electrochemical potential noise, (b) electrochemical current noise, (c) Rsn and Rn, and (d) localization index

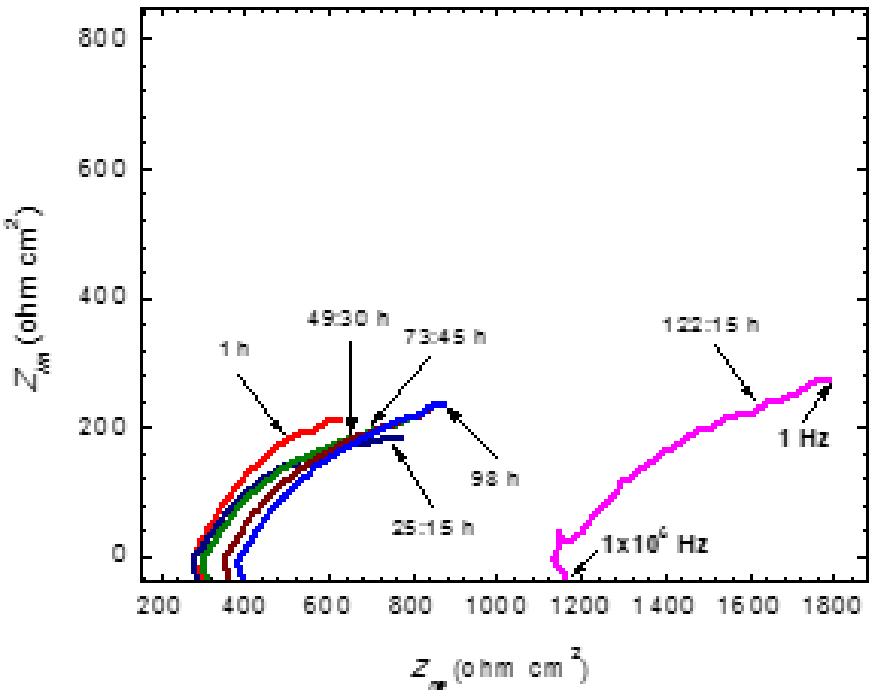

(a)

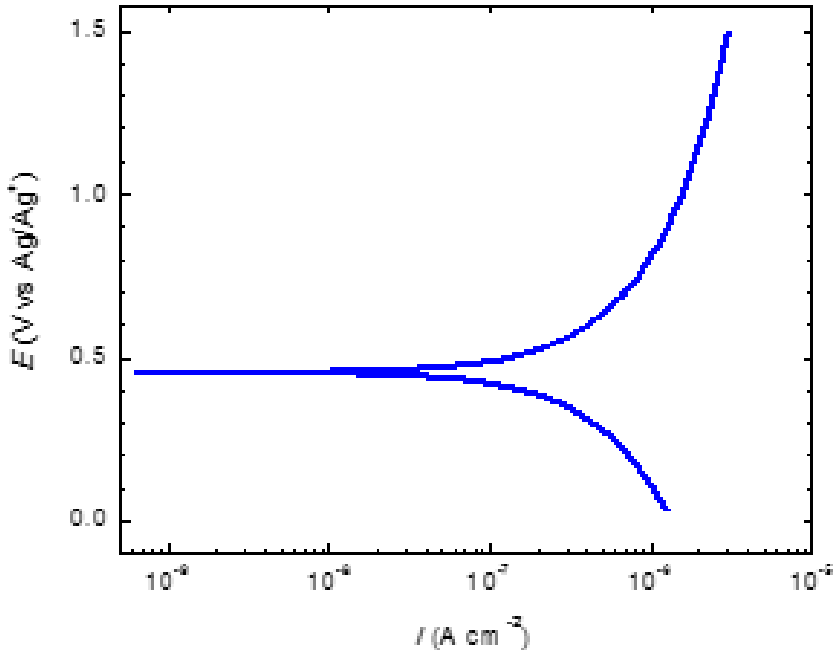

(b)

Figure 10: (a) Nyquist plots at different exposure times and (b) potentiodynamic polarization curve after 123 h

Table 1: Potentiodynamic polarization test data

R_p (KΩ)	E_{corr} (mV vs. Ag/Ag^+)	i_{corr} (μA cm^{-2})	β_a mV dec^{-1}	β_c mV dec^{-1}	Corrosion rate (mm y^{-1})
8.74	453	4.95	198	200	0.12

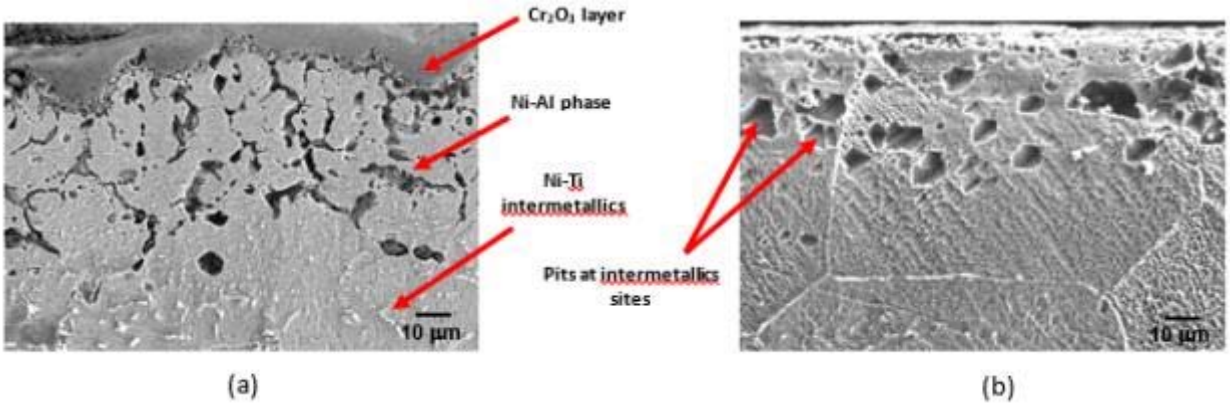

Figure 11: The cross-sectional corroded surface showing the extent of hot corrosion after 123 h: (a) before corrosion and (b) after corrosion

Subtask 2.3 Post-mortem Analysis

Experimental Methods

Effect of SO_2 in Flue Gas on Coal Ash Hot Corrosion of Inconel 740 Alloy - a High Temperature Electrochemical Sensor Study

The objectives of this research work are to test the sensor reliability and sensitivity for in situ corrosion monitoring in different coal-fired boiler environments, especially for the flue gas with and without SO_2, and to develop a method for the quantitative determination of localized corrosion rates in service via the electrochemical techniques. Our developed high temperature electrochemical sensor was applied to study the effect of SO_2 in flue gas on thin film coal ash corrosion of Inconel 740 superalloy at 750 °C. The response of electrochemical noise (EN), electrochemical impedance spectroscopy (EIS), and potentiodynamic polarization (PDP) test data from the sensor is compared with the results from a weight loss test. There is a good correlation between the electrochemical data and the actual degradation processes. The current noise analysis in time and frequency domains for the quantitative determination of hot corrosion rate in service is discussed.

Materials and Heat treatment

The Inconel 740 Ni-based superalloy was chosen to test its hot corrosion resistance. Prior to testing the alloy was given the following sequence of heat treatment: 1150 °C for 4 h followed by air cooling; 1120

°C for 1 h followed by air cooling; 850 °C for 16 h followed by air cooling. The alloy was then cut into samples of 10 mm×10 mm×2 mm in dimension for electrochemical tests and weight loss measurement.

High Temperature Electrochemical Sensor

The sensor was based on a four-electrode system which includes two identical working electrodes (WE1 and WE2), one reference electrode (RE) and one counter electrode (CE). The Inconel 740 alloy was used for the working electrodes. The reference electrode was the Ag/Ag^+ electrode which contained 10 mol% Ag_2SO_4 in the 90 mol% Na_2SO_4 molten salt. The platinum wire was used as a counter electrode.

Corrosive Medium

This research highlights how SO_2 content in flue gas affects the hot corrosion resistance of the Inconel 740 alloy. The alloy was studied in the presence of a synthetic thin coal ash environment and a synthetic flue gas with and without SO_2 at 750 °C. A thin film of a coal ash was established on the alloy surface to obtain a layer thickness of about 1 mm. The coal ash mixture consisted of reagent-grade 29.25 wt.% SiO_2, 29.25 wt.% Al_2O_3, 29.25 wt.% Fe_2O_3, 5.625 wt.% Na_2SO_4, 5.625 wt.% K_2SO_4 and 1 wt.% NaCl. The synthetic flue gas without SO_2 as composed of (in vol.%): 15% CO_2, 4% O_2 and 81% N_2 and the composition of the gas with SO_2 was 15% CO_2, 4% O_2, 80% N_2 and 1% SO_2. The flow rate of the pre-mixed flue gas was 150 ml min^{-1}.

Weight Loss Measurement

The hot corrosion kinetics were determined through the relationship between accumulated mass loss and corrosion time according to ASTM G31. Before the test, the samples were ground on progressively finer grades of emery paper (up to 2500 grit) and then followed by 3 μ diamond paste polishing. The polished and pre-weighed specimens were exposed to the hot corrosive medium for 123 h. Afterwards, the samples were washed in boiling water for 15 minutes to dissolve the remaining coal ash. The corrosion products were then removed by ultrasonic cleaning with acetone before the final weighing. The corrosion rate was calculated in millimeters per year (mm y^{-1}). The scale thickness and penetrated oxide that formed within the alloy matrix and along grain boundaries in the substrate were also measured using the cross-sectional corroded surface analysis. Duplicate experiments were conducted to make sure the results fell within the expected error.

Electrochemical Measurements

The electrochemical behavior of the hot corrosion was studied using open circuit potential (OCP), electrochemical noise (EN), electrochemical impedance spectroscopy (EIS), and potentiodynamic polarization (PDP) measurements. All measurements were taken from a single electrochemical sensor. The EIS measurement was performed with an FRA system after measuring the open circuit potential for one hour. The frequency range considered was from 1×10^5 Hz to 0.1 Hz using 10 mV root mean square as the amplitude of the perturbation signal. The interval of one EIS measurement was about 15 min. Simultaneous measurements of potential noise and current noise were conducted for 24 h. The EIS and EN measurements were carried out alternately during an exposure time of 123 h. PDP was measured with a scan rate of 0.5 mV s^{-1} after 123 h. The electrochemical test data were analyzed using the Metrohm

Autolab/PGSTAT302N with the Nova data acquisition system. The time-series data of the current noise were transformed into frequency domain by using the fast Fourier transformation (FFT) method.

Surface Morphology Characterization

Scanning electron microscopy (SEM) equipped with an energy-dispersive X-ray microanalysis (EDX), and X-ray diffraction (XRD) were used to characterize the microstructure, the corroded surfaces and the corrosion products. The samples were carefully ground and polished to expose cross-sections of corrosion layers.

Results and Discussions

April to June 2012

Effect of SO_2 in Flue Gas on Coal Ash Hot Corrosion of Inconel 740 Alloy - a High Temperature Electrochemical Sensor Study

Open Circuit Potential

The initial corrosion potentials of the alloy were obtained from OCP measurements for 1 h (Figure 12). The potential in the flue gas with SO_2 (150 mV vs Ag/Ag^+) was much higher than that in the flue gas without SO_2 (−60 mV vs Ag/Ag^+). The difference in the potentials clearly indicated that the corrosion in two different flue gas environments were under different corrosion-controlled mechanisms. In any metal-sulfate system, the oxidizing character of sulfate melt must result from the promotion or acceleration of the dissociation of the sulfate ion:

Equation 1 $SO4^{2-} = SO_3 + O^{2-}$

The corrosion of nickel in molten sulfates in the flue gas without SO_2 appears to result from reaction with SO_3 derived from dissociation of SO_4^{2-} anions. The sulfate oxidation could be more predominant in the flue gas with SO_2 because it usually occurs at very positive potentials on the passive nickel surface. SO_2 from the gas phase to the metal surface can take place readily in the melt due to the chemical interaction which is represented by the sulfate-pyrosulfate equilibrium:

Equation 2 $2SO_2+O_2 = 2SO_3$

Equation 3 $SO_3 + SO_4^{2-} = S_2O_7^{2-}$

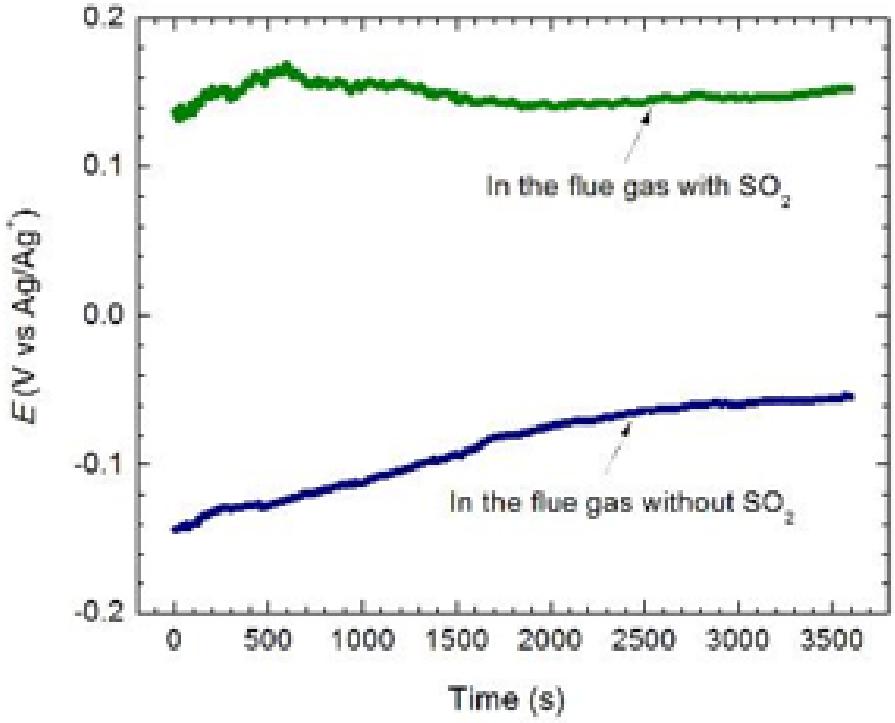

Figure 12: Comparison between OCP values after 1 h exposure

Electrochemical Noise Test Data

The initiation and propagation stages of the hot corrosion process were monitored using the EN measurement. Simultaneous measurements of potential noise and current noise were made every 24 h during 123 h of total experimental immersion. The EN data in the flue gas without SO_2 and with SO_2 environments are given in Figure 13-Figure 16. The time-series of potential noise data showed that electrode potential changed continuously towards more positive values approaching. The values in the flue gas without SO_2 varied from –180 mV (vs Ag/Ag^+) to –80 mV (vs Ag/Ag^+) during 123 h exposure (Figure 13a). In contrast, the potentials in the flue gas with SO_2 gave more stable values (Figure 13b). After 123 h, the potential of the alloy in the flue gas without SO_2 was –80 mV (vs Ag/Ag^+) and that in the flue gas with SO_2 was 380 mV (vs Ag/Ag^+).

The active potential observed in the flue gas without SO_2 could be attributed to a mixed electrode process, which is accompanied by the direct adsorption of the SO_3 species at the electrode interface on the dissolution and passivation of Ni in the sulfate melt:

Equation 4 $SO_4^{2-} + Ni = Ni\text{--}SO_3 + 1/2\ O_2 + 2e$

The tendency of the nickel is to become a Ni, Ni/O^{2-} electrode on approaching the redox potential of the melt, which is approximately (–80 mV vs Ag/Ag^+) in molten Na_2SO_4 in air. The subsequent rise of potential would result from the dissolution nickel and the formation of nickel oxide.

Equation 5 $Ni\text{--}SO_3 + SO_4^{2-} = NiO + 2SO_3 + 2e$

At any particular state of oxidation, the acidity will be determined by the solubility of the metal oxide. The presence of SO_2 in the flue gas can create a direct interaction of the $NaKSO_4$ melt with SO_3 to form low melting point eutectic mixtures of alkali pyrosulfates:

Equation 6 $NaKSO_4 + SO_3 = NaKS_2O_7$

As a consequence, the acidity of the sulfate anion in terms of the acid-base equilibrium $SO_4^{2-} = SO_3 + O^{2-}$ increases leading to the enhancement of the solubility of the corrosion products.

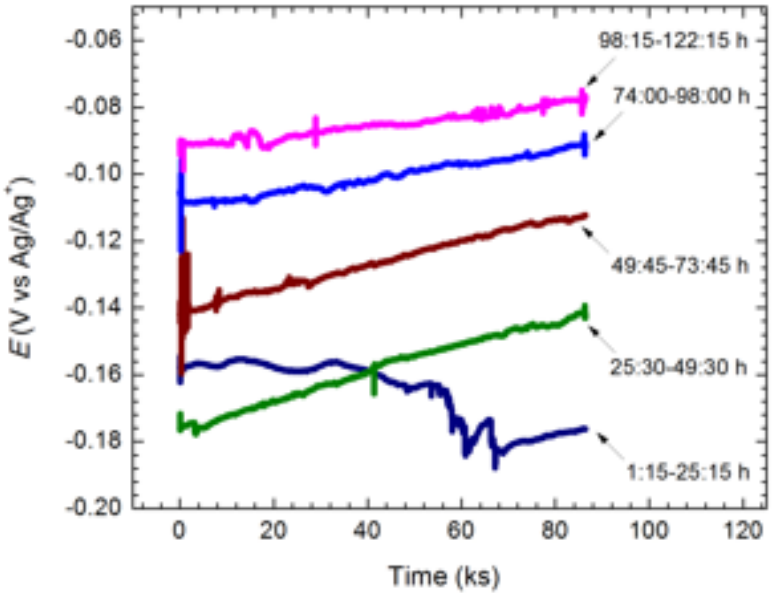

(a)

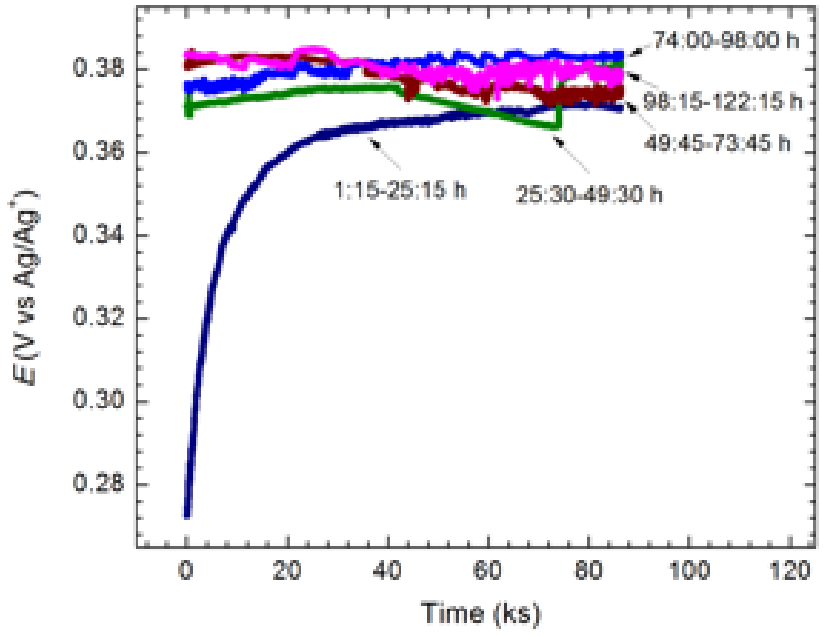

(b)

Figure 13: Time series of the electrochemical potential noise test data at different flue gas environments: (a) in the flue gas without SO2 and (b) in the flue gas with SO2

Variation of the current noise values in the time and frequency domains for two different flue gas environments are shown in Figure 14 and Figure 15. The time records of current noise showed that significant current value changes occurred during 98:15-122:15 h in the flue gas without SO_2 (Figure 14a) while 25:30-49:30 h for the flue gas with SO_2 (Figure 15a) as a consequence of changes in the corrosion stage. These results suggest that the presence of SO_2 in the flue gas shortened the induction stage of localized corrosion. The current noise signatures in the flue gas without SO_2 were characterized by quick changes followed by slow recovery. In contrast, the characteristic current transients in the flue gas with SO_2 were featured with quick changes followed by no recovery. Obviously, these two different current noise signatures could be applied as a means to differentiate the severity of the corrosion. Current noise has a direct relation with the underlying process and if the reaction rate increases, the current noise will also increase. In the hot corrosion process of Ni, the particular increase of the current densities can be observed as soon as Ni begins to be polarized may have been due to the immediate formation of soluble corrosion products. The corresponding power spectral densities (PSDs) in the flue gas without SO_2 and with SO_2 are shown in Figure 14b and Figure 15b respectively. Both of the PSDs are almost independent of the frequency in the region lower than 0.0001 Hz. The trend of the PSDs against the frequency was quite similar, but the values varied with a change in the time as well as the test environments.

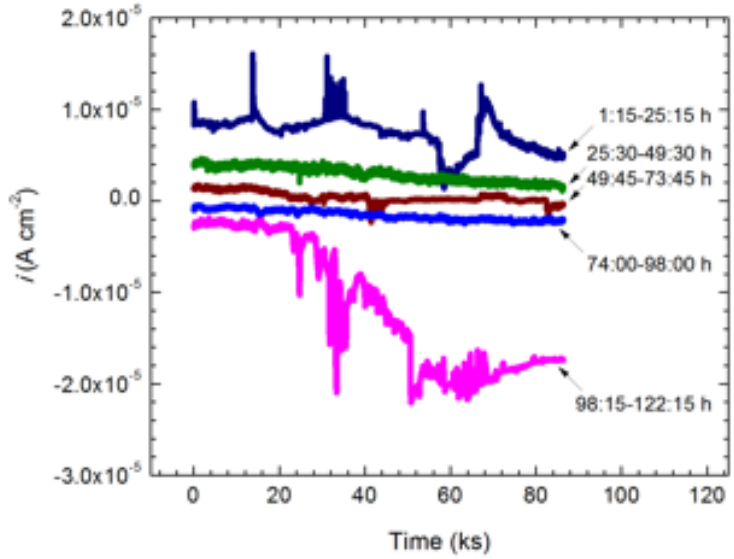

(a)

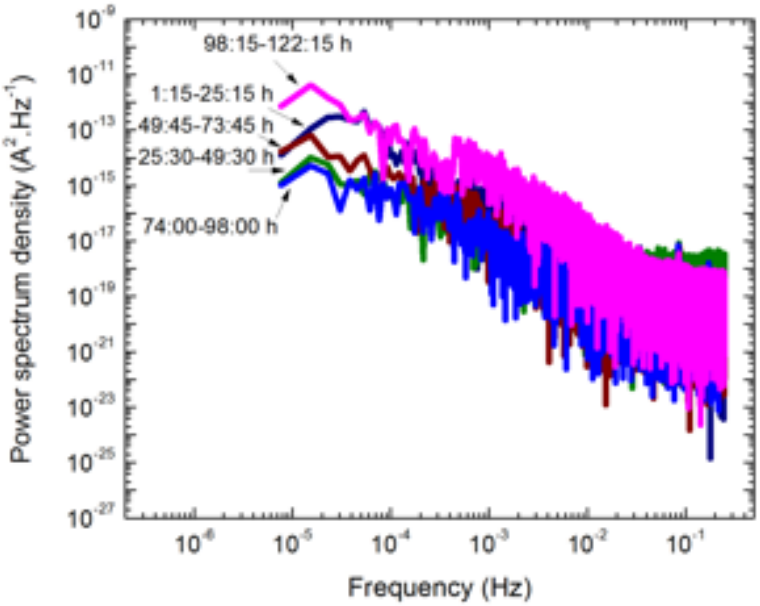

(b)

Figure 14: (a) Time domain and (b) frequency domain of the electrochemical current noise test data in the flue gas without SO2 environment

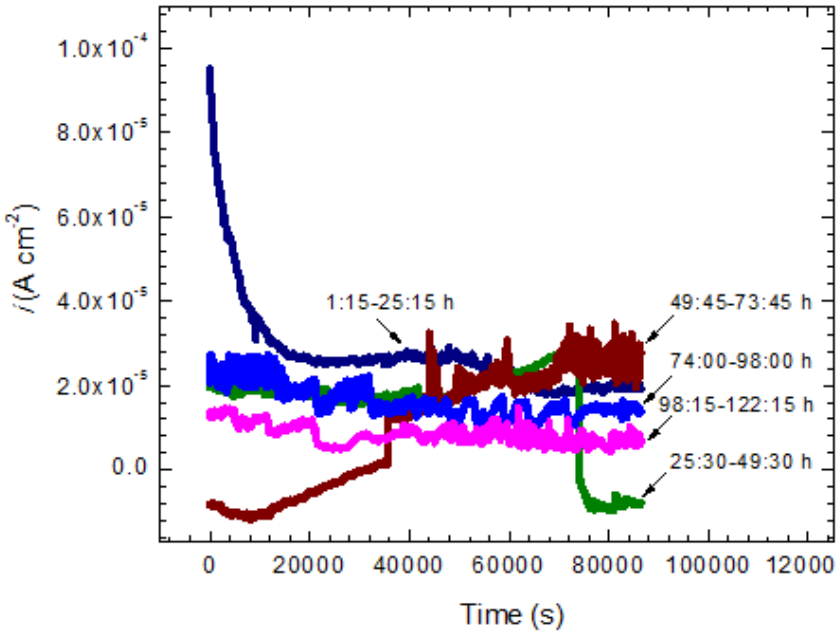

(a)

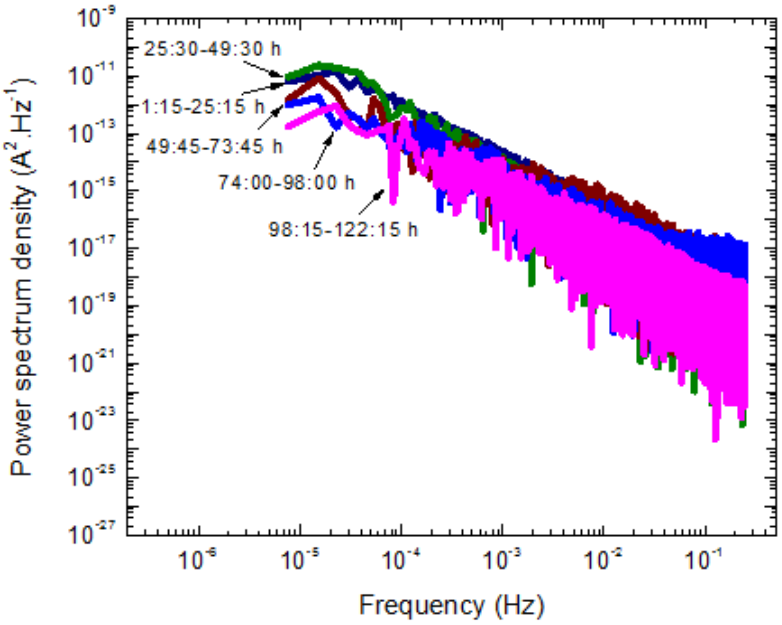

(b)

Figure 15: (a) Time domain, and (b) frequency domain of the electrochemical current noise test data in the flue gas with SO2 environment

The determination of electrochemical noise resistance in the time domain (R_n) and the frequency domain (R_{sn}) can provide reasonable estimates of the corrosion rate. A comparison of R_n and R_{sn} for both flue gas environments is given in Figure 16a. Throughout the exposure time, the values of R_n and R_{sn} in the flue gas with SO_2 were much lower suggesting that the corrosion rates in the flue gas with SO_2 were higher than those in the flue gas without SO_2. The lowest R_n and R_{sn} values (the highest corrosion rate) were observed at 73:45 h in the flue gas with SO_2 and 122:15 h in the flue gas without SO_2 respectively. The localization index, the ratio between the standard deviation of the measured current (σ_i) and the root mean squared value of the current (I_{rms}), can prove if the hot corrosion is under localized attack or not. The localization indexes were close to one when the individual current values are significantly deviating from the average current value and it can be close to zero when the individual current values are slightly deviating from the average current value. The results show that the alloy suffered localized attack in both flue gas environments, but the extents of localization in the flue gas with SO_2 were higher than those in the flue gas without SO_2 (Figure 16b). In order to determine the prevailing corrosion mechanism from the localization index a delicate balance should exist between sufficient trend removal and preventing the loss of valuable data.

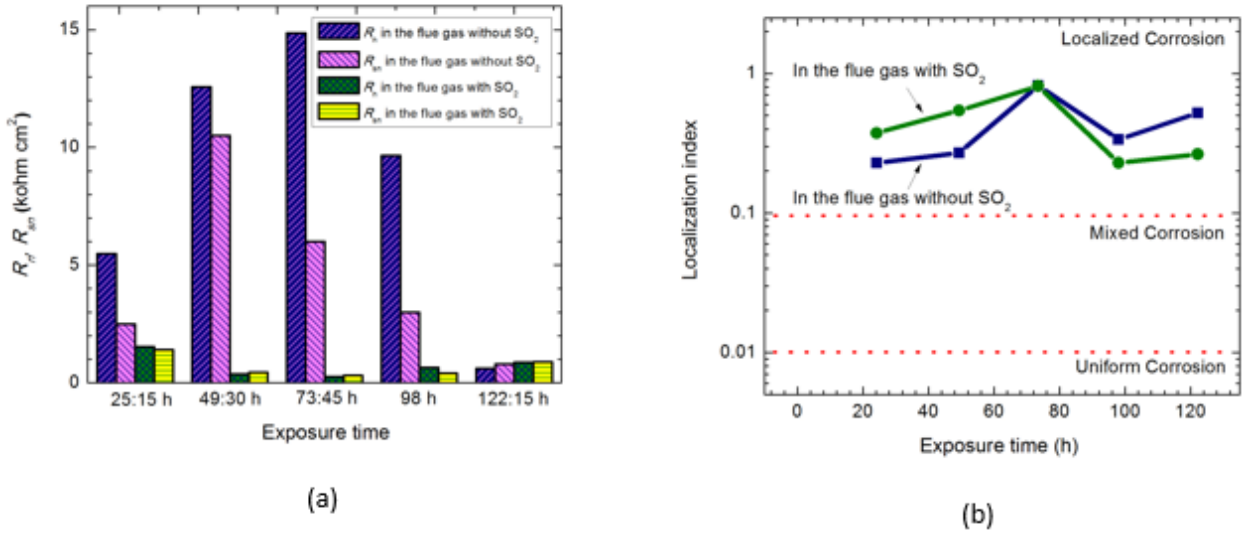

Figure 16: Comparison between the electrochemical noise test data at different flue gas environments: (a) Rn and Rsn and (b) localization index

Electrochemical Impedance Spectra

A typical Nyquist plot obtained in two flue gas environments at different exposures are shown in Figure 17. A change in the solution resistance was observed as the exposure time increased (Figure 17a-Figure 17d). The impedances were highly resistive in nature and it could be due to the resistive effect of the corrosion products dissolved in the molten salt. The porous corrosion products formed on the metal surface are permeable to the molten salt, and thus may influence the diffusion direction of oxidants. The diffusion-dominated controlled process was observed after 122:15 h in the flue gas without SO_2 (Figure 17c). In case of the flue gas with SO_2 the diffusion process started to occur after 49:30 h, however corrosion propagation stages did not clearly show how kinetic information could be obtained (Figure 17d).

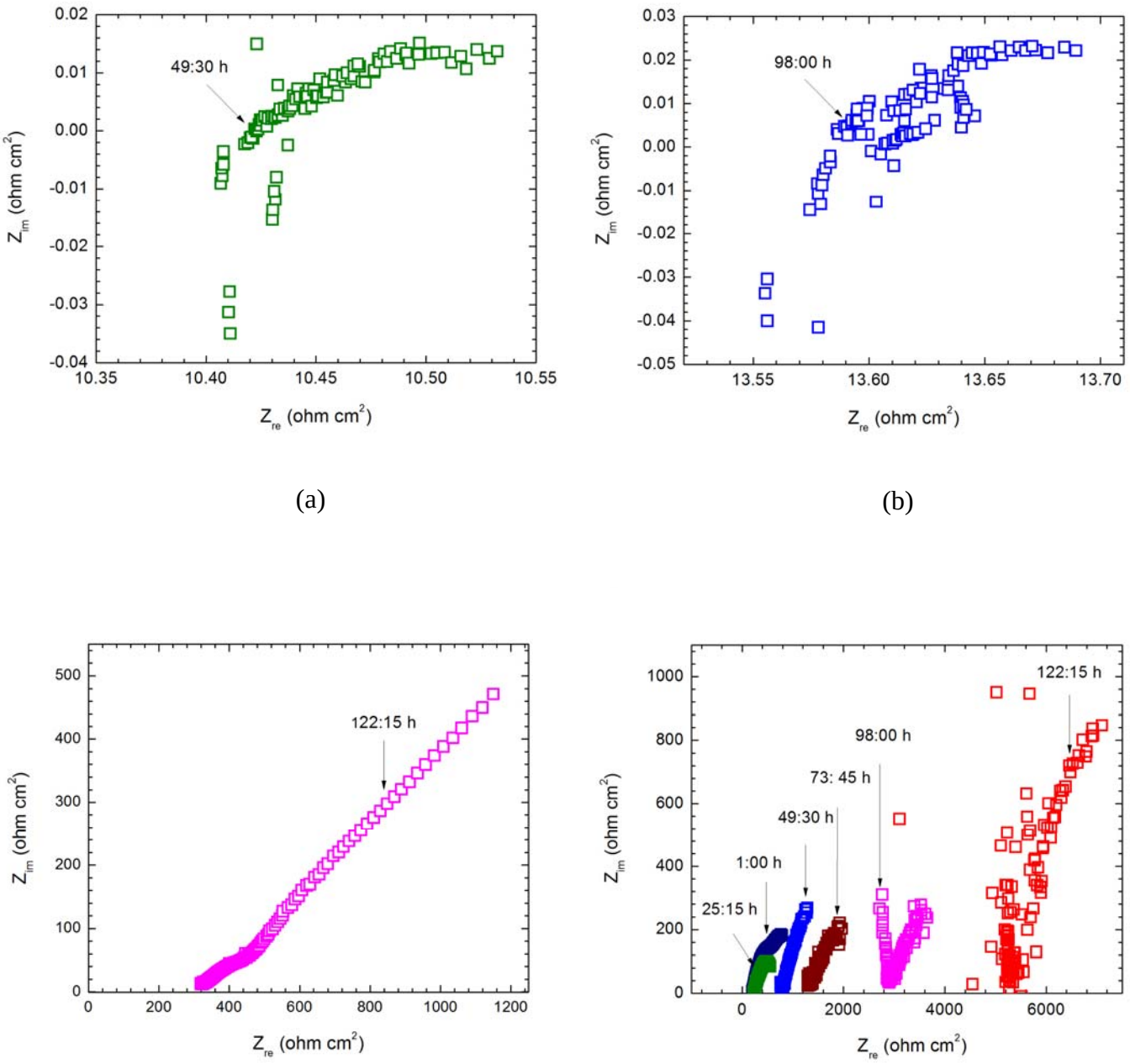

Figure 17: Nyquist plots at different flue gas environments: (a, b, c) in the flue gas without SO2, and (d) in the flue gas with SO2

Potentiodynamic Polarization Curves

The polarization resistance (R_p), corrosion potential (E_{corr}), the corrosion current density (i_{corr}), and the corrosion rate of two different flue gas environments were determined by the potentiodynamic polarization measurements (Figure 18) and the values are summarized in Table 2. The E_{corr} in the flue gas without SO_2 (–68.35 mV vs Ag/Ag^+) was much lower than that in the flue gas with SO_2 (327.75 mV vs Ag/Ag^+). The i_{corr} value and the corrosion rate in the flue gas with SO_2 were higher compared with the flue gas without SO_2. The results confirmed that the response of PDP test data were consistent with the OCP as well as EN measurements.

Table 2: Potentiodynamic polarization test data at different flue gas environments

	R_p ($k\Omega\ cm^{-2}$)	E_{corr} (mV vs Ag/Ag^+)	i_{corr} ($\mu A\ cm^{-2}$)	β_a mV dec^{-1}	β_c mV dec^{-1}	Corrosion rate (mm y^{-1})
In the flue gas without SO_2	6.38	–68.35	24.72	624.48	–866.86	0.59
In the flue gas with SO_2	13.17	327.75	30.88	1684	–2109	0.74

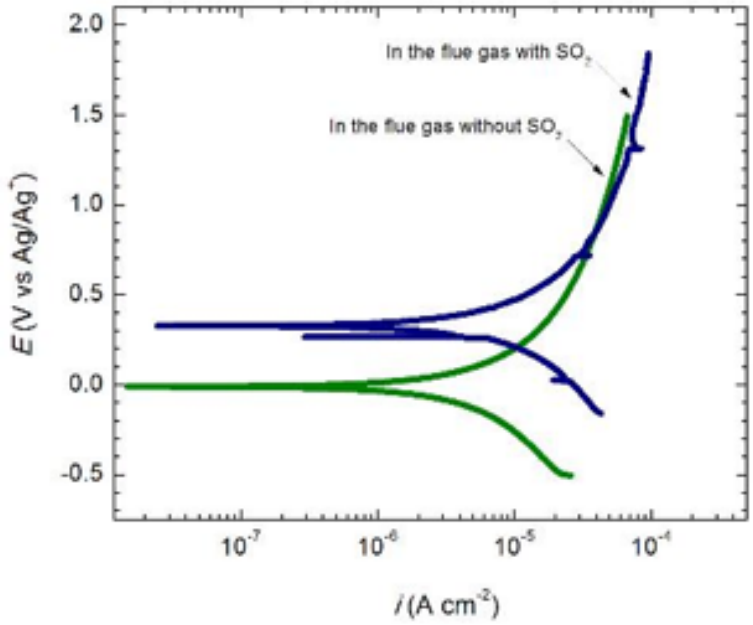

Figure 18: Comparison between potentiodynamic polarization curves at different flue gas environments

Quantitative Evaluation of Corrosion Rate via Electrochemical Noise Technique

Among the electrochemical monitoring techniques EIS gives the frequency-dependent impedance. The low frequency limit of the impedance magnitude can be related to *Rp* and thus the corrosion rate using the Stearn-Geary equation. Since the Nyquist diagrams obtained with both flue gas environments deviated from the typical diffusion-controlled process it was not clear how kinetic information could be obtained. PDP monitoring is useful for sensing the onset of localized corrosion through a decrease in R_p. However, localized corrosion of the unknown active area makes it difficult to determine the current density from R_p even using assumed Tafel slopes. PDP is also considered to be a fast and efficient method for measuring corrosion rate on-site, however the use of a polarization curve is very limited due to its destructive nature.

The prime attraction of EN against other electrochemical techniques is that during the measurement process, the corrosive systems under study are not instrumentally disturbed, and therefore, the systems are kept at their natural corrosion potential. The results of simultaneously monitoring the potential and coupling current from two coupled identical electrodes in EN measurement can be used to quantitatively evaluate corrosion rate. It has also been demonstrated that analysis in the time domain provides direct quantitative information on electrochemical processes that cannot be obtained from frequency-domain analysis. The electrochemical loss calculated from the current values correlate with the true values of metallic loss from the weight loss measurement. According to Faraday's Law expression, whenever there is a large potential difference (e.g. > 100 mV) between anodic and cathodic zones the current value can be used to estimate instantaneous localized corrosion rates (*R*) at the anodic zone. In this study, the maximum value of current noise, i_{max}, for each exposure period was used to calculate *R* using Equation 7 and the corresponding corrosion rates in the time and the frequency domains are presented in Figure 19a.

Equation 7 $$R = \frac{KM}{n\rho} i_{max}$$

where,
K = Constant for converting units
M = Atomic mass
n = Number of electrons freed by the corrosion reaction
ρ= Density

An instantaneous corrosion rate was used to determine total corrosion depths over the total experimental period. This was achieved by summing the corrosion depths over various periods of exposure to give a cumulative result. The calculated total corrosion depths can be correlated quantitatively with the microscopically observed corrosion depths. The result confirms the accuracy of the corrosion measurement method. The corrosion depth (*D*) during the specific period is calculated by Equation 8:

Equation 8 $$D = K \times R \times period$$

where the period is normally 24 h and the corrosion rate is assumed to be constant.

The accumulated mass loss and corrosion depths over the entire duration of exposure are given in Figure 19b and Figure 19c. The *R* values, the accumulated mass loss and corrosion depths in the time domain were higher than the values in the frequency domain for all exposure periods. In comparison with the mass loss values from the weight loss test the results show that there was a good correlation between the observed mass loss values for a 123 h period and its calculated mass loss values from EN analysis in the time domain (Figure 19b).

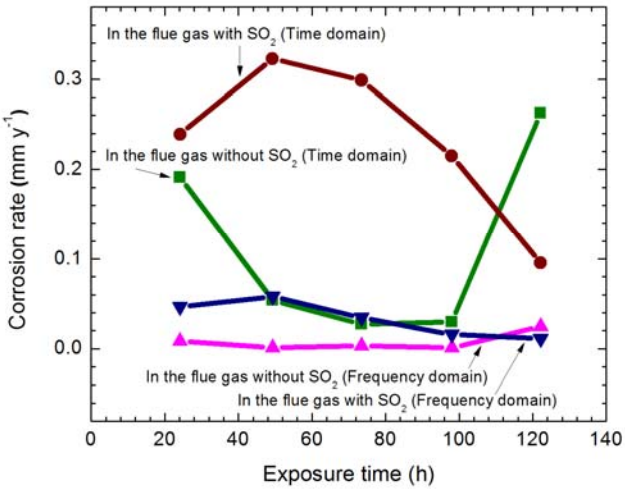

(a)

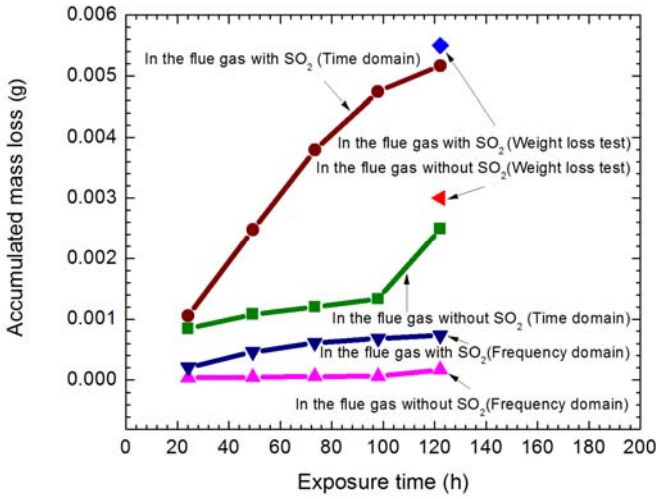

(b)

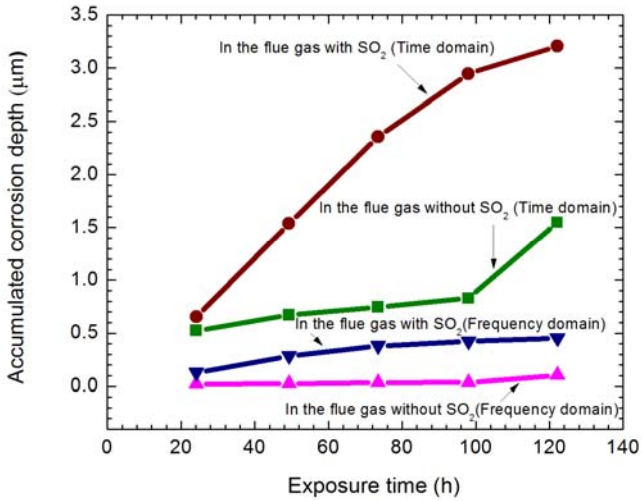

(c)

Figure 19: Comparison between corrosion kinetic data from EN analysis at different flue gas environments: (a) corrosion rates, (b) accumulated mass loss, and (c) accumulated corrosion depths

Corroded Surface and Corrosion Products Analysis

The possible corrosion mechanisms are elucidated on the basis of corroded surface analysis. SEM micrographs of the top and cross sectional corroded surfaces of both environments after 123 h are shown in Figure 20. The top corroded surfaces clearly indicate that the oxide layer formed first followed by localized hot corrosion beneath the layer and the internal corrosion propagated intergranularly as well as intragranularly (Figure 20a and Figure 20c). In the hot corrosion process, the localized corrosion zone may be covered with a nonprotective scale or directly exposed to the molten salts, while the rest (slow corrosion zone) is covered with a more protective scale. The depths of corrosion attack in both flue gas environments can be compared qualitatively from the cross-sectional corroded surface analysis (Figure 20b and Figure 20d). As expected, the extent of corrosion in the flue gas with SO_2 was higher than that in the flue gas without SO_2.

The coal ash hot corrosion process of the Inconel 740 alloy in flue gas with and without SO_2 at 750 °C can be described by the following sequences. In the initial stage, the oxidation of the elements such as chromium, titanium, aluminum, nickel and cobalt occurred at the matrix/oxide interface (Figure 21). XRD analysis confirmed that the oxide layer was rich in Cr_2O_3, TiO_2, Al_2O_3 and $(Ni,Co)Cr_2O_4$ (Figure 22). In this case, (Ni,Co)O can be surrounded with Cr_2O_3 and the solid-state reaction occurs to form $(Ni,Co)Cr_2O_4$ spinel in the scale gradually and dispersed in external oxide layer.

In the propagation stage, two main mechanisms of coal ash hot corrosion; the melting of sulfate salt followed by sulfidation, were expected to occur. If Na_2SO_4 and K_2SO_4 coexist they form a eutectic mixture having a low melting temperature. The eutectic mixture becomes molten when the layer thickness increases and the temperature of the outer surface of the layer reaches the melting point. The appearance of a molten sulphate salt layer is known to be a fundamental prerequisite for the occurrence of hot corrosion and it is shown to be particularly aggressive towards Ni superalloys. From XRD analysis of the top corroded surfaces $NaKS_2O_7$ was observed in the flue gas with SO_2, but no significant peak of $NaKS_2O_7$ was detected in the flue gas without SO_2 (Figure 22). The elemental distribution maps obviously showed the reaction product area containing $NaKSO_4$ together with Ni and Co beneath the oxide layer (Figure 23).

During the exposure period, the matrix dissolved in the molten salt and diffused to the salt/gas interface where it precipitated as metal oxides, sulfates and sulfides. In comparison between the distribution of sulfur at cross-sectional corroded surfaces in the flue gas without SO_2 (Figure 21) and with SO_2 environments (Figure 24), the extent of sulfidation attack was much higher in the flue gas with SO_2. After exposure for 123 h, the corroded metallic flakes were not very adherent and flaked/peeled off and their distribution in the corrosion products for both flue gas environments is shown in Figure 25a-Figure 25d. The results from EDX analysis suggest that the flakes are mainly composed of Cr_2O_3, Al_2O_3 and TiO_2. Besides these oxides nickel, cobalt, potassium and sulfur elements were also observed in the corrosion products of the flue gas with SO_2 as a consequence of sulfidation (Figure 25e). The elemental distribution maps (Figure 26) and XRD analysis (Figure 27) confirmed that the sulfide compounds were Ni_3S_2 and Co_3S_4. The sulfur transfer from the environment to the alloy is determined by direct reaction of the oxide-forming

alloying elements with the SO_2. Strong oxide formers, such as chromium and aluminum, tend to form protective oxide layers but also increase the driving force for sulfidation.

The following oxidation reactions at the matrix/salt interface and the reduction reactions at the salt/gas interface could be anodic and cathodic electrochemical reactions during sulfidation.

The cathodic reactions are:

Equation 9 $S_2O_7^{2-} + 2e = SO_4^{2-} + SO_2 + O^{2-}$

Equation 10 $SO_2 + 6e = S^{2-} + 2O^{2-}$

The anodic reactions are:

Equation 11 $Ni = Ni^{2+} + 2e$

Equation 12 $Co = Co^{3+} + 3e$

Formation of Ni_3S_2 and Co_3S_4 in the corrosion products:

Equation 13 $3Ni + 2S = Ni_3S_2$

Equation 14 $3Co + 4S = Co_3S_4$

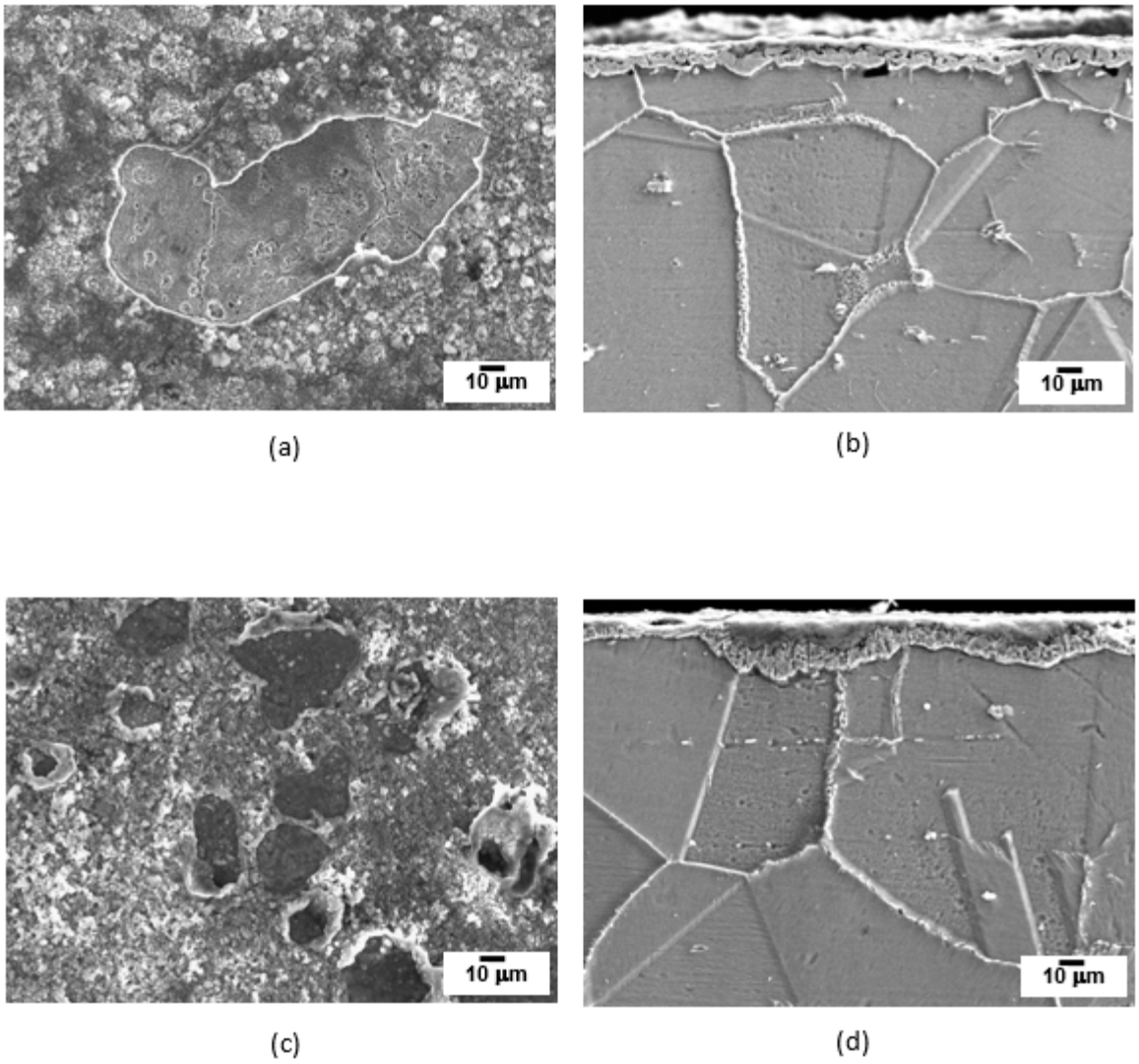

Figure 20 Corroded surfaces in different flue gas environments after 123 h: (a) top and (b) cross-sectional surfaces in the flue gas without SO_2, and (c) top and (d) cross-sectional surfaces in the flue gas with SO_2

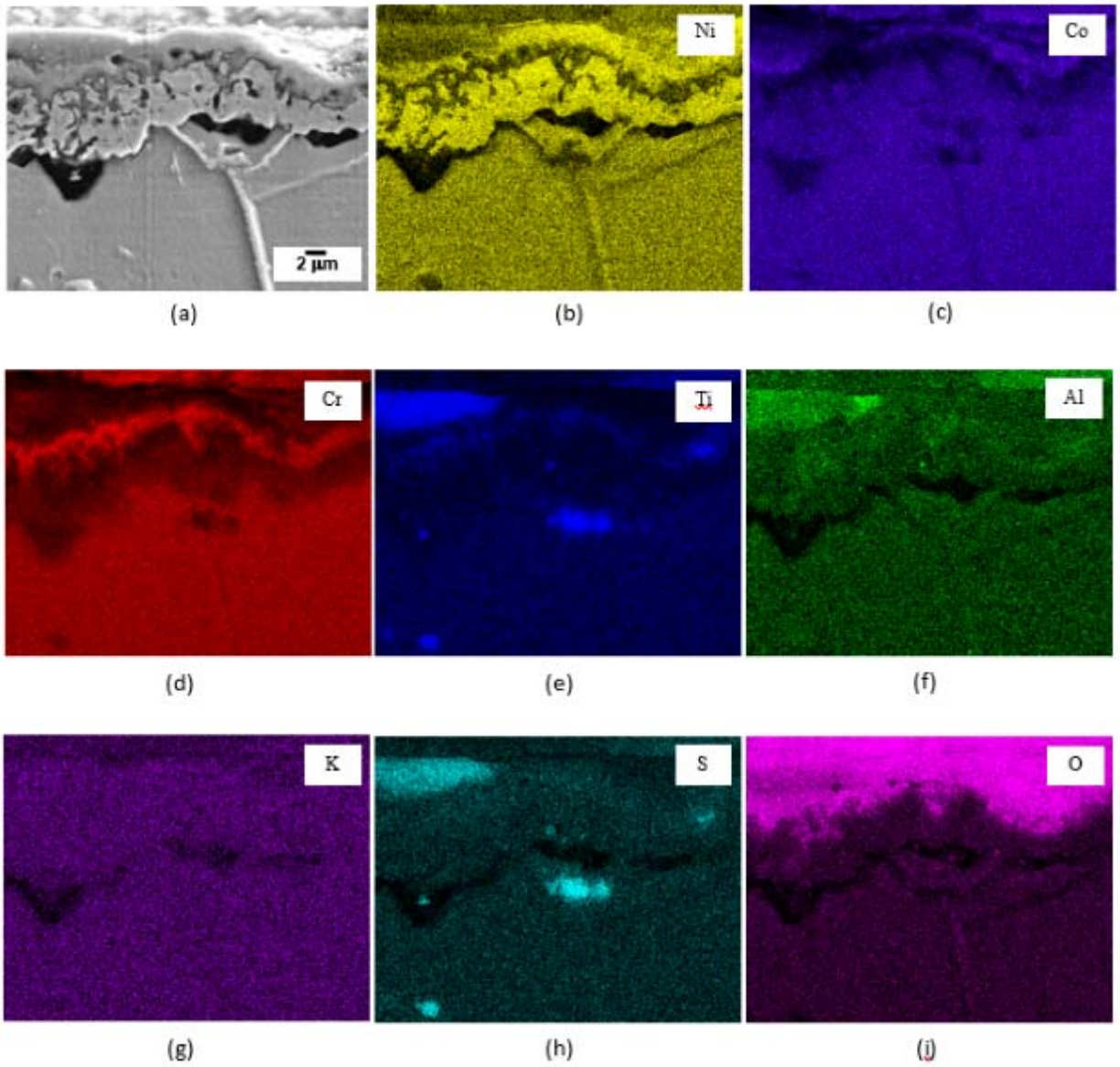

Figure 21 (a) Cross-sectional corroded surface showing metallic oxides formation in the flue gas without SO_2 environment, and (b, c, d, e, f, g, h, i) its corresponding elements mapping

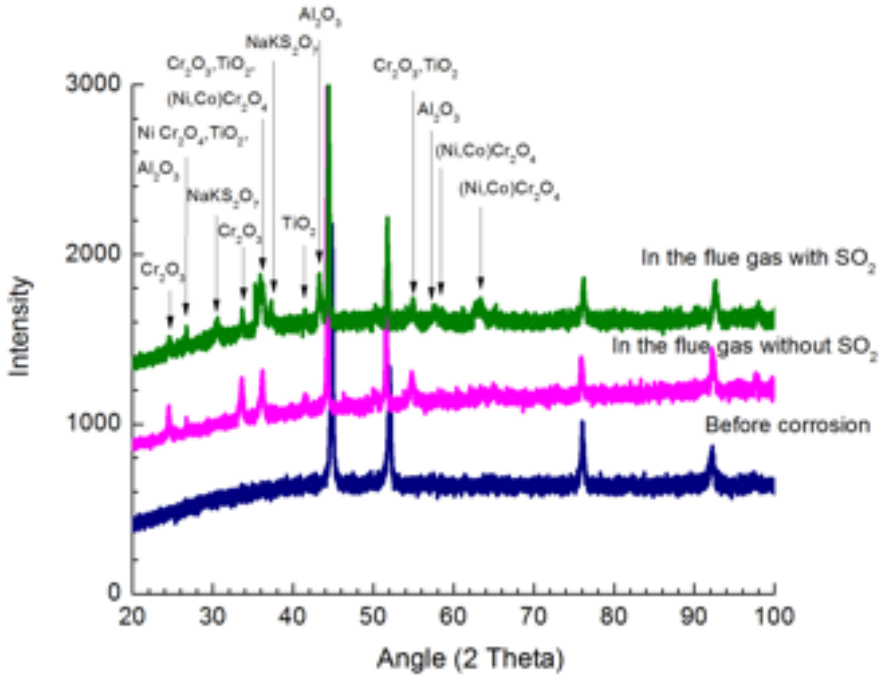

Figure 22 XRD patterns of the top corroded surfaces at different flue gas environments

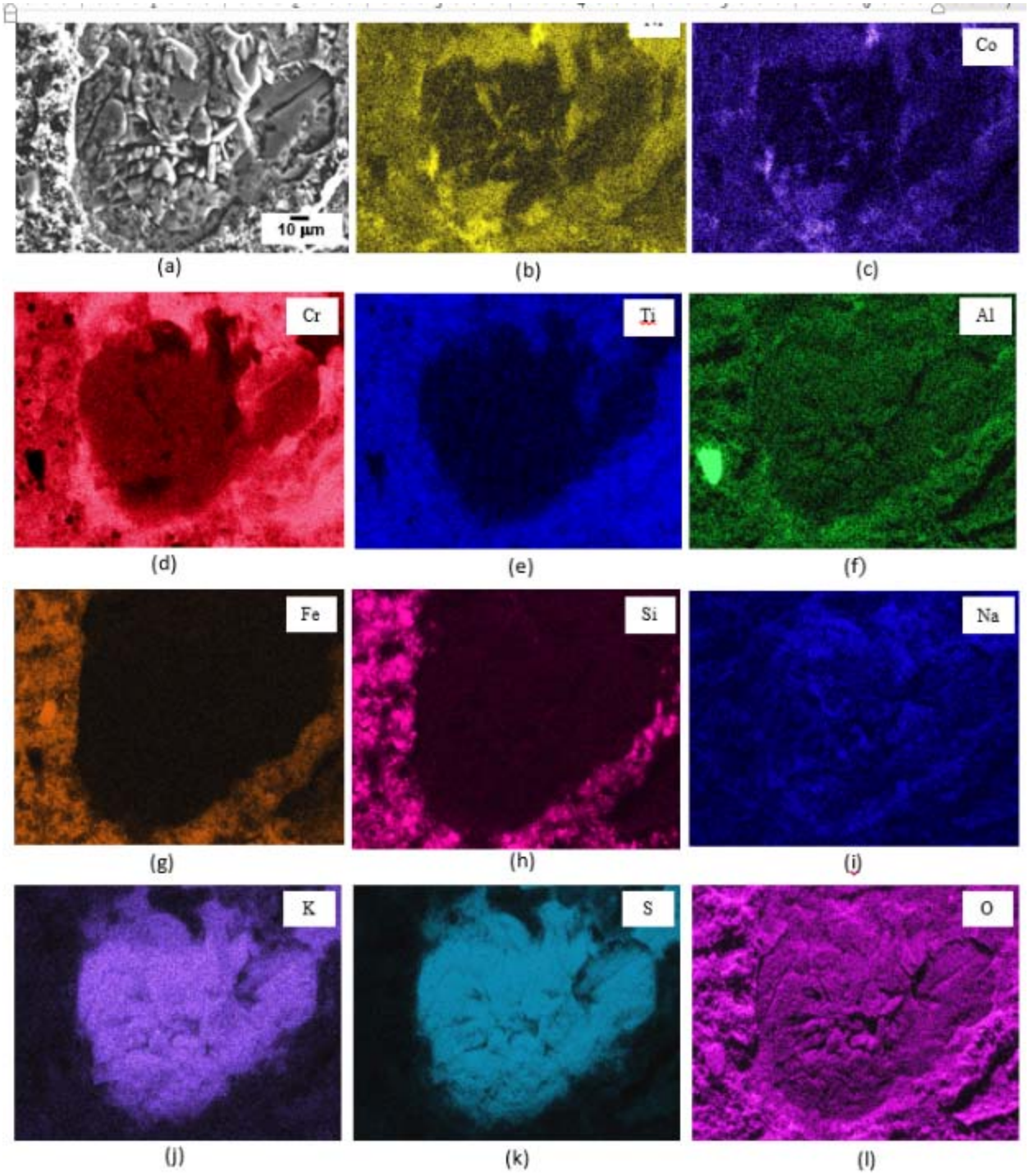

Figure 23 (a) Formation of the molten sulfate salt layer at the top corroded surface in the flue gas with SO_2 environment after 123 h, and (b, c, d, e, f, g, h, i, j, k, l) its corresponding elements mapping

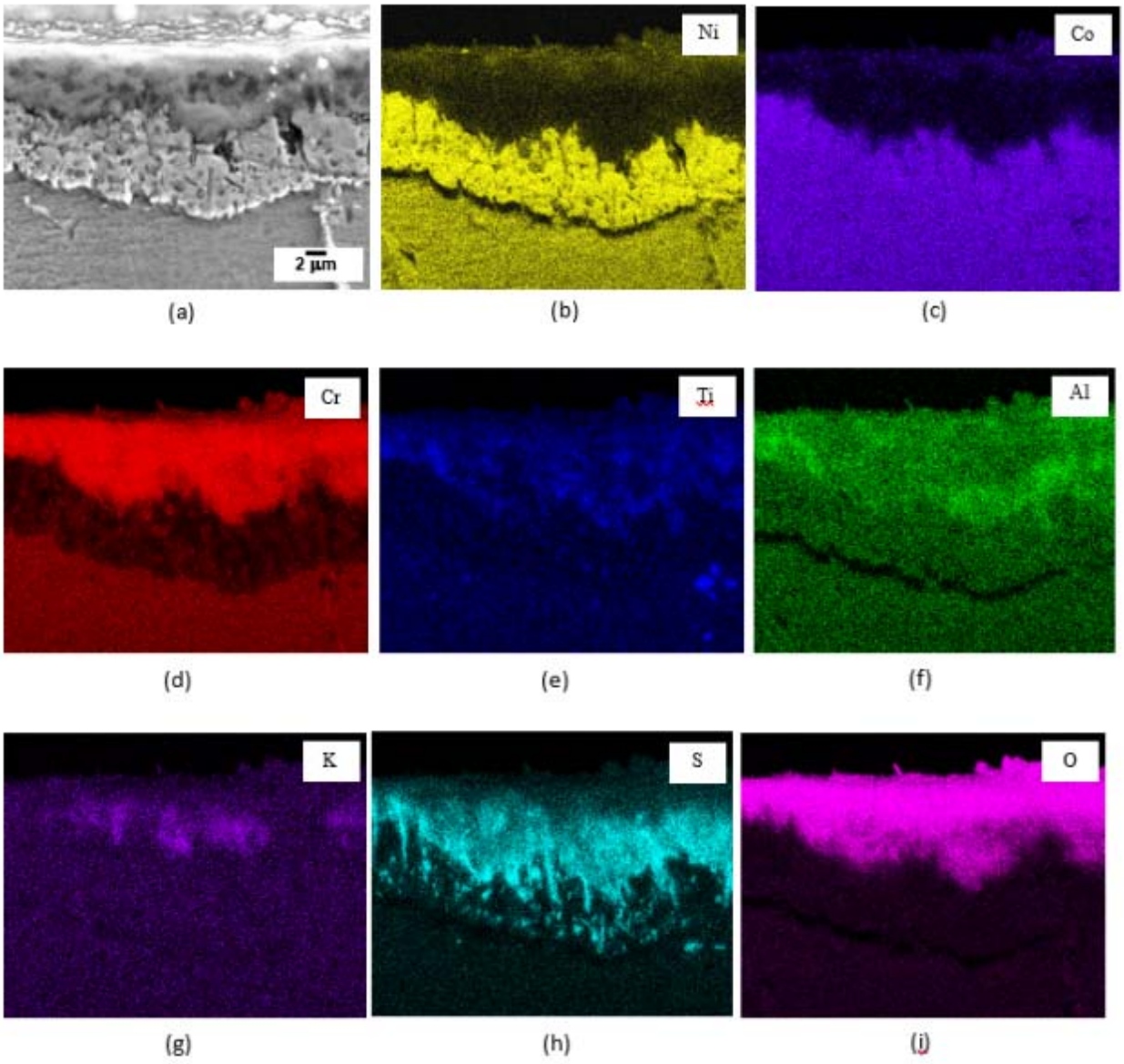

Figure 24 (a) Cross-sectional corroded surface showing highly extent of sulfidation attack in the flue gas with SO_2 environment, and (b, c, d, e, f, g, h, i) its corresponding elements mapping

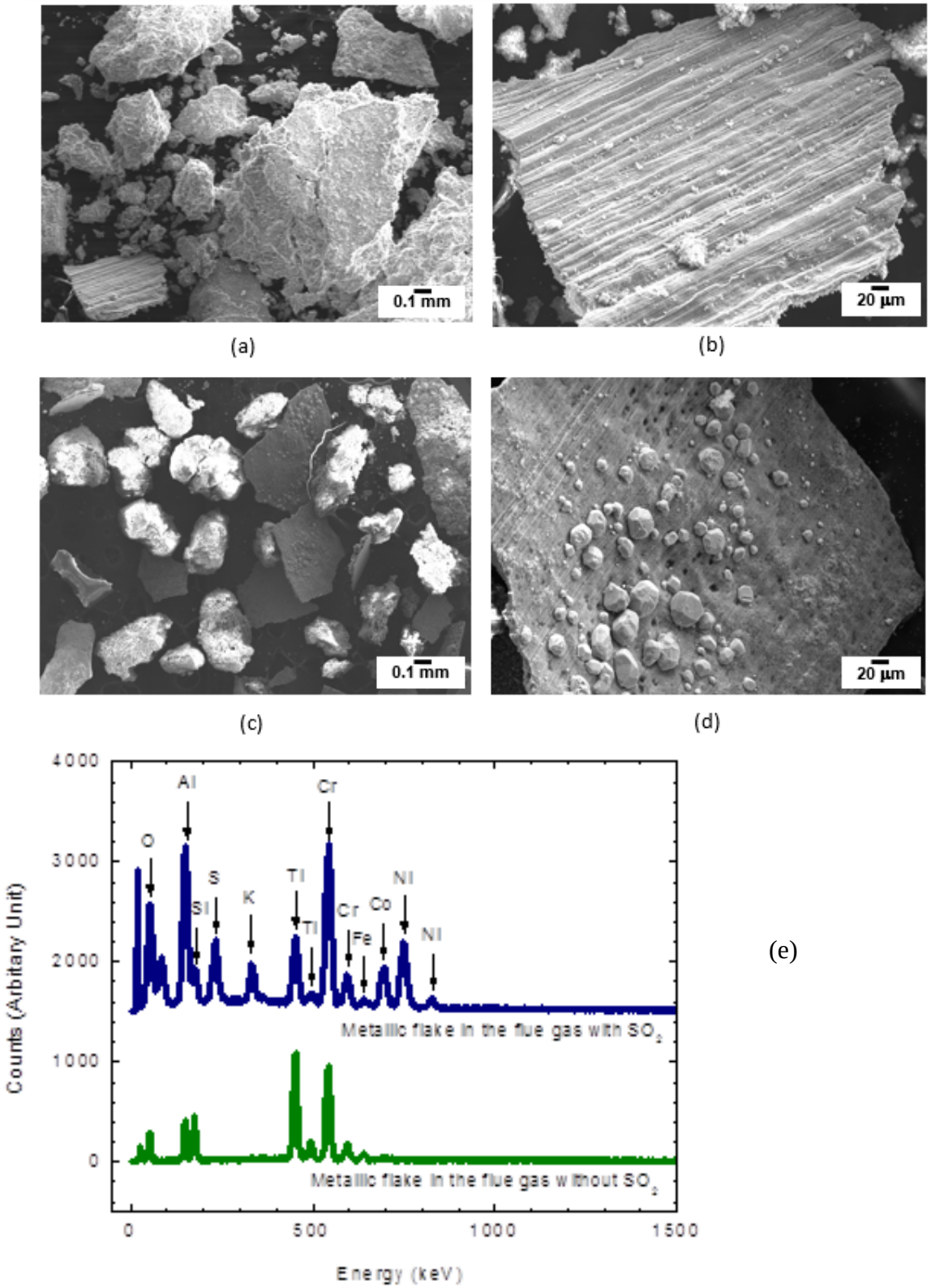

Figure 25 SEM micrograph showing the metallic flakes distribution in the corrosion products (a) in the flue gas without SO_2 environment, (b) closed-up of the metallic flake in (a), (c) in the flue gas with SO_2 environment, (d) closed-up of the metallic flake in (c), and (e) their EDX peaks

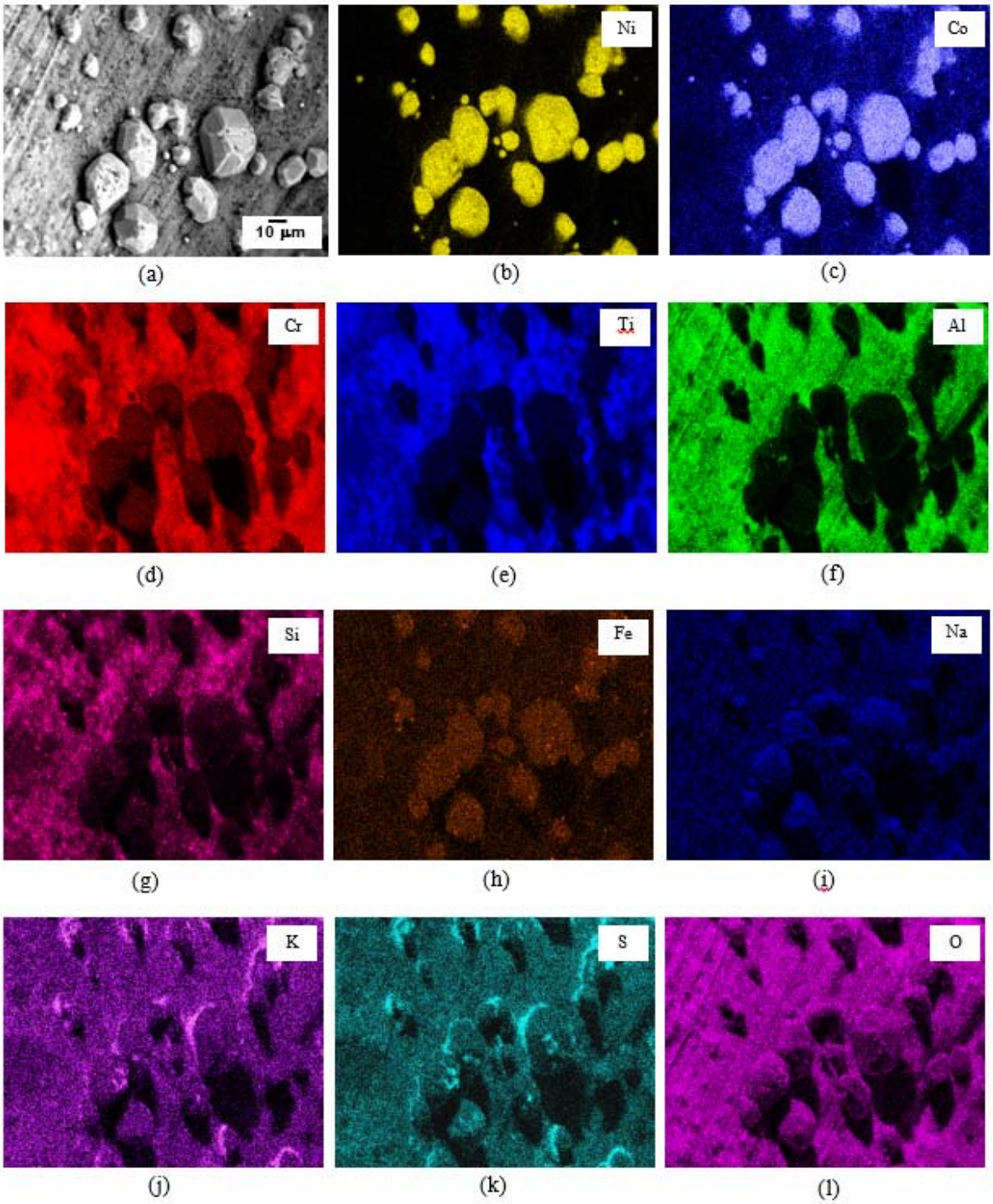

Figure 26 (a) Formation of Ni_3S_2 and Co_3S_4 in the corrosion products from the flue gas with SO_2 environment after 123 h, and (b, c, d, e, f, g, h, i, j, k, l) its corresponding elements mapping

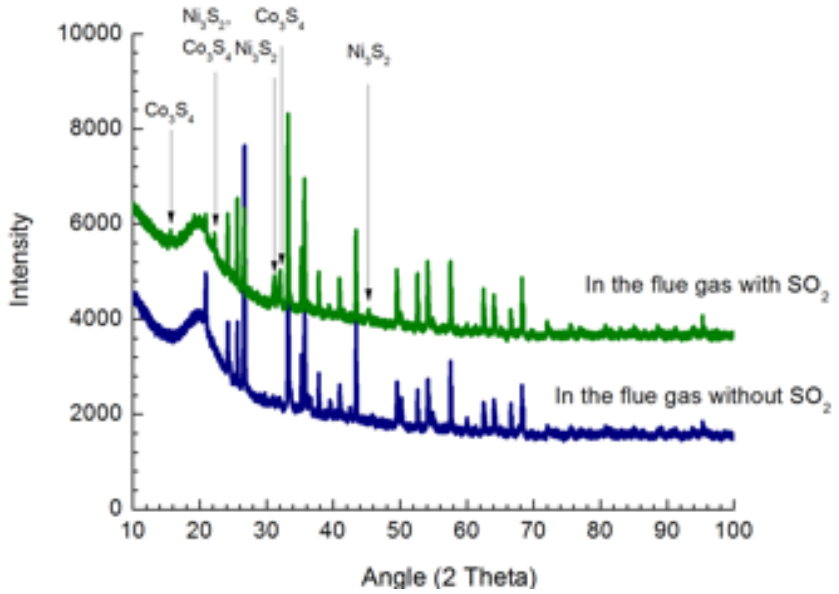

Figure 27 XRD patterns of the corrosion products at different flue gas environments

Conclusions

In this research, the effect of SO_2 content in the flue gas on coal ash hot corrosion behaviour of Inconel 740 alloy has been studied using our novel high temperature corrosion sensor. The sensor can detect the response of OCP, EN, EIS and PDP measurements. The results showed that:

- SO_2 in the flue gas accelerated corrosion damage of the alloy in a coal ash environment. The metal loss was found to be doubled after 123 h exposure with an increase in 1% SO_2 content in the flue gas.
- The alloy corroded via a "low-temperature hot corrosion" mechanism at 750 °C that involved formation of molten alkali sulfates and alkali pyrosulfates eutectic leading to sulfidation attack.
- Formation of reaction product oxides, Cr_2O_3, TiO_2, Al_2O_3 and $(Ni,Co)Cr_2O_4$ was the favourable condition for the initiation of hot corrosion. The sulfidation was predominant in the propagation stage as a consequence of inward-diffusing sulfur.
- The sulfidation attack was more pronounced in the flue gas with SO_2. Ni_3S_2 and Co_3S_4 were observed in the corrosion products.
- The quantitative determination of the corrosion rates via EN technique was proposed and there was a good correlation between the metal loss values from the EN test data and those from the weight loss test data.

Task 3 Electrochemical Modeling and Predictive Model Development

Subtask 3.1 Develop Electrochemical Model to Characterize the General Corrosion of Boiler Tube

Experimental Methods

Effect of Temperature on Coal Ash Hot Corrosion Resistance of Inconel 740 Superalloy

The objectives of this research work are to provide in situ information on the instantaneous rates at any stage of the corrosion process and to address some knowledge gap in the assessment of coal ash hot corrosion as a function of temperature. Coal ash hot corrosion behaviour of Inconel 740 superalloy was studied at 700-800 °C in a synthetic coal-fired boiler environment using our high temperature electrochemical sensor. The results of electrochemical noise analysis show good correlations with those from a weight loss test. Characteristic potential noise patterns correspond with the predominant stages in the corrosion process. While, characteristic current noise patterns indicate the extent of the corrosion. The data show that corrosion resistance of the alloy was significantly reduced at 750 °C and the highest tendency of TiS formation in the internal sulfidation stage led to accelerated intergranular and intragranular corrosion.

Materials and Synthesis Coal Ash Hot Corrosion Environments

The effect of temperature on coal ash hot corrosion behavior of the Inconel 740 Ni-based superalloy was studied in the presence of a synthetic thin coal ash with a synthetic flue gas at 700 °C, 750°C and 800 °C. The alloy has the following chemical composition (in wt.%): Ni-49.45, Cr-24.67, Fe-0.62, Co-19.98, Mo-0.50, Nb-1.47, Al-1.23, Mn-0.3, Ti-1.23, Si-0.29. The alloy was heat treated by the following sequences: 1150 °C for 4 h followed by air cooling; 1120 °C for 1 h followed by air cooling; 850 °C for 16 h followed by air cooling. The composition of the synthetic coal ash electrolyte was reagent-grade 29.25 wt.% SiO_2, 29.25 wt.% Al_2O_3, 29.25 wt.% Fe_2O_3, 5.625 wt.% Na_2SO_4, 5.625 wt.% K_2SO_4 and 1 wt.% NaCl. The synthetic flue gas containing 15 vol.% CO_2, 4 vol.% O_2, 80 vol.% N_2 and 1 vol.% SO_2 was used with the flow rate of 150 ml min^{-1}. The alloy was cut into samples of 10 mm×10 mm×2 mm in dimension for electrochemical tests and weight loss measurement. A thin film of coal ash was deposited on the sample surface to obtain a layer thickness of about 1 mm.

Electrochemical Measurements

The electrochemical behavior of coal ash hot corrosion was studied using open circuit potential (OCP), electrochemical impedance spectroscopy (EIS), electrochemical noise (EN) and potentiodynamic polarization (PDP) measurements. All measurements were taken with our developed high temperature electrochemical sensor. The sensor is constructed with four electrodes: two identical working electrodes (WE1 and WE2), one reference electrode (RE) and one counter electrode (CE). The Inconel 740 alloy was used for the working electrodes. The reference electrode was the Ag/Ag^+ electrode in 10 mol% Ag_2SO_4 and 90 mol% Na_2SO_4 molten salt. The silver wire was immersed in the molten salt. The platinum wire was used as a counter electrode. The initial potentials of the alloy were determined by OCP measurements for 1 h. The EIS measurement was performed in the frequency range from 1×10^5 Hz to 0.1 Hz with an FRA

system. A perturbation signal with amplitude of 10 mV root mean square was used. The interval of one EIS measurement was about 15 min followed by the EN measurement for 24 h. The EIS and EN measurements were carried out alternately during an exposure time of 123 h. The time-sequences data of the current noise were transformed into frequency domain by using the fast Fourier transformation (FFT) method. The PDP was measured with a scan rate of 0.5 mV s^{-1} after 123 h. The electrochemical test data were analyzed using the Metrohm Autolab/PGSTAT302N with the Nova data acquisition system.

Weight Loss Measurement

The weight loss tests were carried out concurrently to compare with the results from the electrochemical tests. Prior to testing, the samples were ground with 180, 320, 600, 1500 and 2500 grit emery papers followed by 3 μ diamond paste polishing. The polished and pre-weighed samples were exposed to the same synthetic thin coal ash and synthetic flue gas environments for 123 h. After completing the tests, the corrosion products were then removed in boiling water for 15 minutes followed by ultrasonic cleaning with acetone. The tests were repeated to verify that the results fell within the expected error.

Surface Morphology Characterization

The top and cross-sectional corroded surfaces were analyzed using scanning electron microscopy (SEM) equipped with an energy-dispersive X-ray microanalysis (EDX), and X-ray diffraction (XRD).

Results and Discussions

January to March 2013

Effect of Temperature on Coal Ash Hot Corrosion Resistance of Inconel 740 Superalloy

Initial Corrosion Potentials

Variations of the initial corrosion potentials at different temperatures are shown in Figure 28. The potential at 750 °C showed positive values of 150 mV (vs Ag/Ag^{+}) within 1 h exposure period, while the negative potentials of 700 °C and 800 °C were continuously approaching more positive values. Sulfidation is a predominant stage in coal ash corrosion of nickel and nickel alloy in molten sulfates in the flue gas with SO_2 and it usually occurs at very positive potentials. The initial potential trends of 700°C, 750°C and 800°C suggest that sulfidation is a favorable corrosion process. Their potential values could depend on the reaction mechanism of low-melting alkali sulfate eutectic mixtures. In this case, the sulfidation potential of each operating temperature can be different and their stable potential values should be analyzed for longer exposure times.

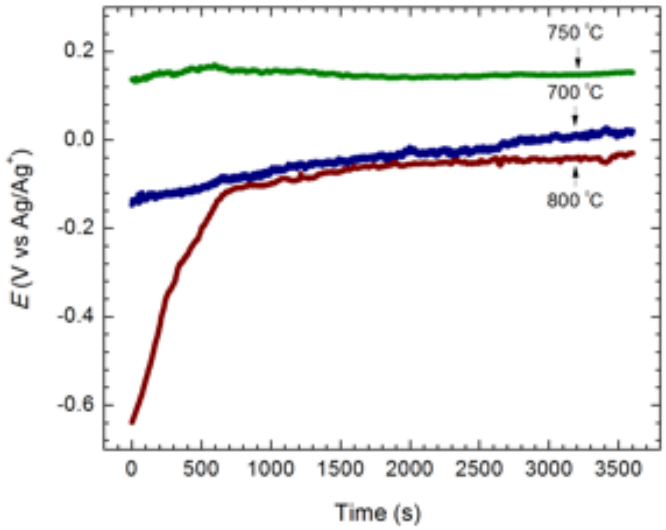

Figure 28 Comparison between OCP values after 1 h exposure

Electrochemical Impedance Spectra

EIS was used to interpret the kinetics of certain reaction steps involved in the hot corrosion process. At 700 °C, the rate control only corresponded to the charge transfer throughout the exposure periods (Figure 29a). In cases of 750 °C and 800 °C there were two step reaction kinetics involved in the hot corrosion process (Figure 29b and Figure 29c). The corrosion initiated with the charge transfer controlled process before 49:30 h followed by the diffusion-dominated process. The coal ash hot corrosion process is controlled by charge transfer and diffusion of a reactant or product species. The reason for the absence of a diffusion-controlled process at 700 °C could be due to the delayed formation of low-melting alkali sulfate eutectic mixtures. The similar behavior is also observed in the hot corrosion of the Mo-rich Ni_3Al-base alloy IC6 at 750-800 °C beneath solid Na_2SO_4 deposits.

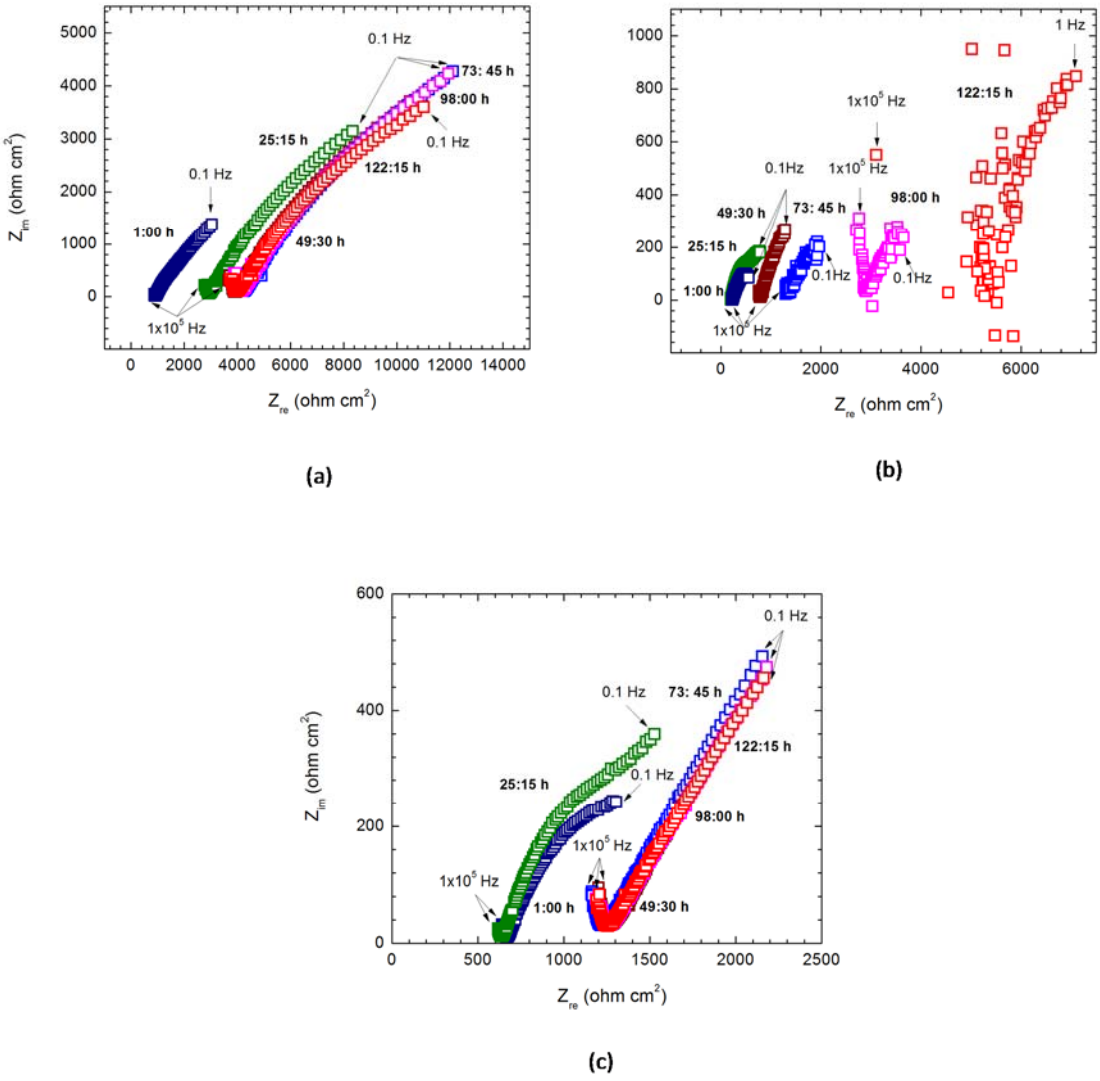

Figure 29 Nyquist plots showing different stages in corrosion process after different exposure times: (a) at 700 ℃, (b) at 750 ℃, and (c) at 800 ℃ (During a 123 h exposure period, six Nyquist plots were obtained at 24:15 h intervals)

Electrochemical Noise Data during Corrosion

Changes from the initiation stage to the propagation stage during the coal ash hot corrosion process were studied using the EN test. At 700 °C, the values of potential varied throughout the exposure time. The potential values varied from 100 mV (vs Ag/Ag^+) to 440 mV (vs Ag/Ag^+) during 123 h exposure (Figure 30a). At 750 °C and 800 °C the potential value became stable at 380 mV (vs Ag/Ag^+) (Figure 30b and Figure 30c). The time-sequences of positive potential noise values confirmed that sulfidation was the predominant process at 700 °C, 750 °C and 800 °C. The sulfidation potential of the alloy at 750 °C in the same synthetic coal-fired boiler environment is 380 mV (vs Ag/Ag^+). The potential noise signatures at 700 °C were characterized by the noise pattern of continuously changing potential approaching more positive values. In case of 750 °C and 800 °C, their characteristic potential noise signatures after 25:15 h were characterized by the noise pattern of positive potential fluctuating randomly in a narrow range. These two different potential noise signatures could represent the two different stages of sulfidation process.

The corresponding time records of current noise at different temperatures are shown in Figure 31. The current values at 700 °C were not stable before 98:00 h (Figure 31a). In contrast, the range of current densities at 750 °C was the highest (Figure 31b) suggesting the highest extent corrosion occurred. In the case of 800 °C the corrosion proceeded with the stable current densities after 25:15 h (Figure 31c). The severity of the coal ash hot corrosion can be evaluated with the characteristic current noise pattern. The noise signature of sudden changes in current values followed by a slow or no recovery corresponds with the accelerated oxidation/sulfidation. At 750 °C sudden changes in current densities followed by no recovery were observed after 49:30 h indicating the accelerated sulfidation (Figure 31b). The maximum current density values of each exposure period can be easily obtained from the trends of the power spectral densities (PSDs) plotted against the frequency (Figure 32). The PSDs were independent of the frequency in the region lower than 0.0001 Hz. The results confirmed that the current density range at 750 °C in the frequency domain was the highest compared with 700 °C and 800 °C (Figure 32a-Figure 32c).

Use of the noise resistance (R_n) as calculated from potential and current noise data is proposed to be equivalent to the polarization resistance (R_p). A powerful analysis of EN acquisitions can also be performed to achieve the noise resistance in the frequency domain (R_{sn}). Both R_n and R_{sn} values are inversely proportional to the corrosion rate and can provide reasonable estimates. The lowest values of R_n and R_{sn} occurred at 750 °C indicating the corrosion rates were the highest (Figure 33a). From a qualitative point of view, the values of statistical parameters of EN, such as the ratio between the standard deviation of the measured current and the root mean squared value of the current can prove if the corrosion is under localized attack. The localization indices suggest that the alloy suffered localized attack at 700-800 °C, but the trends of the localization indices were different from each other (Figure 33b).

Potentiodynamic Polarization Curves

The potentiodynamic polarization technique is useful to evaluate the corrosion rates when the controlling mechanism is by charge transfer. The potentiodynamic polarization curves at different temperatures (Figure 34a) and their corresponding linear i vs E plots (Figure 34b) indicate that the curves of 700 °C and 800 °C are actually ohmic. It is likely due to electron transfer reactions proceeding in parallel to the charge transfer corrosion process. The Al_2O_3, Fe_2O_3 and SiO_2 in coal ash electrolyte mixture likely behave as

semiconductor oxides, even though Na_2SO_4 and K_2SO_4 are ionic. The dissolution of metal and metal oxides in the electrolyte also turns it into an electronic conductor.

The ohmic drop will become an important factor in the coal ash hot corrosion process for which there is a clear separation of the anodic and cathodic corrosion sites. In the presence of a significant influence of ohmic resistance, the polarization curve shape deserves careful examination when processing experimental data. Erroneous information may be obtained if the removal of the contribution of the ohmic drop to the electrode potential is not accurate. It is also difficult to determine quantitatively the corrosion rates from the Tafel extrapolation method because of the very limited Tafel region obtained in the molten salts.

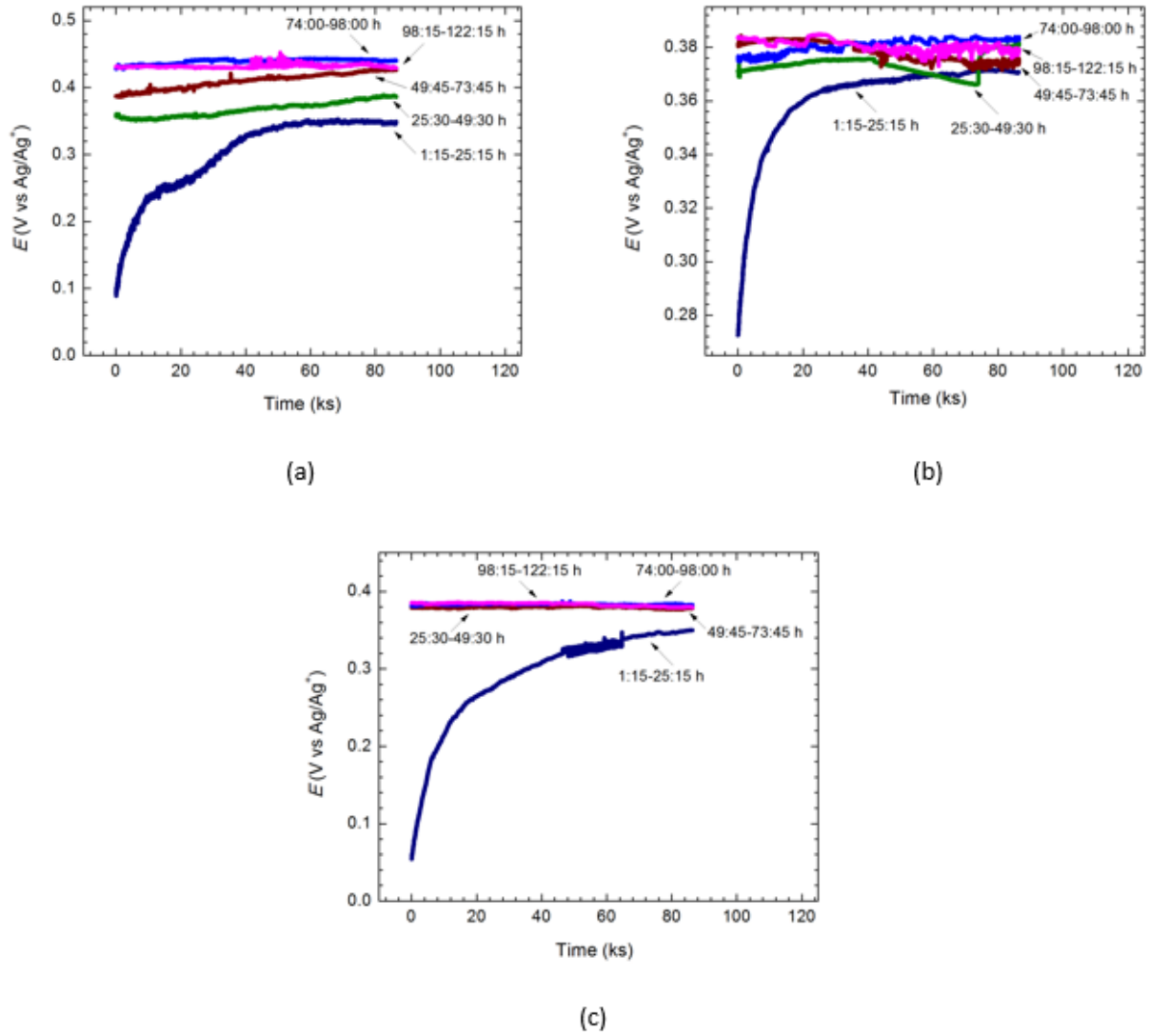

Figure 30 Time sequences of the electrochemical potential noise values: (a) at 700 ℃, (b) at 750 ℃, and (c) at 800 ℃ (One EN measurement took 24 h and five EN measurements of 24 h duration during a 123 h exposure period were conducted)

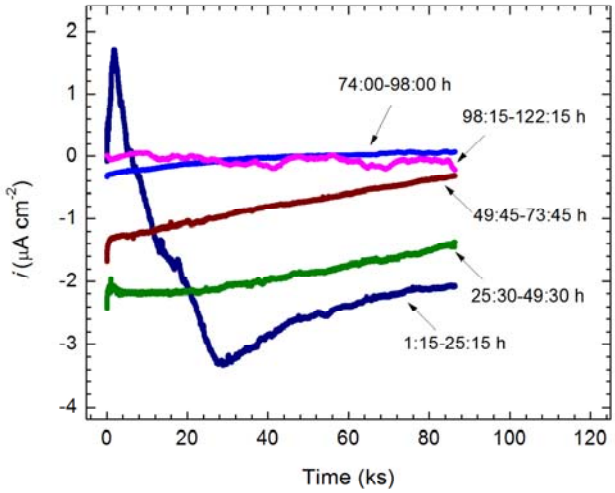

(a)

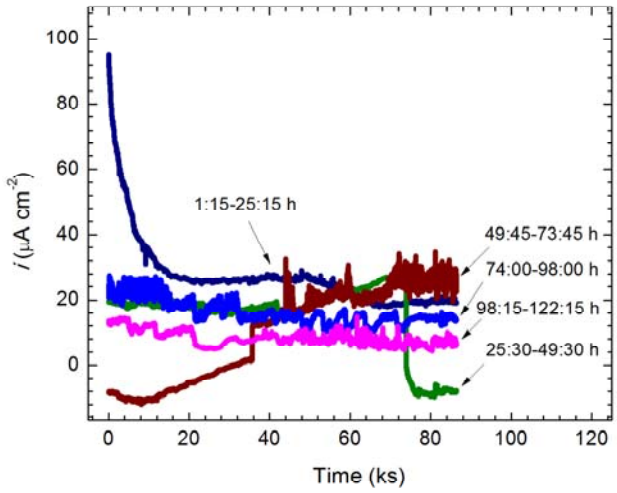

(b)

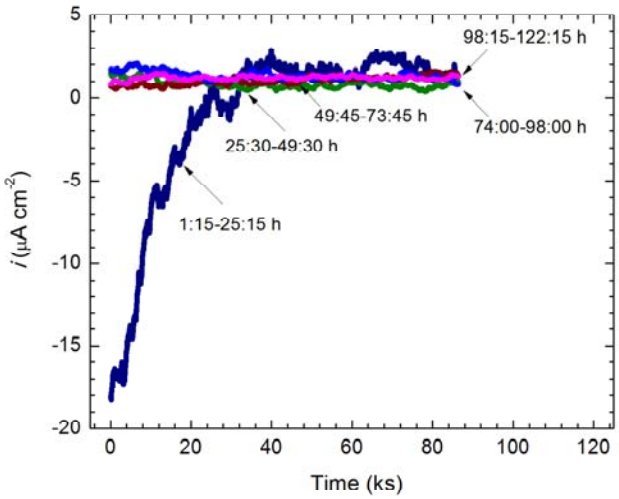

(c)

Figure 31 Time sequences of the electrochemical current noise values: (a) at 700 ℃, (b) at 750 ℃, and (c) at 800 ℃ (the current noise were recorded simultaneously with the potential noise)

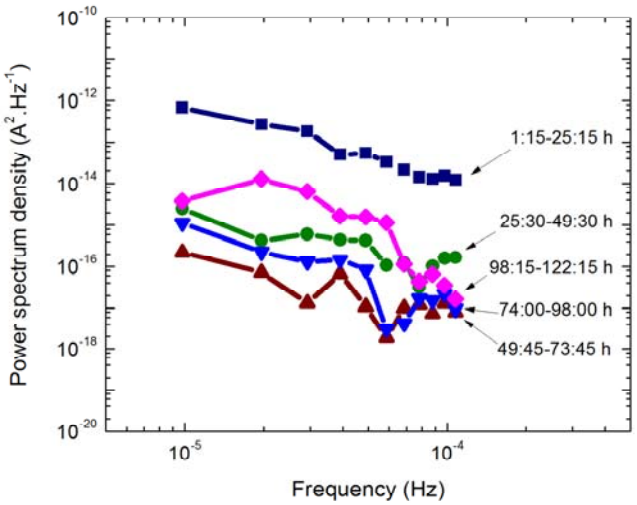

(a)

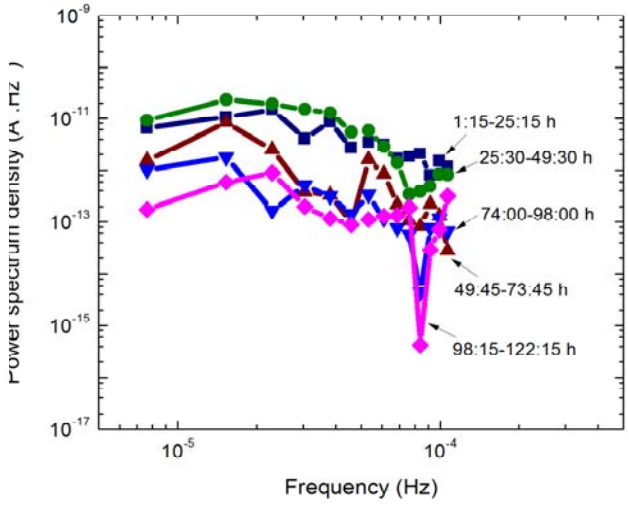

(b

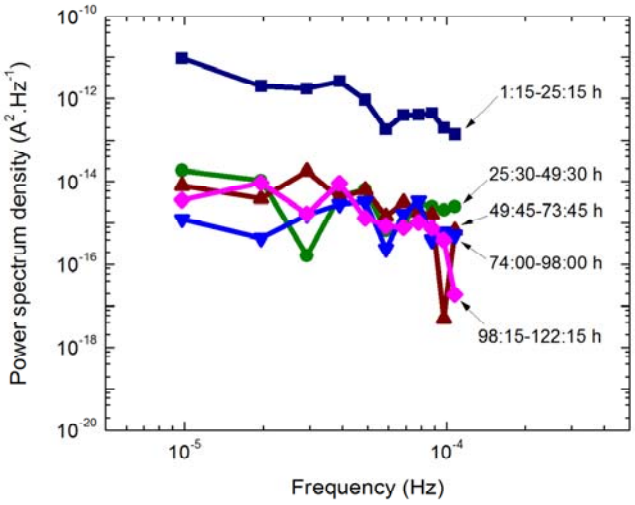

(c)

Figure 32 The electrochemical current noise values in the frequency region lower than 0.0001 Hz: (a) at 700 ℃, (b) at 750 ℃, and (c) at 800 ℃

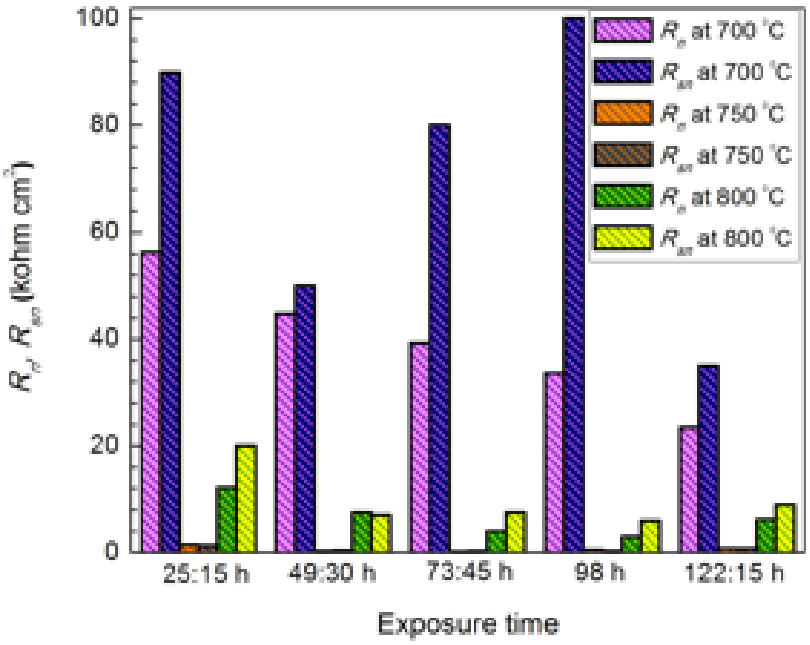

(a)

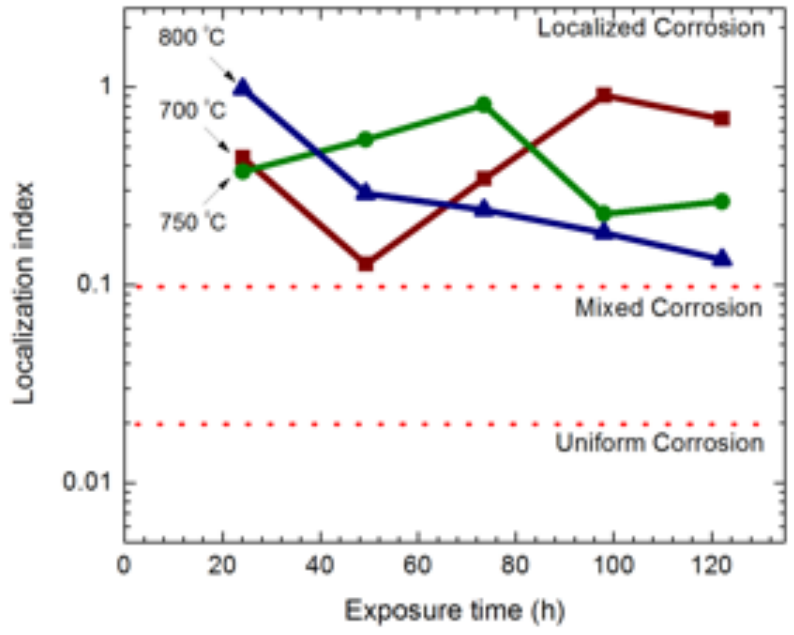

(b)

Figure 33 Comparison between the electrochemical noise test data at different temperatures: (a) R_n and R_{sn} and (b) localization index

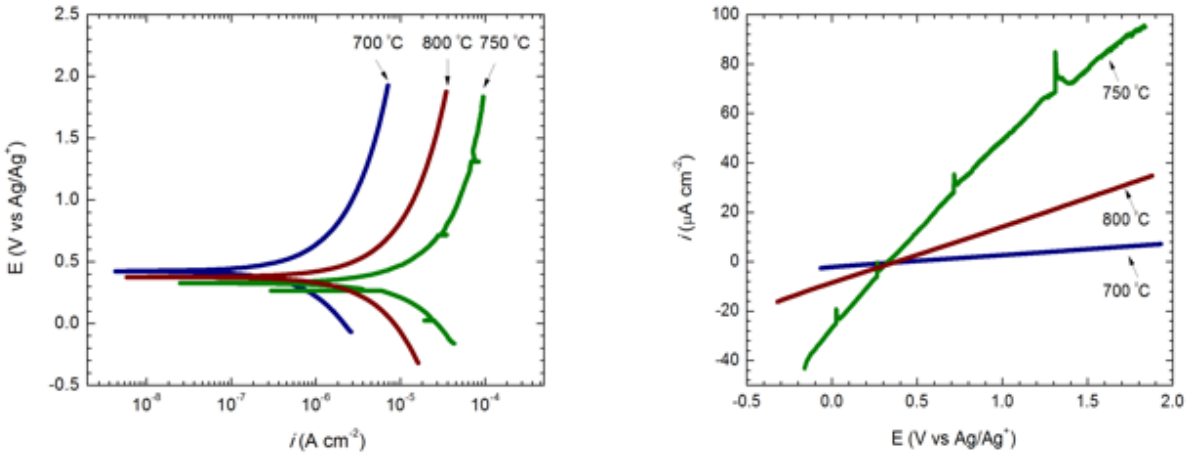

(a) (b)

Figure 34 (a) Potentiodynamic polarization curves at different temperatures and (b) their corresponding linear i vs E plots

Evaluation of Hot Coal Ash Corrosion Rate at Different Temperatures

The application of electrochemical techniques represents a powerful tool to obtain some aspects which are not possible to determine by weight loss technique. After reviewing OCP, EIS, EN and PDP test data, the EN test data appear to be the most suitable for the quantitative determination of instantaneous corrosion rates in service. The instantaneous corrosion rates can be determined by analyzing the current noise data in the time domain for each exposure period. The maximum value of current noise, i_{max}, were used to calculate the corrosion rate via Faraday's Law expression. Detailed information about the corrosion calculation is given in our previous publication.

The instantaneous corrosion rate, the accumulated mass loss and corrosion depths over the entire duration of exposure are given in Figure 35. In comparison with the mass loss values from the weight loss test the results show that the values in time domain could represent the actual mass loss (Figure 35b). The analysis of current noise values in the time domain provides direct quantitative information on electrochemical processes that cannot be obtained from the frequency domain analysis. The results also confirmed that the values at 750 °C were the highest ones (Figure 35a-Figure 35c). The relationship of corrosion rates to temperature follows a normal distribution with a peak rate at 750°C (Figure 36).

Top and Cross-Sectional Corroded Surface Analysis

The values of calculated corrosion depths can be compared with the thickness of the corrosion product layers observed at the cross-sectional surfaces (Figure 37). No obvious corrosion layer was observed at 700 °C (Figure 37a). The deeper layer formed at 750 °C (Figure 37b) compared with 800 °C (Figure 37c). The elemental distribution analysis of the etched cross-sectional surfaces showed that only the external sulfidation occurred in the Cr-rich region at 700 °C (Figure 38). In cases of 750 °C and 800 °C, the internal sulfidation of Ni, Co and Ti proceeded in the Ni-rich region. The distribution of Cr, Ni, Co, Ti, K, S and O at 750 °C indicates that sulfate and sulfide corrosion products formed together with molten alkali sulfate salt (Figure 39).

The corrosion morphology and distribution of metallic sulfates and sufides in the external and internal sulfidation stages can be seen in the top corroded surfaces. The corrosion products of $Cr_2(SO_4)_3$ and CrS were a consequence of the external sulfidation (Figure 40). The internal sulfidation started at the NiO/Cr_2O_3 phase boundaries which could provide access paths for molecular SO_2 transport leading to formation of the intergranular and intragranular metallic sulfide compounds at the Ni substrate (Figure 41). The intergranular sulfides formed along grain boundaries and the intragranular sulfides formed isolated phase in the alloy grain interior. Magnified views of the top corroded surface at 750 °C (Figure 42a and Figure 42b) and its EDX pattern (Figure 42c) suggest that metallic sulfides formed in the Ni-rich region was Ti-rich sulfide. The XRD analysis confirmed that the corrosion products formed in two sulfidation stages were CrS, $Cr_2(SO_4)_3$ Ni_3S_2, Co_3S_4 and TiS, but the peaks of TiS at 750 °C was the most significant (Figure 43).

Coal Ash Hot Corrosion Rates at Different Temperatures

The coal ash hot corrosion rate depends on a complex interaction between alloy chemistry, coal ash chemistry, flue gas composition, and operation temperature. Inconel 740 alloy is known to have a multi-phase microstructure consisting of γ matrix, γ' precipitate, γ-γ' eutectic, carbides and some minor phases. The most important structure changes at elevated temperatures are γ' coarsening, γ' to η transformation and G phase formation. The alloy maintains good microstructure stability to at least 750 °C and can fulfill the requirements of long time high temperature stress rupture strength (100 MPa for 105 h) and corrosion resistance (0.0876 mm y^{-1}) allowance. The present research highlights that the corrosion rates of the alloy in a synthetic coal-fired boiler environment at 750 °C were not in the acceptable range (Figure 35a).

Coal Ash Hot Corrosion Process at Different Temperatures

In the temperature range of 700-800 °C, low melting point eutectics, sodium and potassium pyrosulfate ($(Na,K)_2S_2O_7$) (m.p=575 °C) can be formed. In the fused ($(Na,K)_2S_2O_7$), the reduction of $S_2O_7^{2-}$ (dissolved SO_3) is a more active than that of other oxygen species. When the environment is reducing, the corrosion reaction becomes a competition between oxidation and sulfidation.

Two major sulfidation stages of the coal ash hot corrosion process were identified from electrochemical tests and examination of the corroded surfaces. The first stage was the external sulfidation which was predominant at 700 °C. This stage was characterized by the noise signature represented by continuously increasing potential values (Figure 30a) and the corresponding current values (Figure 31a). The impedance spectra in this stage indicate that charge transfer was the rate controlling step of the corrosion process (Figure 29a). In the external sulfidation stage, the transport of the oxidant from the gaseous environment through the coal ash film resulted in the melting of the sulfate salts, formation of $Cr_2(SO_4)_3$ and CrS in the Cr-rich region (Figure 34a).

The second stage was the internal sulfidation which was observed at 750 °C and 800 °C. This stage was featured with the positive potential fluctuating randomly in a narrow range (Figure 30b and Figure 30c) and the corresponding current values fluctuated randomly in a narrow range (Figure 31b & Figure 31c). The detection of Warburg impedance at low frequency indicates that the corrosion was controlled by the diffusional supply of oxidants (Figure 39b and Figure 39c). The slow diffusion of the oxidant supporting the cathodic reduction reaction may control the corrosion rate. The corrosion product layer formed in the internal sulfidation stage was composed of two layers: Cr-rich sulfide and sulfate mixture layer and Ni-rich internal sulfidation layer (Figure 44b and Figure 44c). The Cr-rich sulfide and sulfate mixture layer contained $Cr_2(SO_4)_3$ molten salt and CrS solid particles. In this case, the protective Cr_2O_3 scale would likely dissolve in the presence of the salt deposit, and if it does dissolve, the acidic solutes of $Cr_2(SO_4)_3$ and CrS may form. As a consequence, SO_2 can penetrate through this layer and react with Ni and Ti to form Ni_3S_2 and TiS, as shown in Figure 43.

The transport of nickel cation vacancies through the barrier sublayer is assumed to be the rate-limiting step of the overall process. With regard to the temperature dependence for the reaction parameters, the rate constant for the reduction reaction and the diffusivity of the active oxidant definitely increase as the temperature increases. In contrast, TiS formation was more favorable in the internal sulfidation stage at

750 °C (Figure 43 and Figure 44b). The localized corrosion sites were generated by microgalvanic action between the cathodic TiS phase and the anodic Ni matrix (Figure 42a) resulting in accelerated intergranular and intragranular corrosion rate. This is the reason why the alloy suffered corrosion with the highest Ni metal loss at 750 °C. The high extent of corrosion at 750 °C was characterized by sudden change in current values followed by no recovery (Figure 41b). The reduction of corrosion rate at 800°C may be explained by the decreasing stability of the chromium sulphate.

Conclusions

- Coal ash hot corrosion behaviour of Inconel 740 superalloy has been successfully studied in the temperature range of 700-800 °C for 123 h using our high temperature electrochemical sensor.
- The corrosion rate of the alloy at 700°C was 0.0012 mmy^{-1} which is much lower than the acceptable value of 0.0876 mm y^{-1}. However, its corrosion resistance significantly reduced at 750°C. The metal loss at 750 °C after 123 h increased to about ten times and then five times compared with 700 °C and 800 °C respectively.
- The potential noise signatures were found to be indicators of different stages in coal ash hot corrosion process, while the extent of corrosion can be in situ monitored from the current noise signatures.
- The noise signature of quick potential continuously approaching more positive values corresponded with the external sulfidation stage. This signature was observed at 700 °C.
- The noise signature of positive potential fluctuating randomly in a narrow range correlated with the internal sulfidation stage. This signature was more prominent at 750 °C and 800 °C.
- The noise pattern of sudden change in current values followed by no recovery corresponded with the accelerated internal sulfidation. This signature can be seen clearly at 750 °C. The formation of the cathodic TiS at 750 °C was responsible to increase intergranular and intragranular corrosion rate at the anodic Ni matrix.
- This work suggests that our high temperature electrochemical sensor could be used in combination with the electrochemical noise analysis to in situ monitor high temperature electrochemical kinetics and the corrosion process.

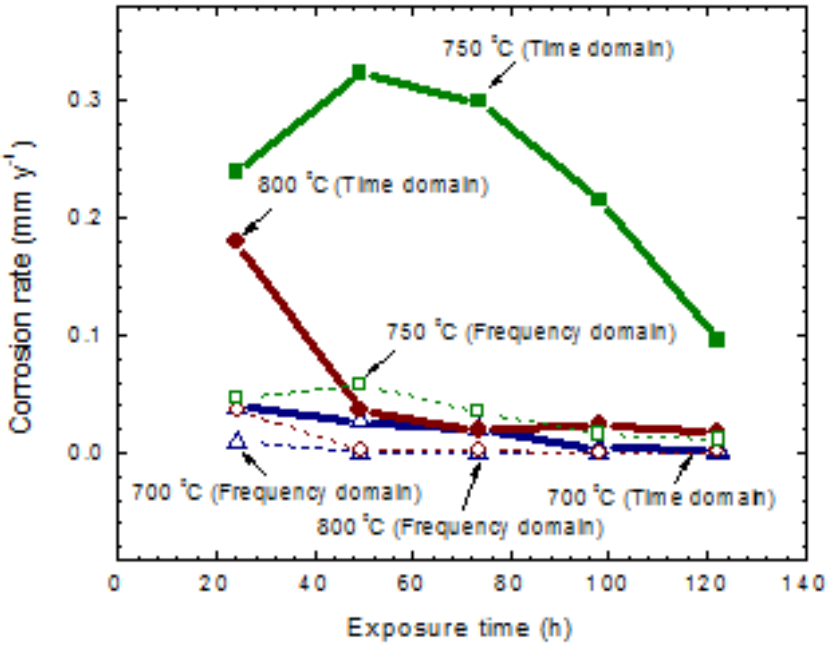
750 °C (Time domain)
800 °C (Time domain)
750 °C (Frequency domain)
700 °C (Frequency domain)
800 °C (Frequency domain)
700 °C (Time domain)
Corrosion rate (mm y-1)
Exposure time (h)
0.0
0.1
0.2
0.3
0
20
40
60
80
100
120
140

(a)

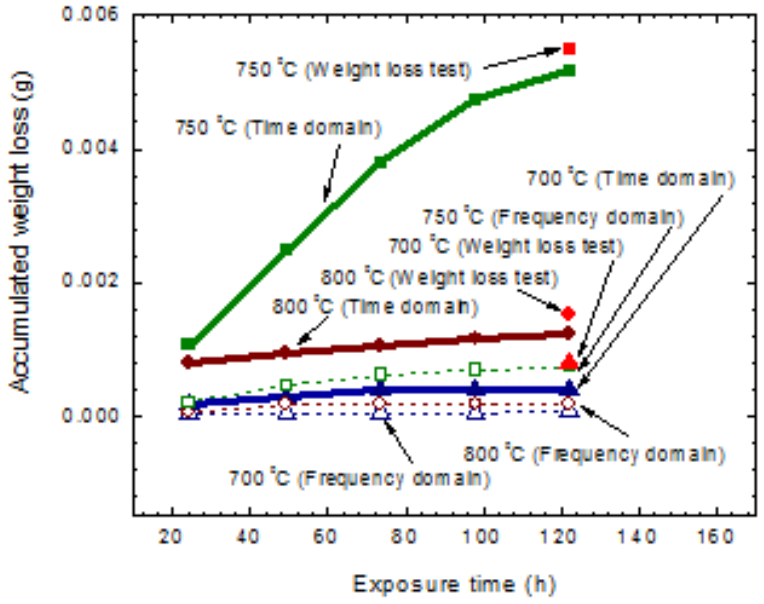
750 °C (Weight loss test)
750 °C (Time domain)
700 °C (Time domain)
750 °C (Frequency domain)
700 °C (Weight loss test)
800 °C (Weight loss test)
800 °C (Time domain)
800 °C (Frequency domain)
700 °C (Frequency domain)
Accumulated weight loss (g)
Exposure time (h)
0.000
0.002
0.004
0.006
20
40
60
80
100
120
140
160

(b)

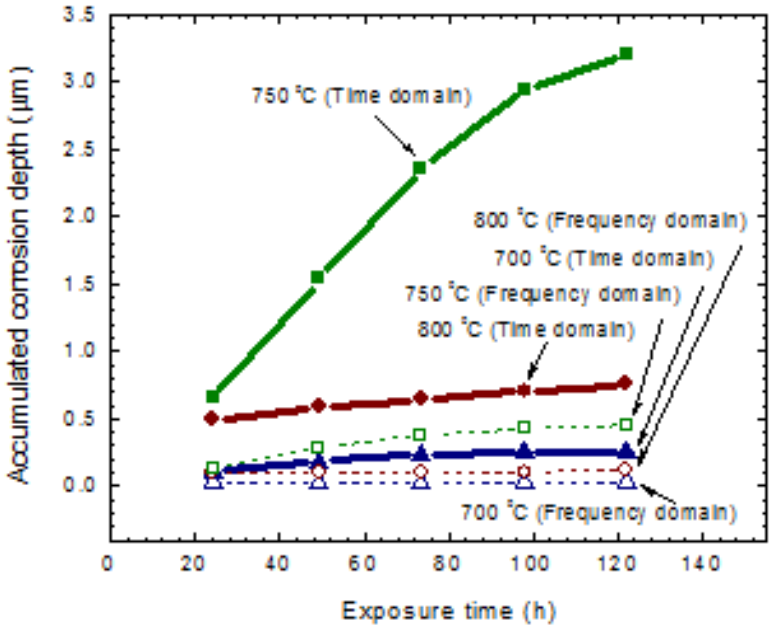

(c)

Figure 35 Comparison between corrosion kinetic data from EN analysis at different temperatures: (a) corrosion rates, (b) accumulated mass loss, and (c) accumulated corrosion depths

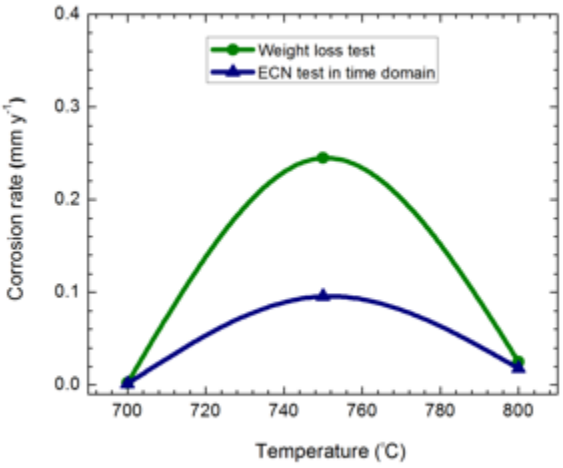

Figure 36 Comparison between corrosion rates data from EN analysis and weight loss test at different temperatures

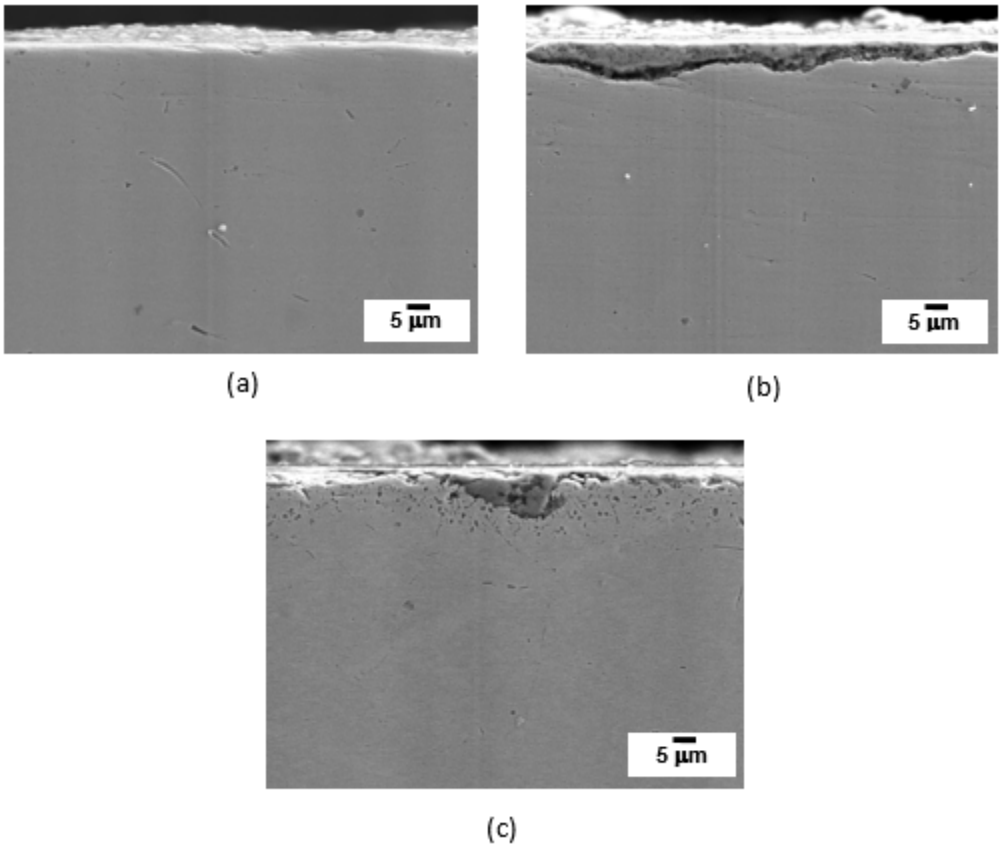

Figure 37 Cross-sectional corroded surfaces showing the extent of corrosion depths: (a) at 700 ℃, (b) at 750 ℃, and (c) at 800 ℃

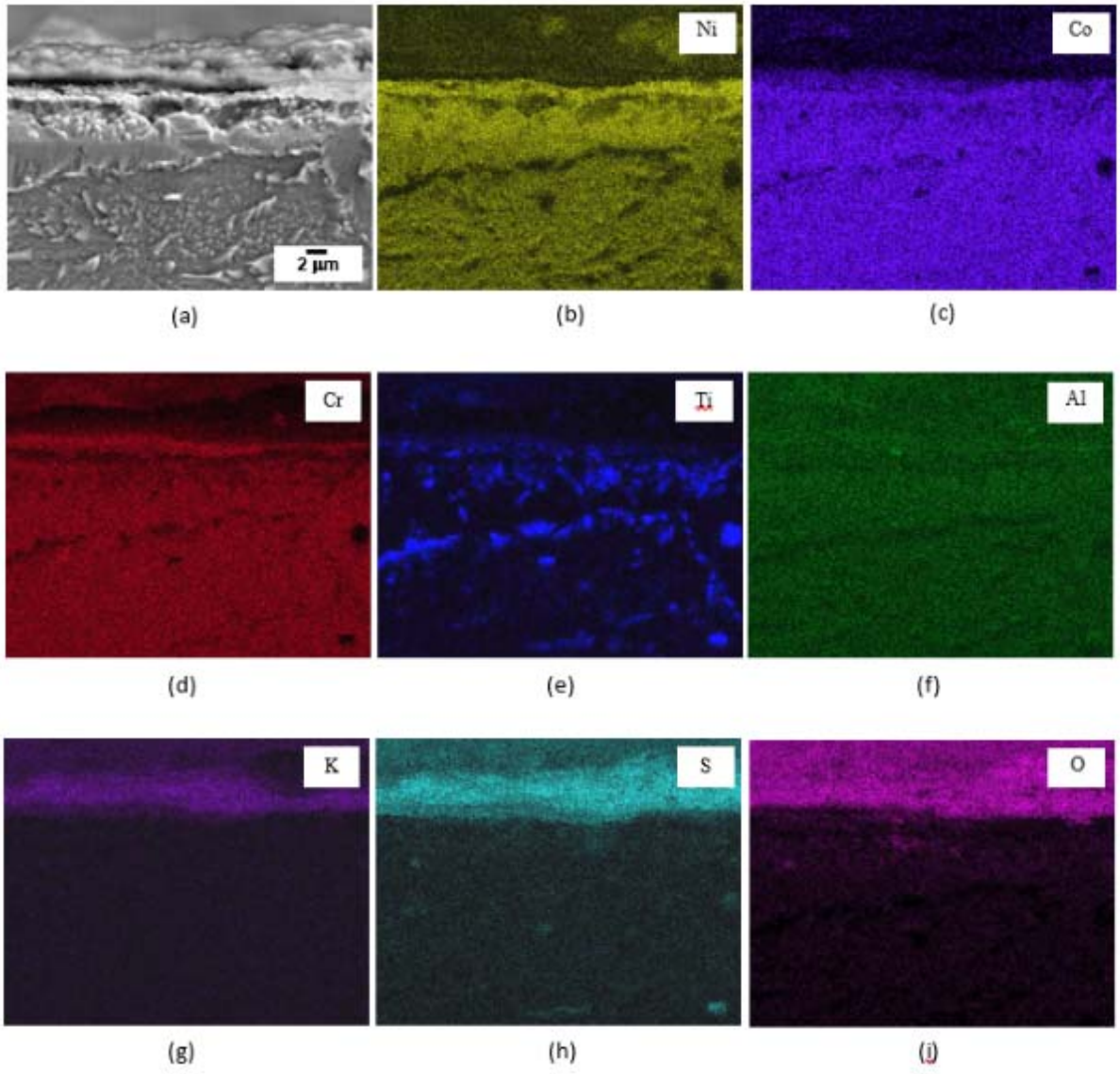

Figure 38 The elements mapping at cross-sectional corroded surface showing formation of metallic sulfates and sufides during the external sulfidation stage at 700 ℃

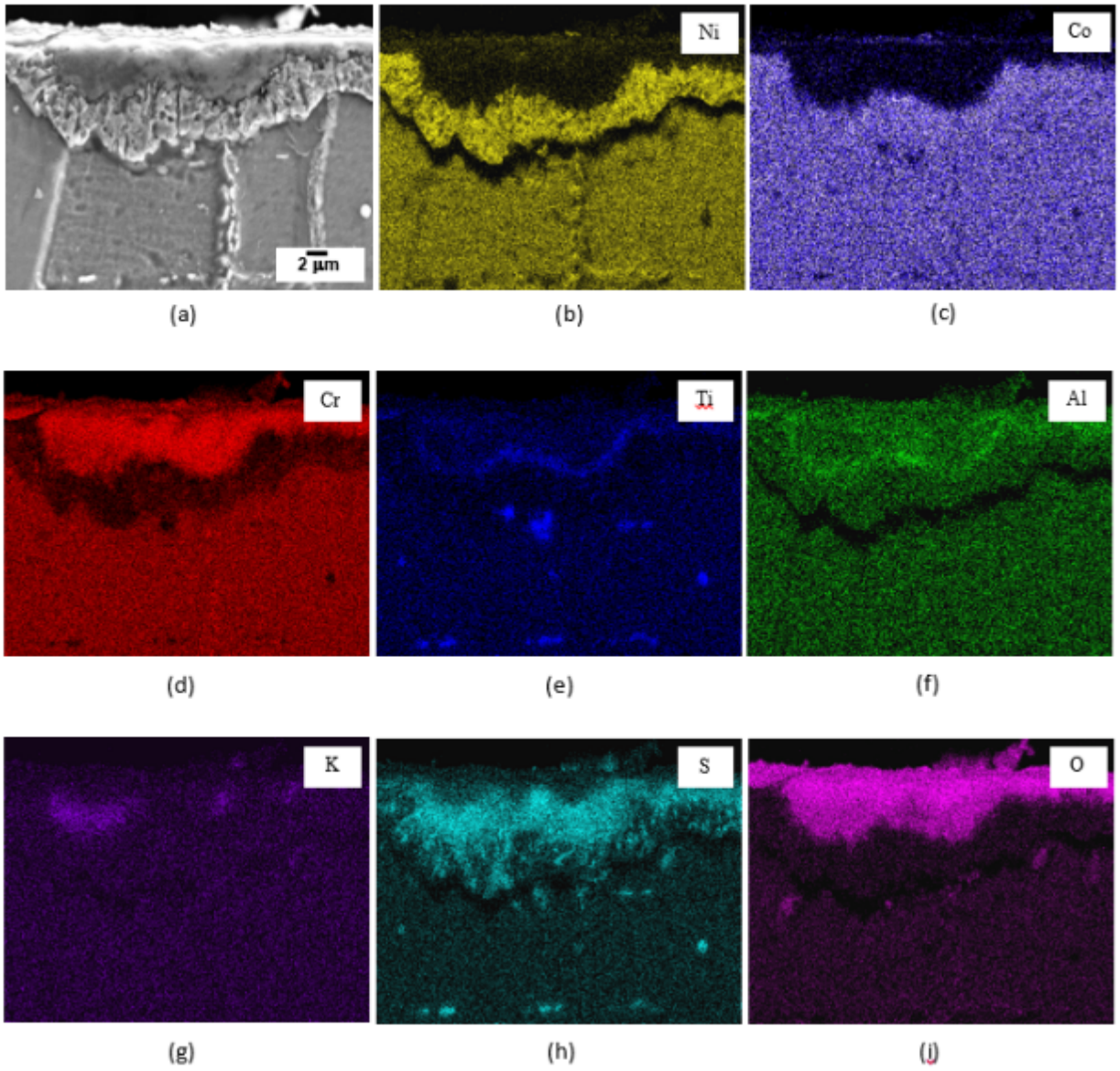

Figure 39 The elements mapping at cross-sectional corroded surface showing formation of metallic sulfates and sufides during the internal sulfidation stage at 750 ℃

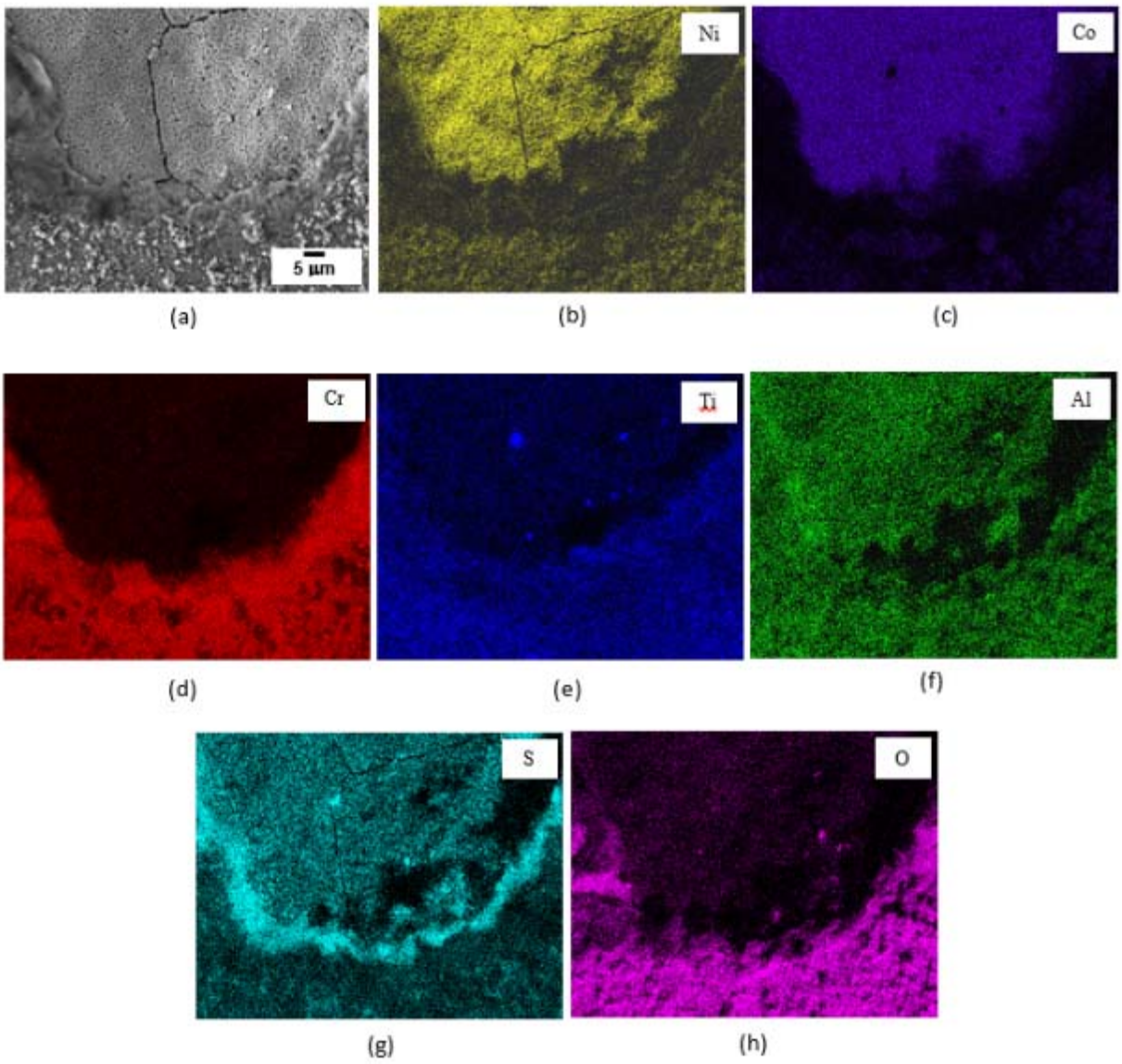

Figure 40 The elements mapping on top corroded surface showing formation of metallic sulfates and sufides during the external sulfidation stage at 700 ℃

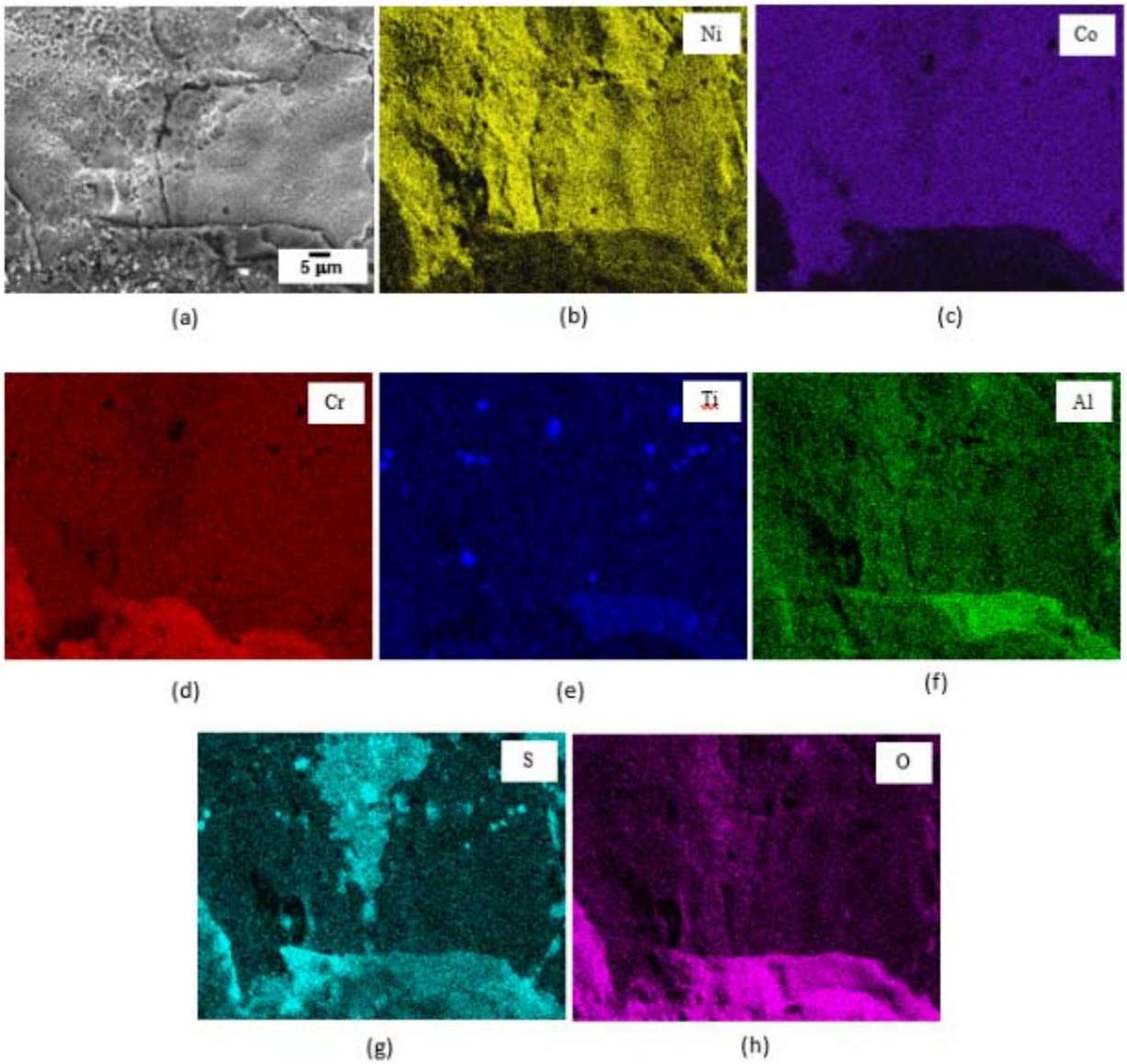

Figure 41 The elements mapping on top corroded surface showing formation of metallic sulfates and sufides during the internal sulfidation stage at 750 ℃

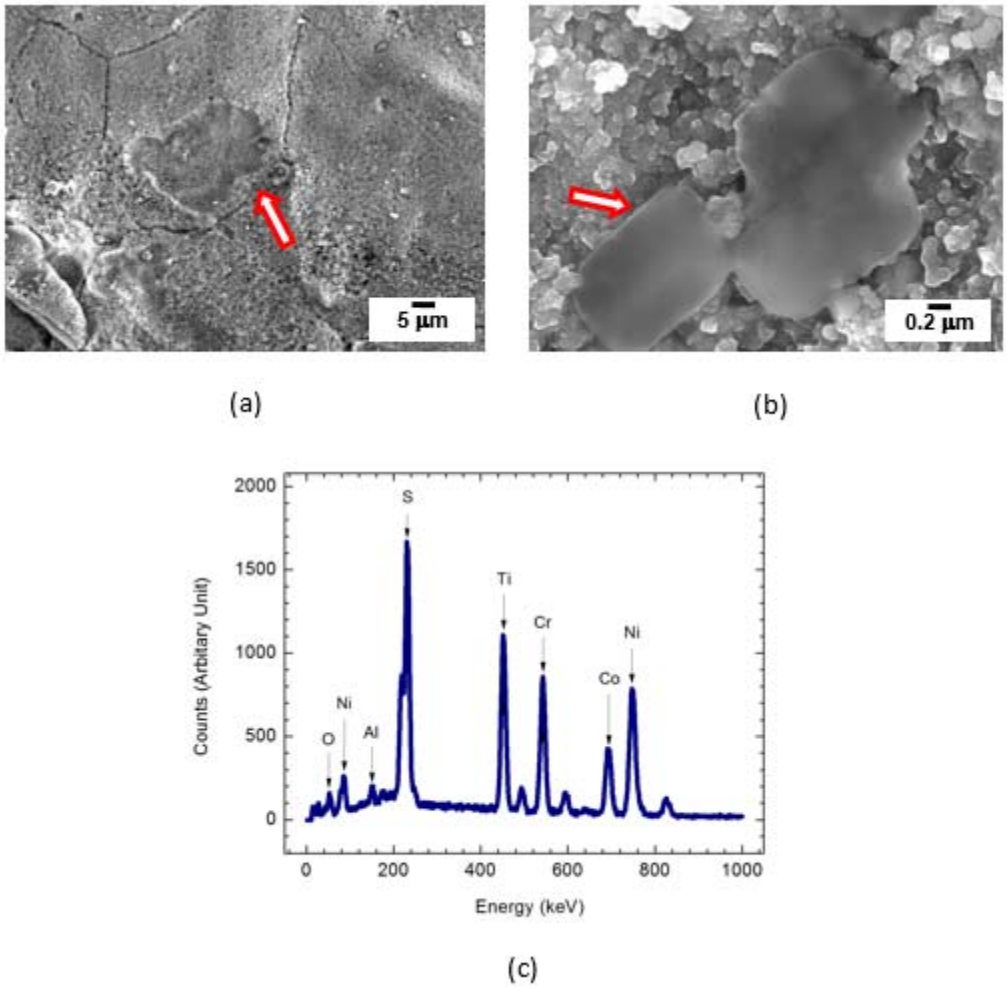

Figure 42 (a) Formation of TiS in the internal sulfidation stage at 750 ℃, (b) magnified view of (a), and (c) EDX pattern of (b)

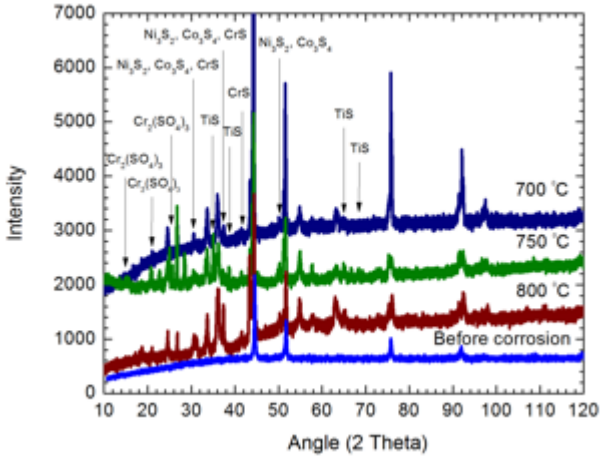

Figure 43 XRD patterns showing metallic sulfates and sulfides formation on top corroded surfaces at different temperatures

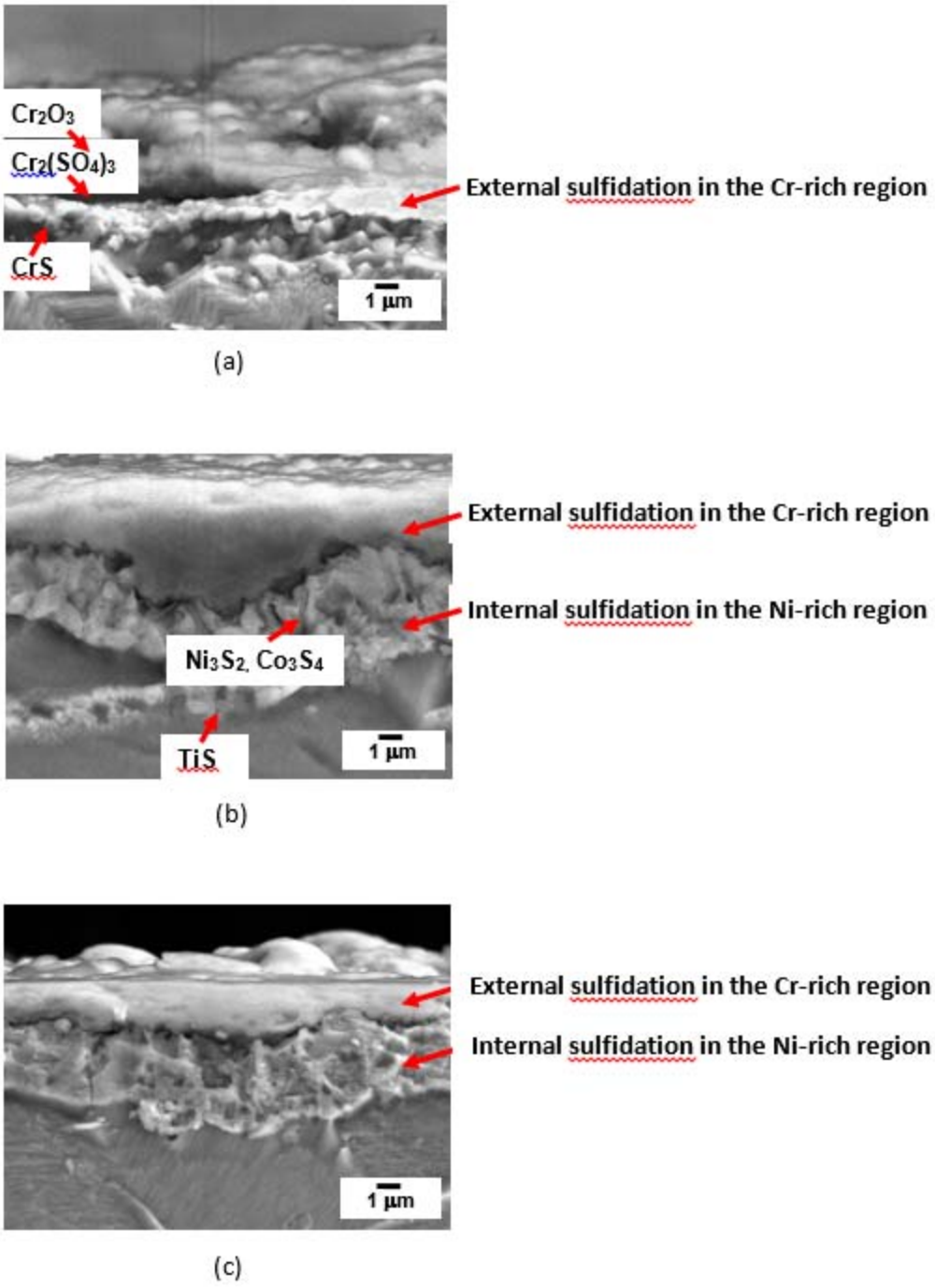

Figure 44 Comparison between the predominant corrosion stages at different temperatures after 123 h: (a) at 700 ℃, (b) at 750 ℃, and (c) at 800 ℃

Subtask 3.2 Develop Predictive System for Localized Corrosion in the Boiler Tubes

Experimental Methods

In Situ Monitoring Coal Ash Hot Corrosion using the Combined High Temperature Electrochemical Sensor with Electrochemical Noise Analysis Method

This research highlights the development of an in situ high temperature corrosion monitoring method that could be used to achieve a high degree of reliability and predictability in detecting the hot corrosion mechanism and the quantitative determination of the corrosion rates. Our previous research proposed that the combined use of our high temperature electrochemical sensor and electrochemical noise analysis can directly correlate the noise signatures to coal ash hot corrosion processes and their reaction kinetics. This paper provides more information about the proposed in situ corrosion monitoring method which can distinguish the mechanism between different high temperature corrosion processes. Five typical noise patterns were found to correlate with the prominent stages in coal ash hot corrosion processes and their different extents of corrosion. The response of noise signatures shows a good correlation with the results from the corroded surface analysis.

Materials and Simulated Coal Ash Hot Corrosion Conditions

The presence of molten alkali sulfate salts in the ambient gas chemistry of coal fired power plants play important roles in controlling the rate of hot corrosion. The ambient atmosphere contains contaminants such as SO_2 or SO_3. Under these conditions the initiation of a low temperature form of hot corrosion is likely to occur in the temperature range 600-800 °C. In this research, typical coal ash hot corrosion experiments are conducted to illustrate the applications of the proposed in situ monitoring method. Detailed information of the experimental conditions was summarized in Table 3.

Table 3: Experiments for different coal ash hot corrosion conditions

Corrosion condition	Notation	Thickness of coal ash	SO_2 content in flue gas
700 °C + Thin coal ash + SO_2	700 °C	1 mm	1 %
750 °C + Thin coal ash + without/with SO_2	750 °C without/with SO_2	1 mm	0 and 1 %
800 °C + Thin coal ash + SO_2	800 °C	1 mm	1 %
800 °C + Deep coal ash + SO_2	Deep coal ash	Totally immersed	1 %
850 °C + Thin coal ash + without/with SO_2	850 °C without/with SO_2	1 mm	0 and 1 %

Inconel 740 superalloy was selected to study its coal ash corrosion behaviour because it is a newly developed superalloy in the application to ultra-supercritical boilers with steam temperatures above 700 °C. The alloy has the chemical composition (in wt.%) of Ni-49.45, Cr-24.67, Fe-0.62, Co-19.98, Mo-0.50,

Nb-1.47, Al-1.23, Mn-0.3, Ti-1.23, Si-0.29. It was heat treated by the following sequences: 1150 °C for 4 h followed by air cooling; 1120 °C for 1 h followed by air cooling; 850 °C for 16 h followed by air cooling.

The experiments were conducted in a horizontal ATS Applied Test Systems model 3350B laboratory box furnace that contained a 95 mm internal diameter x 5 mm thickness x 650 mm long alumina tube. The sensor was inserted into the furnace running with conditions listed in Table 1. The electrodes of the sensor were covered with a synthetic mixture of coal ash. It consisted of reagent-grade 29.25 wt.% SiO_2, 29.25 wt.% Al_2O_3, 29.25 wt.% Fe_2O_3, 5.625 wt.% Na_2SO_4, 5.625 wt.% K_2SO_4 and 1 wt.% NaCl. The synthetic flue gas containing 15 vol.% CO_2, 4 vol.% O_2, 80 vol.% N_2 and 1 vol.% SO_2 was used with the flow rate of 150 ml min^{-1}. The temperature was measured by a thermocouple inserted into the furnace.

Electrochemical Noise Measurement with High Temperature Electrochemical Sensor

The high temperature electrochemical sensor was applied to simultaneously measure electrode potential and current noise to allow the direct comparison and correlation of electrochemical noise and corrosion events. The sensor was based on a four-electrode system. Two identical working electrodes were made of the Inconel 740 alloy. A reference electrode was the Ag/Ag^+ electrode containing 10 mol% Ag_2SO_4 in the 90 mol% Na_2SO_4 molten salt. It was sealed to prevent evaporation of the molten salt at high temperatures. The platinum wire was used for a counter electrode. The electrical connection to four electrodes was shielded with an alumina ceramic tube and sealed with ceramic paste to protect from the corrosive coal ash electrolyte. The detailed information for the design and construction of the sensor is given in our previous publication.

The fluctuations of potential and current simultaneously measured for a system of coupled electrodes every 24 h. The test data were analyzed using the Metrohm Autolab/PGSTAT302N with the Nova data acquisition system. The quantitative relationship between corrosion rate and current noise for coal ash hot corrosion process was determined using our proposed version of Faraday's Law expression. The instantaneous corrosion rate was used to calculate the accumulated mass loss and corrosion depths over the total experimental period of 120 h.

Top and Cross-Sectional Corroded Surface Analysis

To examine and evaluate the behavior, susceptibility, and extent of corrosion in different simulated coal-fired boiler environments the top and cross-sectional corroded surface analysis was conducted using scanning electron microscopy (SEM) equipped with an energy-dispersive X-ray microanalysis (EDX), and X-ray diffraction (XRD).

Study of Localized Under-Coal Ash Deposit Corrosion of Inconel 740 Alloy Using High Temperature Electrochemical Sensor

A high temperature electrochemical sensor has been developed to study localized under-coal ash deposit corrosion (LUDC) behavior of Inconel 740 superalloy. The LUDC process was studied from working electrode surfaces of the sensor that was locally covered by coal ash using the electrochemical impedance spectroscopy (EIS) and electrochemical noise (EN) analyses. Three typical potential noise patterns were found to correlate with the prominent stages in the LUDC process. Two characteristic current noise

patterns indicate the extent of the corrosion. There was a good correlation between the responses of electrochemical test data and the results from corroded surface analysis.

The LUDC of the Inconel 740 alloy was studied under a simulated synthetic flue gas containing coal-fired boiler environment at 750 °C using our developed high temperature electrochemical sensor. The LUDC is considered to be similar to under ''active'' solid deposit corrosion. The sensor was based on a three-electrode system which includes two identical working electrodes (WE1 and WE2), and one reference electrode (RE). The Inconel 740 alloy was used for WE1 and WE2. The reference electrode was the Ag/Ag^{+} electrode which contained 10 mol% Ag_2SO_4 in the 90 mol% Na_2SO_4 molten salt. The Ag wire was inserted into the fused-quartz (GE 214) tube allowing the Ag wire being immersed in the molten salt. The top of the reference electrode was sealed to prevent an evaporation of the molten salt at high temperature. The electrical connection to the test electrodes was shielded with a ceramic tube and sealed with ceramic paste for protection from the hot corrosive environment.

The corrosive medium was a synthetic thin coal ash in a synthetic flue gas environment. A thin film of a coal ash was established on all the electrodes to obtain a layer thickness of about 1 mm. In this case the working electrode surfaces were partially covered with thin film of coal ash. The composition of coal ash mixture was reagent-grade 29.25 wt.% SiO_2, 29.25 wt.% Al_2O_3, 29.25 wt.% Fe_2O_3, 5.625 wt.% Na_2SO_4, 5.625 wt.% K_2SO_4 and 1 wt.% NaCl. The synthetic flue gas composed of (in vol.%): 1% SO_2, 15%CO_2, 4% O_2 and 80% N_2. The flow rate of the pre-mixed flue gas was 150 ml min^{-1}. The hot LUDC tests were conducted in a horizontal ATS Applied Test Systems Model 3350B laboratory box furnace that contained a 95 mm internal diameter x 5 mm thickness x 650 mm long alumina tube. The sensor was inserted into the furnace in the horizontal position.

The kinetics of the electrochemical reactions occurring during the initiation and propagation of the LUDC corrosion was investigated using EIS and EN measurements. Schematic diagrams of the experimental setup for electrochemical measurements are shown in Figure 45. A two-electrode system was used for the EIS measurements. Impedance spectra from the corrosion were acquired in the frequency range of 1×10^5 Hz to 0.1 Hz with a 10 mV amplitude sine wave generated by the FRA module (Figure 45a). The fluctuations of potential and current signals that arise directly from the electrochemical reactions of the LUDC process, taking place on the electrode surface were measured using the optional ECN module (Figure 45b). The potential of the coupled WE1 and WE2 was measured against the RE. The current noise was measured as the current between two identical WE1 and WE2. The electrochemical test data were analyzed using the Metrohm Autolab/PGSTAT302N with the Nova data acquisition system. The EIS and EN measurements were carried out alternately during an exposure time of 494 h.

Scanning electron microscopy (SEM) equipped with an energy-dispersive X-ray microanalysis (EDX), and X-ray diffraction (XRD) were used to characterize top and cross-sectional the corroded surfaces.

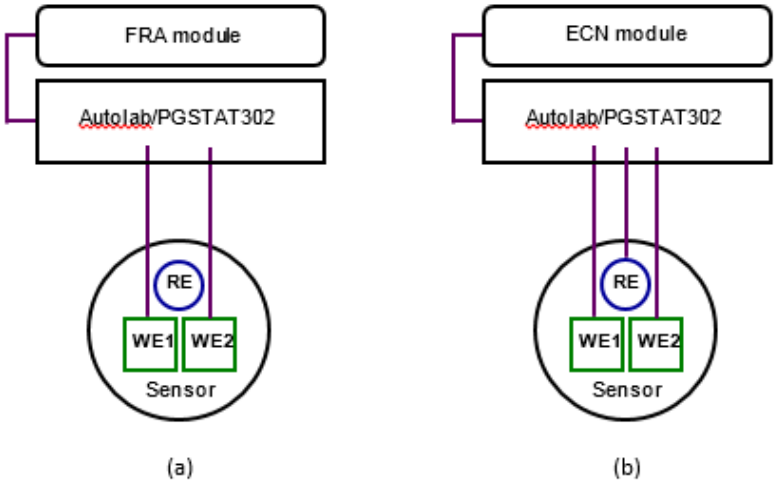

Figure 45 Schematic diagrams showing the experimental setup of the sensor for electrochemical measurements: (a) EIS measurement, and (b) EN measurement

Analysis of Electrochemical Noise by Power Spectral Density Applied to Coal Ash Hot Corrosion Study

The study of corrosion phenomena by electrochemical noise (EN) involves the analysis of random potential or current fluctuations. The usual approach for characterizing a random signal is to estimate its power spectral density (PSD), that is, the distribution of the power of the signal in the frequency domain. The fast Fourier transform (FFT) and the maximum entropy method (MEM) provide algorithms for the estimation of the power spectral density (PSD) of fluctuations. Both FFT and MEM methods were employed for the analysis of electrochemical noise in this study.

The comparison of FFT and MEM methods was carried out by processing the time records taken from simulated coal ash hot corrosion at different conditions using our developed high temperature electrochemical sensor. The sensor was based on a three-electrode system (two identical working electrodes (WE1 and WE2) and one reference electrode (RE). The potential of the coupled WE1 and WE2 was measured against the Ag/Ag^{+}/mullite reference electrode. The current noise was measured as the current between two identical WE1 and WE2. The potential noise and current noise signals measured simultaneously. Inconel 740 superalloy was studied in a simulated coal-fired boiler environment at a temperature range of 650-850 °C. The working electrode has the chemical composition (in wt.%) of Ni-49.45, Cr-24.67, Fe-0.62, Co-19.98, Mo-0.50, Nb-1.47, Al-1.23, Mn-0.3, Ti-1.23, Si-0.29. The corrosion medium was a synthetic mixture of coal ash with the flue gas. The coal ash mixture consisted of reagent-grade 29.25 wt.% SiO2, 29.25 wt.% Al2O3, 29.25 wt.% Fe2O3, 5.625 wt.% Na2SO4, 5.625 wt.% K2SO4 and 1 wt.% NaCl. The synthetic flue gas contained 15 vol.% CO2, 4 vol.% O2, 80 vol.% N2 and 1 vol.% SO2. The oxidation and sulfidation stages were simulated with and without SO2 content. The data points were continuously collected with sampling rates of one data point every 2 seconds.

Results and Discussions

July to September 2013

In Situ Monitoring Coal Ash Hot Corrosion using the Combined High Temperature Electrochemical Sensor with Electrochemical Noise Analysis Method

Characteristic Noise Signatures from Coal Ash Hot Corrosion Process

The oxidation, the external sulfidation, and the internal sulfidation are three major stages of the coal ash hot corrosion process. The predominant stage and amount of corrosion is a function of a number of variables, including the history of the alloy, operating temperature and gas composition, particularly its SO_2 content. The shifting conditions between oxidation and sulfidation can greatly vary the corrosion rate as a consequence of slow-growing oxide scale and fast-growing sulfide scale. The sulfidation attack can be more pronounced in the flue gas with SO_2 compared with in the flue gas without SO_2.

The changes from oxidation to sulfidation stage during the coal ash hot corrosion process were studied at 850 °C in the flue gas both with and without exposure to SO_2 for 360 h. The potential and current noise data were monitored in the flue gas without SO_2 for the first 240 h then the flue gas with SO_2 was monitored for 120 h. Three distinct stages of the coal ash hot corrosion process were observed from the electrode potential records and their extents of corrosion were evaluated with the current noise patterns (Figure 46). The corrosion potentials in the flue gas without SO_2 showed the negative values, but the values in the flue gas with SO_2 shifted to the positive regions (Figure 46a). The results clearly suggest the change of corrosion stage from oxidation to sulfidation. Oxidation is one of the dominant stages in the coal ash hot corrosion process. The high tendency of the nickel oxidation occurs at approximately (−180 mV vs Ag/Ag^+) in molten Na_2SO_4. Sulfidation is the preferable mechanism in the corrosion stage of nickel and nickel alloy in molten sulfates. It usually occurs at very positive potentials. The severity of the corrosion was evaluated with the characteristic current noise pattern. The sudden changes in current densities followed by slow or no recovery were observed during the sulfidation stage indicating the high extent corrosion (Figure 46b). The noise signature of sudden changes in current values followed by a slow or no recovery corresponds with the accelerated oxidation/sulfidation.

Five typical noise patterns can be identified to correlate with the prominent stages and their different extents of the coal ash hot corrosion:

- **(i)** The oxidation stage was featured with a characteristic noise signature of a gradual potential continuously changing in the negative region (*termed noise signature I*).
- **(ii)** The external sulfidation stage correlated to a characteristic noise signature of quick potential continuously approaching more positive values (*termed noise signature II*).
- **(iii)** The internal sulfidation stage corresponded with a characteristic noise signature of positive potential fluctuating randomly in a narrow range (*termed noise signature III*).
- **(iv)** The low extent of oxidation/sulfidation was characterized by the noise signature of current fluctuating with no sudden spike (*termed noise signature IV*).

(v) The accelerated oxidation/sulfidation can be evaluated with the noise signature of sudden change in current values followed by slow or no recovery (*termed noise signature V*).

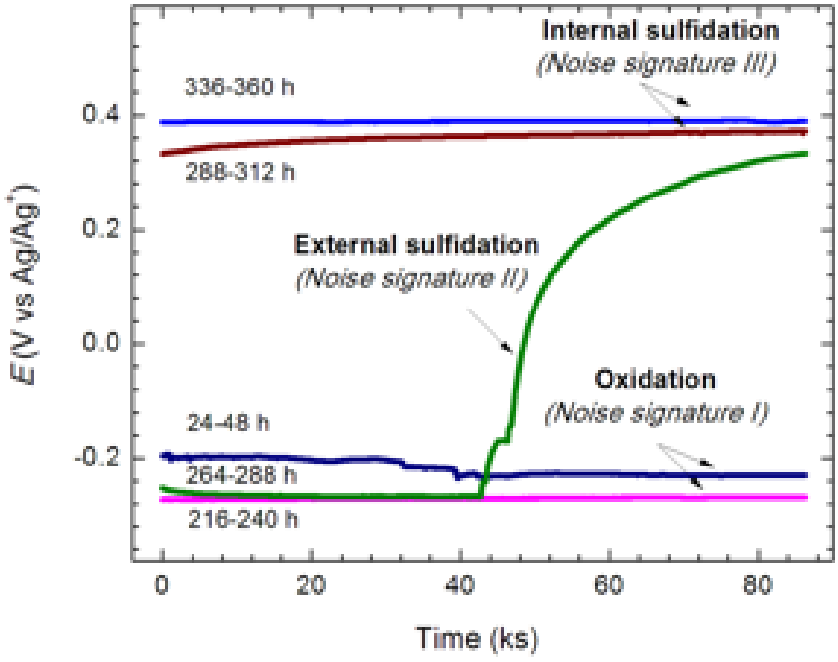

(a)

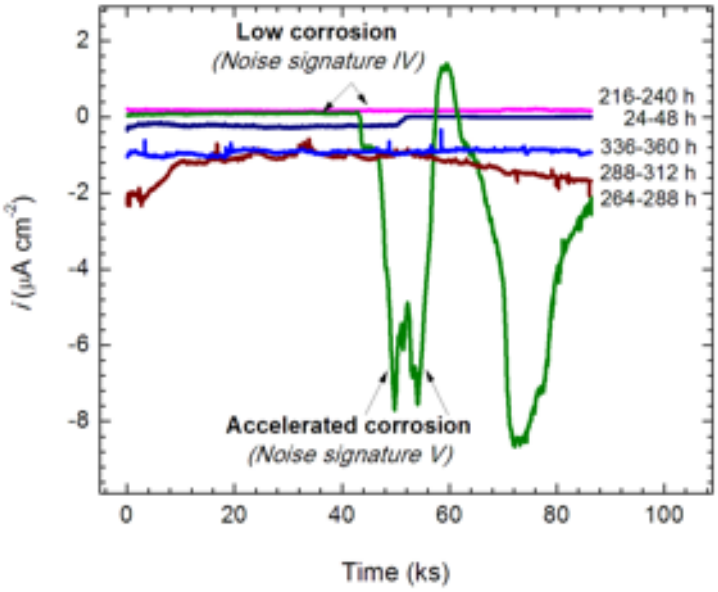

(b)

Figure 46 Three different stages of coal ash hot corrosion process and their extent of corrosion at 850 ℃ without/with SO_2 at different exposure periods: (a) characteristic potential noise signatures, and (b) characteristic current noise signatures

Corrosion Behaviour of Different Stages of Coal Ash Hot Corrosion

A series of experiments in simulated coal-fired boiler environments (Figure 47) were designed to study corrosion behaviour of different stages in the coal ash hot corrosion process.

Oxidation Stage

The indicator for the oxidation tendency was confirmed with the characteristic noise pattern of *noise signature I* (Figure 47). The time-series of potential noise data in the flue gas without SO_2 showed that the values varied from −180 mV (vs Ag/Ag^+) to −80 mV (vs Ag/Ag^+) during 120 h exposure (Figure 47a). Sudden changes in current value (*noise signature V*) occurred during 96-120 h due to changes in the extent of corrosion (Figure 47b). Two separate corrosion product layers were observed in the cross-sectional surfaces (Figure 47c). The existence of the *noise signature V* suggests that accelerated oxidation occurred in the Cr-rich and/or Ni-rich regions.

External Sulfidation Stage

There are two successive stages in sulfidation; the external sulfidation followed by the internal sulfidation. The indicator for the external sulfidation tendency was the *noise signatures II*. *This noise signature* was observed during the external sulfidation at 700 °C (Figure 48). In this stage, the values of positive potential varied throughout the exposure time. At 700 °C the values varied from 350 mV (vs Ag/Ag^+) to 440 mV (vs Ag/Ag^+) during 24-96 h exposure (Figure 48a). The corresponding current values were not stable before 96 h, but no sudden current spike was observed (*noise signature IV)* suggesting no serious corrosion attack (Figure 48b). External metallic sulfidation occurred in the Cr-rich region and the depth and the morphology of the corrosion product layer can be seen in Figure 48c.

Internal Sulfidation Stage

Internal sulfidation is the second stage of sulfidation. The indicator for the internal sulfidation stage was the *noise signatures III*. The internal sulfidation stage was dominant at 750 °C, 800 °C and deep coal ash (Figure 49-Figure 51). The corrosion potentials at 800 °C and 750 °C became stable at a value of 380 mV (vs Ag/Ag^+) (Figure 49a & Figure 50a). In the case of deep coal ash the stable internal sulfidation potential was about 300 mV (vs Ag/Ag^+) (Figure 51a).

The severity of the corrosion can be evaluated with the *noise signatures IV and V*. At 800 °C, the current values fluctuated randomly in a narrow range during the exposure periods (*noise signature IV*) (Figure 51b). *The noise signature V* was found to observe in the internal sulfidation stages at 750 °C and deep coal ash environment indicating accelerated internal sulfidation (Figure 50b & Figure 51b). It is confirmed that the extent of sulfidation attack at 800 °C (Figure 49c) was lower than those at 750 °C and deep coal ash environment (Figure 50c & Figure 51c). The deeper corrosion product layer formed at 750 °C (Figure 50c) compared with deep coal ash (Figure 51c).

Current noise has a direct relation with the reaction rate of the underlying process. In the localized pitting corrosion system, an aggressive local chemistry can develop and facilitate continued a high rate of anodic dissolution. In this case, metastable pitting is a separate process from true pit initiation. A pit nucleation

event is characterized by the current transient of a sharp rise followed by slow recovery. In the hot corrosion process of Ni, the current densities significantly increase with the immediate formation of soluble corrosion products. The noise signature of sudden change in current values followed by no recovery correlated to higher Ni dissolution (Figure 50b) compared with slow recovery (Figure 47b and Figure 51b).

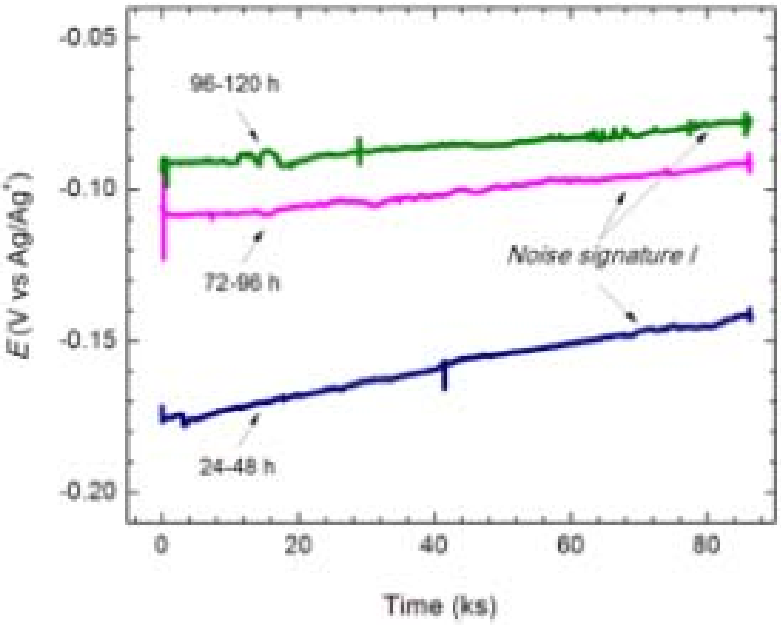

(a)

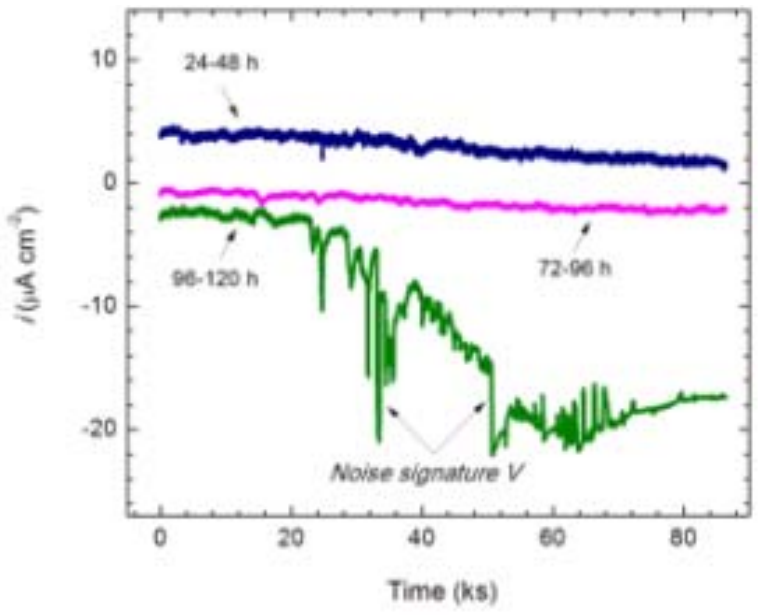

(b)

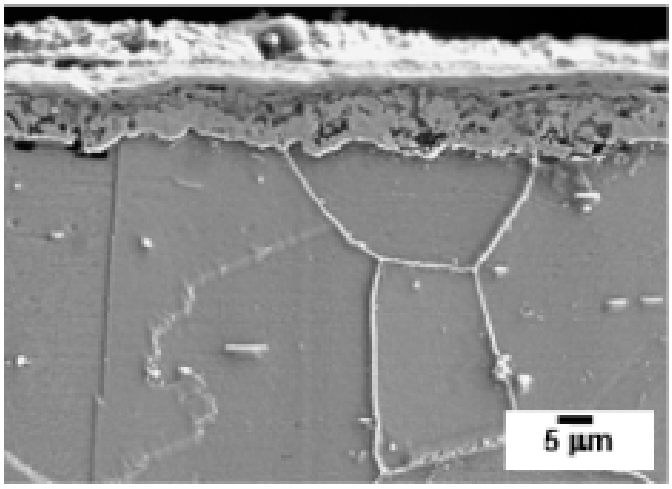

(c)

Figure 47 Oxidation stage of coal ash hot corrosion in the flue gas without SO_2: (a) characteristic potential noise signatures, (b) characteristic current noise signatures, and (c) cross-sectional corroded surface after 120 h

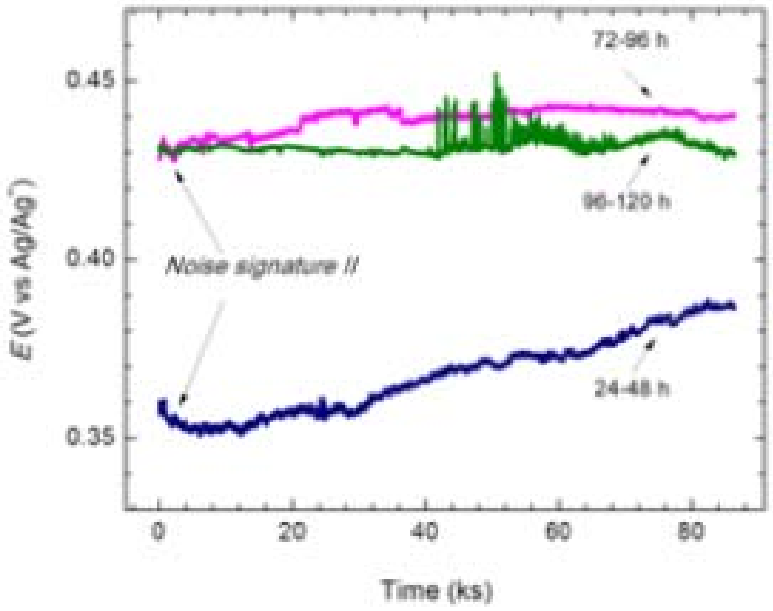

(a)

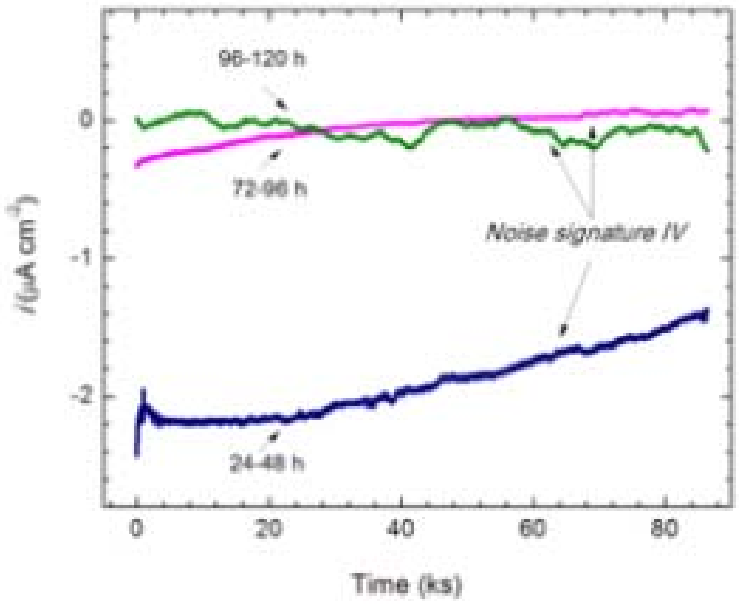

(b)

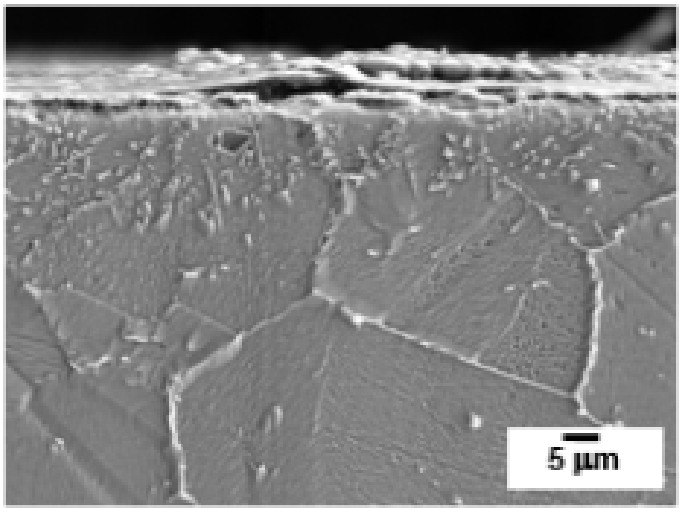

(c)

Figure 48 External sulfidation stage of coal ash hot corrosion at 700 ℃: (a) characteristic potential noise signatures, (b) characteristic current noise signatures, and (c) cross-sectional corroded surface after 120 h

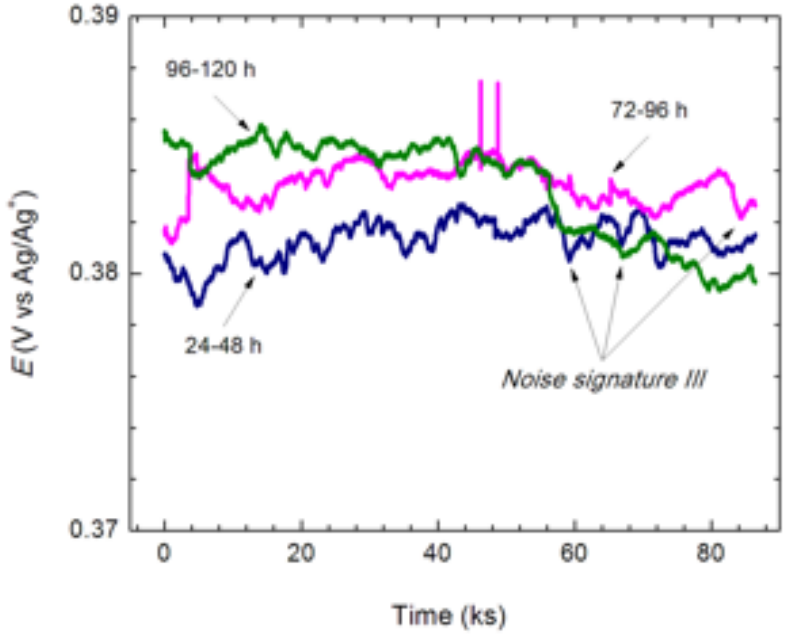
0.39
0.38
0.37
E (V vs Ag/Ag+)
96-120 h
72-96 h
24-48 h
Noise signature III
0
20
40
60
80
Time (ks)

(a)

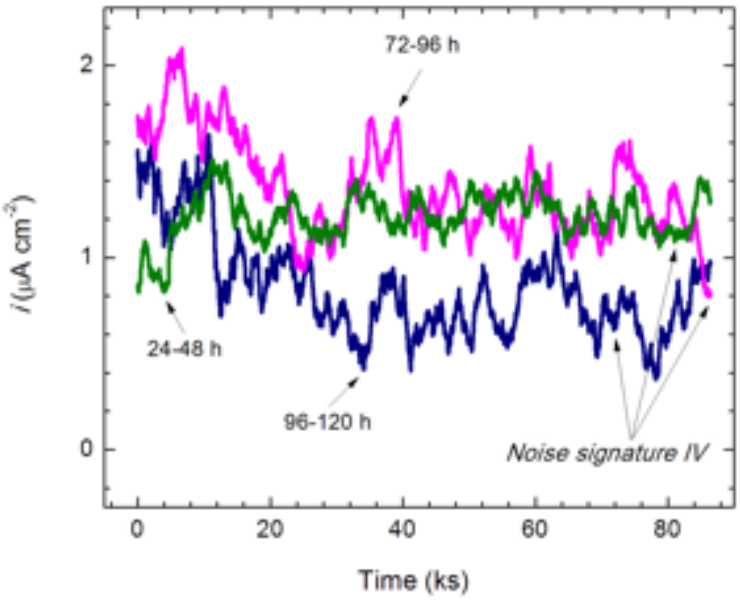
2
1
0
i (μA cm-2)
72-96 h
24-48 h
96-120 h
Noise signature IV
0
20
40
60
80
Time (ks)

(b)

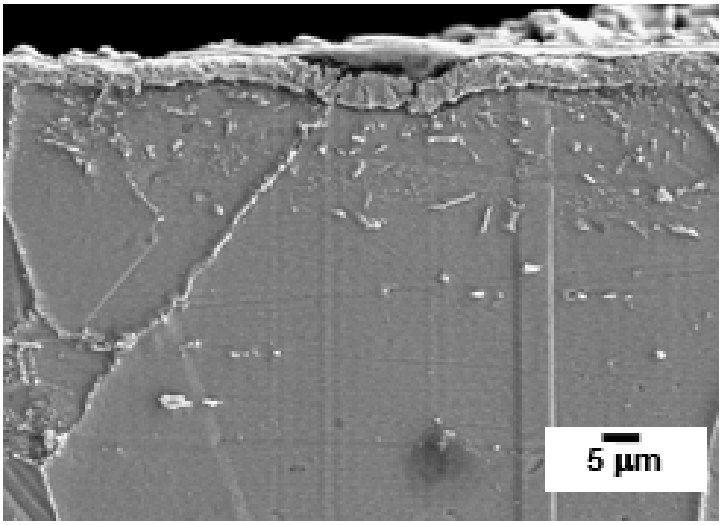

(c)

Figure 49 Internal sulfidation stage of coal ash hot corrosion at 800 ℃: (a) characteristic potential noise signatures, (b) characteristic current noise signatures, and (c) cross-sectional corroded surface after 120 h

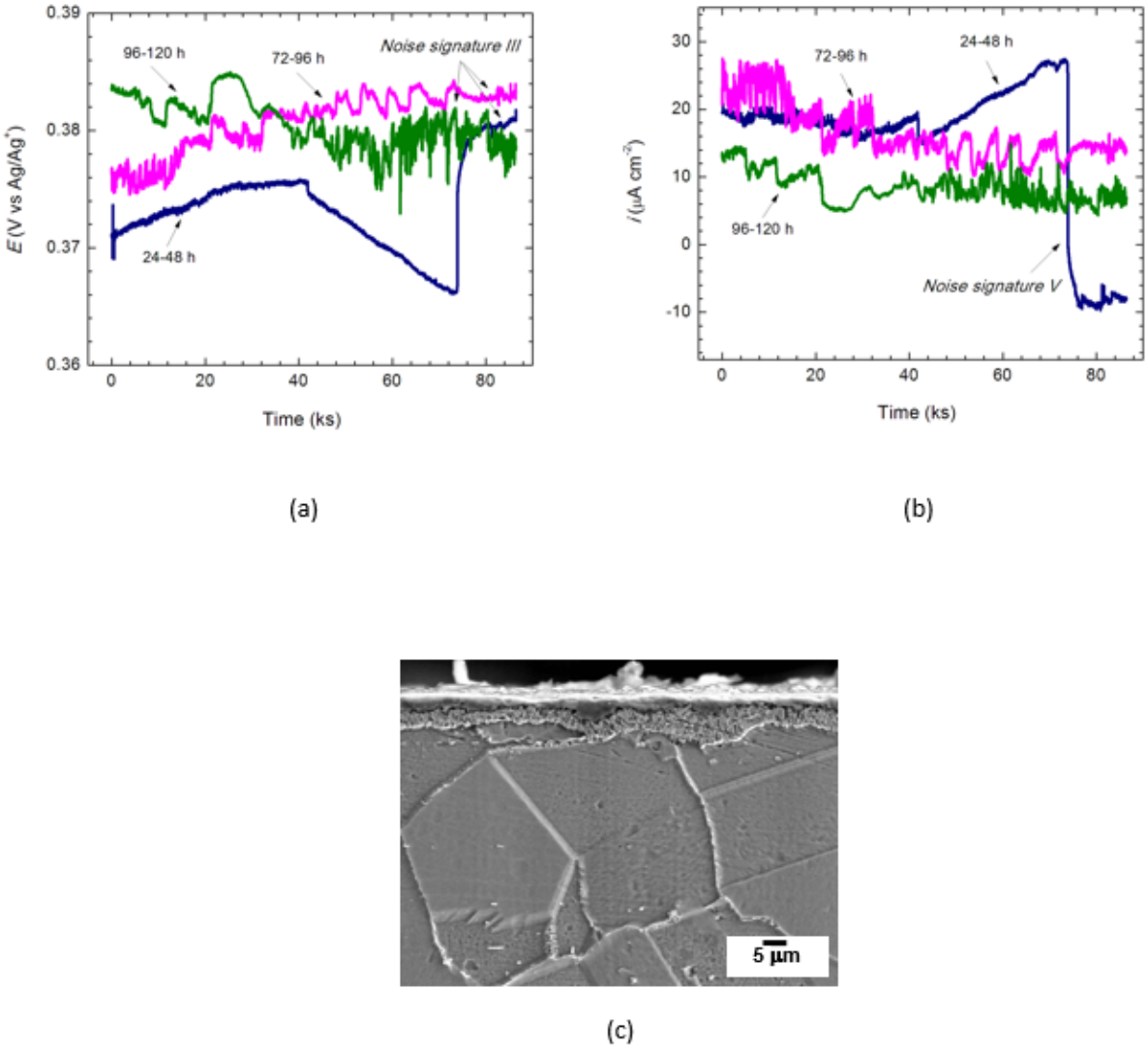

Figure 50 Accelerated internal sulfidation stage of coal ash hot corrosion at 750 ℃: (a) characteristic potential noise signatures, (b) characteristic current noise signatures, and (c) cross-sectional corroded surface after 120 h

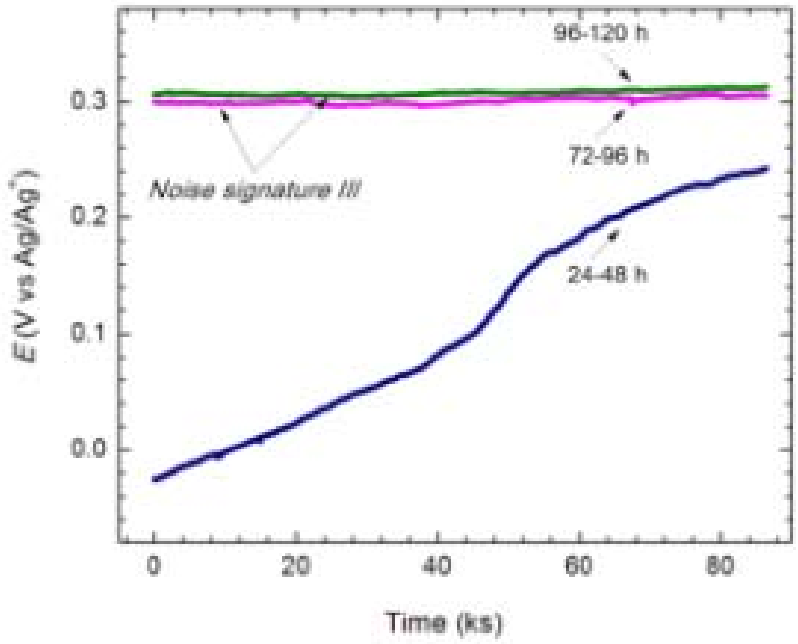
96-120 h
72-96 h
Noise signature III
24-48 h
E (V vs Ag/Ag+)
0.3
0.2
0.1
0.0
0
20
40
60
80
Time (ks)

(a)

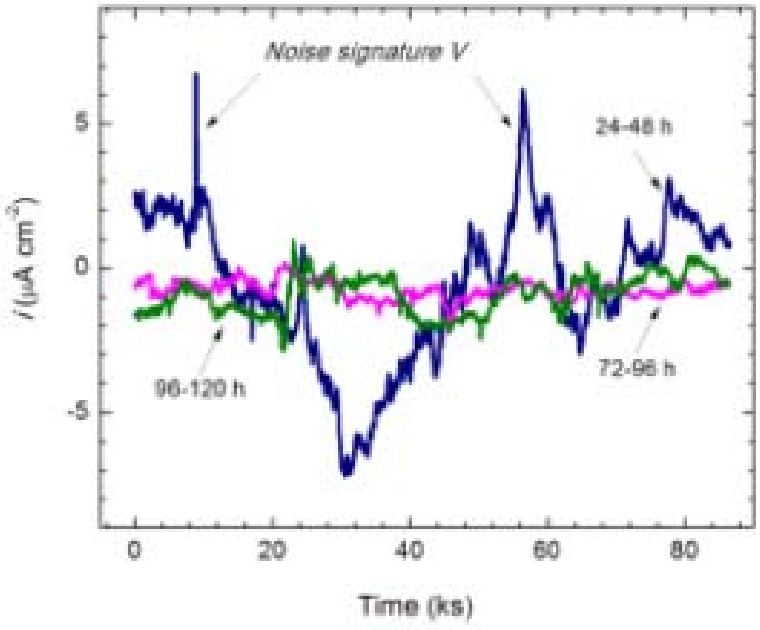
Noise signature V
24-48 h
72-96 h
96-120 h
I (μA cm-2)
5
0
-5
0
20
40
60
80
Time (ks)

(b)

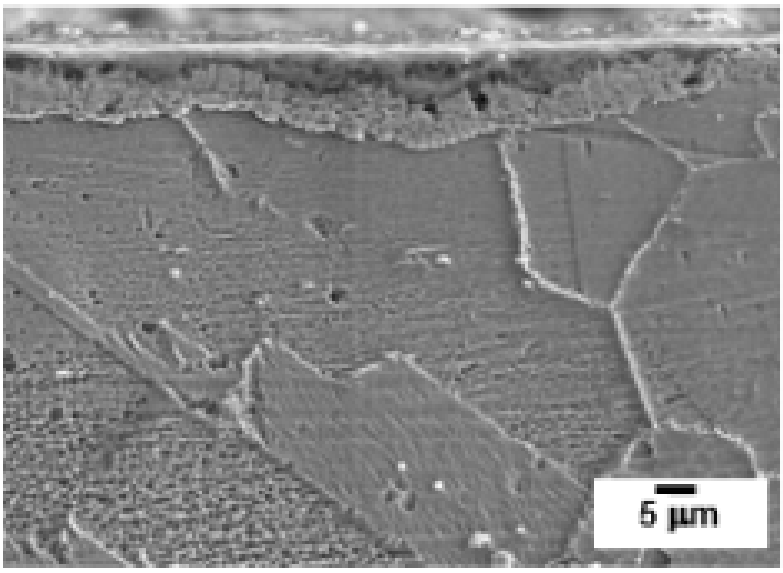

(c)

Figure 51 Accelerated internal sulfidation stage of coal ash hot corrosion in deep coal ash: (a) characteristic potential noise signatures, (b) characteristic current noise signatures, and (c) cross-sectional corroded surface after 120 h

Evaluation of Corrosion Rates of Oxidation and Sulfidation via Electrochemical Current Noise

The current noise analysis in the time domain was used to evaluate the corrosion rate, mass loss and corrosion depth varied with time (Figure 52). The instantaneous corrosion rates in different coal ash corrosion stages for the entire duration of exposure are given in Figure 52a. The corrosion rates of the alloy at 700°C were the lowest value compared with those in other coal-fired boiler environments. However, its corrosion resistance was significantly reduced at 750°C. The changes in instantaneous corrosion rate were used to determine accumulated mass losses and corrosion depths over the total experimental period. The metal losses (Figure 52b) and the depths of corrosion Figure 52c) at 750 °C after 120 h increased to about ten times and five times compared with 700 °C and 800 °C respectively. The presence of SO_2 in the flue gas accelerated the corrosion damage of the alloy in the coal ash environment. The extent of corrosion was found to be doubled with an increase in 1% SO_2 content in the flue gas. The corrosion attack in deep coal ash was higher compared with thin coal ash at 800 °C.

Operating temperature plays an important role in the sulfidation tendency of coal ash hot corrosion of Ni-based superalloys. A high sulfidation tendency can be observed in the temperatures lower than 800 °C due to the formation of low-melting alkali sulfate eutectic mixtures. But, the sulfidation tendency decreases in the high temperature form of hot corrosion because of the reduced stability of the sulfate compounds at temperatures higher than 800 °C. The relationship of corrosion rates to temperature follows a normal distribution with a peak rate at 750°C. From corroded surface analysis at 750 °C, the localized corrosion sites are generated by microgalvanic action between the cathodic TiS phase and the anodic Ni matrix resulting in accelerated intergranular and intragranular sulfidation. This is the reason

why the alloy suffered the highest internal sulfidation rate at 750 °C. The reduction of sulfidation rate at 800°C may be explained by the decreasing stability of the chromium sulphate.

Evolution of Oxidation and Sulfidation via Corroded Surface Analysis

A complex interaction between operating temperatures, coal ash chemistry as well as flue gas composition influences the coal ash hot corrosion behaviour. Of these, temperature plays the most important role in the high sulfidation attack observed in coal ash hot corrosion. As temperature increased from 700 °C to 750 °C and 800 °C, the external sulfidation proceeded to internal sulfidation. The corrosion morphology and the corrosion products formed in the oxidation and sulfidation stages were studied from the top and cross-sectional corroded surfaces (Figure 53-Figure 56). In comparison, no sulfidation attack was observed in the flue gas without SO_2 during 120 h (Figure 53), but the sulfidation tendency was the highest at 750 °C (Figure 54).

The corrosion product layers were composed of two separate layers indicating metallic oxidation/sulfidation which preferentially occurred in the Cr-rich and Ni-rich regions (Figure 53a and Figure 54a). The elemental distribution analysis confirmed the formation of metallic (Cr, Ni, Co, Al and Ti) oxides was the favourable condition for the oxidation stage in the flue gas without SO_2, but no obvious sulfur diffusion was observed (Figure 53). The major oxide corrosion products are Cr_2O_3, $(Ni,Co)Cr_2O_4$, Al_2O_3 and TiO_2. In the sulfidation stage, the distribution of Cr, Ni, Co, Ti, K, S and O indicates that sulfate and sulfide corrosion products could form in the Cr-rich and Ni-rich regions (Figure 54).

Different morphologies of the localized attack in the oxidation and sulfidation stages can be seen in Figure 55 and Figure 56. The intergranular and intragranular corrosion preferentially occurred in the internal sulfidation stage (Figure 56). The localized corrosion sites (Figure 56b) were generated by microgalvanic action between the cathodic metallic sulfide phase and the anodic Ni matrix leading to accelerated intergranular and intragranular corrosion rates. The XRD analysis shows that no significant peaks of the sulfate/sulfide were observed in the oxidation stage. $Cr_2(SO_4)_3$, CrS, Ni_3S_2, Co_3S_4 and TiS were formed in the internal sulfidation stage and the peaks of TiS in the accelerated internal sulfidation stage was the most significant (Figure 57). The high tendency of TiS formation leads to accelerated intergranular and intragranular corrosion.

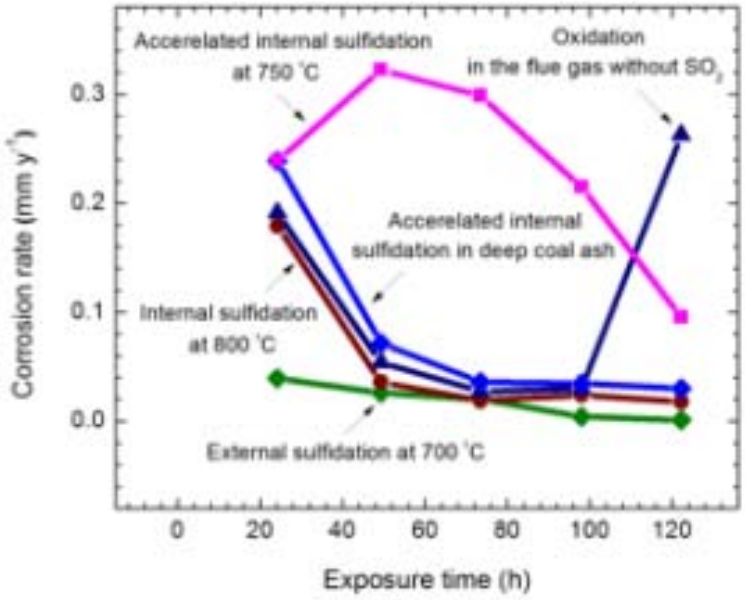
Accerelated internal sulfidation
at 750 °C
Oxidation
in the flue gas without SO2
Accerelated internal
sulfidation in deep coal ash
Internal sulfidation
at 800 °C
External sulfidation at 700 °C
Corrosion rate (mm y-1)
0.0
0.1
0.2
0.3
0
20
40
60
80
100
120
Exposure time (h)

(a)

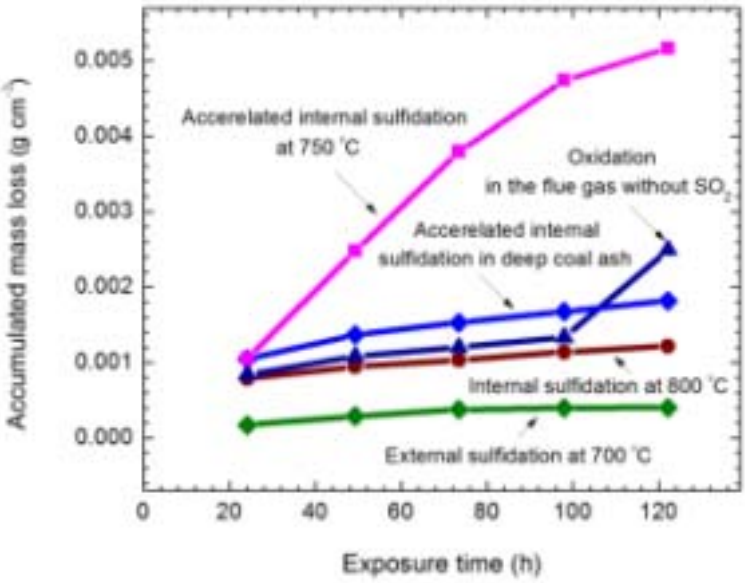
Accerelated internal sulfidation
at 750 °C
Oxidation
in the flue gas without SO2
Accerelated internal
sulfidation in deep coal ash
Internal sulfidation at 800 °C
External sulfidation at 700 °C
Accumulated mass loss (g cm-2)
0.000
0.001
0.002
0.003
0.004
0.005
0
20
40
60
80
100
120
Exposure time (h)

(b)

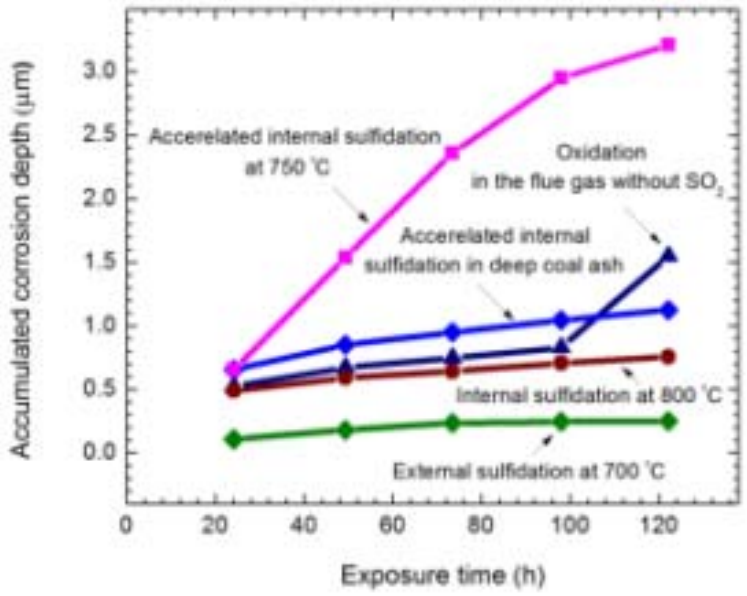

(c)

Figure 52 Comparison between corrosion kinetics data from EN analysis at different coal ash hot corrosion stages: (a) corrosion rates, (b) accumulated mass loss, and (c) accumulated corrosion depths

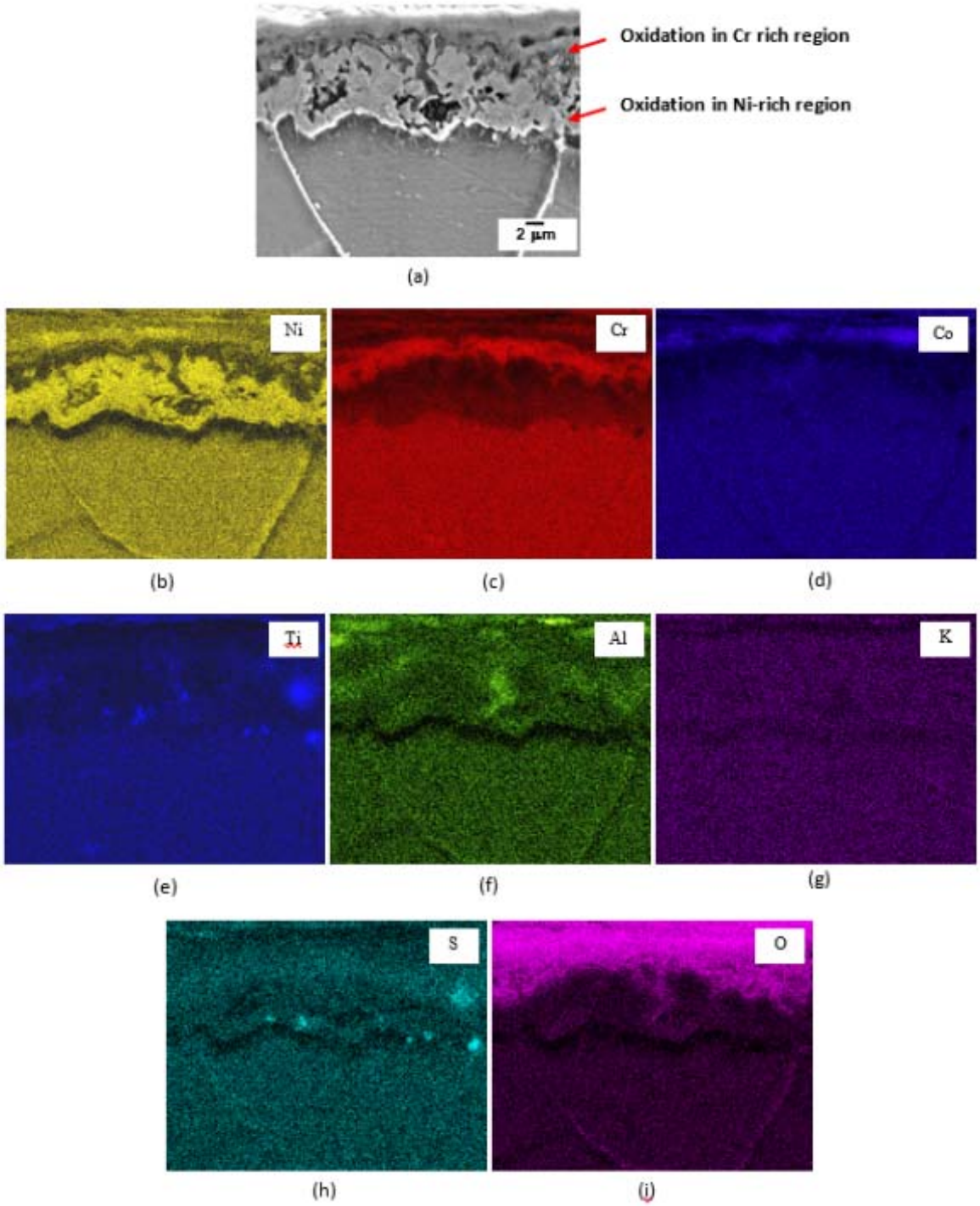

Figure 53 The elements mapping at cross-sectional corroded surface showing formation of metallic oxides during oxidation stage

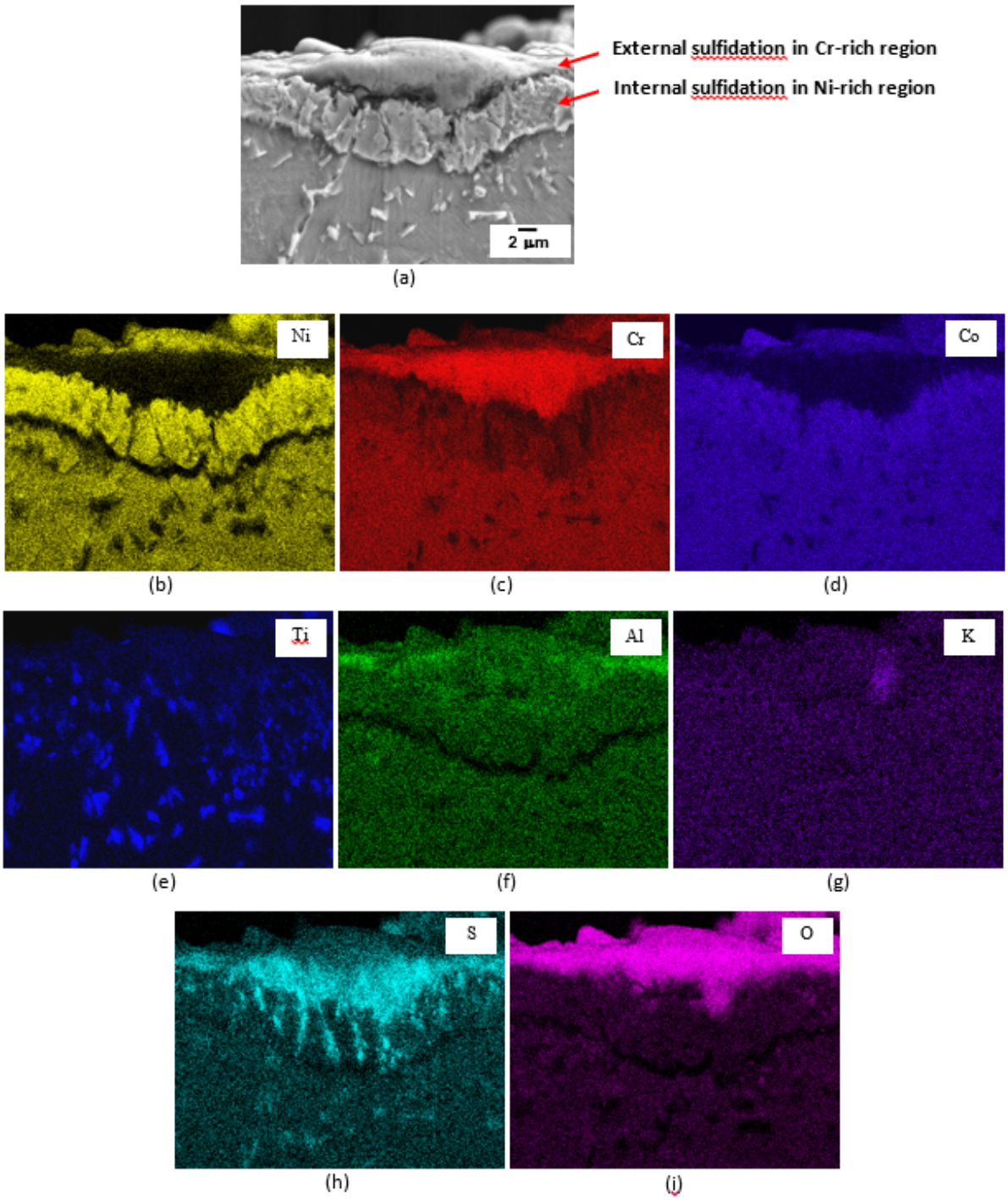

Figure 54 The elements mapping at cross-sectional corroded surface showing formation of metallic sulfates and sulfides during accelerated internal sulfidation stage

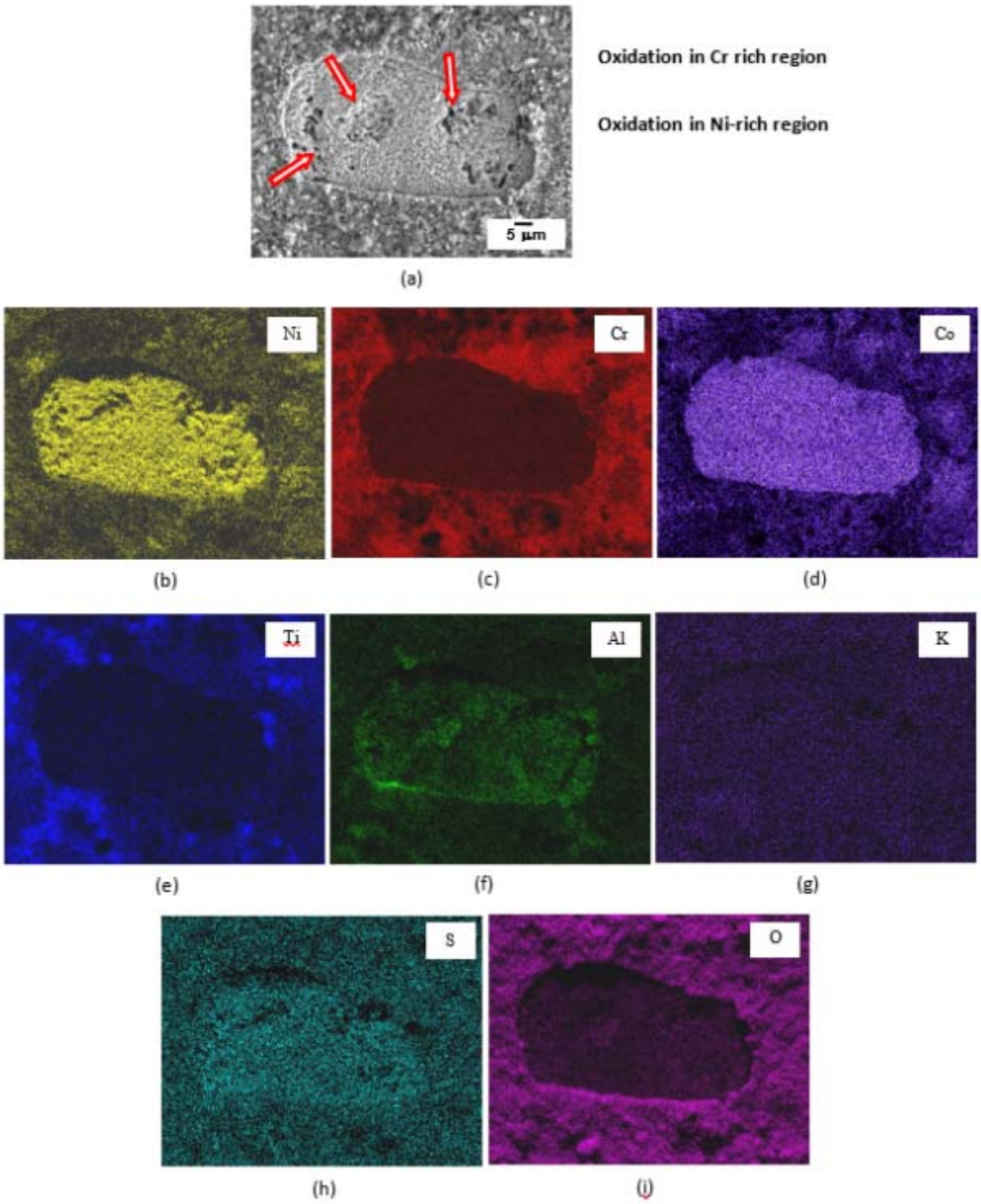

Figure 55 The elements mapping at the top corroded surface showing localized Ni-rich corroded areas during oxidation stage

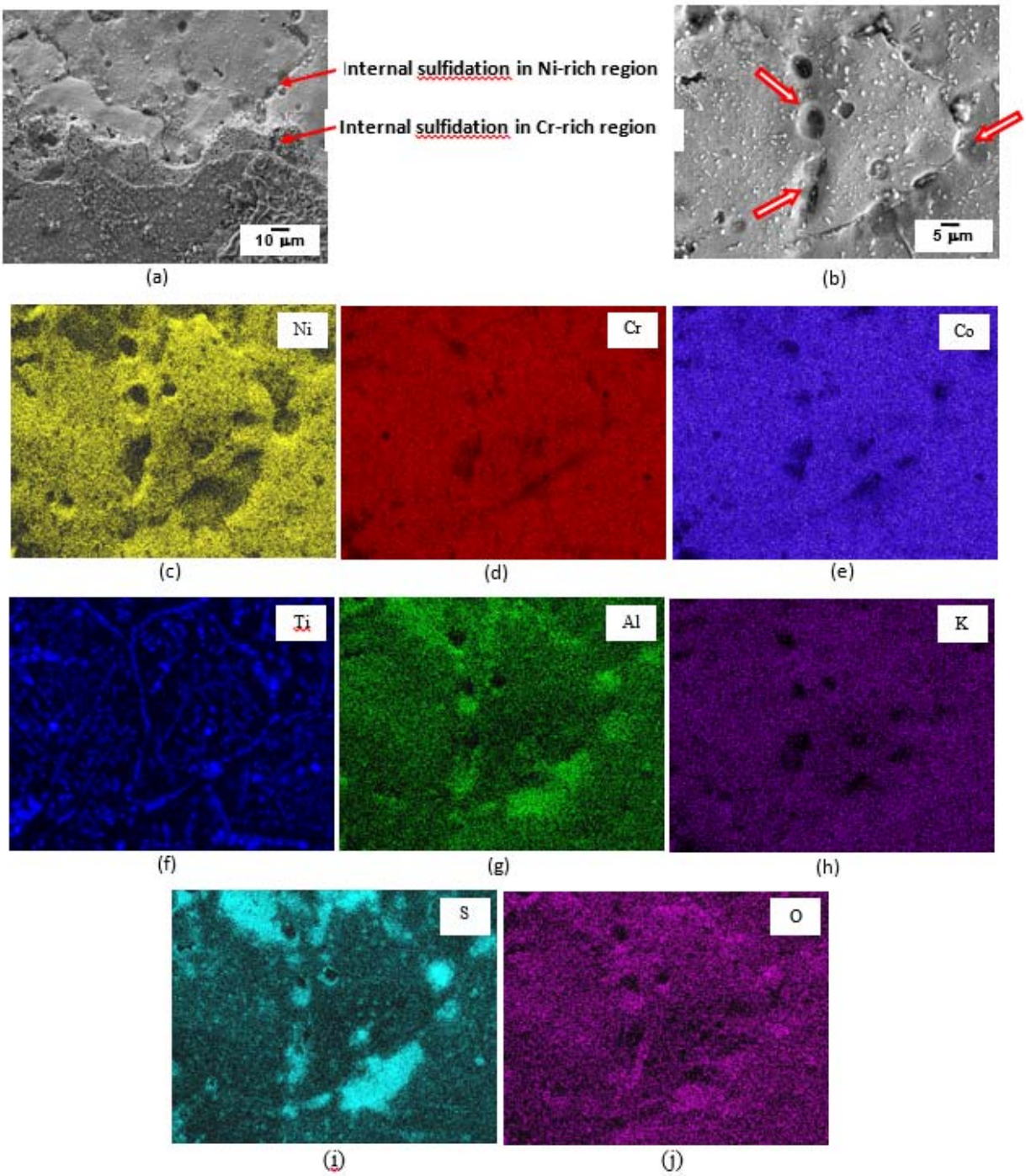

Figure 56 The elements mapping at the top corroded surface showing intergranular and intragranular corrosion in Ni-rich corroded areas during accelerated internal sulfidation stage

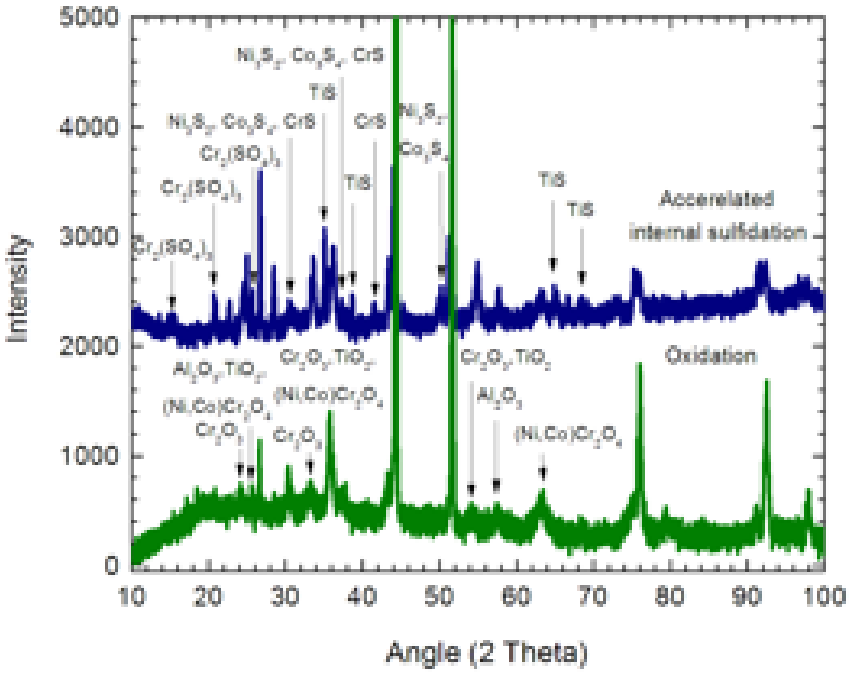

Figure 57 XRD patterns showing metallic oxides, sulfates and sulfides formation on top corroded surfaces at oxidation and sulfidation stages

July to September 2014

Study of Localized Under-Coal Ash Deposit Corrosion of Inconel 740 Alloy Using High Temperature Electrochemical Sensor

Electrochemical Impedance Spectra

The impedance behavior of different kinetics of certain reaction steps involved in the LUDC process is analyzed using the EIS. The measured and the calculated Nyquist plots plus the Bode diagrams of the phase angle and the total impedance magnitude are presented in Figure 58. The plot data clearly show two main corrosion stages. The appearances of semicircles with higher frequency and lower magnitude of impedance was attributed to a charge transfer process throughout exposure of 244 h. The spectra after 319 h exhibited a behavior containing a straight line of impedance (Warburg impedance) (Figure 58a). Generally, the oxidation and sulfidation are two major stages of the coal ash hot corrosion process. The corrosion process is initiated with the charge transfer controlled process of the oxidation stage followed by the diffusion-dominated process of the sulfidation stage. The Bode plots show the high impedance values during the transition stage between the oxidation and sulfidation of LUDC. But, the values decreased with the longer exposure time as a consequence of the accelerated sulfidation (Figure 58b). The time constants were not clearly pronounced on the phase angle plots of the sulfidation stage during 319-444 h (Figure 58c).

In the LUDC, The direct oxidation attack at the coal ash uncovered region could be initiated with the charge transfer controlled process. After certain exposure time, formation of coal ash sulphate eutectic deposits can lead to the diffusion-dominated process in the sulfidation stage at the coal ash covered region. Appropriate equivalent electric circuits were used to simulate the experimental impedance spectra of two different corrosion stages (Figure 59). In the equivalent circuit model for the oxidation stage, R_{ca} represents the resistance of the coal ash layer and C_{ca} is its capacitance in parallel. The oxide scale of the working electrodes during the oxidation stage may be considered as an oxide capacitor. To compensate for non-homogeneity of the oxide layer, constant phase element (CPE) was used in the fitting procedure. Thus, R_{ox} represents the charge transfer resistance of the oxide layer and CPE_{ox} is its capacitance in parallel (Figure 59a). In the sulfidation stage the corrosion is controlled by the diffusion of oxidant in the bulk melt, and an equivalent circuit of double-layer capacitance parallel with charge-transfer resistance in series with a Warburg resistance (W) (Figure 59b). W in equivalent circuit represents that the sulfidation is occurring due to both kinetic and diffusion mechanism. R_e represents the electrolyte resistance.

For the corrosion of Inconel 740 superalloy completely covered with a thin film of coal ash, the two steps reaction kinetics are the most predominant between 750 °C and 800 °C and the sulfidation process starts to occur after 48 h. In case of the LUDC at 750 °C, this process was observed after 319 h.

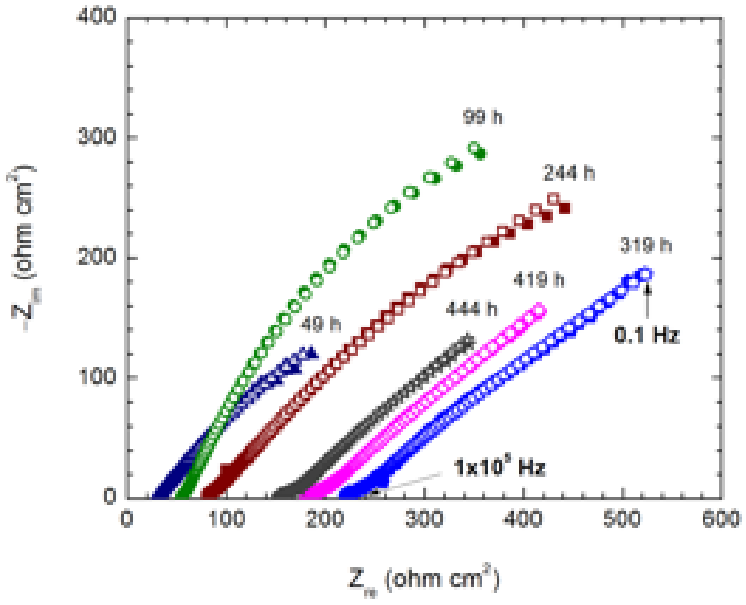

(a)

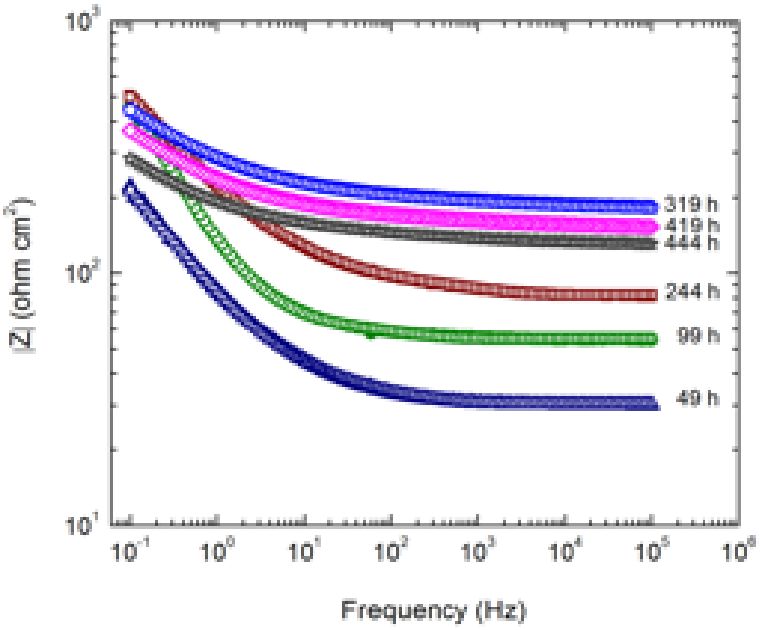

(b)

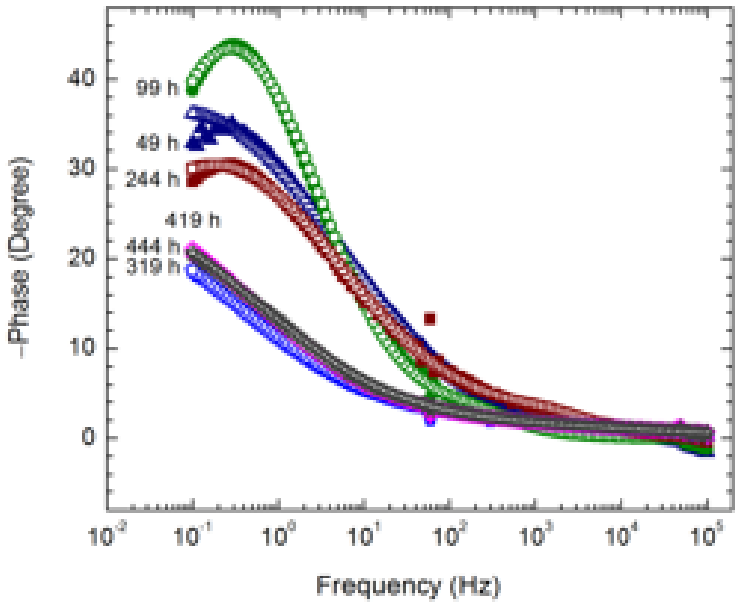

(c)

Figure 58 Nyquist and Bode plots measured at the corroded surface as a function of time at 750 ℃: (a) Nyquist plots and (b, c) Bode plots. Close symbol: experimental data; Open symbol: simulation data

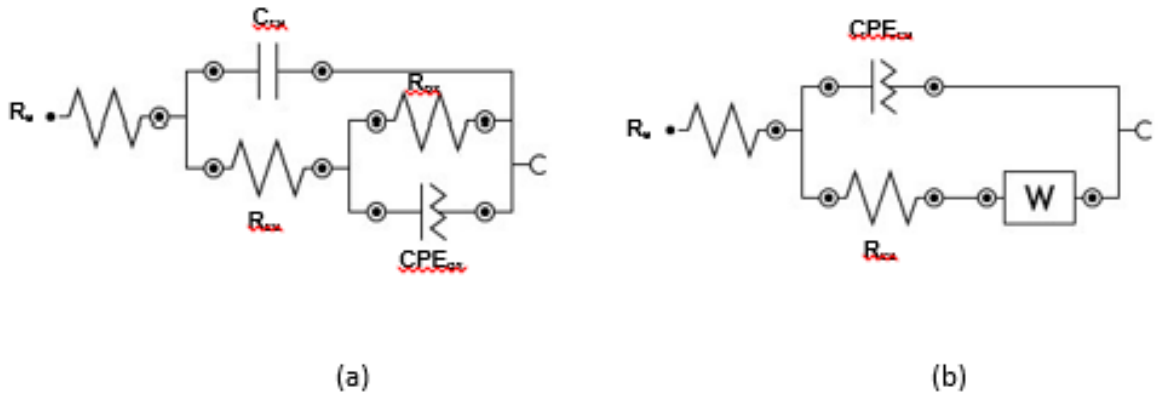

Figure 59 Equivalent electric circuits representing the impedance spectra for the localized under-coal ash deposit corrosion process of Inconel 740 superalloy; (a) equivalent circuit for the oxidation stage and (b) equivalent circuit for the sulfidation stage

Electrochemical Noise Data

The predominant stages during the LUDC process were studied by comparing and analyzing the potential and current noise signals from time and frequency domains (Figure 60-Figure 64). Simultaneous measurements of potential noise and current noise were made every 24 h during 494 h of exposure time (Figure 60-Figure 62). Three characteristic stages of the LUDC can be identified with three typical potential noise patterns and their extents of the corrosion can be evaluated with two characteristic current noise patterns.

The first stage of corrosion was characterized by the noise pattern of continuously changing potential approaching less negative values. The potential values varied from –300 mV (vs Ag/Ag^+) to –50 mV (vs Ag/Ag^+) during 244 h exposure Figure 60a). The negative corrosion potentials confirmed that oxidation was the predominant process. The high tendency of the nickel oxidation occurs at approximately (–180 mV vs Ag/Ag^+) in molten coal ash. The oxidation currents were characterized by the noise signature of current fluctuating with no sudden spike indicating pure oxide scale formation with low scaling rates (Figure 60b).

The second stage of corrosion was featured with the characteristic potential noise pattern of the cyclic oscillations. The oscillations occurred within a potential range of –50 mV (vs Ag/Ag^+) and 120 mV (vs Ag/Ag^+) during 269-319 h (Figure 61a). A potential gradient can be created as a result of varied oxygen and sulfur diffusion to the metal surface under the coal ash deposit. The positive corrosion potentials suggest a transition from oxidation to sulfidation because sulfidation usually occurs at very positive potentials. The sulfidation initiated in the higher current densities range of 1-30 $\mu A\ cm^{-2}$ that suggests the formation of sulfide-rich corrosion products with high scaling rates (Figure 61b). The electrochemical noise oscillations may be observed for localized corrosion under less protective film.

The third stage of corrosion was featured with potential changes in positive direction in a narrow range. As shown in Figure 62a, the electrode potential fluctuated within 235-290 mV over a 120 h period. The

stable sulfidation potential of 280 mV (vs Ag/Ag^{+}) was observed after 494 h. The noise patterns of sudden change in current values followed by slow or no recovery were observed in this corrosion stage. These signals corresponded with the high extent of sulfidation. The maximum current density values were increased from 30 to 40 $\mu A\ cm^{-2}$ (Figure 62b). The alloy suffers the serious sulfidation attack during coal ash hot corrosion at 750 °C.

The time-series data of the potential and current fluctuations were transformed into frequency domain to determine their power spectra densities (PSD) which express the signal power as a function of frequency. The low frequency and the slope of PSD plots can give important mechanistic and kinetic information about an electrochemical corrosion process. In this study, the PSD data for potential as well as current noise were obtained using a Hanning window at coefficient 30 of the maximum entropy method (MEM). Typical PSD slopes of three different stages of the LUDC are shown in Figure 63. Both of the PSDs are independent of the frequency in the region lower than 0.0001 Hz (Figure 63a and Figure 63b). The low frequency end of the spectra during the oxidation stage (99 h) and the sulfidation stage (419 h) were found on the plateau, however, that of the oxidation-sulfidation transition (319 h) was observed on the straight line.

In case of corrosion systems generating $1/f^{\beta}$ noise, linear sloped PSD spectra within an accessible frequency bandwidth are detected. The slopes of the linear part of the spectrum (β) provides information on the type of corrosion. General corrosion is considered to give high slope of $\beta>2$ while $\beta<2$ is for localized corrosion process. The PSD slopes of potential spectra clearly show the mechanistic information of the LUDC (Figure 63a) and the kinetic values for mechanism can be interpreted from the corresponding current spectra (Figure 63b). A variation of the slope was observed during the oxidation-sulfidation transition stage (Figure 63a and Figure 63b). Any phenomenon that occurs on the electrode passivation or diffusion produces the variation of the slope. The characteristic of slope ($\beta<2$) was observed in the oxidation and sulfidation stages indicating the localized form of corrosion. The lower β value and higher level of current power values of the sulfidation stage indicate its highly extent of localized attack compared with the oxidation stage.

The results from PSD analysis was confirmed with the changes in the noise resistance in the frequency domain (R_{sn}) and localization index (Figure 64). The higher values of R_{sn} were observed during the oxidation stage of the LUDC. In contrast, the R_{sn} values significantly reduced during the sulfidation stage indicating the severe corrosion attack (Figure 64a). Continuous increase in the localization index during the sulfidation stage suggests high degree of localization (Figure 64b). Decrease in the localization index can be observed during general corrosion or passivation process.

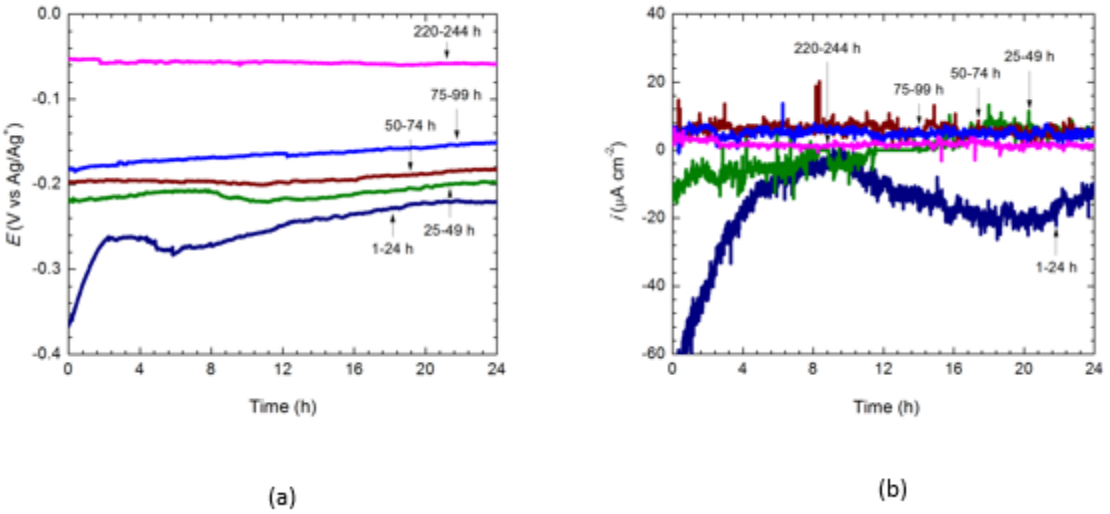

Figure 60 Time series of the electrochemical noise signals from localized under-coal ash deposit corrosion during 1-244 h (a) potential noise signals, and (b) current noise signals

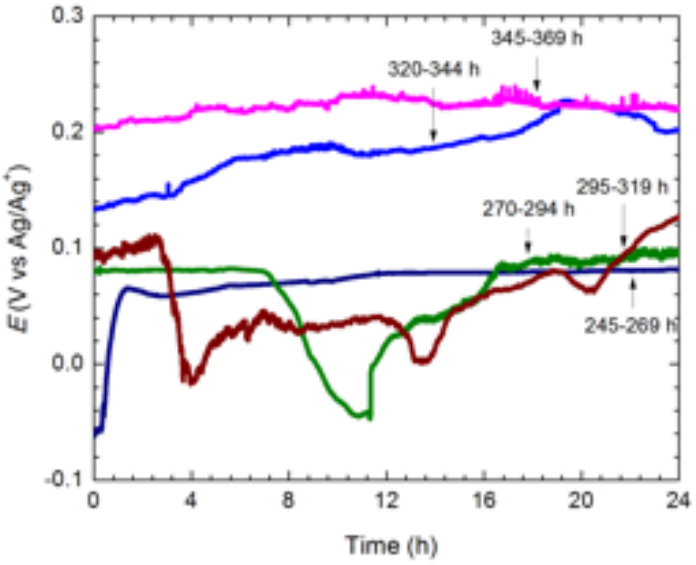

(a)

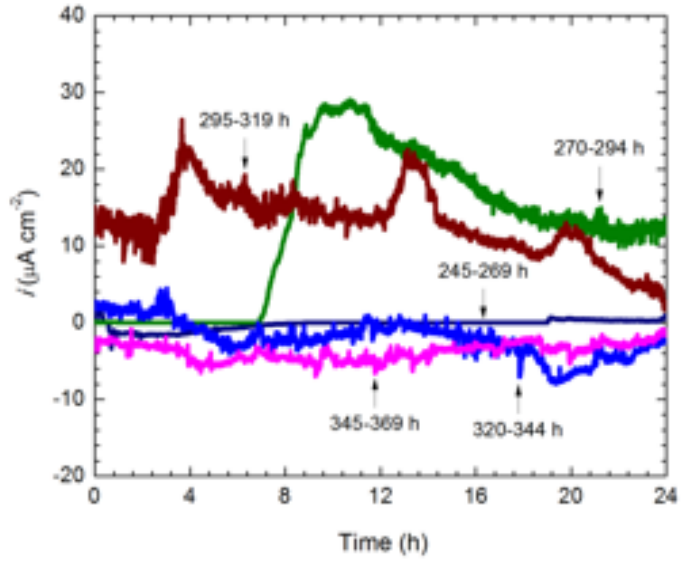

(b)

Figure 61 Time series of the electrochemical noise signals from localized under-coal ash deposit corrosion during 245 -369 h (a) potential noise signals, and (b) current noise signals

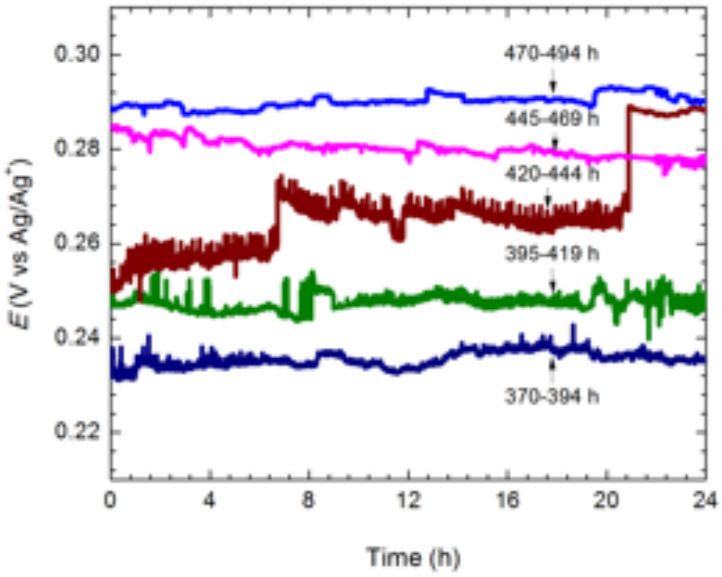

(a)

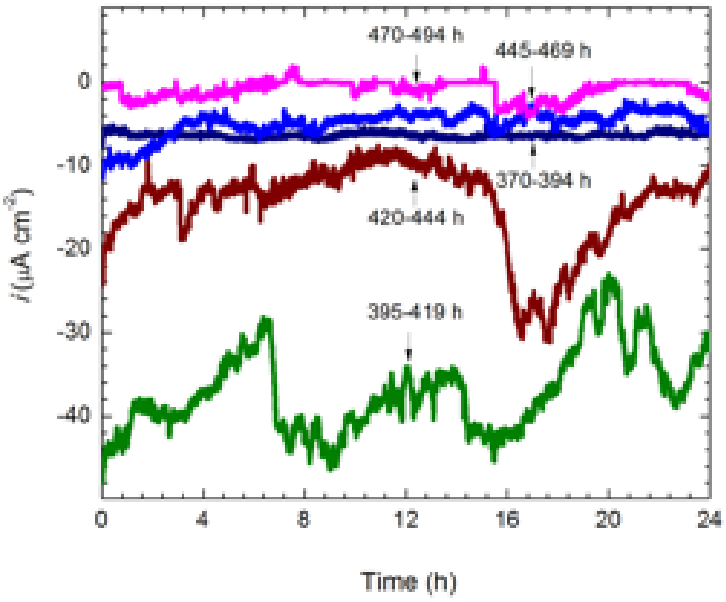

(b)

Figure 62 Time series of the electrochemical noise signals from localized under-coal ash deposit corrosion during 370-494 h: (a) potential noise signals, and (b) current noise signals

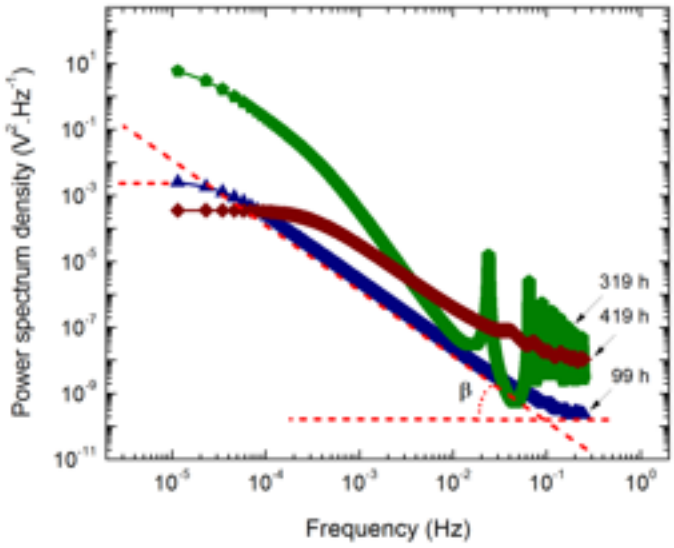

(a)

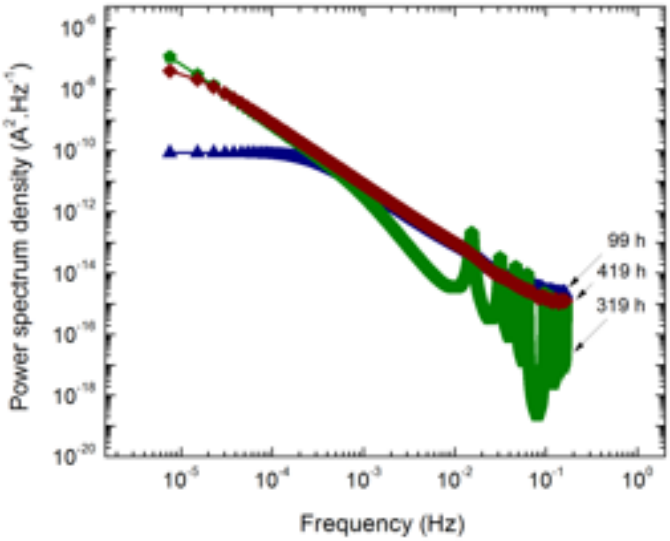

(b)

Figure 63 Typical PSD slopes of three different stages of localized under-coal ash deposit corrosion; (a) potential spectra, and (b) current spectra

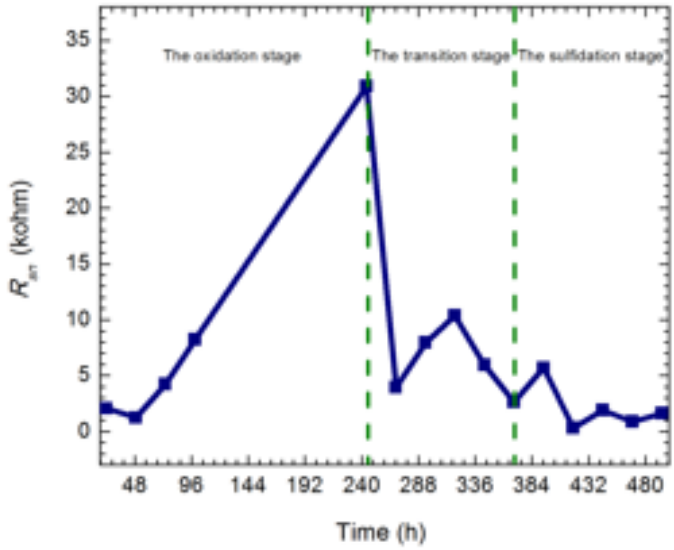

(a)

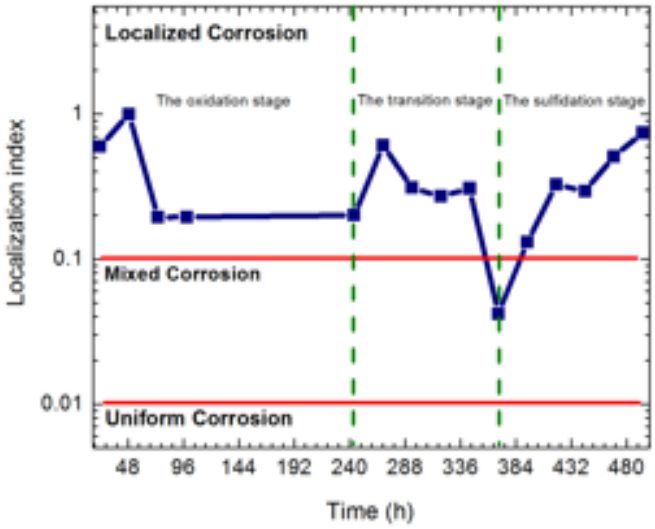

(b)

Figure 64 Comparison between the electrochemical noise test data from three different stages of localized under-coal ash deposit corrosion as a function of time: R_{sn}, and (b) localization index

Evolution of Localized Under-Coal Ash Deposit Corrosion via Corroded Surface Analysis

The top and cross-sectional corroded surfaces after 244 h and 494 h were analyzed for evolution of the LUDC. Three distinct areas on the corroded surfaces can be discerned from the optical micrographs and SEM micrographs (Figure 65 and Figure 66). The rings in Figure 65a and Figure 66a indicate the areas between the coal ash covered region and uncovered region.

In the oxidation stage of corrosion before 244 h, the highly oxidized areas were observed at the coal ash uncovered region (the arrows shown in Figure 65a). In the sulfidation initiation and propagation stages during 494 h, the most serious corrosion attack can be seen near and inside the coal ash covered regions (the arrows shown in Figure 66a). Close-up views of SEM micrographs clearly show higher extents of sulfidation close and inside the coal ash covered region after 494 h compared with 244 h (Figure 65b and Figure 66b).

Nickel alloys in the coal gasification environment exhibit a transition from pure oxide scale formation with low scaling rates to the formation of sulfide-rich corrosion products with high scaling rates. In the transition stage from oxidation to sulfidation the primary oxide film became overgrown by the sulfide layer (Figure 67 and Figure 68). The boundary between oxidation and sulfidation is not precisely defined. At a given temperature, it depends not only oxygen and sulphur pressure but also the duration of the experiment. There is a tendency at a given sulphur pressure for the border to shift with increasing time to somewhat higher oxygen pressures. Our results showed no significant difference in the morphology as well as the depth of corrosion at the coal ash uncovered and covered regions during the oxidation stage (Figure 67a-Figure 67c). As a result of varied oxygen and sulfur diffusion to the metal surfaces due to longer exposure time, the different extent of corrosion attack was observed at three distinct areas after 494 h (Figure 68a-Figure 68c). The morphology of the corroded layers due to the oxidation (Figure 68a) was distinguished from the corroded layer due to the sulfidation (Figure 68b and Figure 68c). As expected, the corrosion attack was much higher inside the coal ash covered region and its corrosion depth increased to three times (Figure 68c).

From the elements mapping after exposure for 244 h and 494 h, different extents of the oxidation and the sulfidation at coal ash uncovered and covered areas can be compared (Figure 69-Figure 73). Before 244 h the oxidation was the predominant process at coal ash uncovered area as well as covered area (Figure 69 and Figure 70). At coal ash covered area, the alloy could dissolve in the molten sulfate salt and diffuse to the salt/gas interface where it precipitated as metal oxides, sulfates and sulfides. The oxide layer formed first followed by localized sulfidation beneath the layers. Although the thick oxide layer was observed the metallic sulfates and sulfides formation was not obvious (Figure 70). It could be due to the short exposure time to establish the sulfidation process. After 494 h the oxidation could be predominant at coal ash uncovered area as a consequence of no molten coal ash sulfate salt, which is essential for the sulfidation to proceed kinetically. The elements mapping of the coal ash uncovered area clearly shows no significant sulfur diffusion beneath its oxide layer (Figure 71). As expected, the serious sulfidation attack occurred near and inside the coal ash covered areas (Figure 72-Figure 73). The higher depth of oxides and sulfur diffusion were observed near and inside the coal ash covered regions (Figure 72 and Figure 73). The propagation and stabilization of sulfidation was a continued chemical reaction between the deposit and

the underlying material inside the coal ash covered region. In contrast, the corroded layer inside the coal ash covered region became three times deeper (Figure 73) than the oxide layer at uncovered region (Figure 71).

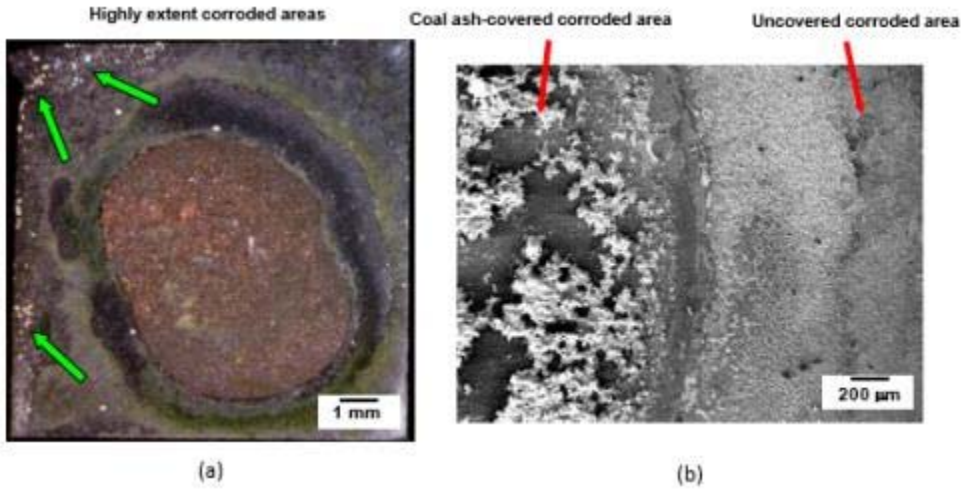

Figure 65 Top localized under-coal ash deposit corroded surfaces after 244 h: (a) optical micrograph, and (b) SEM micrograph

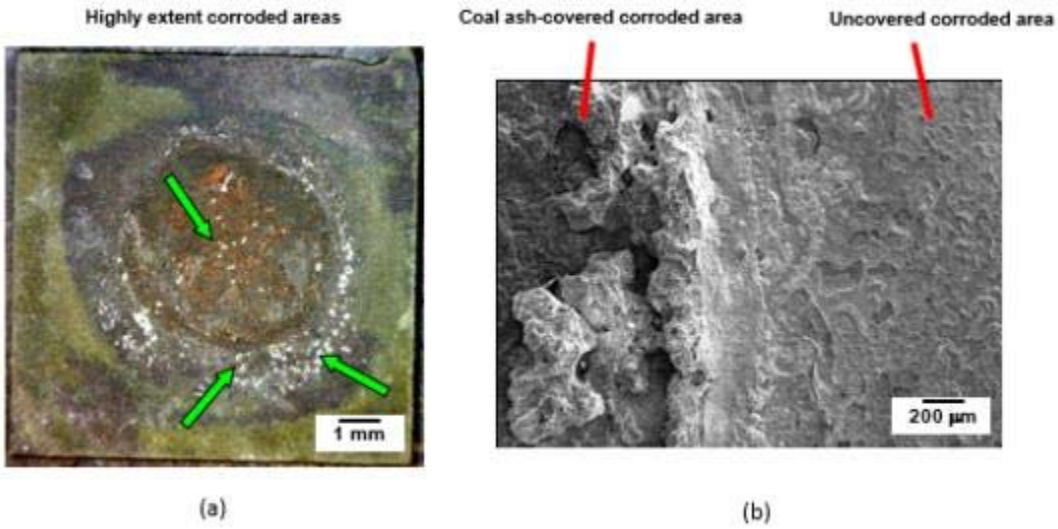

Figure 66 Top localized under-coal ash deposit corroded surfaces after 494 h: (a) optical micrograph, and (b) SEM micrograph

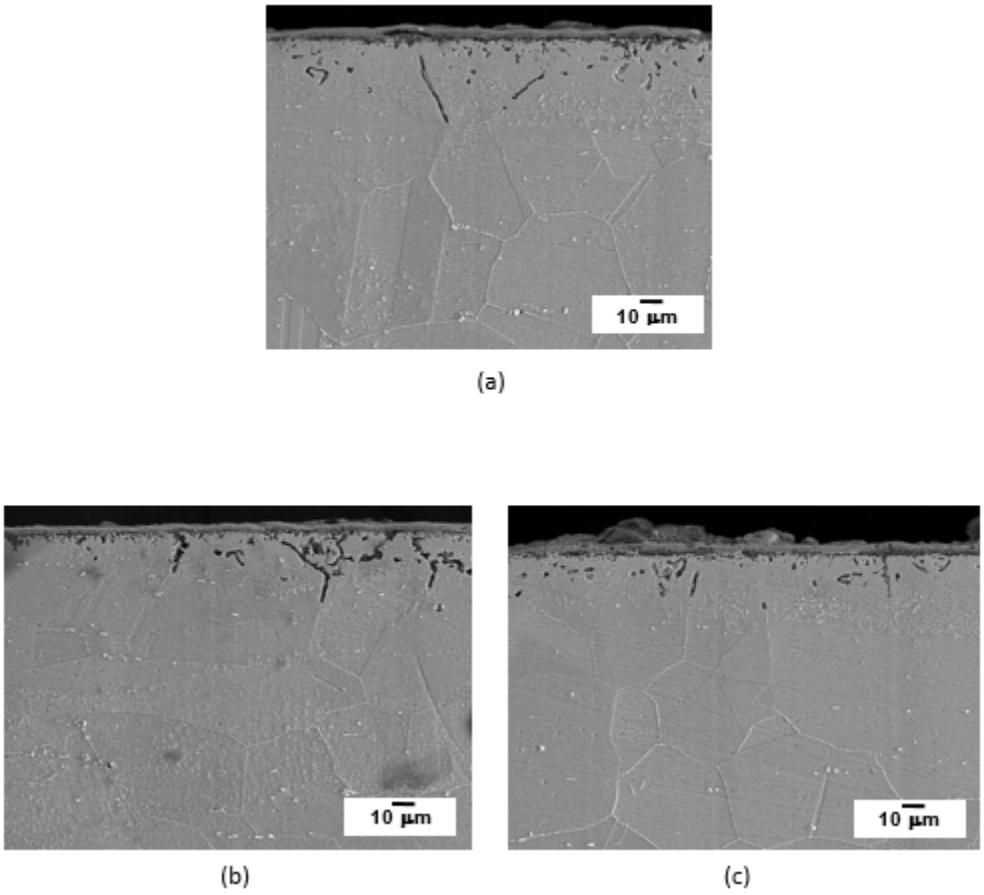

Figure 67 Cross-sectional corroded areas after 244 h: (a) under coal ash uncovered area, (b) under the area between coal ash uncovered and covered areas, and (a) under coal ash covered area

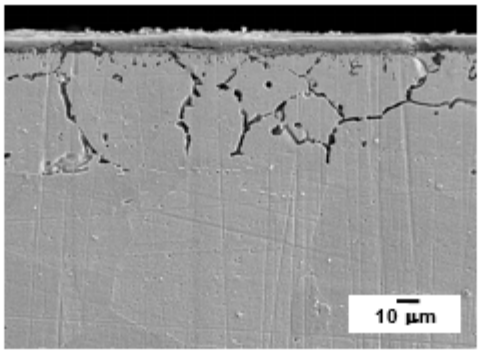

(a)

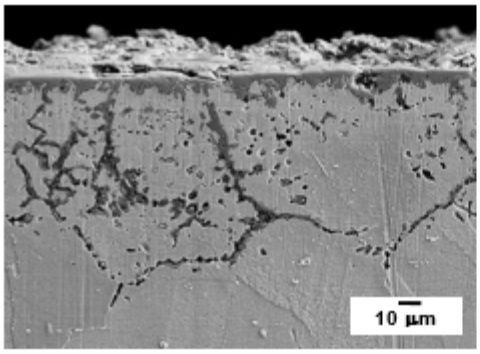

(b)

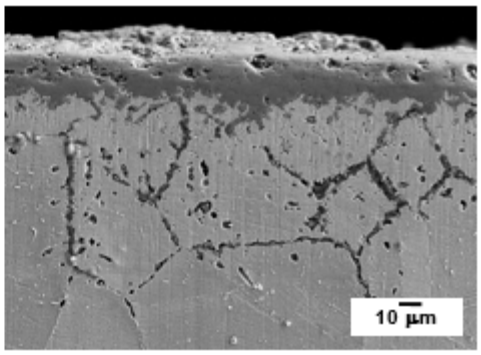

(c)

Figure 68 Cross-sectional corroded areas after 494 h: (a) under coal ash uncovered area, (b) under the area between coal ash uncovered and covered areas, and (a) under coal ash covered area

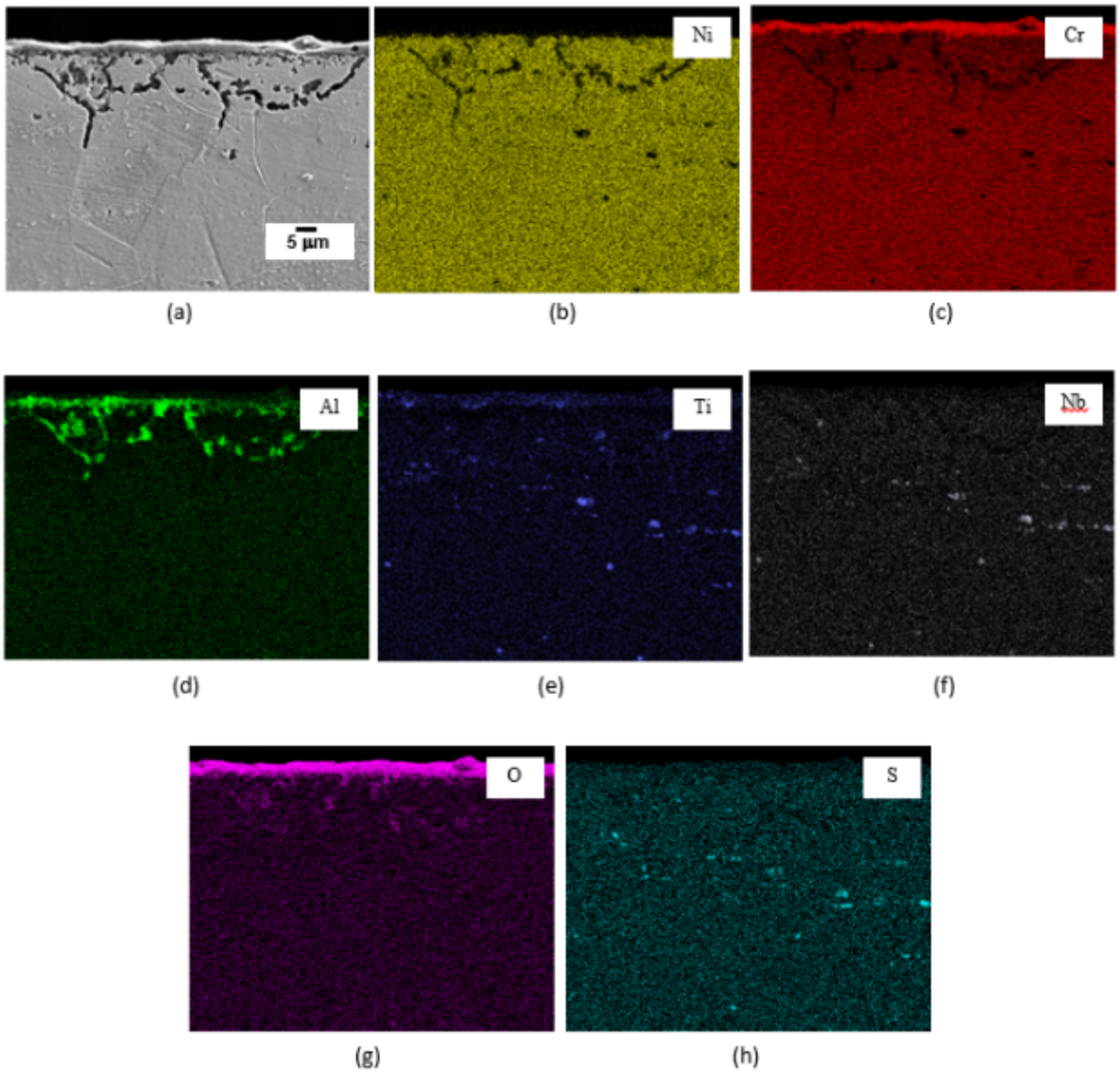

Figure 69 The elements mapping at cross-sectional coal ash uncovered area after 244 h showing the extent of oxidation

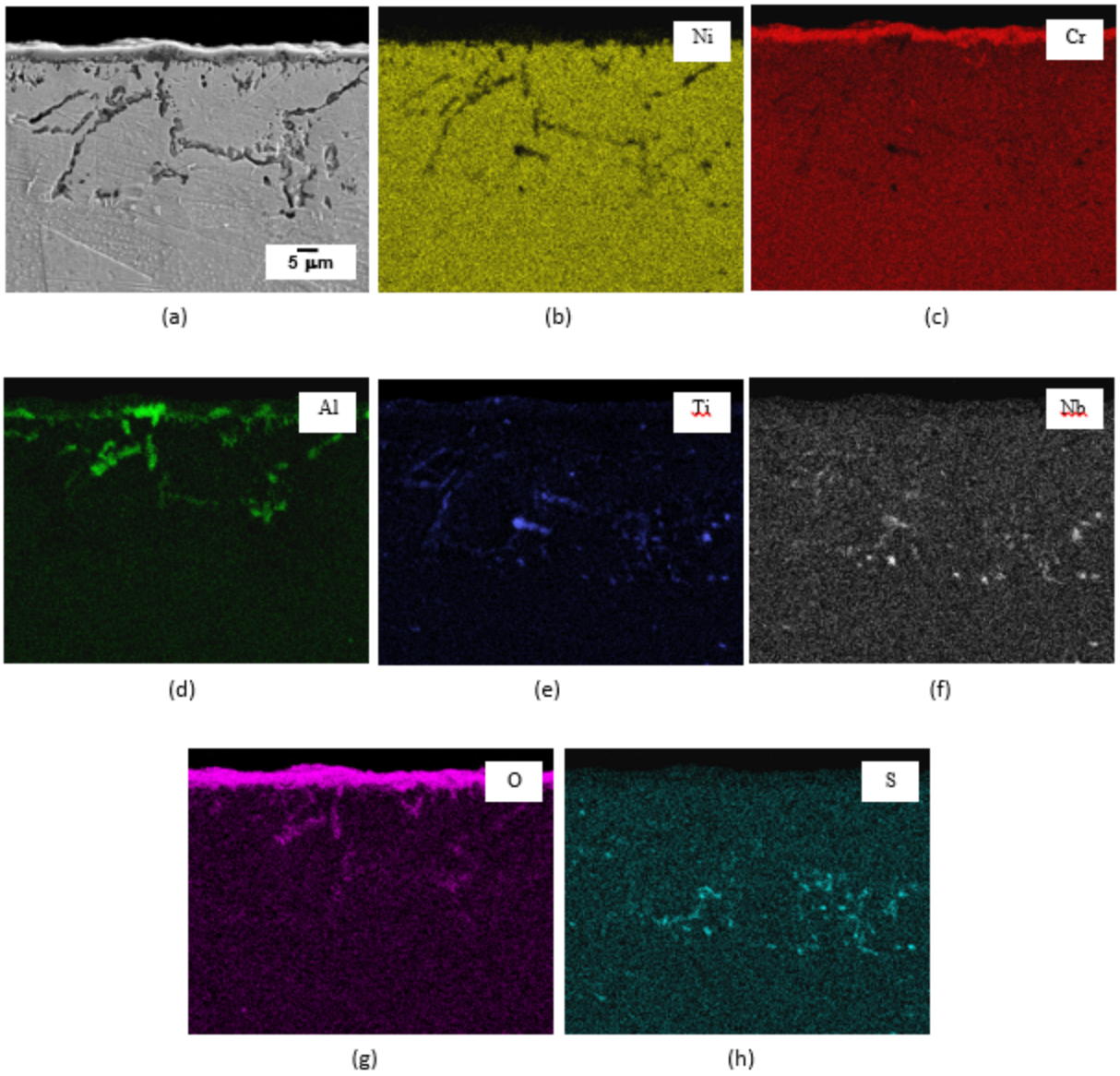

Figure 70 The elements mapping at cross-sectional coal ash covered area 244 h showing the extent of oxidation and sulfidation

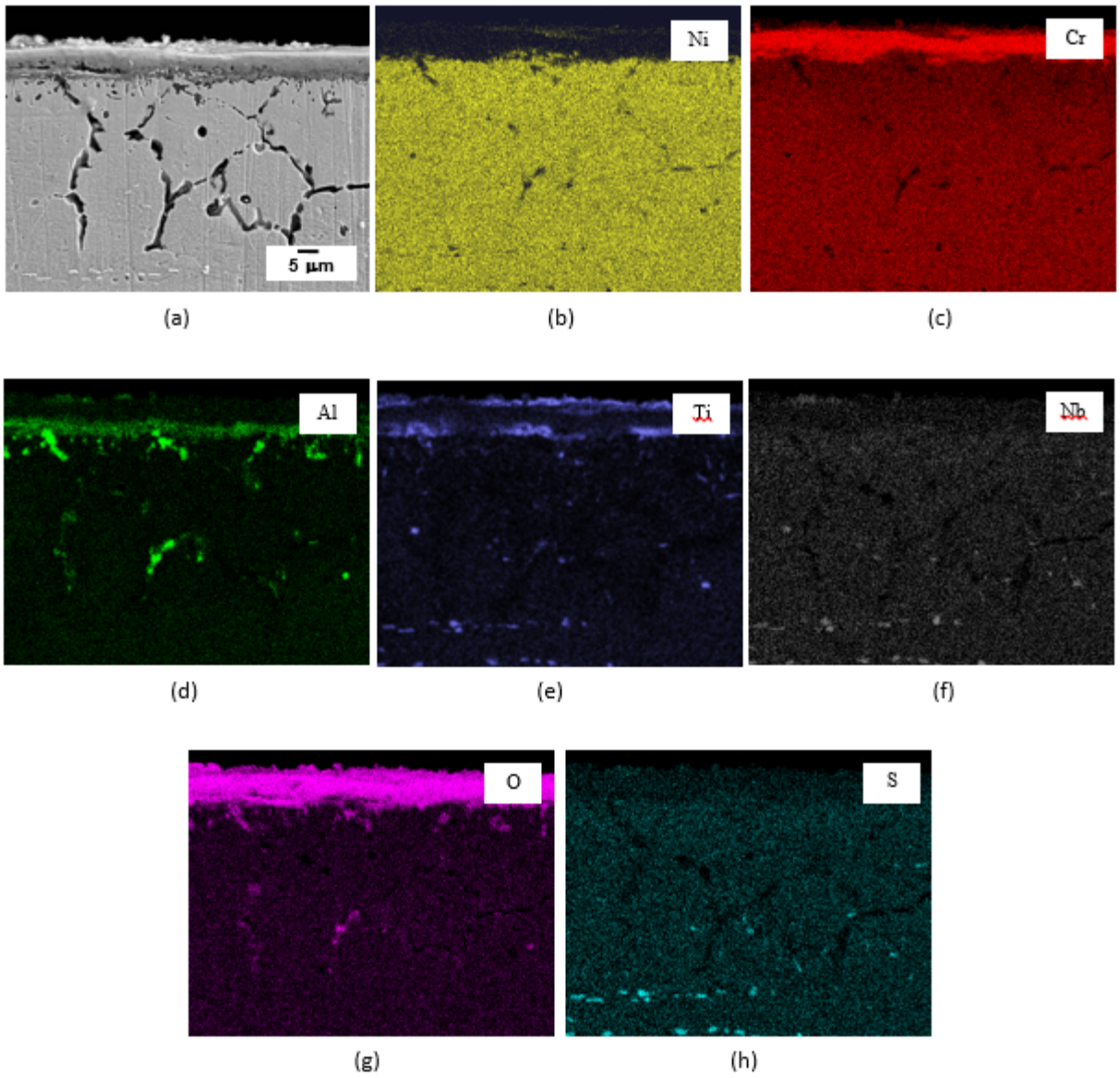

Figure 71 The elements mapping at cross-sectional coal ash uncovered area after 494 h showing the extent of oxidation

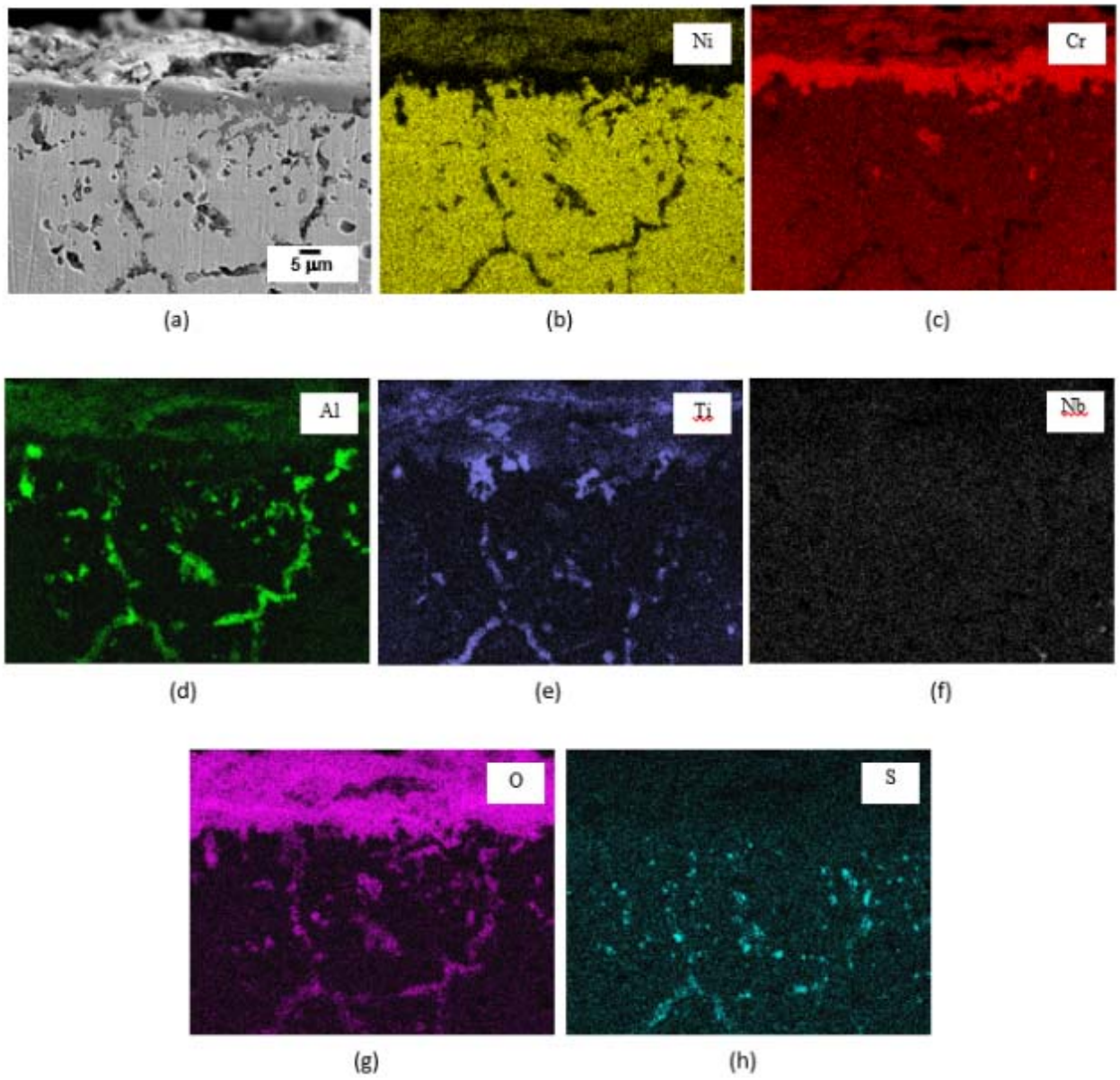

Figure 72 The elements mapping at cross-sectional area between coal ash uncovered and covered areas after 494 h showing the extent of oxidation and sulfidation

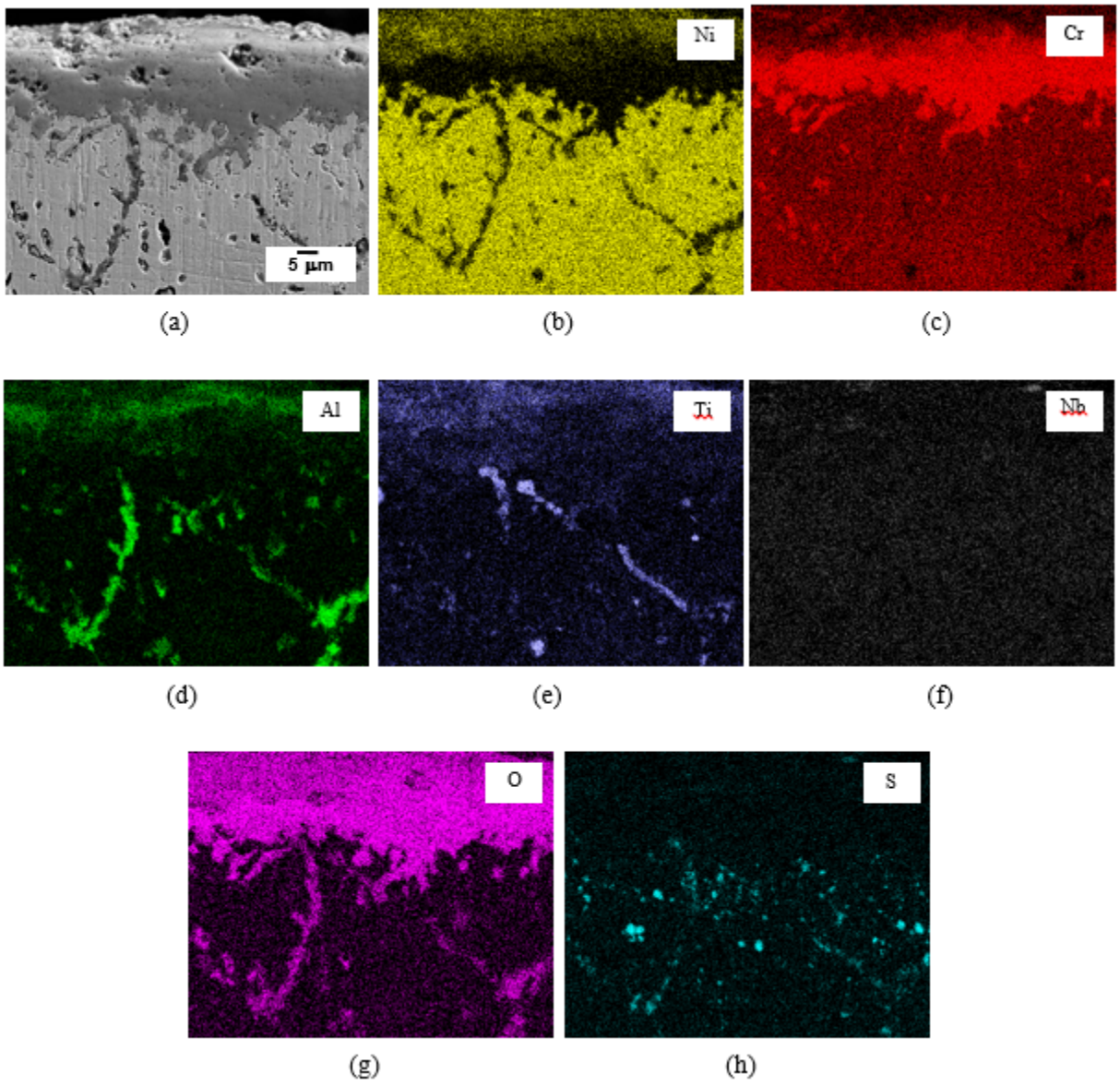

Figure 73 The elements mapping at cross-sectional coal ash covered area after 494 h showing the extent of oxidation and sulfidation

Analysis of Electrochemical Noise by Power Spectral Density Applied to Coal Ash Hot Corrosion Study

Typical time-dependent electrochemical noise signals of coal ash hot corrosion under uniformly covered coal ash are shown in Figure 74-Figure 77. The potential noise signatures in time domain can distinguish different stages of coal ash hot corrosion process. At the given temperature the corrosion potentials in the flue gas with SO_2 (Sulfidation stage) were more positive compared with the corrosion potentials in the flue gas without SO_2 (Oxidation stage) (Figure 74a, Figure 75a and Figure 76a). The noise signatures of current fluctuating with sudden spike were observed during the sulfidation stage. These signatures were prominent at 750 °C and 850 °C (Figures 74b, 75b and 76b). But, the sulfidation current at 850 °C was the highest (Figure 76b).

In case of the electrochemical noise signals from localized under-coal ash deposit corrosion (LUAC) at 750 °C, the oxidation, transition from oxidation to sulfidation and the accelerated sulfidation were three typical stages of the LUAC. Their extents of the corrosion can be evaluated with two characteristic current noise patterns (Figure 77). The results also confirmed that sulfidation potentials is more positive compared with the oxidation potential. The oxidation stage was characterized by the noise pattern of potential with less negative values (Figure 77a). The noise signature of current fluctuating with no sudden spike during oxidation indicates the low extent of corrosion. The transition from the oxidation to sulfidation was featured with the characteristic potential noise pattern of the cyclic oscillations. In this stage, sulfidation initiated with significant increase of current. The sulfidation stage correlated to potential changes in positive direction. The accelerated sulfidation can be evaluated with the noise signature of sudden change in current values (Figure 77b).

Power Spectral Density Analysis of Electrochemical Noise Signals of Coal Ash Hot Corrosion Process

The time-series data of the potential and current fluctuations were transformed into frequency domain to determine their power spectra densities (PSD) which express the signal power as a function of frequency. The low frequency and the slope of PSD plots can give important mechanistic and kinetic information about oxidation and sulfidation processes. In this study, the PSD data for potential as well as current noise were obtained using a Hanning window at FFT and coefficient 30 and 1000 of the MEM.

Typical FFT plots of E_{corr} and i_{corr} fluctuations of oxidation and sulfidation during coal ash hot corrosion processes are shown in Figure 78-Figure 81. All FFT plots are almost independent of the frequency in the region lower than 0.0001 Hz. The trend of the PSDs of each oxidation and sulfidation against the frequency was quite similar, but the values varied with a change in temperatures as well as the test environments. The results confirmed that the current power of the sulfidation was the higher compared that of the oxidation (Figure 78b, Figure 79b, Figure 80b and Figure 81b).

The FFT and MEM method give similar results for calculating power spectral densities. Since the MEM can produce smooth spectra without ensemble averaging, it has an advantage over the FFT (Figure 82-Figure 84). Another important difference between the FFT method and the MEM is that the latter requires an appropriate choice of coefficient value (Figure 85-Figure 87). Small coefficient 30 value values give smooth spectra frequency resolution (Figure 85a, Figure 86a, Figure 87a). But, the PSD spectra of E_{corr} and i_{corr}

fluctuations and spectral noise impedance show more reasonable information the kinetic values for mechanism of the oxidation and sulfidation processes (Figure 85b, Figure 86b and Figure 87b).

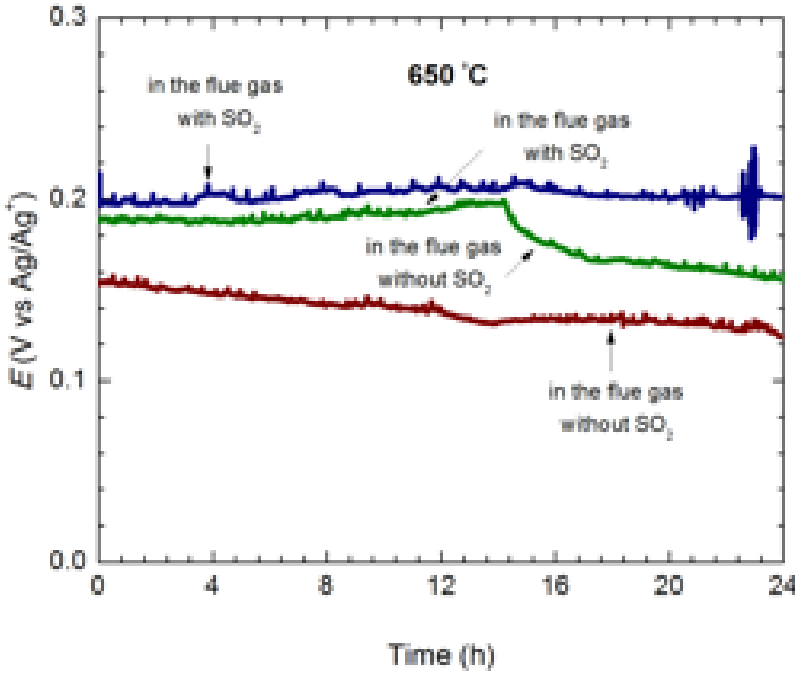

(a)

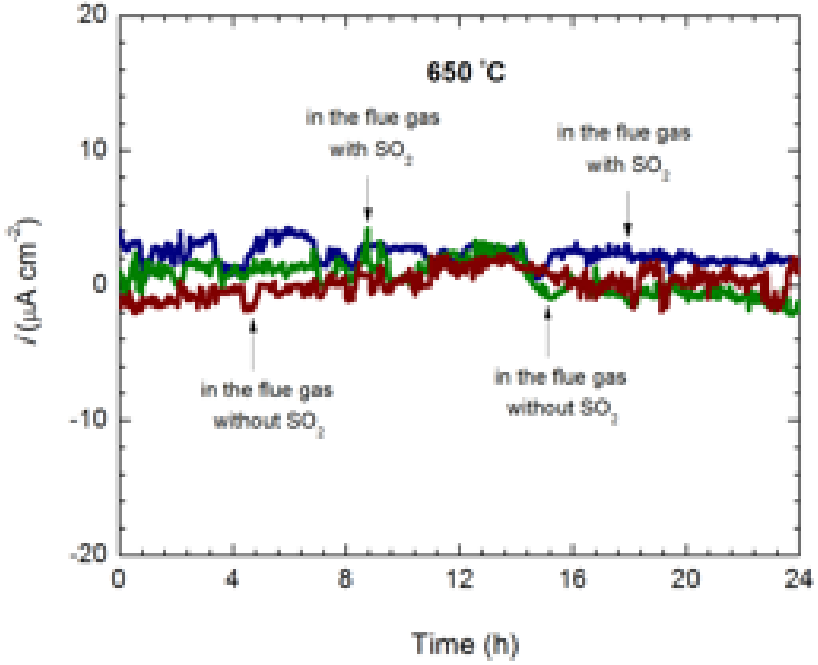

(b)

Figure 74 Typical time-dependent electrochemical noise signals of coal ash hot corrosion process in the different flue gases at 650 ℃: (a) potential noise signals, and (b) current noise signals

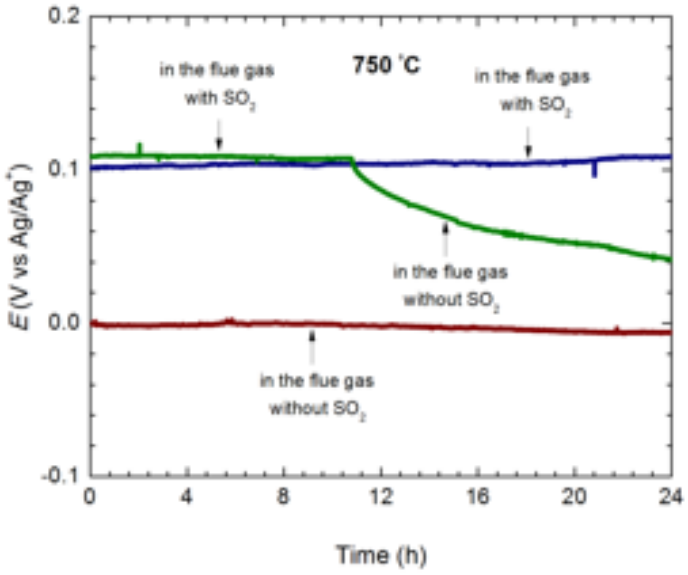

(a)

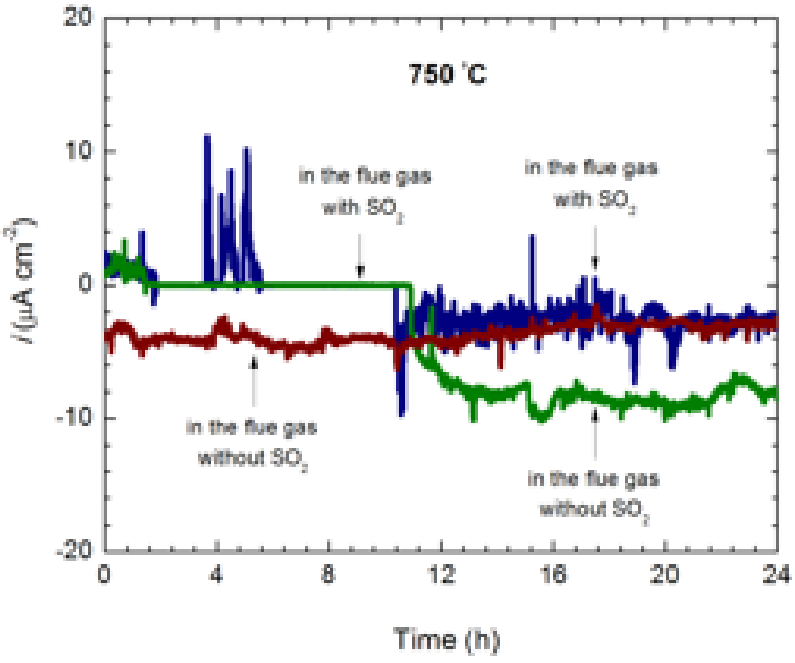

(b)

Figure 75 Typical time-dependent electrochemical noise signals of coal ash hot corrosion process in the different flue gases at 750 ℃: (a) potential noise signals, and (b) current noise signals

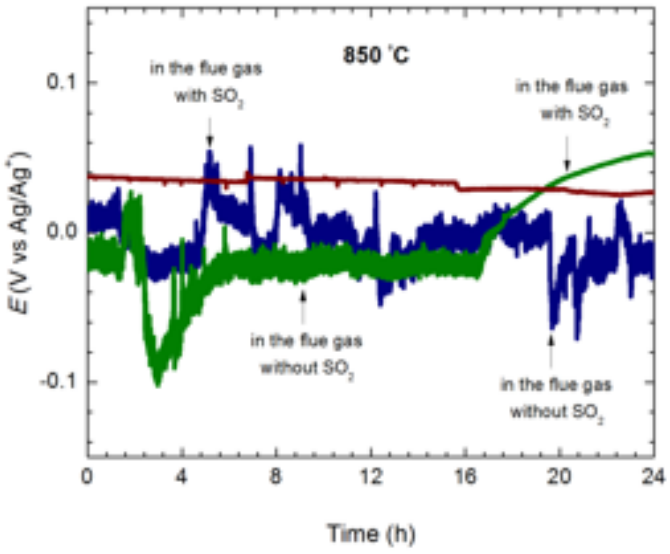

(a)

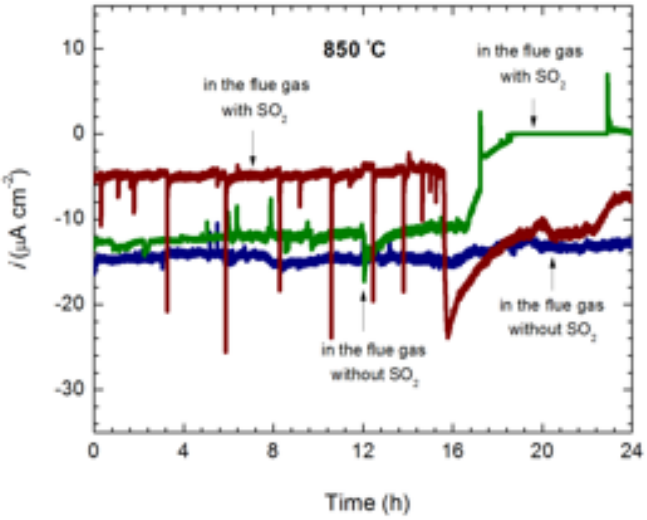

(b)

Figure 76 Typical time-dependent electrochemical noise signals of coal ash hot corrosion process in the different flue gases at 850 ℃: (a) potential noise signals, and (b) current noise signals

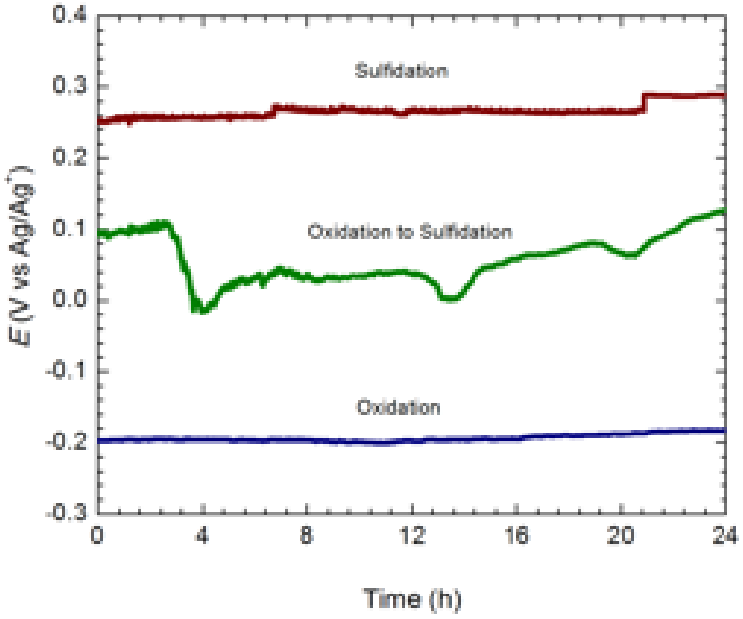

(a)

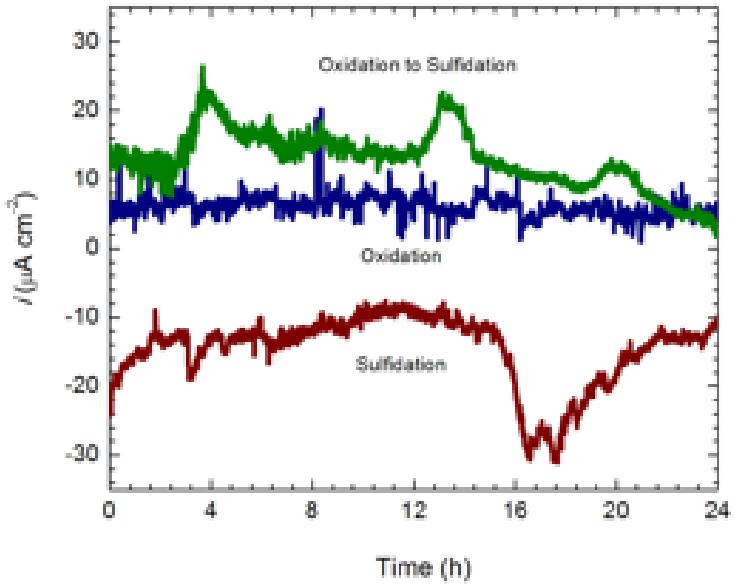

(b)

Figure 77 Typical time-dependent electrochemical noise signals of LDAC corrosion process at 750 ℃: (a) potential noise signals, and (b) current noise signals

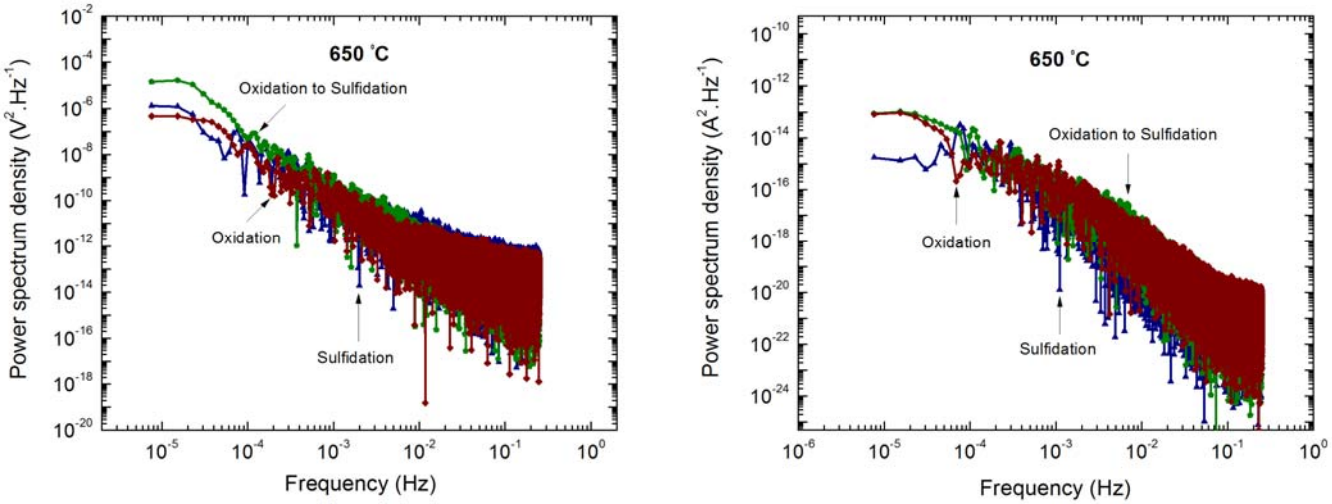

(a) (b)

Figure 78 Typical PSD plots of E_{corr} and i_{corr} fluctuations of oxidation and sulfidation during coal ash hot corrosion at 650 ℃ using FFT (a) E_{corr}, and (b) i_{corr}

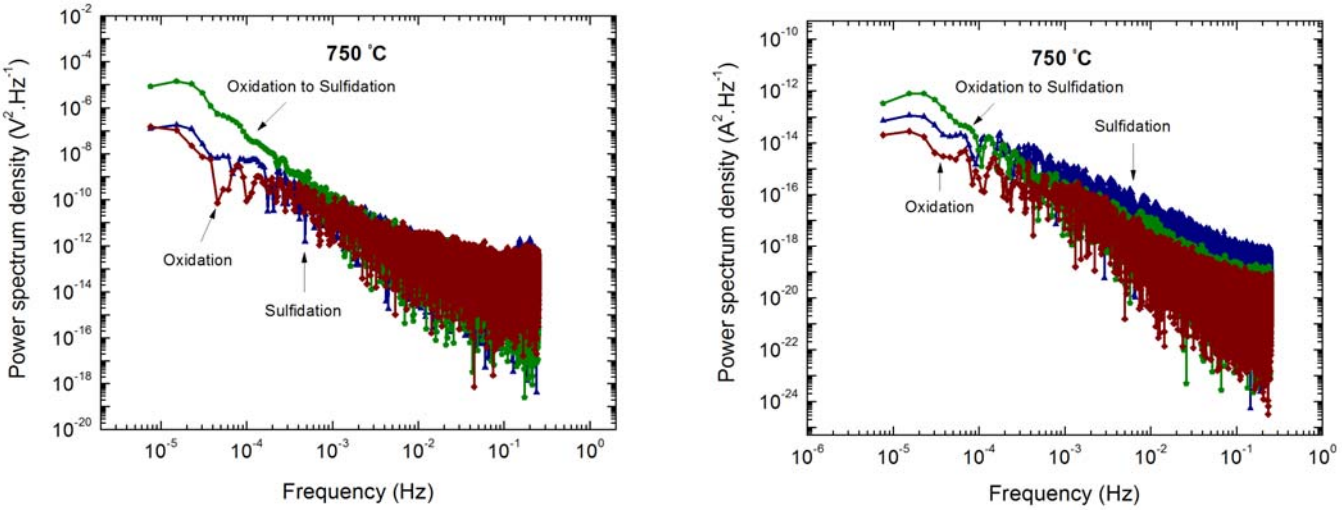

(a) (b)

Figure 79 Typical PSD plots of E_{corr} and i_{corr} fluctuations of oxidation and sulfidation during coal ash hot corrosion at 750 ℃ using FFT (a) E_{corr}, and (b) i_{corr}

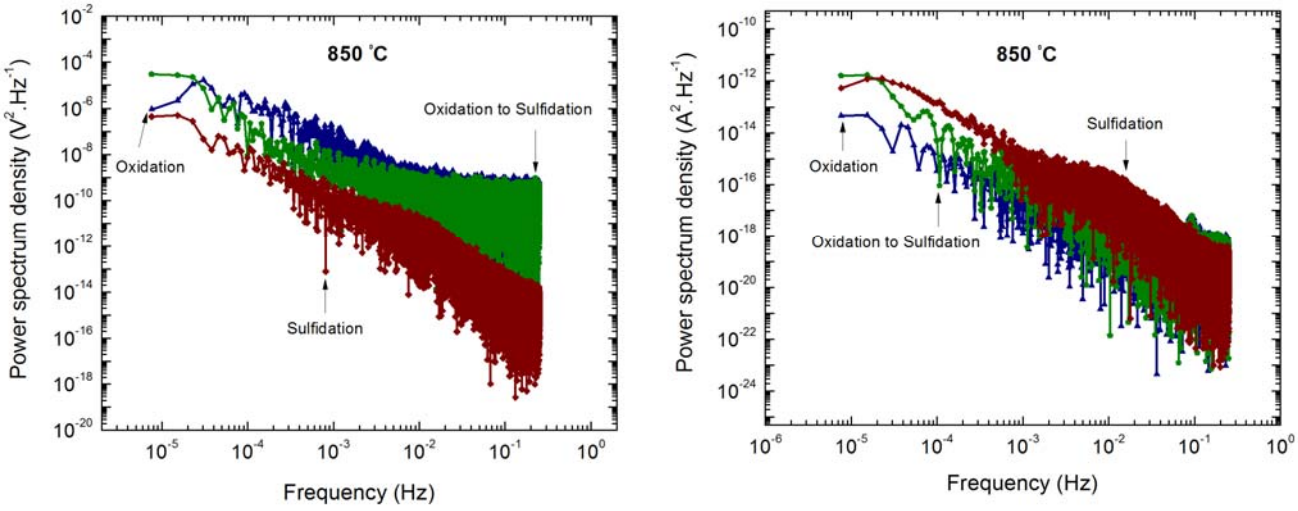

(a) (b)

Figure 80 Typical PSD plots of E_{corr} and i_{corr} fluctuations of oxidation and sulfidation during coal ash hot corrosion at 850 ℃ using FFT (a) E_{corr}, and (b) i_{corr}

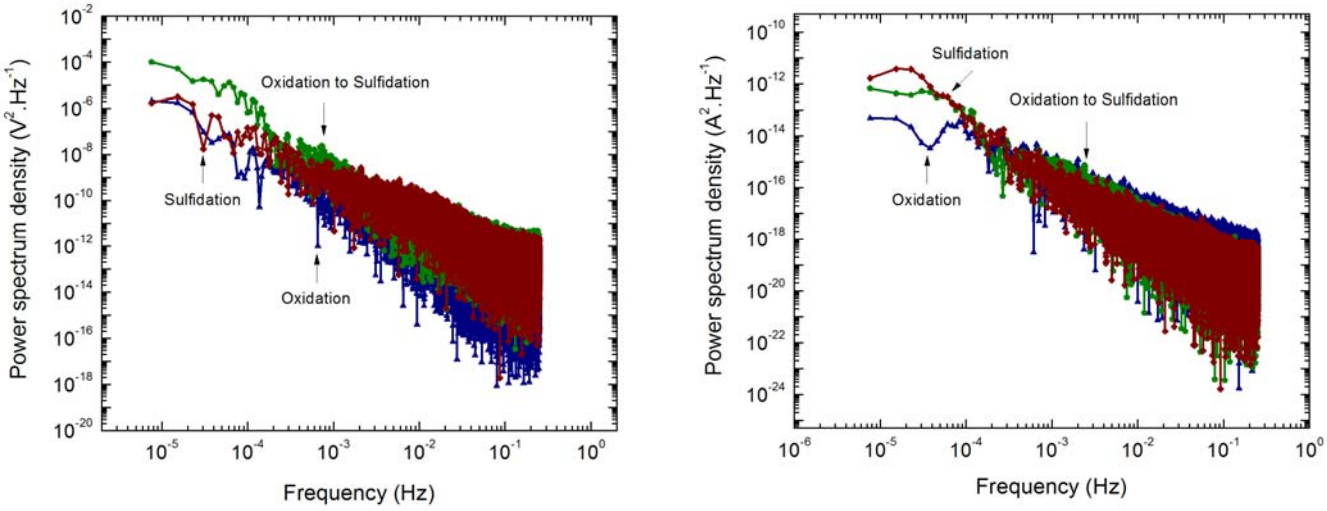

(a) (b)

Figure 81 Typical PSD plots of E_{corr} and i_{corr} fluctuations of LUAC process at 750 ℃ using FFT: (a) E_{corr}, and (b) i_{corr}

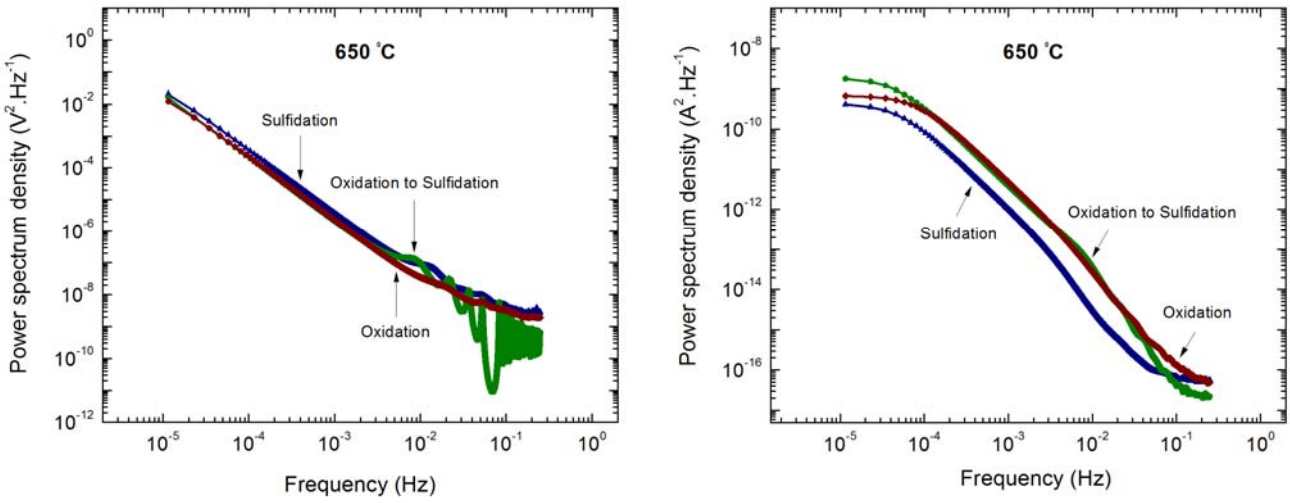

(a) (b)

Figure 82 Typical PSD plots of E_{corr} and i_{corr} fluctuations of oxidation and sulfidation during coal ash hot corrosion at 650 ℃ using MEM (a) E_{corr}, and (b) i_{corr}

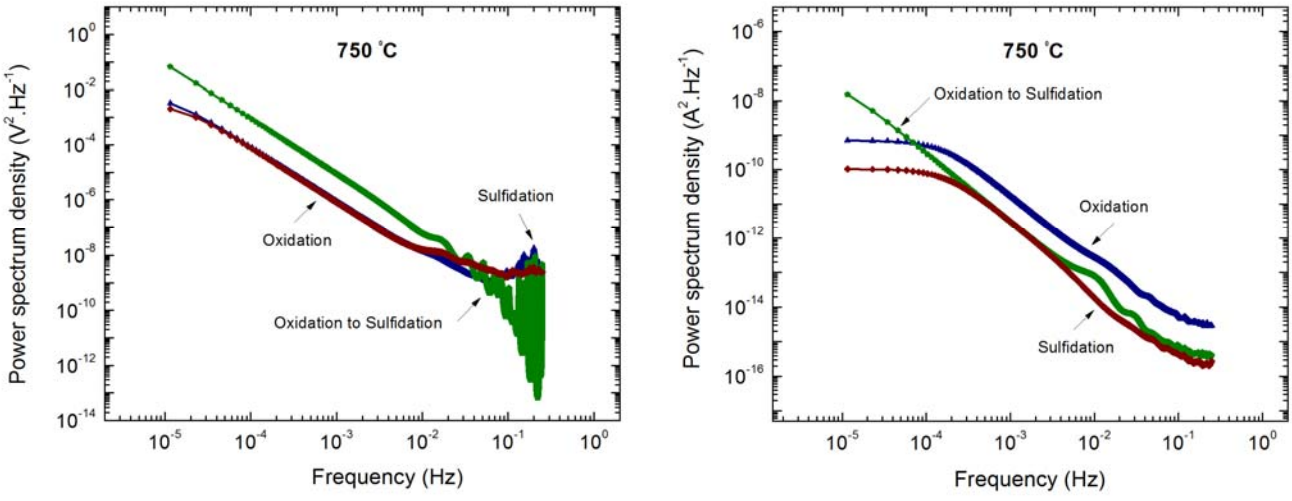

(a) (b)

Figure 83 Typical PSD plots of E_{corr} and i_{corr} fluctuations of oxidation and sulfidation during coal ash hot corrosion at 750 ℃ using MEM (a) E_{corr}, and (b) i_{corr}

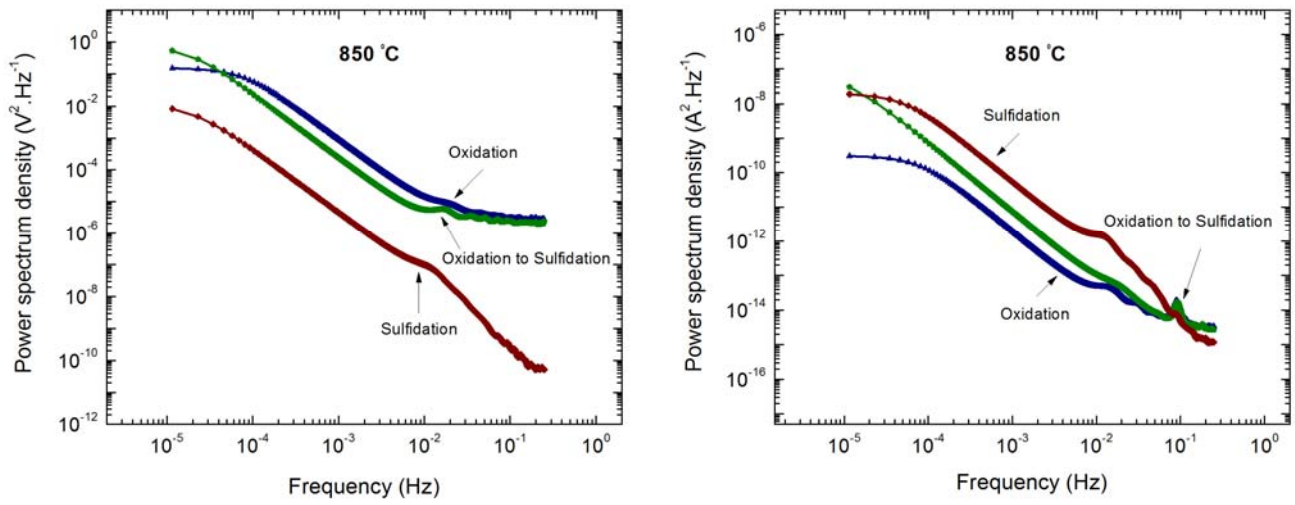

(a) (b)

Figure 84 Typical PSD plots of E_{corr} and i_{corr} fluctuations of oxidation and sulfidation during coal ash hot corrosion at 850 ℃ using MEM: (a) E_{corr}, and (b) i_{corr}

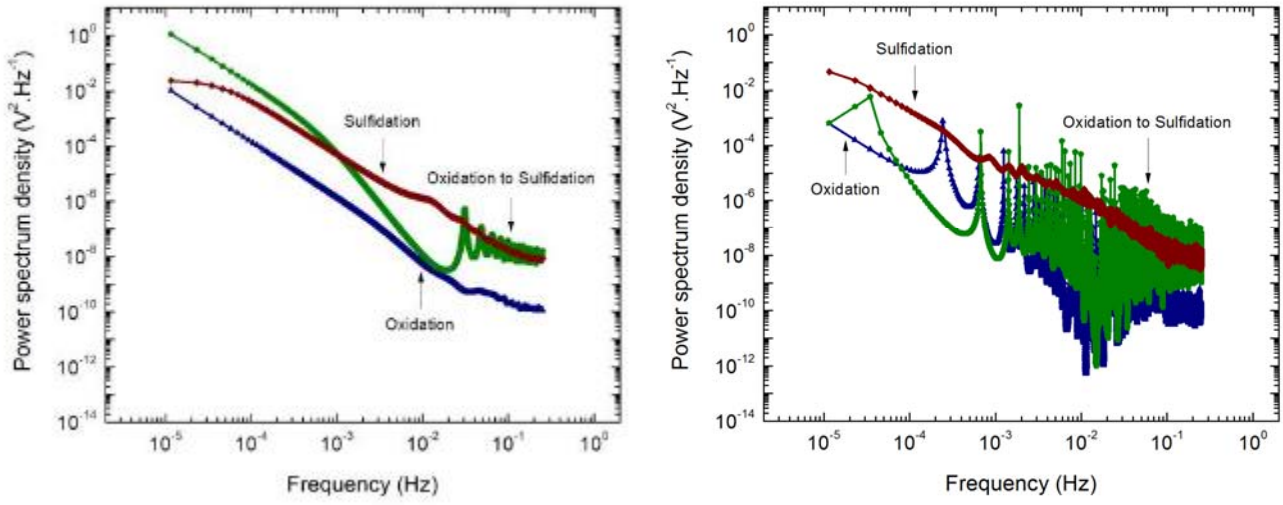

(a) (b)

Figure 85 Typical PSD plots of E_{corr} fluctuations of LUAC process at 750 ℃ using different coefficient values of the MEM: (a) M=30, and (b)) M=1000

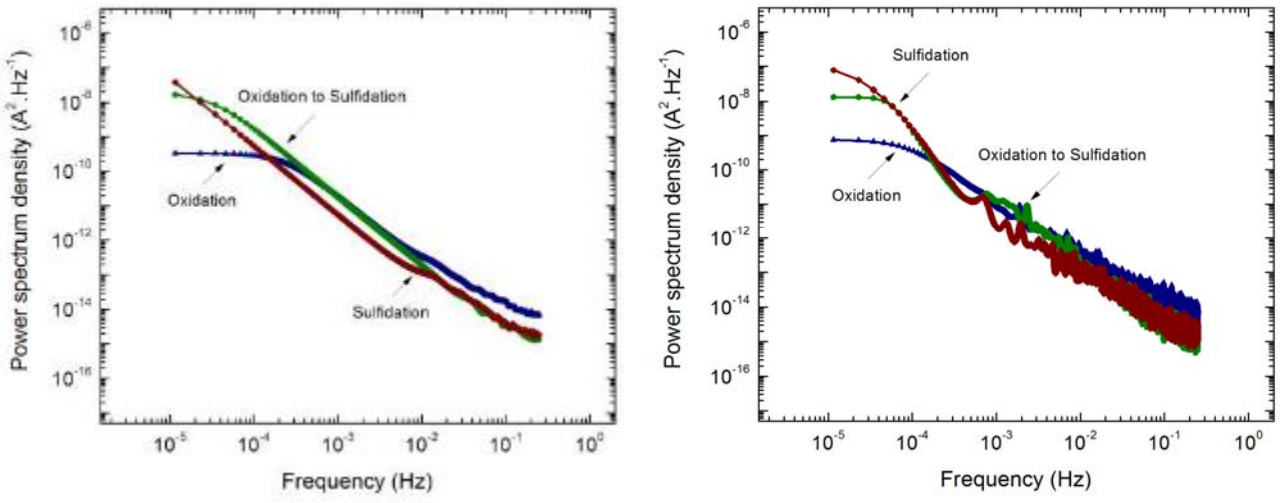

(a) (b)

Figure 86 Typical PSD plots of E_{corr} fluctuations of LUAC process at 750 ℃ using different coefficient values of the MEM: (a) M=30, and (b)) M=1000

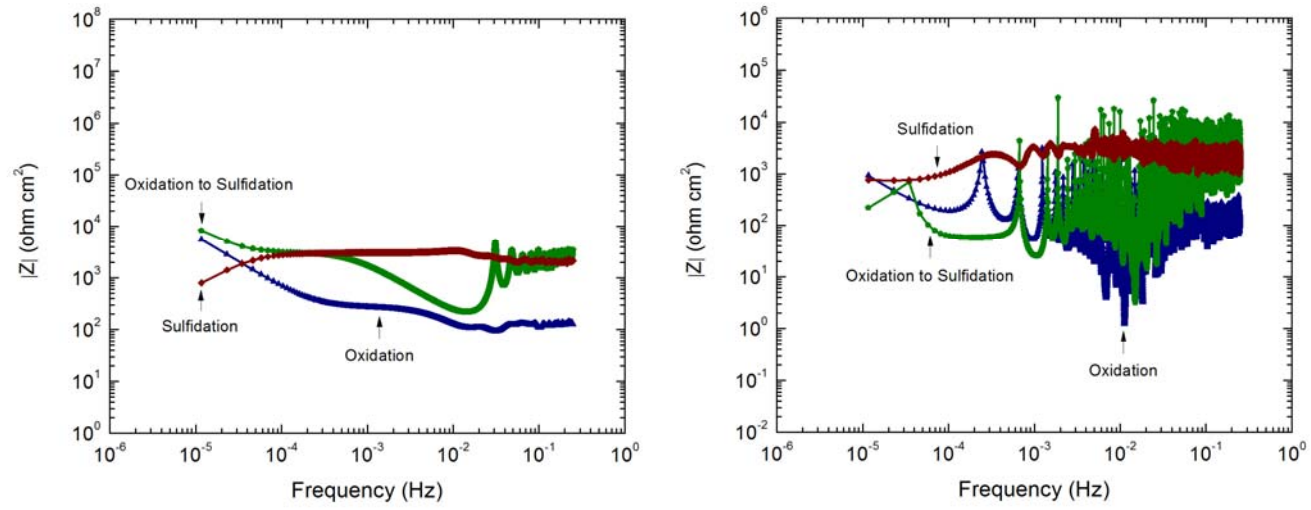

(a) (b)

Figure 87 Typical spectral noise impedance of LUAC corrosion process at 750 ℃ using different coefficient values of the MEM: (a) M=30, and (b)) M=1000

Conclusions

- The oxidation and sulfidation were the two prominent stages of under-coal ash deposit corrosion of the alloy.
- The oxidation stage was characterized by the noise signature of a gradual potential continuously changing in the negative region. The low oxidation attack correlated to the current transient of a sharp rise followed by quick recovery.
- The sulfidation stage was featured with potential changes in positive direction in a range within 235-380 mV (vs Ag/Ag^{+}). The high extent of sulfidation was characterized by the noise signature of a sharp current spike followed by no recovery.
- The intergranular oxidation attack was the predominant process during the oxidation stage. In the transition stage from oxidation to sulfidation, the primary oxide layer became overgrown by the sulfide layer. The serious sulfidation attack occurred inside the coal ash covered areas. Its corrosion depth was increased to three times compared with the oxide depth at uncovered region after 494 h.
- Analysis of electrochemical noise signals by power spectral density (PSD) was applied to coal ash hot corrosion study. PSD plots using FFT and MEM gave more information for mechanism of the oxidation and sulfidation processes.

Task 4 Development of Self-Powered Telecommunication Devices

Subtask 4.1 Hardware Selections and Modeling of TEG Array

Experimental Methods

Hardware Selections and Modeling of TEG Array

The thermoelectric generator selected for this phase of the project is an integrated unit of multiple TEG modules, heat sink, and self-powered cooling fan. Figure 88 shows photos taken of the TEG during a test to determine the open circuit voltage output as a function of temperature. The hot and cold sides of the TEG are labeled as well as the self-powered cooling fan.

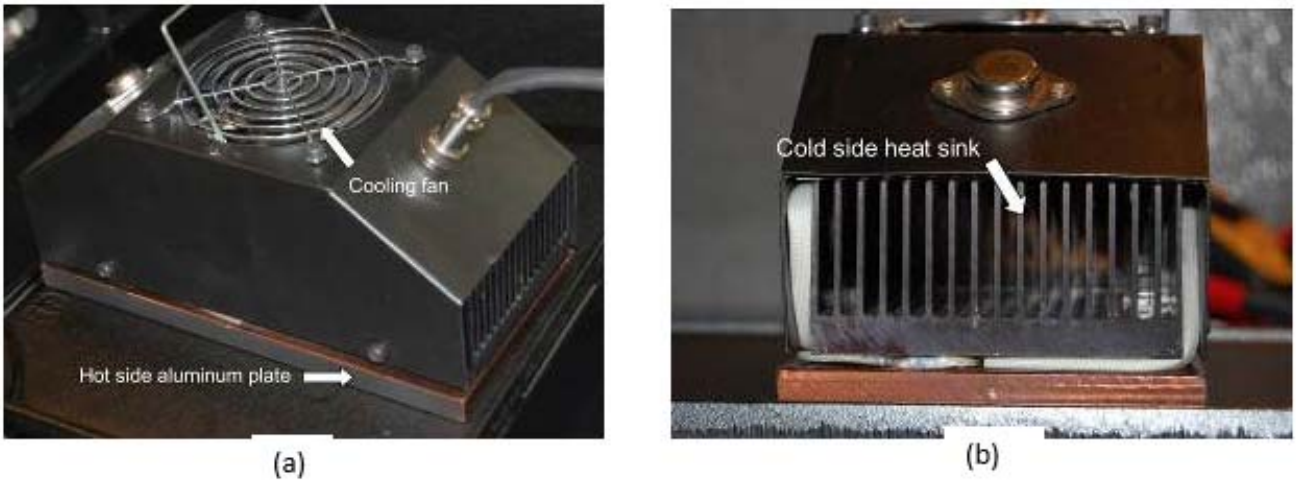

Figure 88 TEG During Test to determine open circuit voltage test

Results and Discussions

January to March 2012

Hardware Selections and Modeling of TEG Array

A performance test was conducted to determine the open circuit voltage of the TEG as a function of temperature. In this test the heat source was a cast iron plate heated by an open flame natural gas burner. Figure 89 shows the relationship between the temperature difference (between the source and ambient conditions) and the output voltage. The red line superimposed on the graph illustrates the linear relationship between a temperature difference of 100 °C and about 205 °C. The voltage became nonlinear after this point and appeared to be approaching a maximum value when the source temperature reached its upper limit. The TEG was successful in a lab demonstration to supply sufficient power for the wireless transmitter within this temperature range, additional tests will be conducted to further characterize the TEG performance.

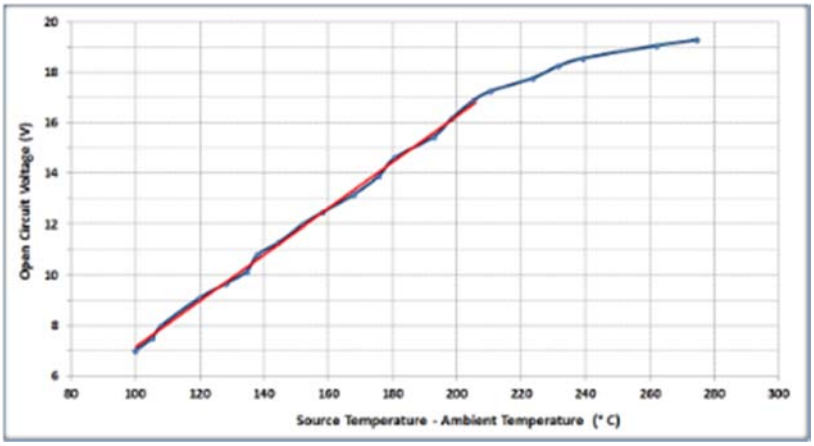

Figure 89 ***Relation of Open Circuit Voltage to Temperature***

April to June 2012

The latest generation of the TEG includes power conditioning circuitry with battery buffering- see Figure 90. The output to the wireless transmitter is nearly a constant 13.5 VDC which allowed us to eliminate the 12 to 24 VDC voltage converter and power supply which resulted in reducing the power requirement of the transmitter to less than 2 Watts. The rechargeable battery pack also provides up to 3 amp hours when fully charged when there is no heat source available. Figure 90a is an internal view of the TEG with the housing and one heat sink removed. Figure 90b is a photo of the internal circuitry of the voltage regulator and battery buffering module. Figure 90c is the circuit schematic.

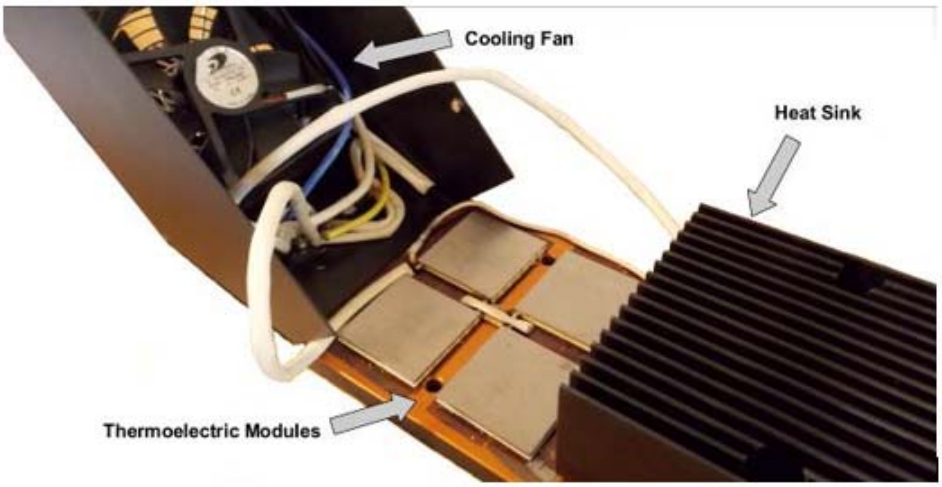

(a)

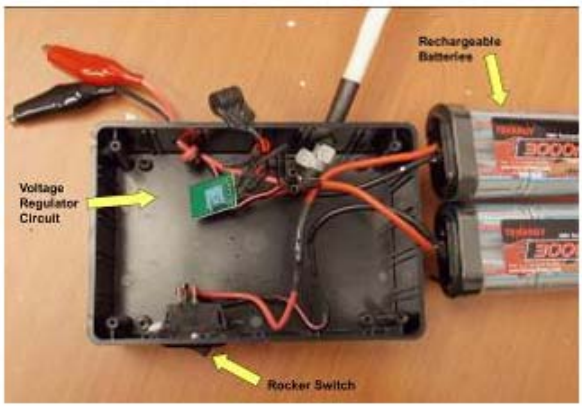

(b)

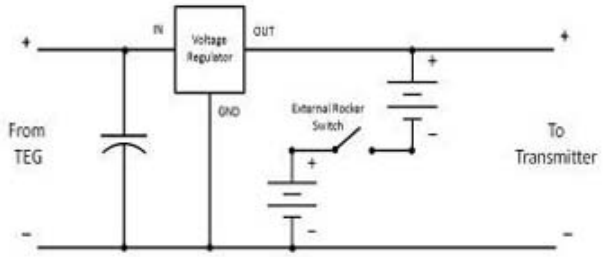

(c)

Figure 90 (a) internal view of the TEG with the housing (b) Its voltage regulation, and (c) Battery buffering Circuit

July to September 2012

From the trials conducted in the second quarter it is apparent that signal conditioning prior to the voltage to current converter is necessary. Although the input resistance of the voltage to current converter is one Megaohm, direct connection of the sensor resulted in ~ 150 mV signal loss. Due to the practical availability of a commercial solution, a unity gain amplifier circuit was designed and constructed. A JFET Op Amp was selected due to the extremely high input resistance (10^{12} ohms). Figure 91 shows the schematic diagram of the circuit as well as the actual construction of the prototype.

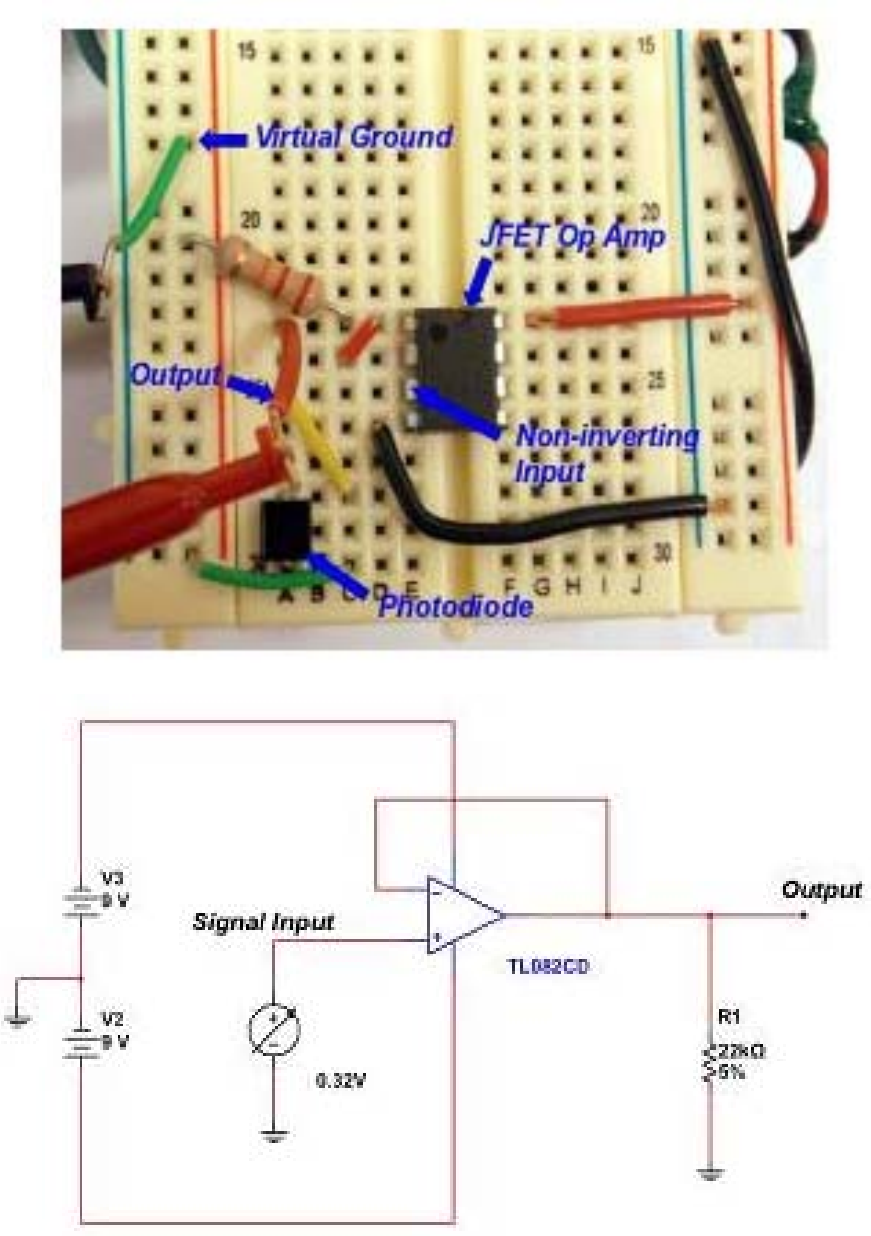

Figure 91 JFET Op Amp Unity Gain Amplifier Circuit for Signal Conditioning

A performance test of the unity gain amplifier circuit was conducted using a photodiode as the signal source under varying conditions of light intensity. The results of that test are shown in Figure 92. Both input and output voltages were recorded at a 10 second sample interval and the curves are superimposed on the graph.

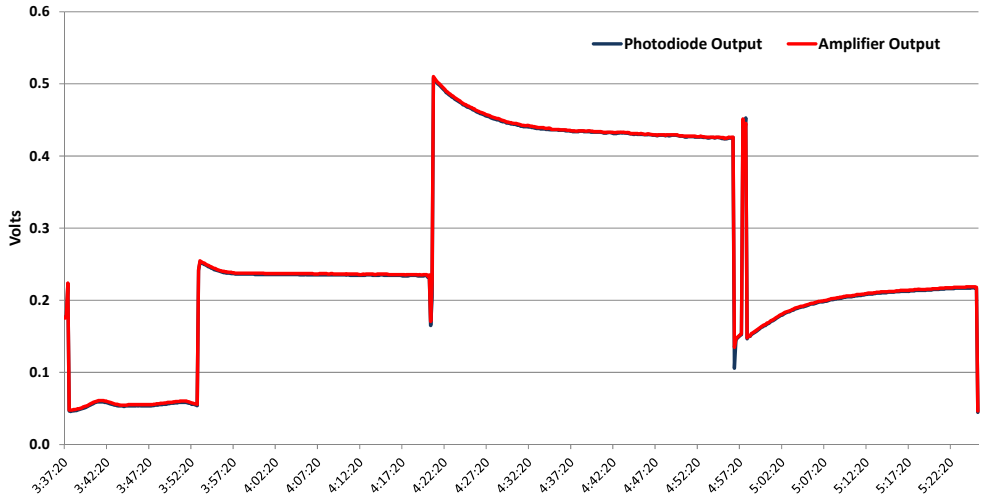

Figure 92 Test Results of Unity Gain Amplifier Using Photodiode as a Signal Source

To test the prototype design, two nine volt batteries were used as the rail to rail power source. This is, of course, unacceptable for our self-powered wireless communication system since the TEG output is a regulated 13.5 VDC. To obtain the dual rail power supply with the virtual ground required for op amp functionality a "rail splitter" circuit was designed and tested. The schematic for this circuit integrated with the unity gain op amp is shown in Figure 93.

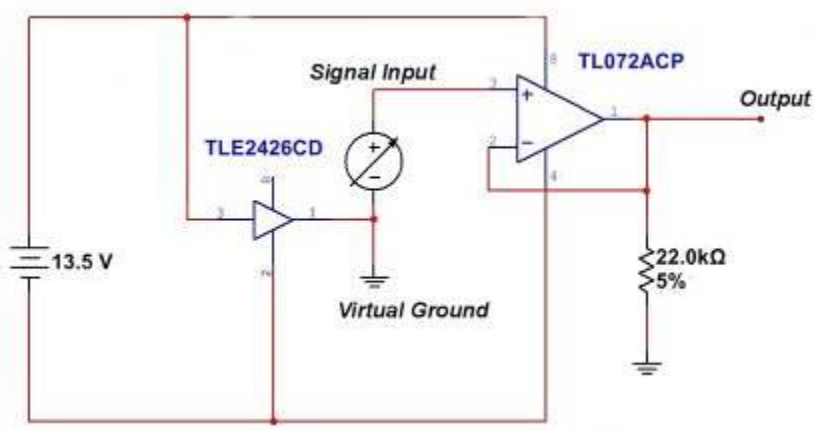

Figure 93 Schematic of Rail Splitter with Downstream Unity Gain Amplifier

A performance test of this circuit was also conducted using a photodiode as the signal source under varying conditions of light intensity but with a 13.5 VDC power supply to simulate the TEG voltage. The results of this test are shown in Figure 94. Both input and output voltages were recorded at a 10 second sample interval and the curves are superimposed on the graph.

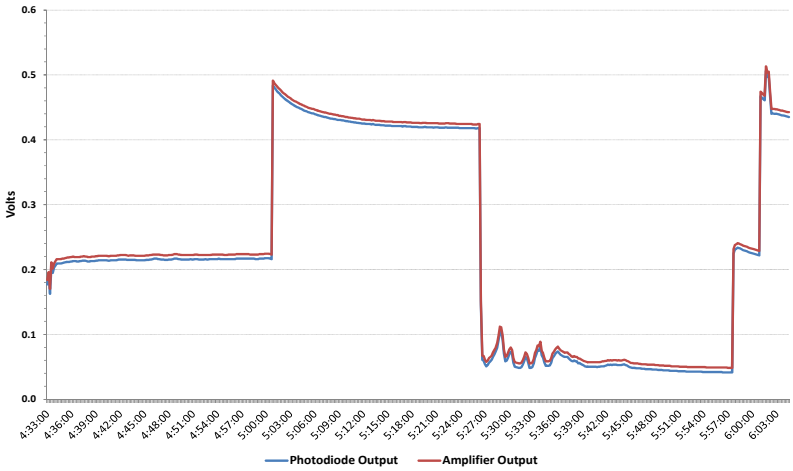

Figure 94 Test Results of Unity Gain Amplifier Using Photodiode as a Signal Source and Powered by 13.5 VDC Single Rail Supply

January to March 2012

The basic structure of the wireless communication system is represented by the block diagram shown in Figure 95. The hardware chosen is a 1 Watt transmitter with frequency-hopping, spread spectrum technology in the 902-928 MHz ISM band. This was chosen to minimize signal degradation that may be accentuated with higher frequency carrier signals.

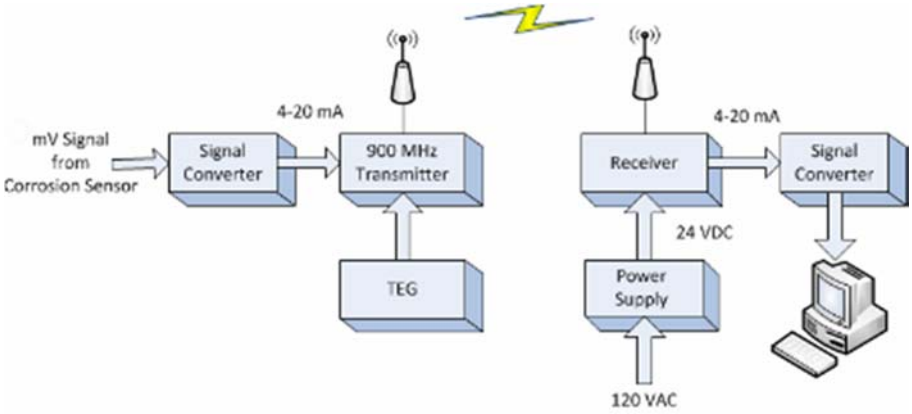

Figure 95 Block Diagram of Wireless Communication System

The wireless transmitter/receiver was successfully demonstrated in a laboratory setting with a simulated signal using the discrete input/output functionality of the device. The initial test was conducted with the transmitter powered by a 12 VDC regulated power supply. Upon successful completion of that test, the TEG was used for the transmitter power supply with an electric hot plate as the heat source (Figure 96). The voltage output of the TEG fluctuated within a three volt range under load during this test but the functionality of the transmitter was not affected. The discrete input signal was transmitted and received successfully.

Figure 96 Lab Test of Wireless Transmitter

Figure 97 shows the receiver hardware including a 24 VDC power supply. Although the wireless transmitter is intended to be self-powered via a TEG, we anticipated a simulated control room environment for the receiver therefore it was designed for a 120 VAC supply.

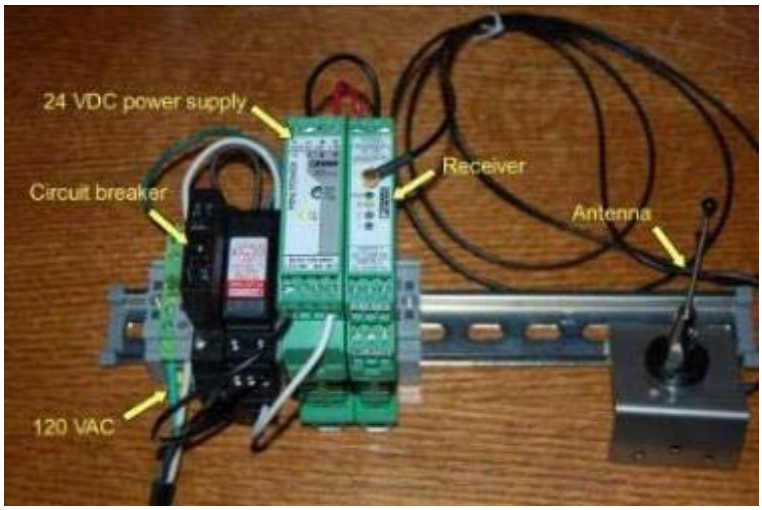

Figure 97 Configuration of Wireless Receiver

April to June 2012

Figure 98 shows the complete transmitter test setup with a hot plate serving as the heat source. The TEG is connected to the voltage regulator and rechargeable battery pack. The wireless transmitter configuration consists of an ON – OFF circuit breaker and configurable signal converter mounted to a rail as shown. The signal conditioner converts the millivolt signal from the corrosion sensor (the white wires in the figure) to a 4 – 20 mA output to the transmitter.

Figure 98 Wireless Transmitter Connected to TEG and Corrosion Sensor

Figure 99 shows a plot of output data from the corrosion sensor which was transmitted from the lab to the receiver remotely located in another office in the Engineering Research Building.

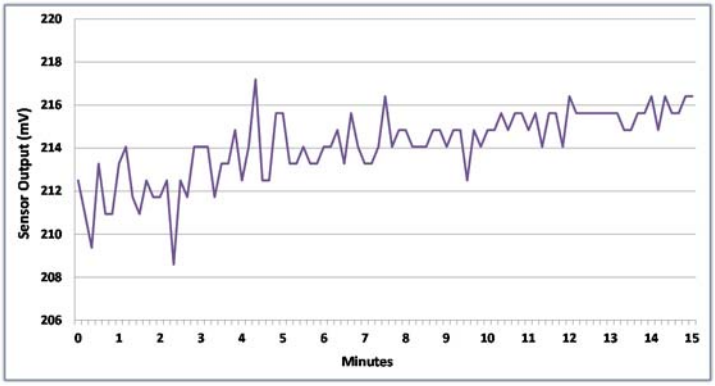

Figure 99 Sample of Corrosion Sensor Data Received from Transmitter

While we demonstrated the functionality of the self-powered wireless system in transmitting and receiving an analog signal, there are other design considerations that must be addressed further.

July to September 2012

We have conducted several tests of the wireless transmission of the potential mV signal from the corrosion sensor. Although all of the tests have demonstrated the capability of the wireless system, we have also experienced signal degradation when comparing measurements from the Autolab electrochemical laboratory instrument. The data is shown in Figure 100. The curves represent sensor data recorded by the Autolab instrument and the output data from the wireless receiver at a one second sample interval for about 2.5 hours. Second order polynomial regressions fitted to both curves are identical except for the intercept which shows an approximate 70 mV difference. The cause of this voltage difference is not fully understood and may be an anomaly of the corrosion sensor. Since this trial incorporated the JFET unity gain amplifier shown in Figure 101, it was repeated with the latest "rail splitter" circuit design shown in Figure 102.

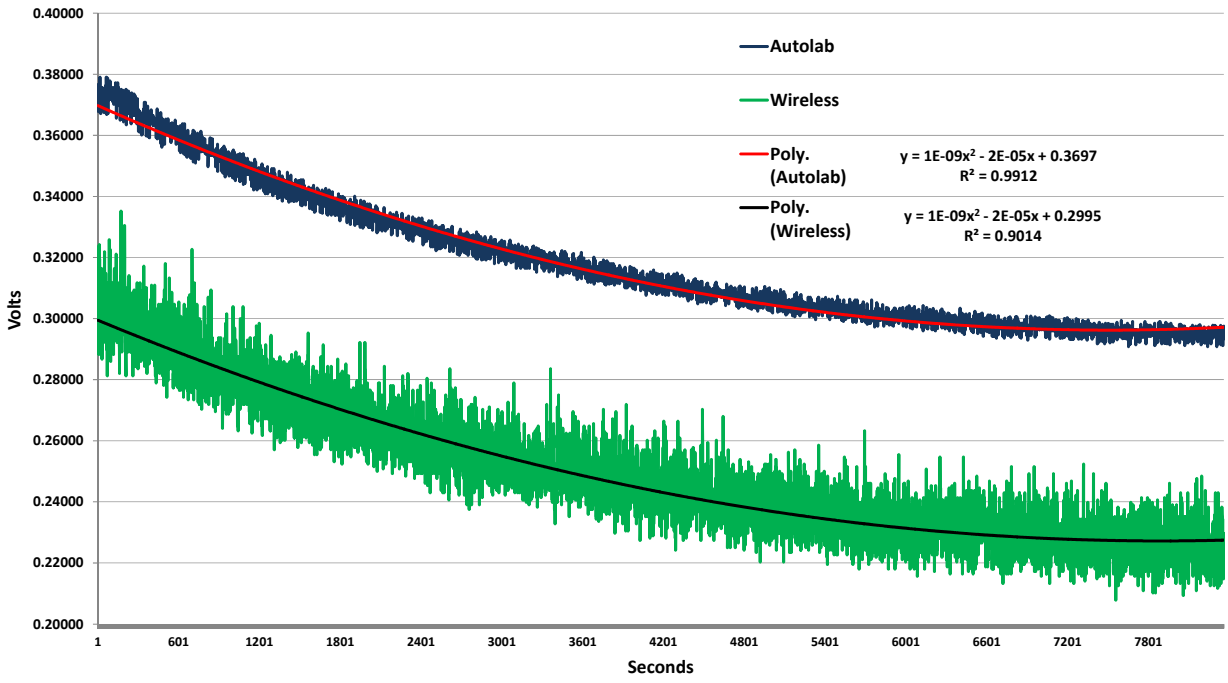

Figure 100 Corrosion Sensor Test Results with Unity Gain Amplifier and Wireless Communication System Powered by the Thermoelectric Generator

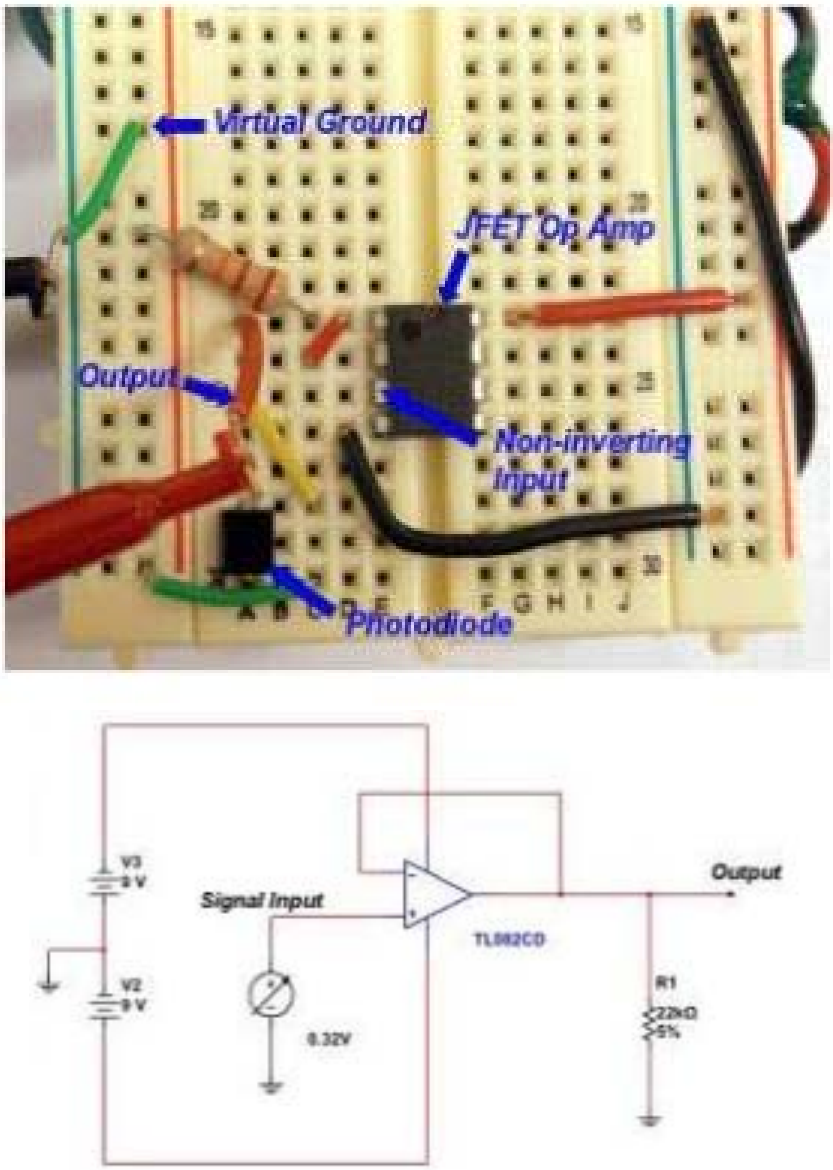

Figure 101 JFET Op Amp Unity Gain Amplifier Circuit for Signal Conditioning

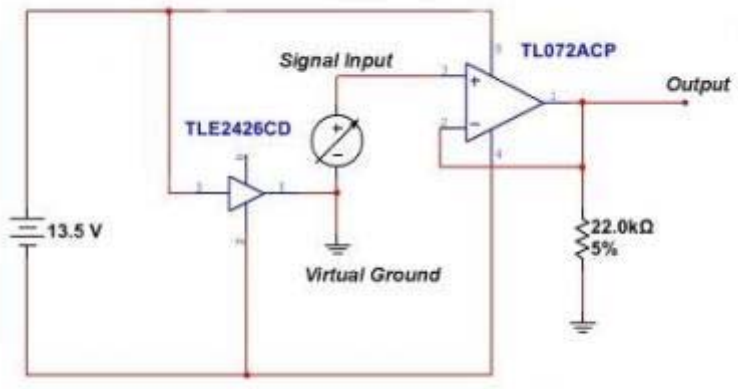

Figure 102 Schematic of Rail Splitter with Downstream Unity Gain Amplifier

October to December 2012

Although the capability of the wireless communication system has been demonstrated in the laboratory and in a pilot plant environment, it was of interest to improve the interface between the corrosion sensor and the commercial wireless system. Figure 103 is a screen shot of the integrated interface circuitry designed and simulated in National Instrument's Multisim™ 13.0. The three circuit elements consist of a "rail splitter" which converts the 13.5 VDC supplied by the thermoelectric generator to a dual rail ±6.75 VDC supply with virtual ground; a JFET unity gain amplifier to serve as a high impedance input to the mV signal between the working electrode and reference electrode; and a high gain ($x10^6$) JFET amplifier to convert the µA noise signal to a low voltage signal that can be transmitted via the wireless communication system. This interface has been built on a protoboard to facilitate design modifications and was tested to verify functionality when powered by the thermoelectric generator.

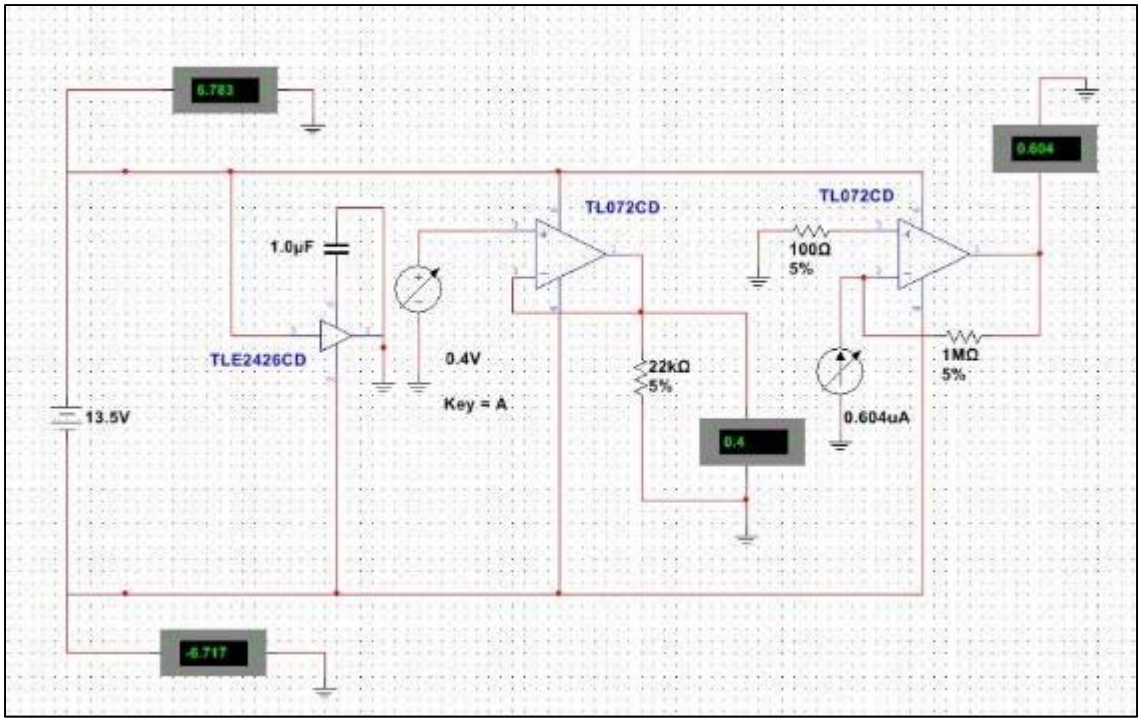

Figure 103 NI Multisim™ Schematic of Interface Circuitry

October to December 2014

A 24 hour trial was conducted with this new design to directly measure the output voltage of the TEG under full load. The TEG supplied ample power for both transmitters and associated components. The results of this test are shown in Figure 104.

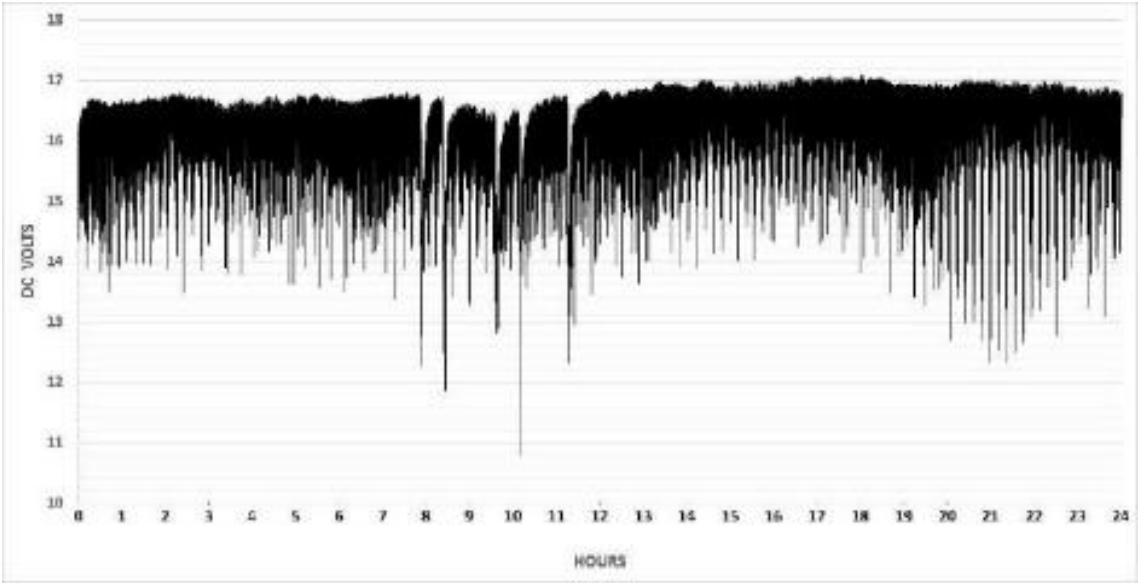

Figure 104 TEG voltage test

This TEG output voltage was sampled and recorded at 10 second intervals for 24 hours. The average voltage over this period was 16.12 volts with a standard deviation of 0.737. The maximum voltage recorded was 17.08 volts and the minimum was 10.78 volts. This trial was be repeated to measure surface and ambient temperature along with output voltage to better understand the correlation among those variables.

Two trials were conducted to characterize the performance of the TEG. The first trial, shown in Figure 105, is a scatter plot of the open circuit output voltage as a function of temperature over a 24 hour period. The temperature represented is the difference between the temperature (°F) measured with a K-type thermocouple at the surface of the TEG and the ambient air temperature (°F). The result is the ΔT across the TEG modules. This relationship can be reasonably approximated with a linear regression equation with an R^2 of 0.87.

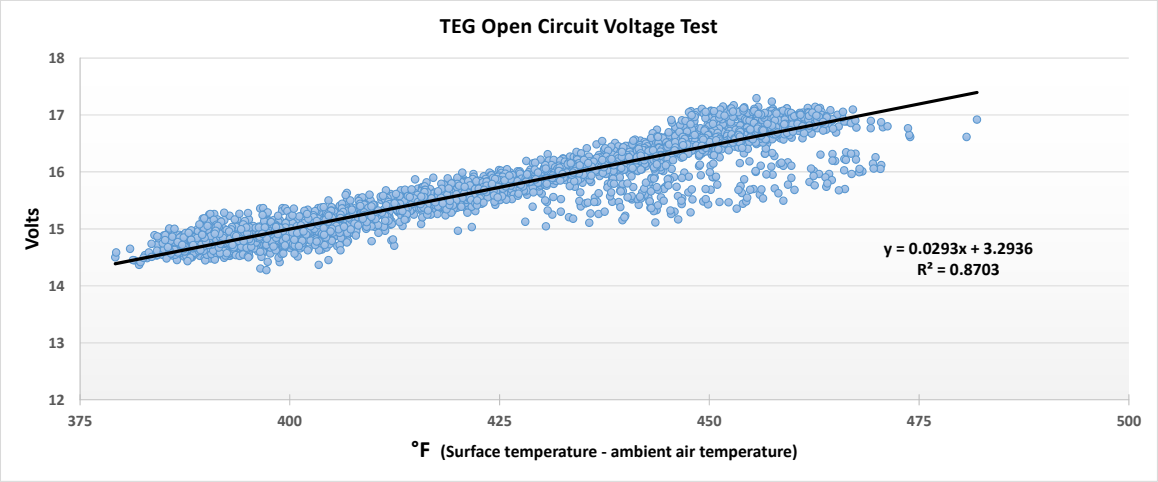

Figure 105 TEG Open Circuit Voltage vs Temperature

The second trial measured the output voltage of the TEG under full load. Figure 106 is a scatter plot of this full load voltage as a function of temperature over a 24 hour period. As in the open circuit trial, the temperature represented is the difference between the temperature (°F) measured with a K-type thermocouple at the surface of the TEG and the ambient air temperature (°F). Both scatter plots show a variation in temperature greater than 100 °F.

A hot plate was used as the heat source for the TEG in both of these trials. The ON – OFF control mode of the resistance heating element and the relatively modest power capacity of the hot plate are the primary causes of this temperature variation. The wide variation in voltage across the temperature range in Figure 106 is likely due to power fluctuations of the Phoenix Contact RAD-ISM-900-SET-DC-UD transmitter. The average power consumption of this transmitter is specified at 1.8 Watts with the peak power consumption rated at 8.4 Watts. This transmitter utilizes frequency hopping spread spectrum technology in the frequency band of 902 to 928 MHz.

The thermoelectric generator used in these trials has a rated maximum output of 20 Watts of which up to 5 Watts is consumed by the cooling fan. At the average power consumption of 1.8 Watts for each transmitter there are 11.4 Watts available which is sufficient for the power demands of the interface circuits, DC-DC converters as well as the signal converters. However, if both transmitters require peak power then the TEG will briefly exceed its maximum rating and operate at a reduced voltage. It is suspected that the inherent temperature variations due to the hot plate controls and the demand fluctuations of the transmitters result in the temperature and voltage variation shown in Figure 106. A TEG array with a higher power output coupled with a constant heat source accessible in a fossil fuel fired combustion system would most likely result in significantly less variation.

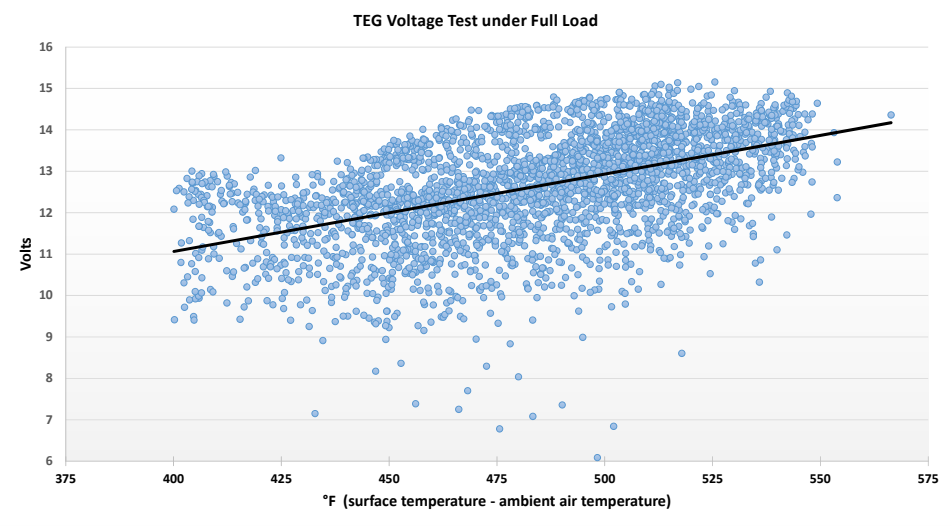

Figure 106 TEG Voltage under Load vs Temperature

Conclusions

- To improve the interface between the corrosion sensor and the commercial wireless system two JFET operational amplifiers were utilized to serve as high impedance buffers.
- The three circuit elements consist of a "rail splitter" which converts the 24 VDC supplied by the thermoelectric generator and DC to DC converter to a dual rail ±12 VDC supply with virtual ground; a JFET unity gain amplifier to serve as a high impedance input for the mV signal between the working electrode and reference electrode; and a high gain ($3x10^5$) JFET amplifier to convert the µA noise signal between the WE1 and WE2 to a low potential signal that can be transmitted via the wireless communication system.
- The interface has been built and tested to verify functionality when powered by the thermoelectric generator.

Subtask 4.2 Demonstrate TEG and Wireless Communication System Functionality under Laboratory Conditions

Experimental Methods

Development of Self-Powered Wireless High Temperature Electrochemical Sensor for In Situ Corrosion Monitoring of Coal-Fired Power Plant

This research highlighted the effectiveness of our novel high temperature electrochemical sensor for in situ coal ash hot corrosion monitoring in combination with the application of wireless communication and an energy harvesting thermoelectric generator (TEG). This self-powered sensor demonstrated the successful wireless transmission of both corrosion potential and corrosion current signals to a simulated control room environment.

Sensing Strategy of Self-Powered Wireless High Temperature Electrochemical Sensor

The key innovation of the sensing strategy is the combination of the high temperature corrosion sensor with electrochemical noise analysis technology and the application of a self-powered wireless sensor network. The conceptual design of the sensing system is shown in Figure 107. The design includes four individual modules: (1) High temperature electrochemical sensor; (2) Potential/current amplification system; (3) Wireless communication system; and (4) Thermoelectric generator for energy harvesting.

High Temperature Electrochemical Sensor

The sensor was based on a four-electrode system which includes two identical working electrodes (WE1 and WE2), one reference electrode (RE) and one counter electrode (CE). The schematic design of the sensor is shown in Figure 108. It was specially designed to utilize the response of ENA, EIS and LPR to study the corrosion behaviour. However, for real time wireless transmission of electrochemical signals ENA is the most suitable technique to detect and analyze the corrosion process as well as corrosion rates.

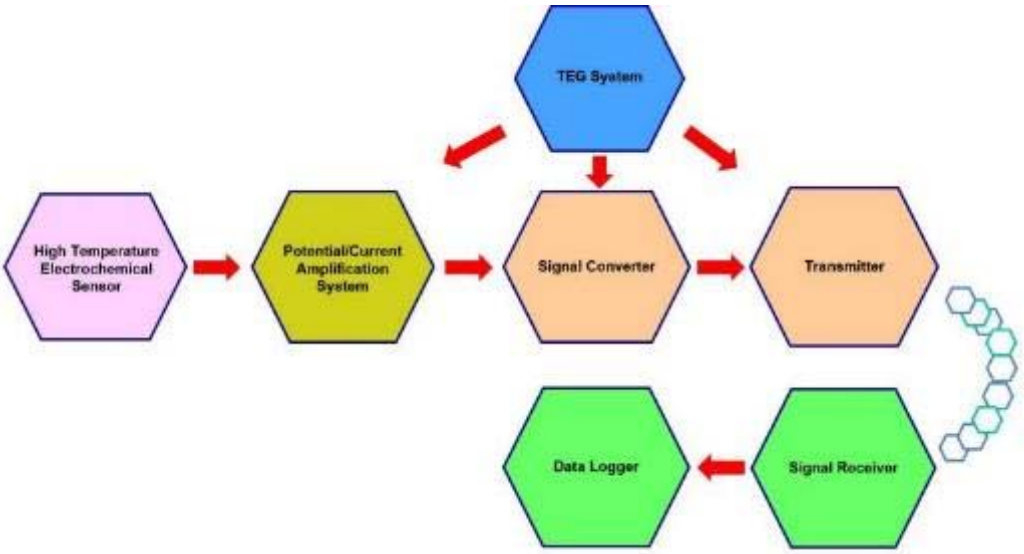

Figure 107 Conceptual design of self-powered wireless high temperature electrochemical sensor system

Figure 108 Schematic design of our novel high temperature corrosion sensor

The monitoring principle of an electrochemical noise based high temperature electrochemical sensor is the direct transmission of thermodynamic and kinetic responses represented by electrochemical hot corrosion reactions. Different potential levels are imposed due to the activity of corrosion and the current flow is proportional to the extent of corrosion. Time-dependent fluctuations of potential noise signal can be recorded from the WE1 and RE while the WE1 and WE2 transmit the current noise signal. The potential/current noise signals from the sensor were conditioned by a JFET operational amplifier interface for transmission by the wireless communication system.

The working electrodes were fabricated using the same materials as the structure being monitored. One of the unique aspects of the sensor is the inclusion of a solid state Ag/Ag^{+} reference electrode to measure the potential between this reference electrode and the working electrode that is sensitive to specific ionic species under high temperature conditions. The reference electrode contained 10 mol% Ag_2SO_4 in the 90 mol% Na_2SO_4 molten salt. The Ag wire was inserted into the fused-quartz (GE 214) tube to allow the Ag wire to be immersed in the molten salt. The top of the reference electrode was sealed to prevent an evaporation of the molten salt at high temperatures. Its stability allowed the sensor to have a good

reference point and better isolate the electrochemical corrosion information from other noise in the environment. A platinum wire was used as a counter electrode.

Potential/Current Amplification System

To improve the interface between the corrosion sensor and the commercial wireless system two JFET operational amplifiers were utilized to serve as high impedance buffers (Figure 109). Figure 109a is a screen shot of the integrated interface circuitry designed and simulated in National Instrument's Multisim™ 13.0. The three circuit elements consist of a "rail splitter" which converts the 24 VDC supplied by the thermoelectric generator and DC to DC converter to a dual rail ±12 VDC supply with virtual ground; a JFET unity gain amplifier to serve as a high impedance input for the mV signal between the working electrode and reference electrode; and a high gain ($3x10^5$) JFET amplifier to convert the μA noise signal between the WE1 and WE2 to a low potential signal that can be transmitted via the wireless communication system. This interface has been built and tested to verify functionality when powered by the thermoelectric generator.

Wireless Communication System

The wireless sensor network can demonstrated the capability of a state-of-the-art commercial wireless system to manage the data transmission requirements of the potential and current noise signals generated by the high temperature electrochemical sensor system. The hardware chosen was a one Watt transmitter with frequency-hopping, spread spectrum technology in the 902-928 MHz ISM band. This was chosen to minimize signal degradation that may be accentuated with higher frequency carrier signals. The signal converter will convert the mV output of the JFET amplifiers to a 4-20 mA signal to be transmitted wirelessly to a remote receiver. The transmitter configuration consists of a 12 to 24 V DC to 24 V DC power supply, an ON-OFF circuit breaker and a configurable signal converter mounted to a rail as shown in Figure 110. The DC to DC converter is powered by a thermoelectric generator providing a regulated 24 VDC to the signal converter, transmitter, and JFET amplifiers.

Thermoelectric Generator for Energy Harvesting

Thermoelectric generators utilize the principle of the Seebeck effect to convert a temperature difference across a semiconductor module to an electric voltage. Although typical efficiencies are only in the range of 5 to 8%, it is a viable method for energy harvesting to power remote devices for applications with a constant source of high quality heat. The thermoelectric generator selected for this phase of the project was a commercially available integrated unit of multiple TEG modules, heat sinks, and a self-powered cooling fan (Figure 111). Figure 110a shows the TEG in operation with a hot plate as the heat source and Figure 111b is an exploded view. This TEG also includes a voltage regulation module. The output of the TEG is a regulated 13.8 VDC and is used to maintain a charge on a 12 V DC lead acid battery. The rechargeable lead acid battery is rated at 4.5 amp hours when fully charged if there is no heat source available.

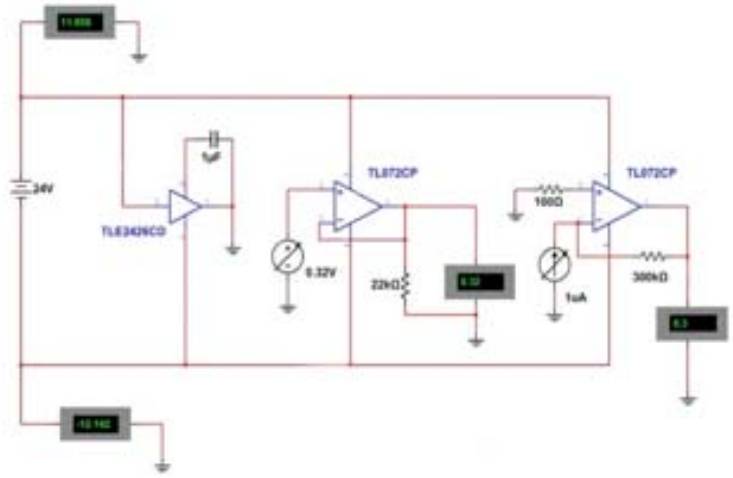

(a)

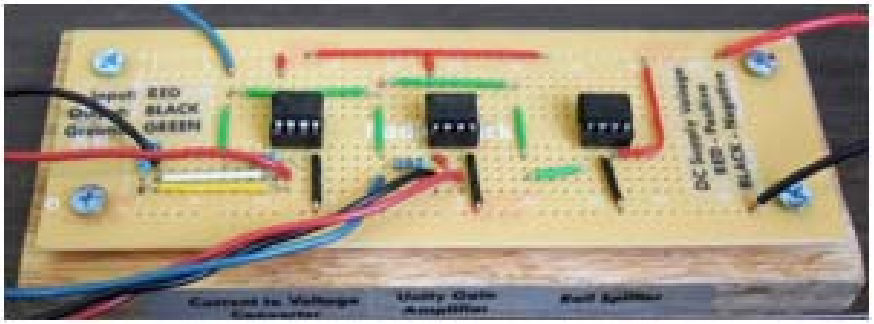

(b)

Figure 109 (a) Schematic diagram of rail splitter with downstream unity gain amplifier and current to voltage converter, and (b) photograph of circuit board of (a)

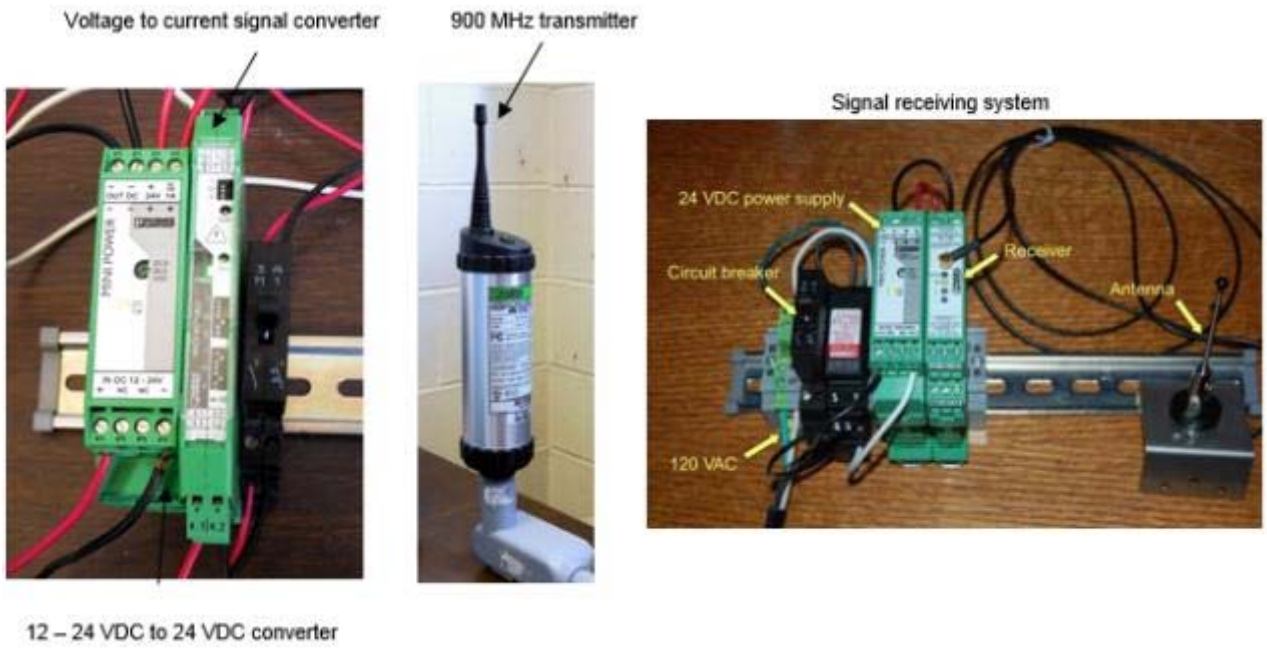

Figure 110 Photographs showing the components in the wireless communication system

(a)

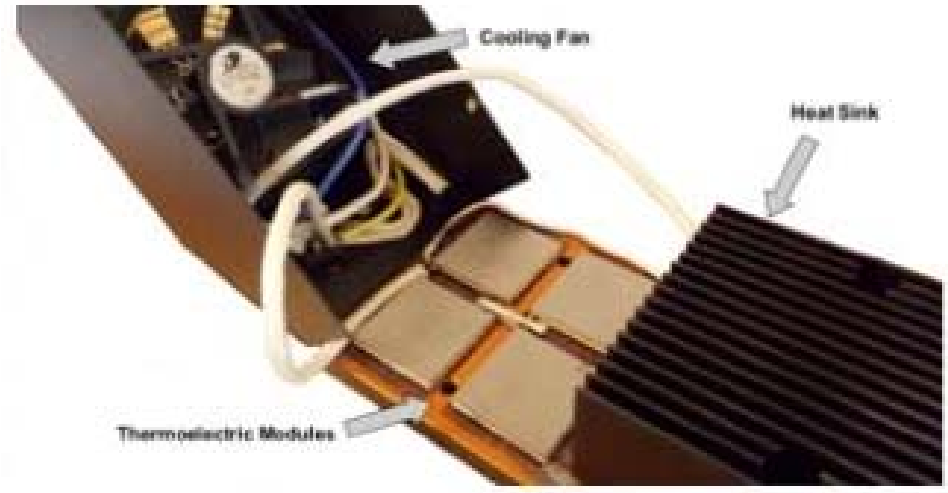

(b)

Figure 111 (a) A commercially available energy-harvesting thermoelectric generator operating in a laboratory environment, and (b) exploded view of (a)

Results and Discussion

October to December 2014

Concurrent Wireless Transmission of Coal Ash Hot Corrosion Signals of a High Temperature Electrochemical Sensor

The key innovation of this research was the synergy of the high temperature sensor technology based on the science of electrochemical noise measurement and state-of-the-art wireless communication technology. Wireless electrochemical potential and current noise signals from a simulated coal ash hot corrosion process were concurrently transmitted and recorded. The Savitzky-Golay least square polynomial smoothing was proposed to extract the real noise from the raw electrochemical noise signal of the nonstationary coal ash hot corrosion process. The resulting conditioned electrochemical noise signals from the sensor clearly distinguished the mechanism between different coal ash hot corrosion processes and their reaction kinetics.

Wireless High Temperature Electrochemical Sensor Networks

The design of the sensing networks includes three individual modules: (i) High temperature electrochemical sensor; (ii) Potential/current amplification system; and (iii) Wireless communication system. For concurrent measurements of potential noise and current noise signals from a single sensor, our developed high temperature electrochemical sensor was modified. The modified sensor was based on a five-electrode system (three identical working electrodes (WE1, WE2 and WE3), one reference electrode (RE) and one counter electrode (CE)). The WE1 and WE2 transmit the current noise signal while the potential noise signal can be recorded from the WE3 and RE.

In trials, the potential and current noise signals were transmitted independently via the same transmitter/receiver system. In the evolution of the present system, a second transmitter/receiver set including signal conditioner and DC to DC converter was added to the system architecture so that the potential and current noise signals can be transmitted concurrently. This also required modifications to the interface circuitry to electrically isolate the two signals. Figure 112 shows the wireless system with both transmitters in operation powered by the thermoelectric generator. The components as shown in Figure 112 are:

1) Thermoelectric generator
2) TEG output attached to a terminal strip with digital voltmeter
3) DC to DC converters (12-24 VDC input with regulated 24 VDC output)
4) Signal wires from high temperature electrochemical sensor
5) JFET unity gain amplifier
6) High gain ($3x10^5$) JFET current-to-voltage amplifier
7) Signal conditioners (±1 volt input with 4-20mA output)
8) Wireless transmitters (1 W) with frequency-hopping, spread spectrum technology in the 902-928 MHz ISM band.

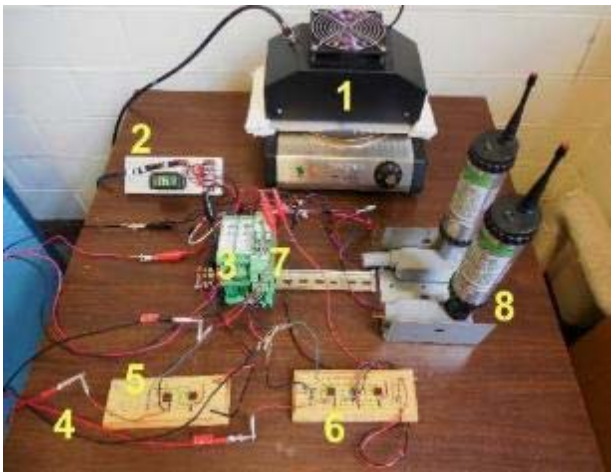

Figure 112 Hardware layout for concurrent potential and current noise signals transmission from high temperature electrochemical sensor

January to March 2013

Development of Self-Powered Wireless High Temperature Electrochemical Sensor for In Situ Corrosion Monitoring of Coal-Fired Power Plant

Corrosion Signals Directly Measured from the Sensor Output

In this research the potential and current signals produced by coal ash hot corrosion of IN 740-1 alloy were first analyzed directly with a Metrohm Autolab/PGSTAT302N with the Nova data acquisition system to compare the corrosion signals output from the sensor with and without wireless communication system. The alloy has the chemical composition (in wt.%) of Ni-49.45, Cr-24.67, Fe-0.62, Co-19.98, Mo-0.50, Nb-1.47, Al-1.23, Mn-0.3, Ti-1.23, Si-0.29. The corrosion medium was a synthetic mixture of coal ash with the flue gas. The coal ash mixture consisted of reagent-grade 29.25 wt.% SiO_2, 29.25 wt.% Al_2O_3, 29.25 wt.% Fe_2O_3, 5.625 wt.% Na_2SO_4, 5.625 wt.% K_2SO_4 and 1 wt.% NaCl. The synthetic flue gas contained 15 vol.% CO_2, 4 vol.% O_2, 80 vol.% N_2 and 1 vol.% SO_2.

Coal ash hot corrosion is the result of competition between oxidation and sulfidation which affect alloys exposed to high temperature combustion gases containing sulfate coal ash. The shifting conditions between oxidation and sulfidation can greatly vary the rate coal ash hot corrosion as a consequence of slow-growing oxide scale and fast-growing sulfide scale. It depends on a complex interaction between operation temperatures, coal ash chemistry as well as flue gas composition. The sulfidation attack can be more pronounced in the flue gas with SO_2 compared to flue gas without SO_2. The transition from oxidation to sulfidation or from sulfidation to oxidation can be distinguished by different potential and current values (Figure 113). The variation of potential values from oxidation to sulfidation clearly suggests that sulfidation occurred at very positive potentials compared with oxidation Figure 113a). The current spikes were observed during the sulfidation stage indicating the high extent of localized corrosion (Figure 113b).

In contrast, the corrosion current of the alloy in the sulfidation stage was much higher than that in the oxidation stage.

It is expected that the oxidation/sulfidation potentials and corrosion current values of the material will be different in different coal ash hot corrosion conditions. In order to evaluate coal ash hot corrosion potential and current ranges, the potential and current noise signals of IN 740-1 alloy were analysed in simulated coal-fired boiler environments with different temperatures, different SO_2 contents in the flue gas and different thickness of coal ash for 120 h (Figure 114). In comparison between the corrosion potential values of each condition the values varied from −80 mV (vs Ag/Ag^+) to 450 mV (vs Ag/Ag^+) as a consequence of different coal ash conditions (Figure 114a). The stable oxidation potential was observed at approximately −80 mV vs Ag/Ag^+. The sulfidation potential of the alloy was in the range between 300 mV (vs Ag/Ag^+) and 450 mV (vs Ag/Ag^+). The reaction current of oxidation/sulfidation can be evaluated with the current noise values (Figure 114b). The sudden changes in current densities were observed during corrosion indicating high extent of corrosion attack. In this case, the current spike was as high as about 40 μAcm^{-2} (Figure 114b).

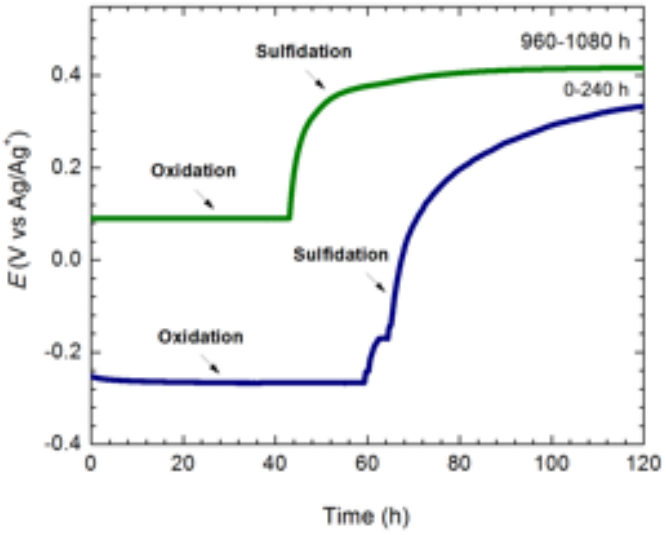

(a)

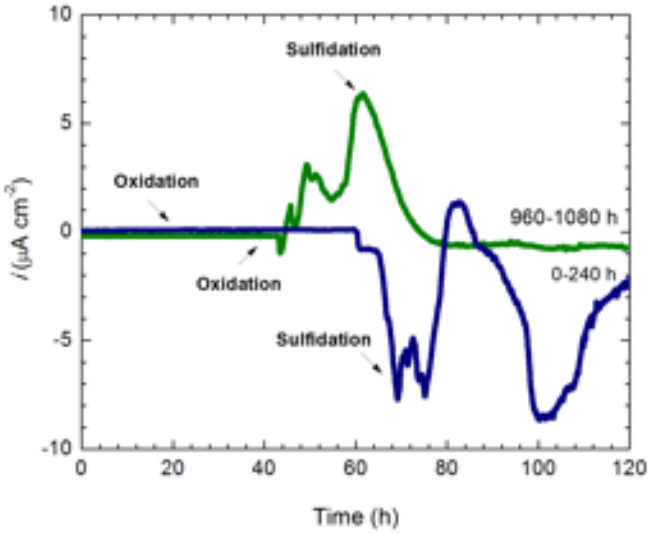

(b)

Figure 113 Time sequences of the electrochemical noise signals produced by oxidation and sulfidation stage at two different exposure periods: (a) potential noise signals, and (b) current noise signals

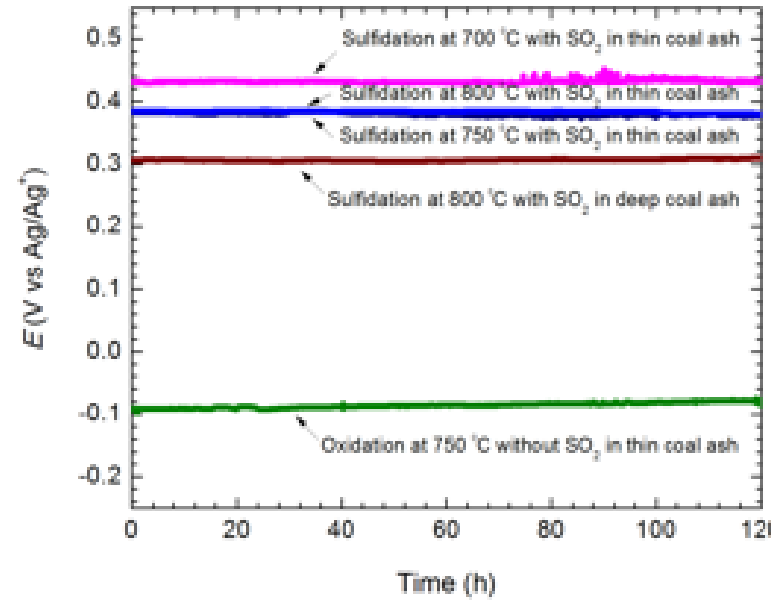

(a)

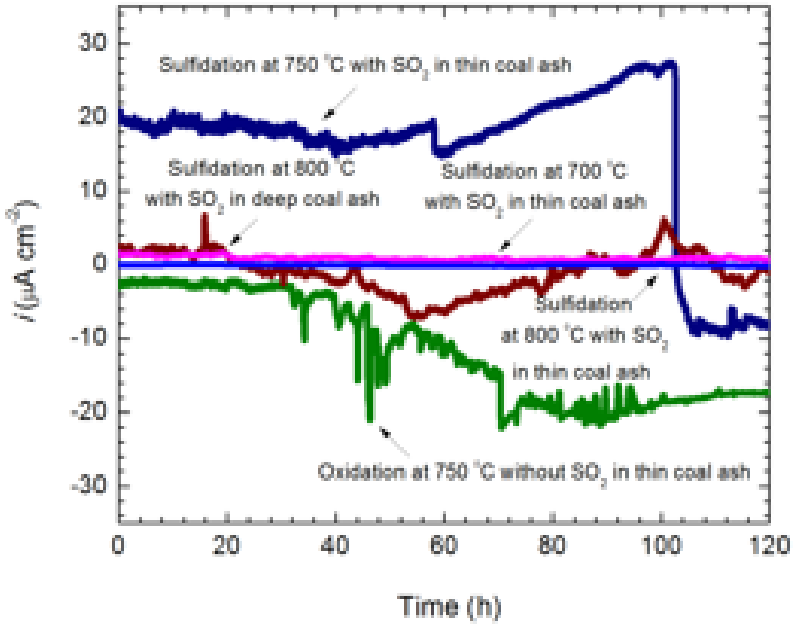

(b)

Figure 114 The electrochemical signals produced by different coal ash hot corrosion conditions: (a) potential noise signals, and (b) current noise signals

Corrosion Signals Transmitted by the Sensor via the Self-powered Wireless Communication System

The potential and current signals produced by the oxidation and sulfidation stages of coal ash corrosion were transmitted via the wireless communication system to evaluate its sensitivity (Figure 115). The signals were amplified by the JFET interface that serves as a high impedance unity gain amplifier for the potential signal and a high gain current to voltage amplifier for the current signal. The measured current was calculated by dividing the measured voltage signal by the gain factor of the amplifier. The output of the JFET amplifier is in good agreement with the expected values.

The raw noise signals transmitted from the wireless communication exhibited higher peak-to-peak amplitudes compared with those measured by the Autolab instrument. The Autolab instrument has a smoothing algorithm which can effectively condition the sensor output to reduce the intrinsic noise from the electrochemical reaction. The extraction of the real signal from the raw data is the essential step of electrochemical noise analysis. A smoothing algorithm such as moving average, polynomial and linear trend removal can be used to smooth the noise data. The transition from the sulfidation stage to oxidation stage was clearly observed after Savitzky-Golay least square polynomial smoothing (Figure 115a and Figure 115b).

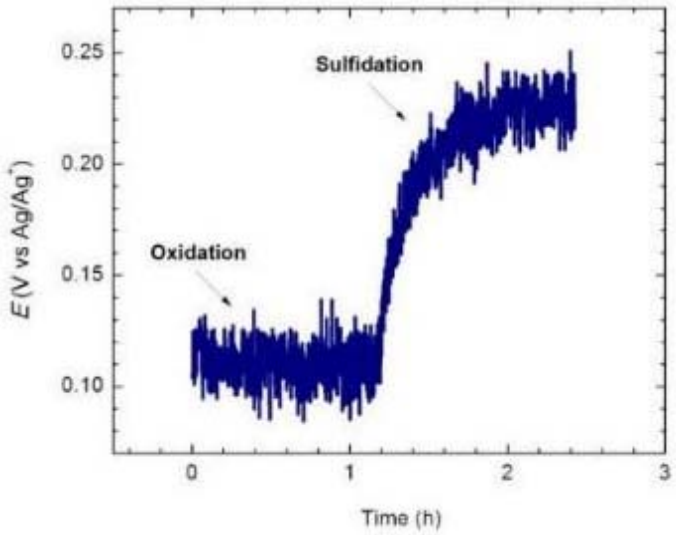

(a)

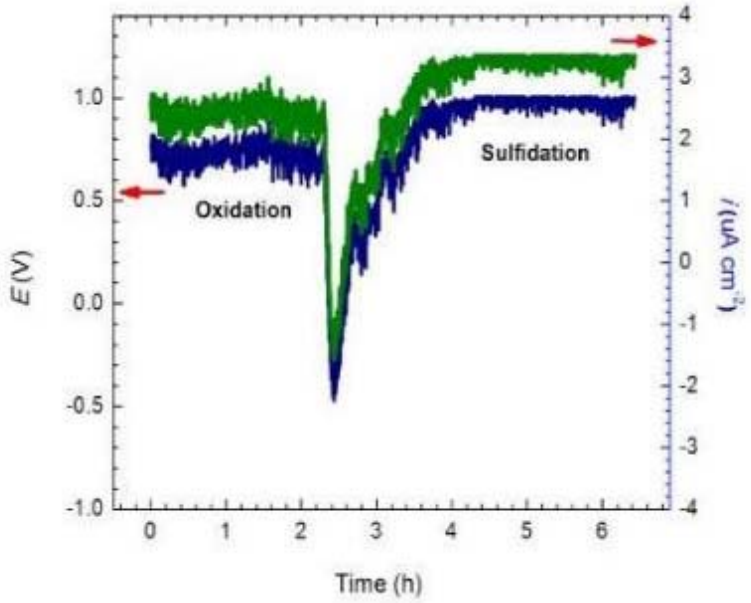

(b)

Figure 115 The signals transmitted via the wireless communication system in the oxidation and sulfidation stages: (a) potential noise signals, and (b) current noise signals

Performance Evaluation of the Sensor

The main performance parameter of the sensor is the sufficient correlation of the data from electrochemical signals and the corrosion rates of materials in service. Trials were conducted for 10 days to test the sensibility and reliability of the sensor. The corrosion potential and current signals produced from the oxidation and sulfidation stages at different coal ash hot corrosion conditions are shown in Figure 116. The high temperature reference electrode provides a reference point for all the electrochemical readings, but the signal is too noisy to analyze quantitatively, especially for the potential measurement (Lighter color signals in Figure 116a and Figure 116b). In this case, Savitzky-Golay smoothing was carried out independently for both the potential and the current noise signals. This method worked very well in all of the coal ash corrosion systems without losing useful data (Darker color signals in Figure 116a and Figure 116b).

The real-time potential and current signal distribution can be applied as the benchmark to qualitatively identify the oxidation and sulfidation processes during coal ash hot corrosion. The performance parameters of the sensor are summarized in Table 4. The quantitative relationship between corrosion rate and current noise for the coal ash hot corrosion can be determined through the adoption of Faraday's Law. The maximum value of current noise, i_{max}, for each exposure period is used to calculate corrosion rates. An instantaneous corrosion rate can be used to determine the accumulated mass loss and corrosion depths over the entire duration of exposure.

The accuracy of kinetic responses of current noise test data from the sensor can be evaluated with the values from a weight loss test. In comparing the accumulated mass loss for different coal ash hot corrosion conditions of Figure 114b and their corresponding mass loss values from the weight loss test, the results demonstrate a good correlation between the electrochemical data and the actual degradation processes (Figure 117). The same conclusion can be drawn for the wireless current signals of Figure 116b.

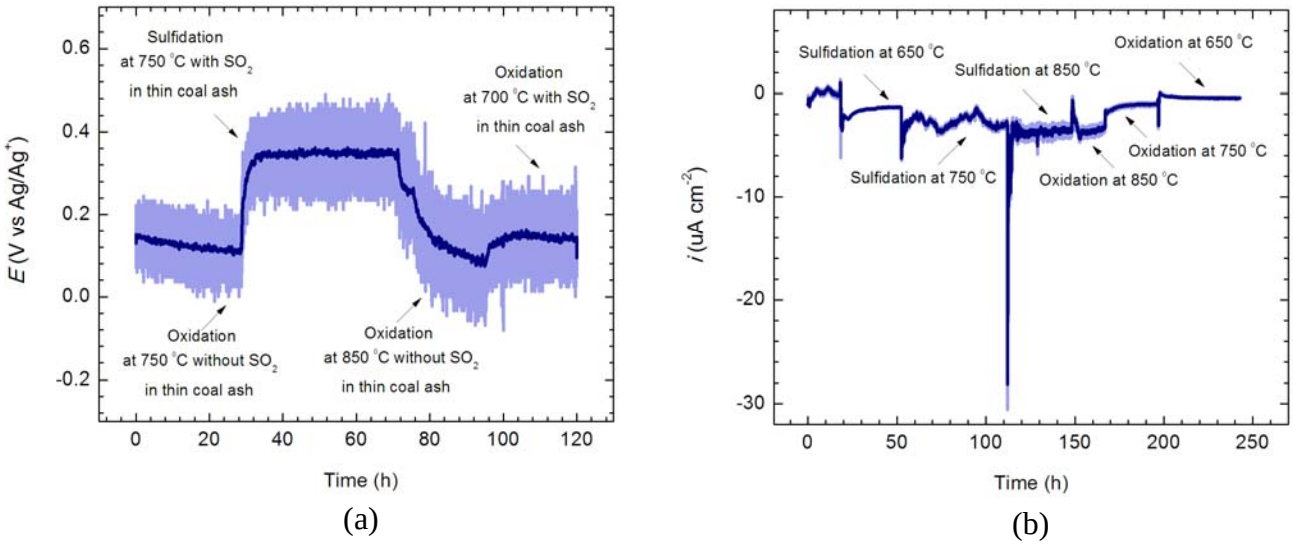

Figure 116 The signals transmitted via the wireless communication system in different coal ash hot corrosion conditions: (a) potential noise signals, and (b) current noise signals

Table 4 The performance parameters of the sensor

	Coal ash hot corrosion process	
	Oxidation	Sulfidation
Corrosion potential	<200 mV (vs Ag/Ag^+)	200~500 mV (vs Ag/Ag^+)
Corrosion current	Oxidation current is much lower than sulfidation current at a given temperature	

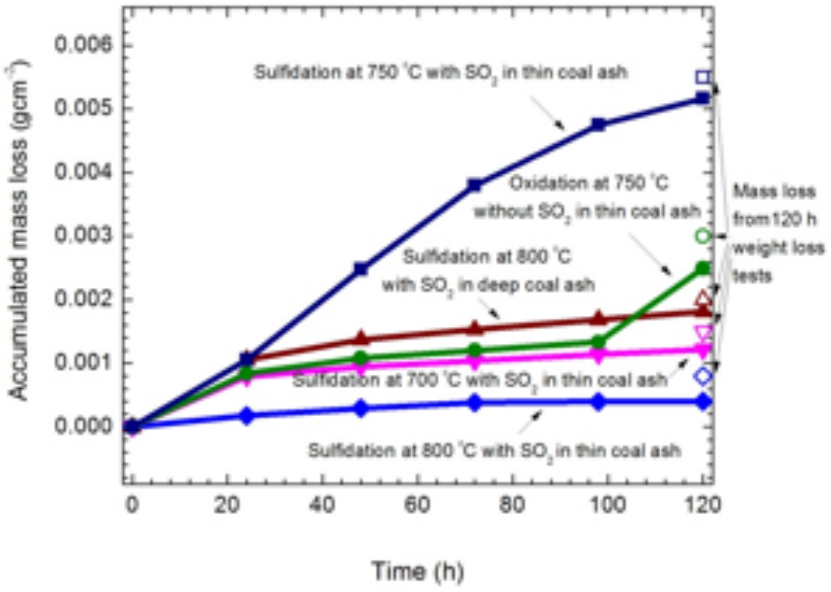

Figure 117 Comparison between corrosion rates data from current noise signal analysis and weight loss test

October to December 2014

Concurrent Wireless Transmission of Coal Ash Hot Corrosion Signals of a High Temperature Electrochemical Sensor

The potential and current signals produced by the oxidation and sulfidation stages in coal ash hot corrosion process of Inconel 740 superalloy in a simulated coal-fired boiler environment at a temperature range of 650-850 °C were concurrently recorded. The alloy has the chemical composition (in wt.%) of Ni-49.45, Cr-24.67, Fe-0.62, Co-19.98, Mo-0.50, Nb-1.47, Al-1.23, Mn-0.3, Ti-1.23, Si-0.29. The corrosion medium was a synthetic mixture of coal ash with the flue gas. The coal ash mixture consisted of reagent-grade 29.25 wt.% SiO_2, 29.25 wt.% Al_2O_3, 29.25 wt.% Fe_2O_3, 5.625 wt.% Na_2SO_4, 5.625 wt.% K_2SO_4 and 1 wt.% NaCl. The synthetic flue gas contained 15 vol.% CO_2, 4 vol.% O_2, 80 vol.% N_2 and 1 vol.% SO_2. The oxidation and sulfidation stages were simulated with and without SO_2 content. The data points were continuously taken with sampling rates of one data point every 10 seconds.

The nature of the wireless potential and current noise signals from the oxidation and sulfidation stages can be seen in Figure 118. Corrosion potential and current values of each oxidation and sulfidation stages can be identified from the signals, but the values are too noisy to analyze quantitatively, especially for the potential signal (Figure 118a and Figure 118b). The electrochemical noise signal of the nonstationary coal ash hot corrosion process may generate a DC drift component and it may overlap the useful signal. The extraction of real noise from the raw noise-time record is the essential step of noise analysis. A smoothing algorithm such as moving average, polynomial or linear trend removal can be used to remove the DC drift

from "raw" noise data. A delicate balance should exist between sufficient trend removal and preventing the loss of valuable data.

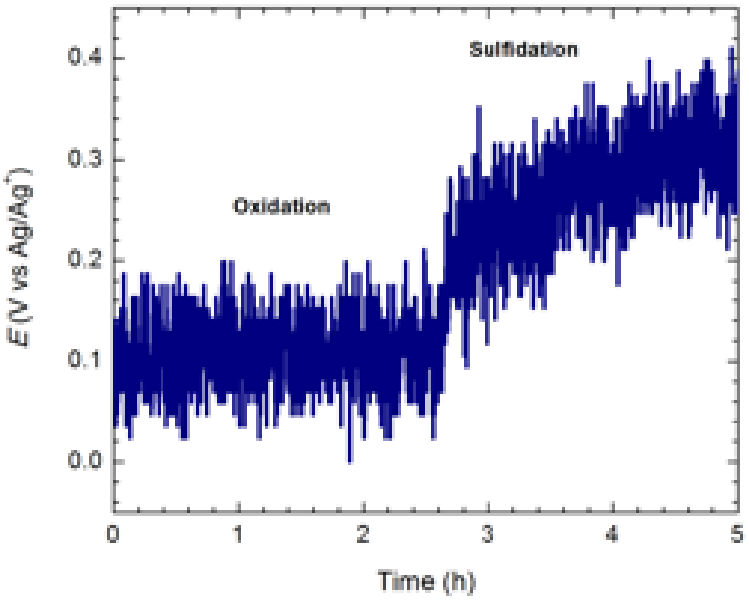

(a)

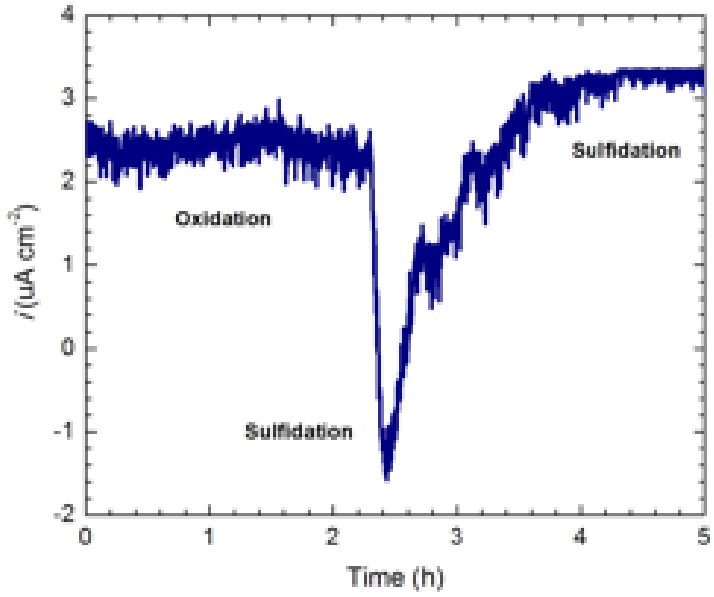

(b)

Figure 118 Electrochemical noise signals wirelessly transmitted during the oxidation and sulfidation stages of coal ash hot corrosion: (a) potential signal, and (b) current signal

Smoothing of Corrosion Potential and Current Noise Signals

In this research, two methods of data smoothing, adjacent averaging and Savitzky-Golay least square polynomial, were used to smooth the noise of measured signals. The two filtering method were used in Origin by opening the smoothing tool. Smoothing by adjacent averaging essentially takes the average of

specified data points around each point in data and replaces that point with the new average value. The Saviztky-Golay smoothing is based on the least squares polynomial fitting across a moving window within the data in the time domain. It performs a local polynomial regression to determine the smoothed value for each data point. The effect of least square polynomial smoothing on the same input potential and current signals from Figure 118 was illustrated in Figure 119. The signals after smoothing with the 100-point adjacent average method were compared with that of the 100-point Savitzky-Golay (n=5). Clearly, the potential noise amplitude is reduced by the adjacent average smoothing (Figure 119a). However, this smoothing method works more effectively if the data contains no cyclic pattern. In case of the sharp current spike, it produced significant distortions and reduced the signal intensity (Figure 119b). This is a serious limitation for obtaining the maximum current value which must be used to determine the corrosion kinetics.

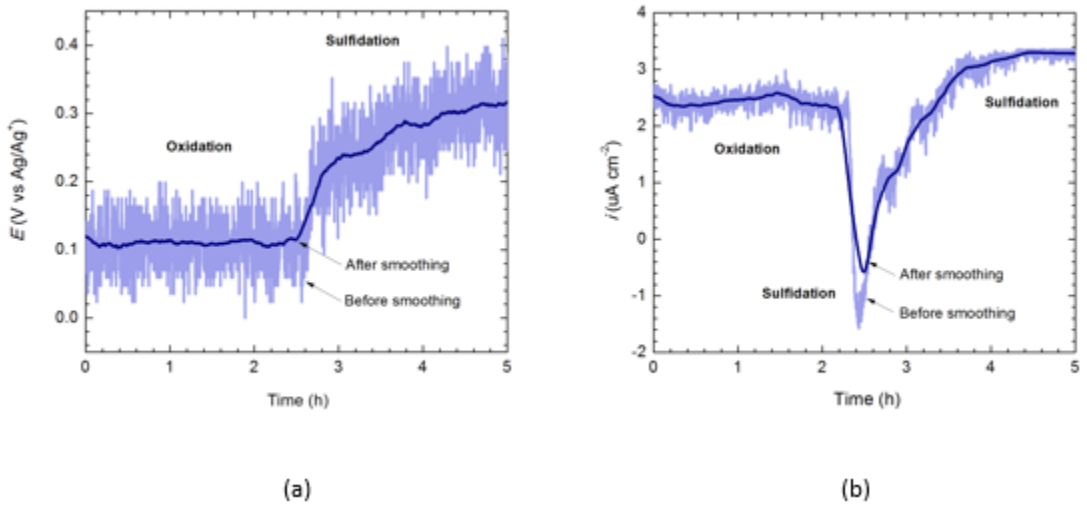

Figure 119 Electrochemical noise signals of Figure 108 after smoothing with the 100-point adjacent average: (a) potential signal, and (b) current signal

By contrast, Saviztky-Golay smoothing tends to preserve data features such as peak height and width (Figure 120) which are usually 'washed out' by adjacent averaging. The fitting/differentiation of the signals can be improved by changing the polynomial order (Figure 120a and Figure 120b). The magnified current signals obtained with Saviztky-Golay filters for 10-point n=5, 100-point n=5, 100-point n=1, and 300-point n=5 were shown in Figure 120c. In comparison, 100-point n=5 filter resulted in a high level of smoothing without reducing the signal intensity. But, 100-point n=1, and 300-point n=5 filters produced a sharp noise reduction. Typically, a high or a moderate order polynomial allows a high level of smoothing without attenuation of data features. However, there are significant distortions of the signal by the smoothing filter, which increases with increasing filter bandwidth.

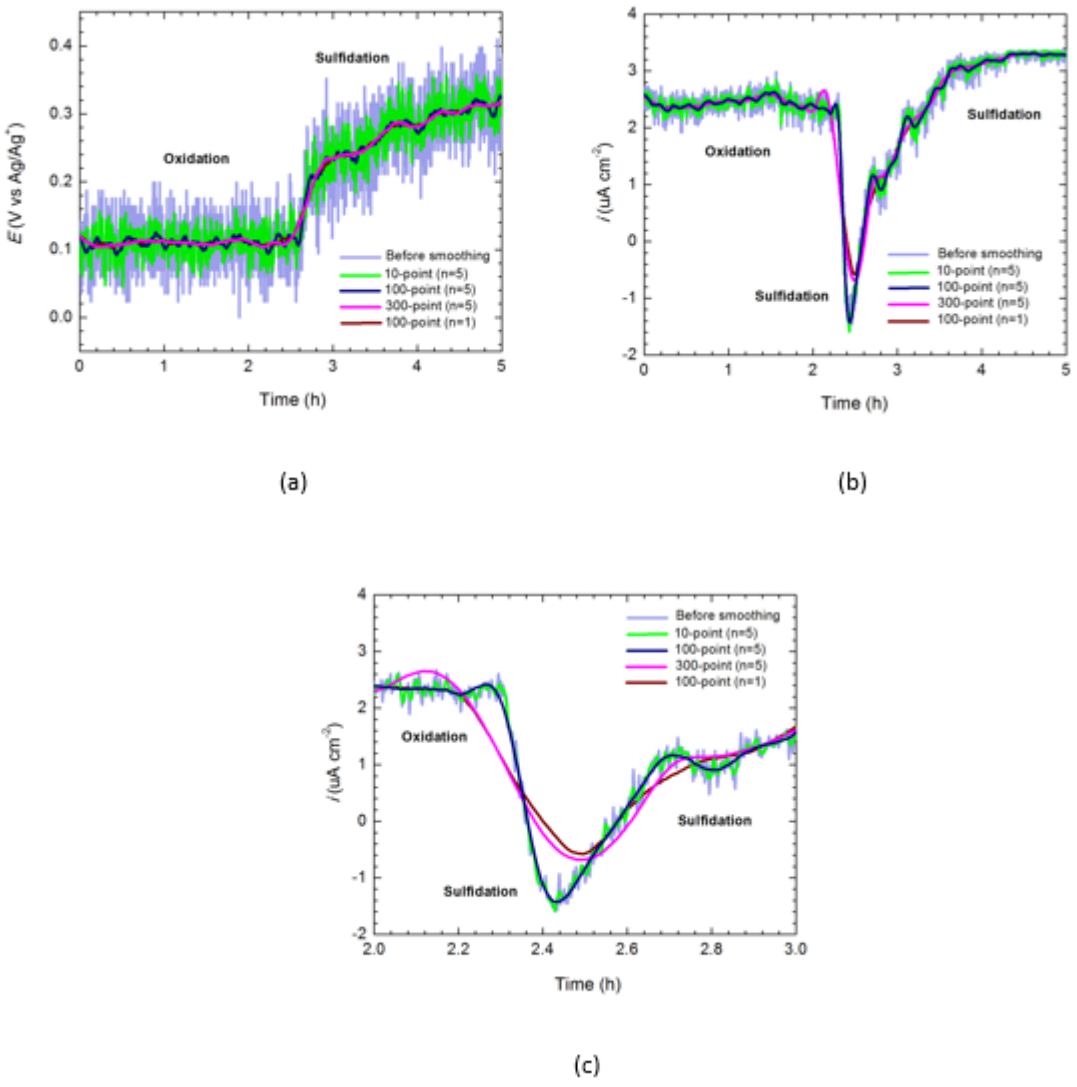

Figure 120 Electrochemical noise signals of Figure 108 after Savitzky-Golay smoothing with different points and polynomial degrees: (a) potential signal, (b) current signal, and (c) the magnified graph of (b)

Long-Term Stability and Reliability of the Sensor

In order to simulate long-term use, trials were conducted for 20 days to test the sensibility and reliability of the sensing system. The concurrent corrosion potential and current signals produced from the oxidation and sulfidation stages at different temperatures are shown in Figure 121. The potential and current signals were analysed using the Saviztky-Golay smoothing algorithm. The darker signals in Figure 121a represent smoothing with the 100-point Savitzky-Golay (n=5). After smoothing, the results of the potential signals can clearly identify the main mechanisms of coal ash hot corrosion process at different temperatures (Figure 121a): (i) at the given temperature sulfidation potentials is more positive compared with the oxidation potentials, and (ii) the oxidation tendency of the alloy at 850 °C was higher than those at 650 °C and 750 °C.

The noise signature of current fluctuating with no sudden spike correlated to the low extent of oxidation/internal sulfidation. The noise pattern of sudden change in current values followed by slow or no recovery corresponded with the accelerated oxidation/internal sulfidation. The main performance parameter of the sensor is the correlation between the data from current signals and the corrosion rates of materials in service. The quantitative relationship between corrosion rate and current noise for the coal ash hot corrosion can be determined through the adoption of Faraday's Law (Figure 121b). The maximum value of current noise, i_{max} is used to calculate corrosion rates,

Equation 15 $$R(mmy^{-1})\left[R = \frac{KM}{n\rho} i_{max} \text{ in Equation 7}\right]$$

An instantaneous corrosion rate can be used to determine the accumulated mass loss and corrosion depths. This was achieved by summing the corrosion depths over various periods of exposure to give a cumulative result. The corrosion depth, D (μm), during the specific period is calculated by $D = K \times R \times$period in *Equation 8*.

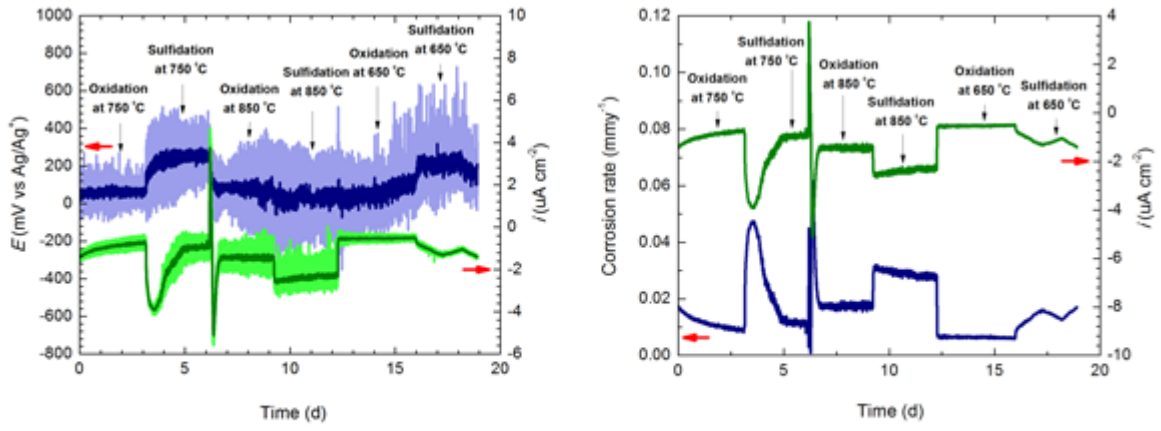

(a) (b)

Figure 121 Concurrent potential and current signals transmitted via the wireless communication for 192 h: (a) after smoothing with the 100-point Savitzky-Golay (n=5), and (b) instantaneous corrosion rate of (a)

Conclusions

- Combined concepts of the electrochemical noise based high temperature sensor and wireless communication system were successfully demonstrated.
- Wireless electrochemical potential and current noise signals from a simulated coal ash hot corrosion process were concurrently transmitted and recorded.

- Characteristic patterns in the wireless potential and current noise signals can clearly identify the oxidation and sulfidation stages of coal ash hot corrosion process after data smoothing with the 100-point Savitzky-Golay (n=5).

Subtask 4.3 Demonstrate TEG and Wireless Communication System Functionality under Industrial Operating Conditions

Experimental Methods

WRI-WVU Corrosion Sensor Testing Phase I High Temperature Electrochemical Sensor Testing in Coal Derived Flue Gas Exposure

The wireless communication was demonstrated at WRI's Combustion Test Facility (CTF). The location of the corrosion sensor and wireless transmitter is shown in Figure 122. Additional testing showed that the integrity of the carrier signal between the transmitter and receiver was maintained when the receiver was located up to a distance of 500 feet from the transmitter. It should also be noted that the wireless transmitter was powered by the TEG using a hot plate as the heat source. Measurements taken at the Combustion Test Facility did not show any heat source that was greater than 240 °C as shown in Figure 123.

WRI has provided use of a CTF for testing of the corrosion sensor under real coal derived flue gas. The sensor was tested over the course of several days each. It was exposed to real coal derived flue gas as well as natural gas fired flue gas generated during warm up periods of the CTF. Furthermore, it was exposed to several thermal cycles during the warm up and shut down periods of the daily CTF operations.

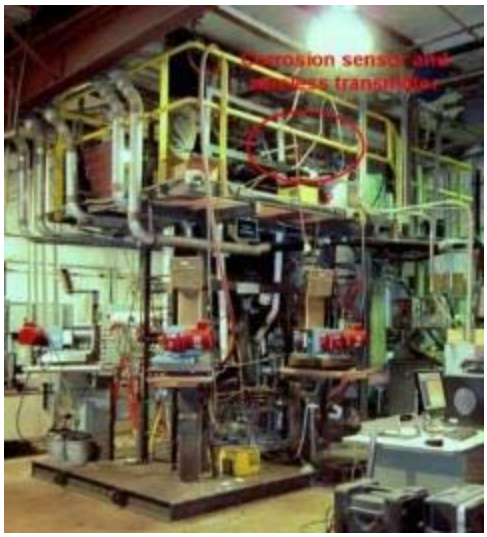

Figure 122 Corrosion and Wireless Sensor Location at Combustion Test Facility

Figure 123 Temperature Reading at Combustion Test Facility

Combustion Test Facility

WRI's CTF is a nominal 250,000 Btu/hr balanced-draft system designed to replicate a pulverized coal-fired utility boiler. A schematic of the CTF is shown in Figure 124. In its present configuration, the unit is set up to simulate a tangential-fired boiler (Figure 125), but may be easily adapted to wall-fired or other configurations. The fuel feed system consists of screw-based feeders and pneumatic transport to four burners inserted in the corners of a refractory-lined firebox. The burners can be angled to attain different tangential flow characteristics in the firebox. The unit is equipped with appropriately sized heat-recovery surfaces such that the time/temperature profile of a utility boiler is replicated. These surfaces comprise water-cooled panels that simulate the waterwall, an air-cooled superheater, reheater, two economizers and preheater. CTF includes provisions for preheating the combustion air to mimic a utility air preheater.

The system also includes over-fire air injection ports for combustion staging and several port of injecting sorbents into the furnace. The CTF is equipped with two baghouses, electrostatic precipitator (ESP) and spray dry absorber (SDA).

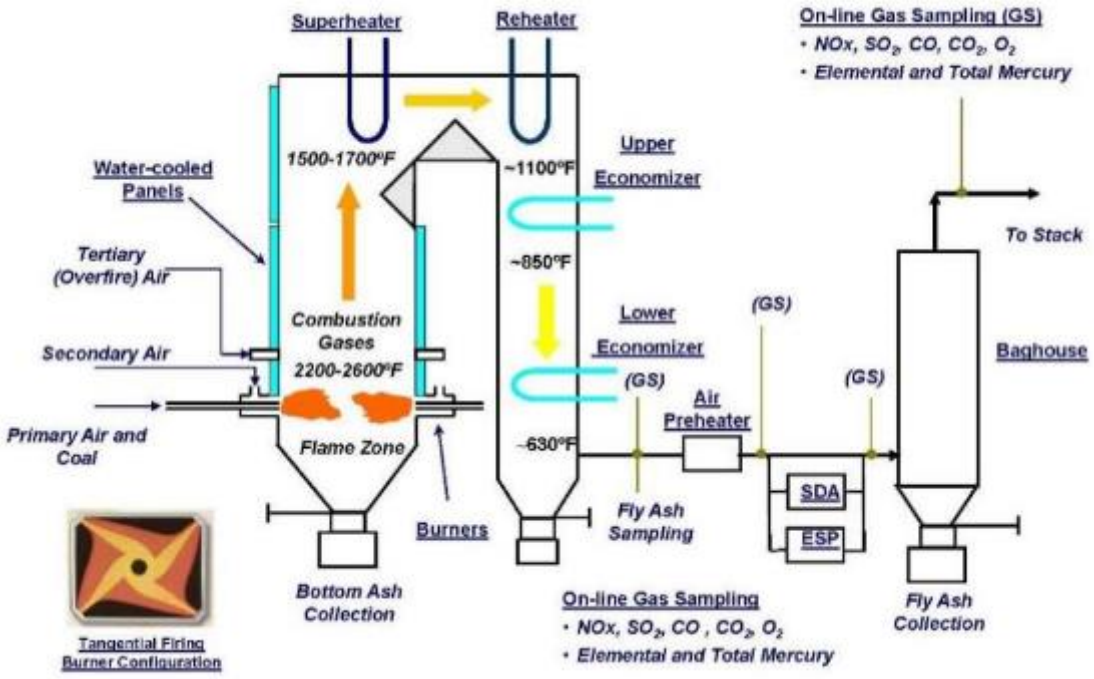

Figure 124 Schematic of the Combustion Test Facility

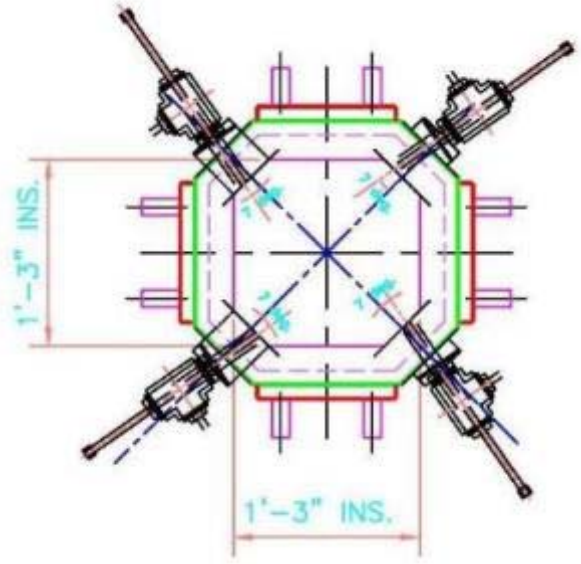

Figure 125 Schematic of the Combustion Test Facility

Test Set-Up and Conditions

The sensor location used was an available place between the superheater and reheater shown in Figure 126. The sensor and weight loss coupons were inserted into the port and set at the center of the flue gas flow (Figure 127). During the first test (1/14 thru 1/17) the sensor was removed after the first day of exposure. The following 3 days the sensor remained in the furnace without being removed until the end of the day on 1/17/2013. Depositions of coal fly ash on the sensor after first day of exposure and after 4 days of exposure are also shown in Figure 128a and Figure 128b. The following Table 5 shows the major gas constituents and operating conditions of the plant during the testing periods. The maximum temperature and normal operating temperature observed throughout this testing was approximately 1080 °F (583 °C) at thermocouple (TC) 14. This temperature did fluctuate throughout the testing period during the warm up and shut down cycles of the facility however the normal operating temperature is 980-1150 °F in this location depending on length of run time and BTU input. The chemical compounds containing in coal fly ash samples from WRI can be analyzed by the XRD analysis (Figure 129).

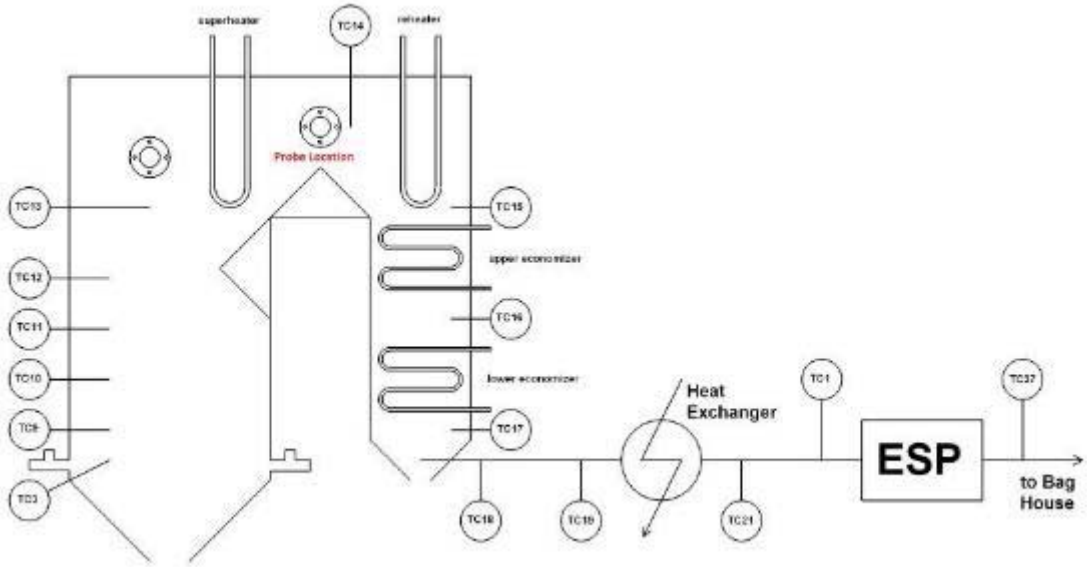

Figure 126 Corrosion sensor Location

Figure 127 Corrosion sensor with weight loss Coupons

Figure 128 Deposition of coal fly ash on the sensor (a) after first day of exposure, and (b) after 4 days of exposure

Table 5 ***Major gas components in combustion conditions***

Test Day 1-14-2013 Corrosion Sensor 1			
Coal	27.40 *lb/hr*	H_2O	9.75 *%*
Primary Air	10.00 *lb/hr*	CO_2	12.63 *%*
Secondary Air	17.60 *lb/hr*	CO	10.41 *ppm*
Tertiary (Overfire) Air	74.00 *lb/hr*	NO_x	257.64 *ppm*
		SO_2	919.01 *ppm*
		HCl	14.28 *ppm*
Test Day 1-15-2013 Corrosion Sensor 1			
Coal	27.40 *lb/hr*	H_2O	10.35 *%*
Primary Air	10.00 *lb/hr*	CO_2	13.91 *%*
Secondary Air	17.60 *lb/hr*	CO	15.89 *ppm*
Tertiary (Overfire) Air	74.00 *lb/hr*	NO_x	272.40 *ppm*
		SO_2	1037.47 *ppm*
		HCl	16.29 *ppm*
Test Day 1-16-2013 Corrosion Sensor 1			
Coal	24.00 *lb/hr*	H_2O	11.10 *%*
Primary Air	8.40 *lb/hr*	CO_2	13.29 *%*
Secondary Air	14.80 *lb/hr*	CO	15.03 *ppm*
Tertiary (Overfire) Air	62.00 *lb/hr*	NO_x	248.60 *ppm*
		SO_2	992.70 *ppm*
		HCl	10.72 *ppm*

Test Day 1-17-2013 Corrosion Sensor 1			
Coal	24.00 *lb/hr*	H_2O	11.53 *%*
Primary Air	8.00 *lb/hr*	CO_2	13.85 *%*
Secondary Air	14.00 *lb/hr*	CO	21.58 *ppm*
Tertiary (Overfire) Air	58.00 *lb/hr*	NO_x	236.02 *ppm*
		SO_2	1040.62 *ppm*
		HCl	7.40 *ppm*
Test Day 1-22-2013 Corrosion Sensor 2			
Coal	24.00 *lb/hr*	H_2O	10.62 *%*
Primary Air	8.00 *lb/hr*	CO_2	14.14 *%*
Secondary Air	14.00 *lb/hr*	CO	23.94 *ppm*
Tertiary (Overfire) Air	58.00 *lb/hr*	NO_x	240.20 *ppm*
		SO_2	1046.47 *ppm*
		HCl	7.88 *ppm*
Test Day 1-23-2013 Corrosion Sensor 2			
Coal	24.00 *lb/hr*	H_2O	10.71 *%*
Primary Air	8.40 *lb/hr*	CO_2	13.94 *%*
Secondary Air	14.80 *lb/hr*	CO	17.35 *ppm*
Tertiary (Overfire) Air	62.00 *lb/hr*	NO_x	255.12 *ppm*
		SO_2	1051.37 *ppm*
		HCl	7.41 *ppm*
Test Day 1-24-2013 Corrosion Sensor 2			
Coal	24.00 *lb/hr*	H_2O	11.23 *%*
Primary Air	8.40 *lb/hr*	CO_2	13.83 *%*
Secondary Air	14.80 *lb/hr*	CO	24.60 *ppm*
Tertiary (Overfire) Air	62.00 *lb/hr*	NO_x	250.50 *ppm*
		SO_2	1048.38 *ppm*
		HCl	6.98 *ppm*

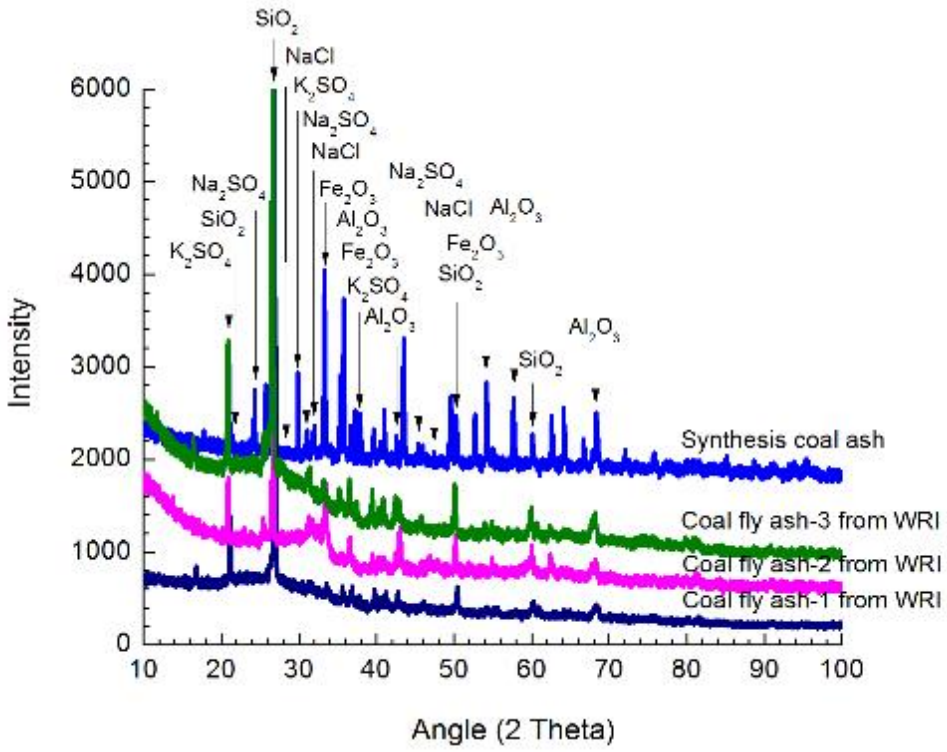

Figure 129 Comparison between XRD patterns of coal fly ash samples from WRI and synthesis coal ash

Results and Discussions

January to March 2013

WRI-WVU Corrosion Sensor Testing Phase I
High Temperature Electrochemical Sensor Testing in Coal Derived Flue Gas Exposure

During this time the wireless receiver was also tested for connectivity at extended distances and it was discovered that even through the walls of two metal buildings approximately 350 ft apart connectivity was still active; however beyond this length connectivity was lost through the buildings. The results obtained from the data acquisition system for voltage and amperage recorded by the Keithly Instrument (Figure 130) and the HOBO data loggers (Figure 131) were simply provided WVU for review and analysis.

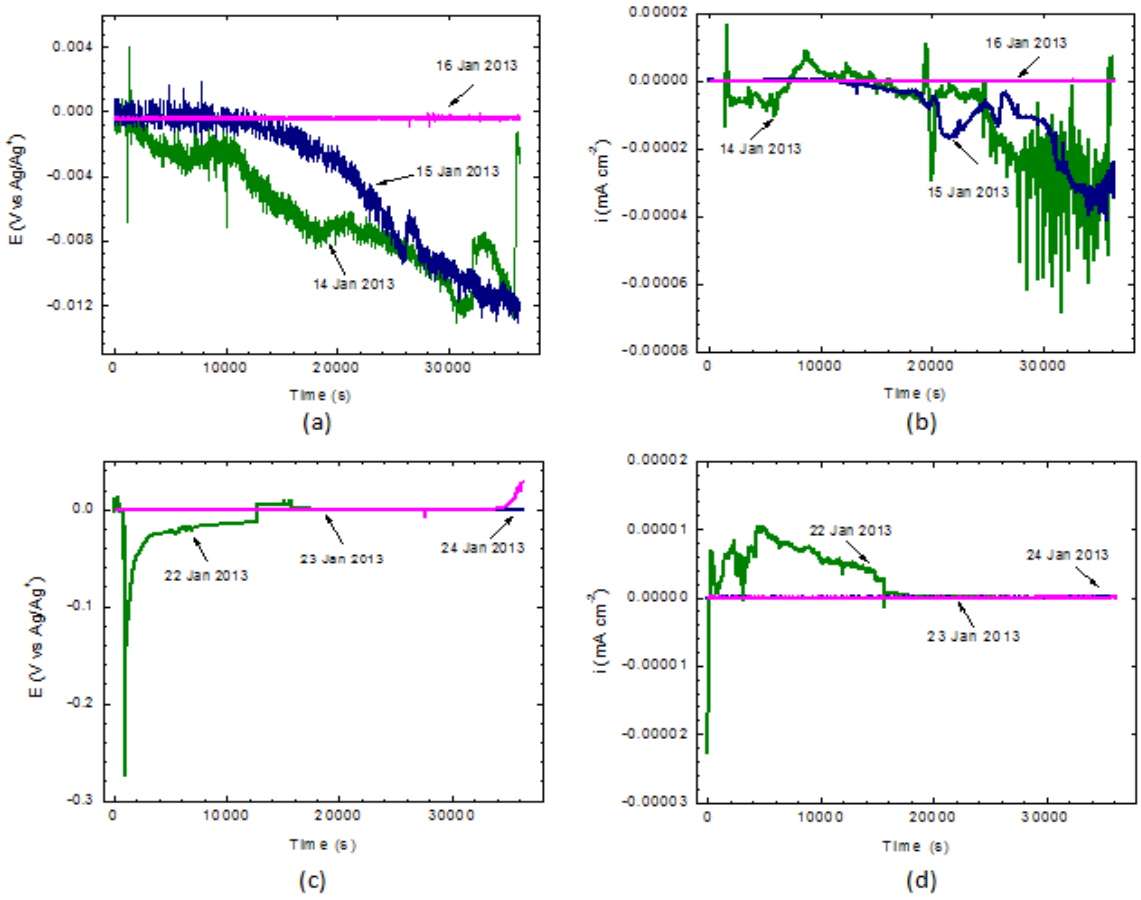

Figure 130 Time series of the electrochemical test data in coal fly ash and flue gas environments from coal combustion test: (a), (c) potential values and (b), (d) current values

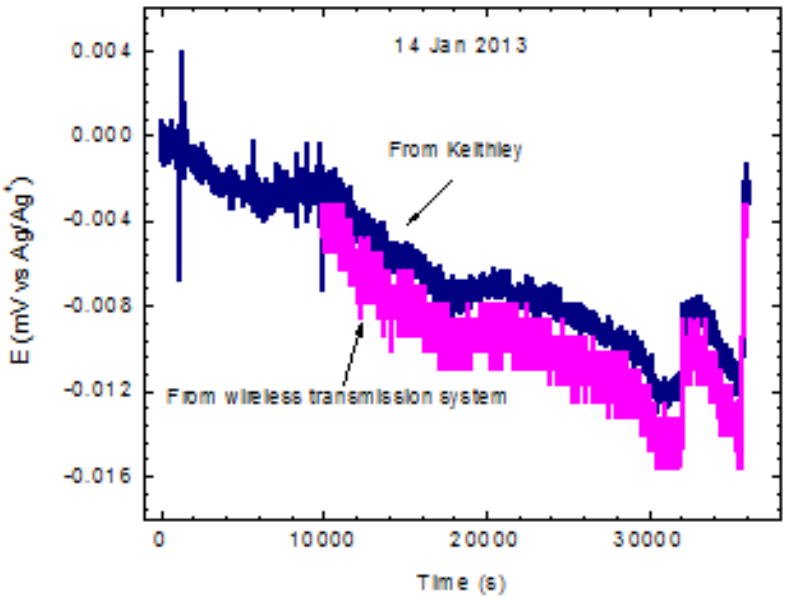

(a)

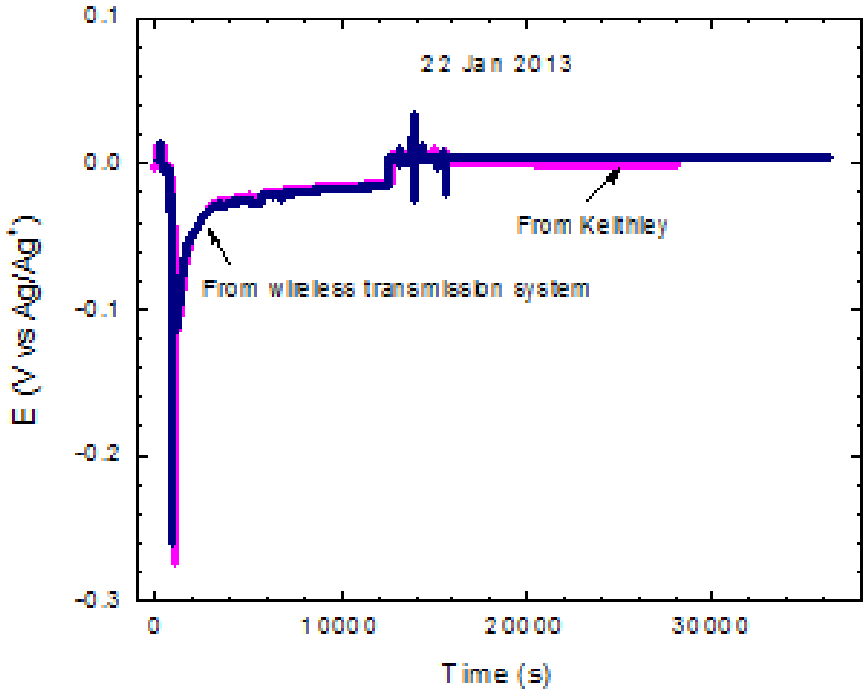

(b)

Figure 131 Comparison between the potential test data from Keithley instrument and from wireless communication system: (a) on 14 Jan 2013, and (b) on 22 Jan 2013

Conclusions

- This research highlighted the application of a self-powered wireless high electrochemical sensor for in situ coal ash hot corrosion monitoring in combination with an energy harvesting thermoelectric generator (TEG).
- Validation of lab-scale results has been successfully performed with real time USC boiler systems in WRI. The sensor demonstrated the successful wireless transmission of both corrosion potential and corrosion current signals to a simulated control room environment.

Task 5 In-situ Corrosion Monitoring Testing in Industrial USC Boiler Setting

Experimental Methods

WRI-WVU Corrosion Sensor Testing Phase II: Concurrent Wireless Transmission of Corrosion Signals of a High Temperature Electrochemical Sensor in Coal Derived Flue Gas Exposure

WRI provided use of the Combustion Test Facility (CTF) for testing of WVUs corrosion sensor with real coal derived flue gas. The sensor and associated electronics were provided to WRI and installed in the Combustion Test Facility PC boiler. The corrosion sensor was installed between the super-heater and re-heater heat tubes and wired to the data acquisition system. The CTF was operated for approximately 48 hours continuously on a sub-bituminous coal from the Powder River Basin. The corrosion sensor was installed and monitored during the entire 48 hour period.

WRI's coal combustion test facility is a nominal 250,000 Btu/hr balanced-draft system designed to replicate a pulverized coal-fired utility boiler. In its present configuration, the unit is set up to simulate a tangential-fired boiler, but may be easily adapted to wall-fired or other configurations. The fuel feed system consists of screw-based feeders and pneumatic transport to four burners inserted in the corners of a refractory-lined firebox. The burners can be angled to attain different tangential flow characteristics in the firebox. The unit is equipped with appropriately sized heat-recovery surfaces such that the time/temperature profile of a utility boiler is replicated. These surfaces comprise water-cooled panels that simulate the waterwall, an air-cooled superheater, reheater, two economizers and preheater. CTF includes provisions for preheating the combustion air to mimic a utility air preheater. The system also includes over-fire air injection ports for combustion staging and several port of injecting sorbents into the furnace. The CTF is equipped with two baghouses, electrostatic precipitator (ESP) and spray dry absorber (SDA).

Test Set-Up and Conditions

The test set-up used for this experiment is shown in Figure 132 and Figure 133. The electronics assembly was provided by WVU and replicated at WRI using equipment provided by WVU. The sensor location used was an available sensor between the superheater and reheater shown in Figure 134. The sensor was inserted into the port and set at the center of the flue gas flow.

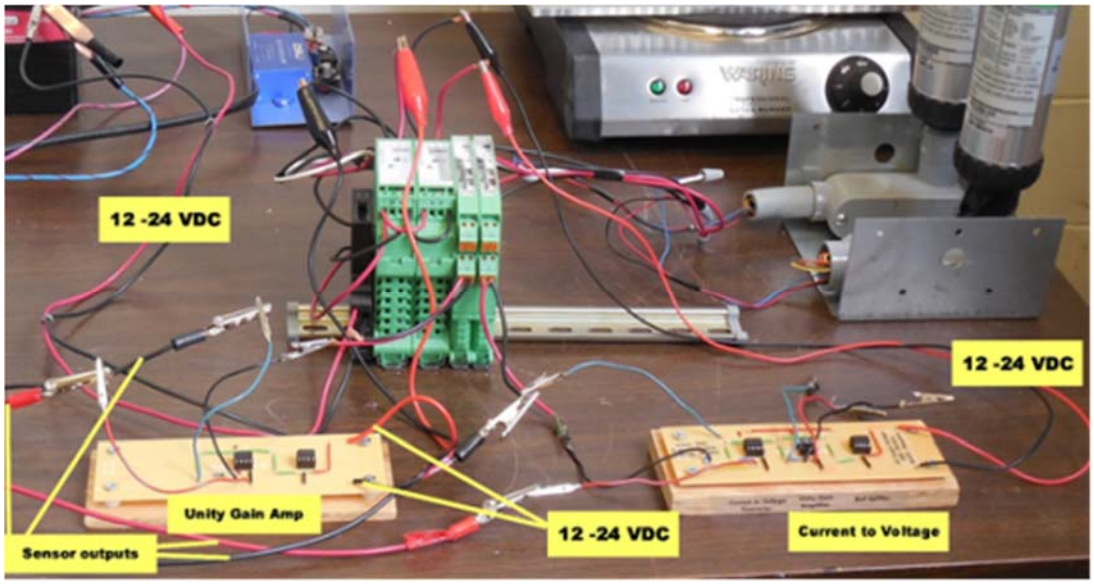

Figure 132 Component wiring diagram provided by WVU

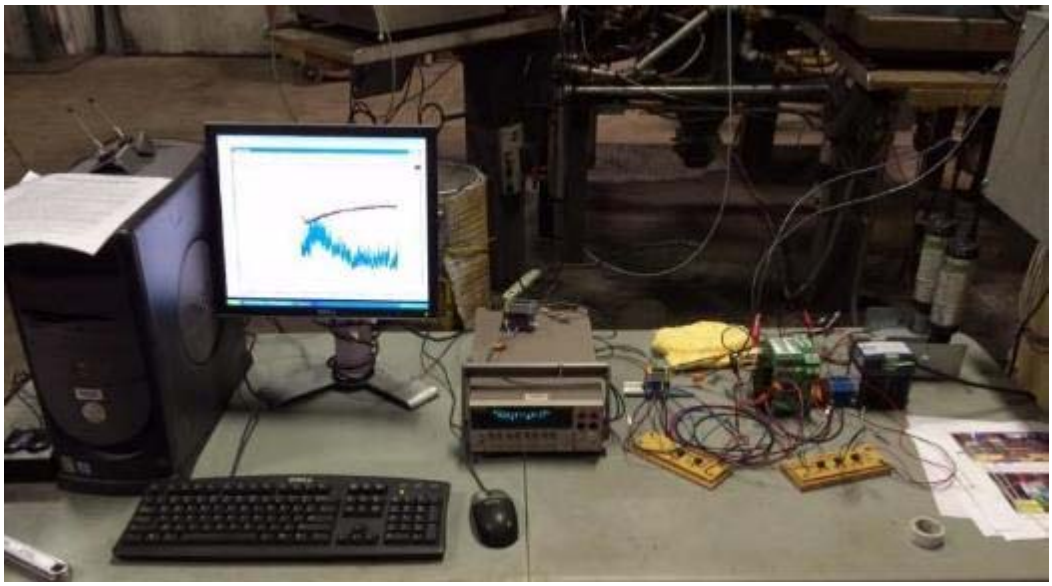

Figure 133 Component assembly as used at WRI during testing

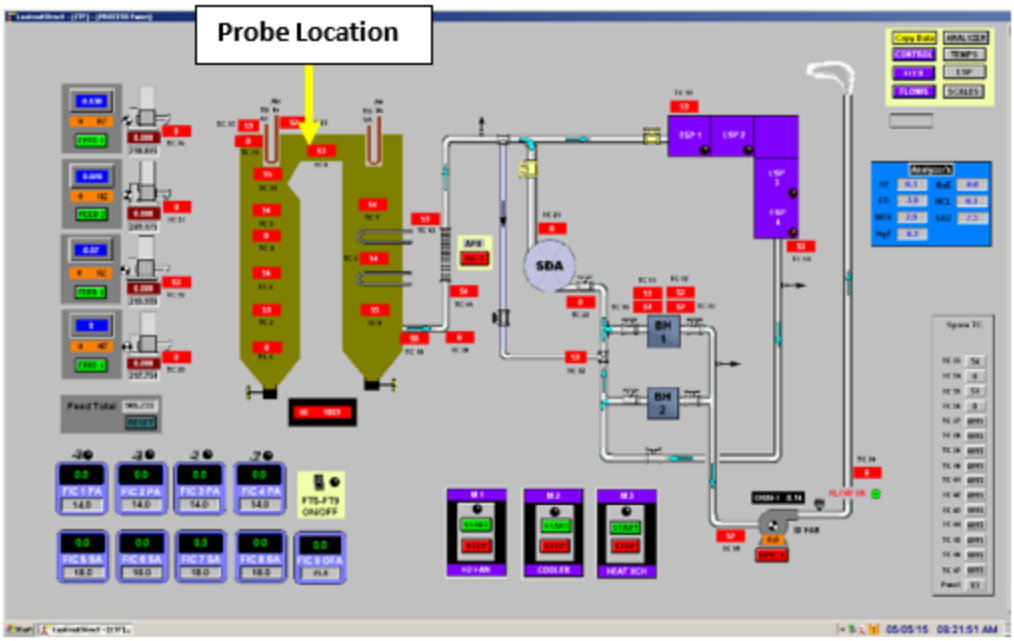

Figure 134 Sensor location

The furnace was operated under typical testing conditions during the corrosion sensor exposure; Table 6 shows the average operating conditions during the testing. Upon reaching steady state operating conditions the corrosion sensor was inserted in the port. The sensor was specially designed for concurrent measurements of potential noise and current noise signals from a single sensor. The new sensor was based on a five-electrode system (three identical working electrodes (WE1, WE2 and WE3), one reference electrode (RE) and one counter electrode (CE)). The schematic design and the photo of the sensor are shown in Figure 135a and Figure 135b.

The location of the corrosion sensor described above had an average temperature of 1084 °F (584°C) and the profile is shown in Figure 136. This temperature can vary slightly depending upon operating conditions and any events occurring during operation. As shown in the profile a slight temperature increase can be seen as the testing continued and heat recovery surfaces responded to the surrounding conditions.

Table 6 Average Operating Conditions and Flue gas Composition for test duration

Test Period 4-26-15 to 4-28-15			
Coal	20.00 *lb/hr*	H_2O	11.20 *%*
PA	14.00 *lb/hr*	CO_2	12.70 *%*
SA	17.90 *lb/hr*	CO	9 *ppm*
OA	45.00 *lb/hr*	NO_x	175 *ppm*
		SO_2	367 *ppm*

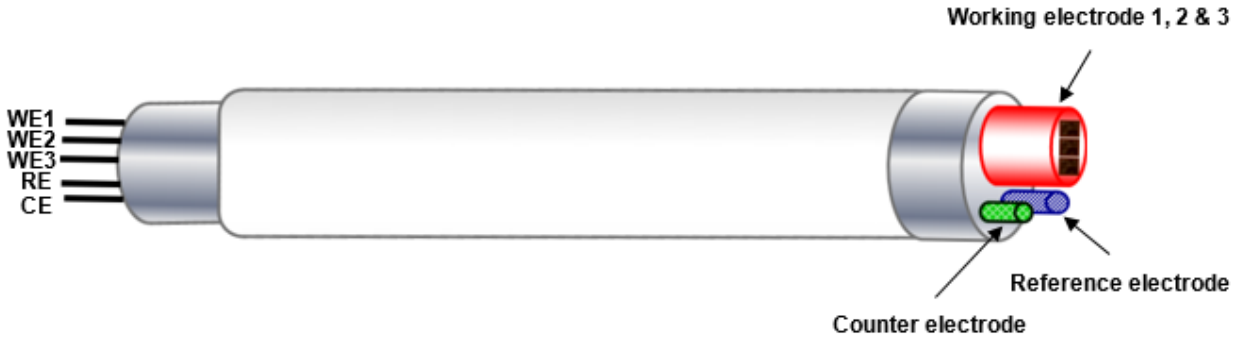

(a)

(b)

Figure 135 (a) Optimized design of high temperature corrosion sensor, and (b) photograph showing the dimensions of the sensor components

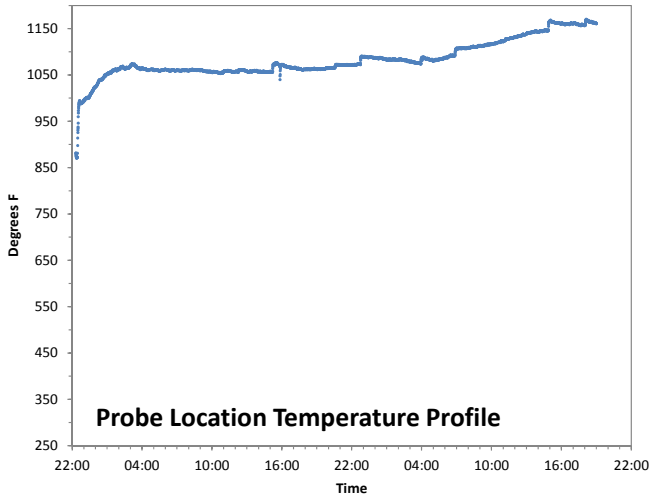

Figure 136 Corrosion sensor temperature profile

Coal and Ash Analysis

The following Table 7 and Table 8 are chemical analysis for the coal used during testing. Startup was conducted using an alternate coal however the vast majority of testing was completed using Powder River Basin Coal from the Spring Creek Mine. Furthermore, an ash analysis is also provided but was completed from the coal itself at the lab and may differ slightly from the samples provided to WVU.

Table 7 Proximate/ultimate analysis of test coal sample

REPORT OF ANALYSIS

Lab Number: P1772
Sample ID: WRI-Coal-05212014

Proximate Analysis	As Received wt%	Moisture Free wt%	Moisture & Ash Free wt%	ASTM Method	Date Analyzed	Analyst
Moisture	26.02	*****	*****	D7582	05/27/14	RB
Ash	2.85	3.86	*****	D7582	05/27/14	RB
Volatile Matter	30.41	41.10	42.75	D7582	05/27/14	RB
Fixed Carbon	40.72	55.04	57.25	calculated		
Total	100.00	100.00	100.00			

Ultimate Analysis	As Received wt%	Moisture Free wt%	Moisture & Ash Free wt%	ASTM Method	Date Analyzed	Analyst
Moisture	26.02	*****	*****	D7582	05/27/14	RB
Ash	2.85	3.86	*****	D7582	05/27/14	RB
Carbon	53.36	72.13	75.03	D5373	05/27/14	RB
Hydrogen	3.60	4.87	5.07	D5373	05/27/14	RB
Nitrogen	0.63	0.85	0.89	D5373	05/27/14	RB
Sulfur	0.31	0.42	0.44	D4239	05/28/14	RB
Oxygen	13.22	17.87	18.6	calculated		
Total	100.00	100.00	100.00			

	As Received Btu/lb	Moisture Free Btu/lb	Moisture & Ash Free Btu/lb	ASTM Method	Date Analyzed	Analyst
Heating Value	9,235	12,484	12,985	D5865	05/28/14	ES

Hydrogen and Oxygen values reported do not include hydrogen and oxygen in the free moisture associated with the sample.

Reported results calculated by ASTM D3180. Results are an average of two runs.

Table 8 Elemental analysis of test coal ash

REPORT OF ANALYSIS

Lab Number: P1772
Sample ID: WRI-Coal-05212014

COAL ASH ANALYSIS	Wt. % Ignited Basis	Method	Date Analyzed	Analyst
Silicon Dioxide, % as SiO2	22.35	XRF	6/3/2014	CW
Aluminum Oxide, % as Al2O3	18.35	XRF	6/3/2014	CW
Iron Oxide, % as Fe2O3	5.18	XRF	6/3/2014	CW
Calcium Oxide, % as CaO	20.36	XRF	6/3/2014	CW
Magnesium Oxide, % as MgO	4.54	XRF	6/3/2014	CW
Sodium Oxide, % as Na2O	9.26	XRF	6/3/2014	CW
Potassium Oxide, % as K2O	0.75	XRF	6/3/2014	CW
Titanium Dioxide, % as TiO2	1.34	XRF	6/3/2014	CW
Manganese Dioxide, % as MnO2	0.04	XRF	6/3/2014	CW
Phosphorus Pentoxide, % as P2O5	0.23	XRF	6/3/2014	CW
Strontium Oxide, % as SrO	0.98	XRF	6/3/2014	CW
Barium Oxide, % as BaO	1.10	XRF	6/3/2014	CW
Sulfur Trioxide, % as SO3	15.52	XRF	6/3/2014	CW
Alkalies as Na2O, wt%	9.75	XRF	6/3/2014	CW
Base to Acid Ratio	0.95	XRF	6/3/2014	CW
Silica Ratio	0.43	XRF	6/3/2014	CW
T250, °F	2132	XRF	6/3/2014	CW

Results and Discussions

January to March 2015

WRI-WVU Corrosion Sensor Testing Phase II: Concurrent Wireless Transmission of Corrosion Signals of a High Temperature Electrochemical Sensor in Coal Derived Flue Gas Exposure

The sensor remained in this location for the duration of testing. Post exposure pictures are provided in Figure 137. As shown in these photos significant accumulation of ash was observed on the corrosion sensor at the completion of the exposure testing.

Figure 137 Corrosion sensor post-exposure after 45 h

During testing the corrosion potential and current signals from the sensor were recorded concurrently from wireless communication system using HOBO data acquisition system (Figure 138). For comparison, the signals were also recoded with WRI's Keithly Instrument with LabTech Software (Figure 139). The recoded signals were analysed using the Saviztky-Golay smoothing algorithm. The darker signals in represent smoothing with the 100-point Savitzky-Golay (n=5) (Figure 140). There was a good correlation between corrosion potential and current values from wireless communication system (Figure 140a) and from Keithley instrument (Figure 140b).

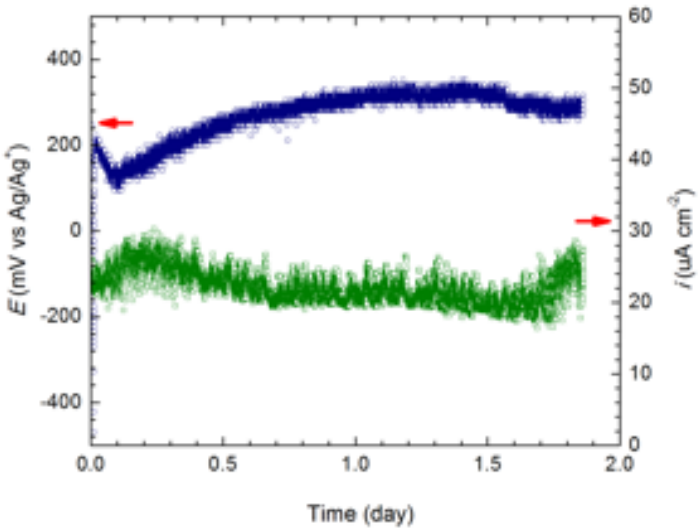

Figure 138 Corrosion potential and current signals recorded from wireless communication system using HOBO data acquisition system

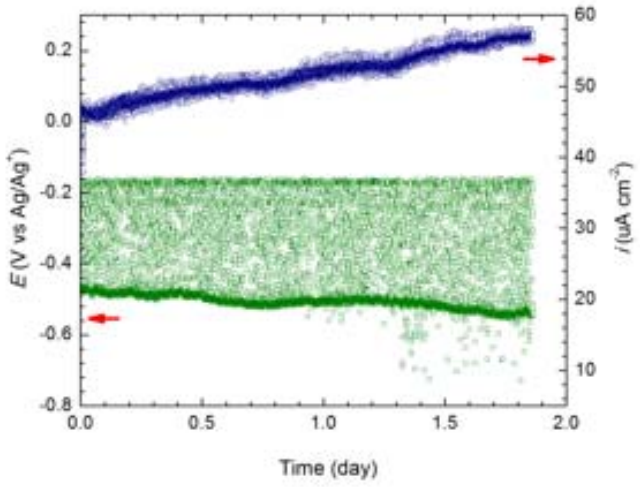

Figure 139 Corrosion sensor potential and current signals recorded during testing from the Keithly Instrument/LabTech

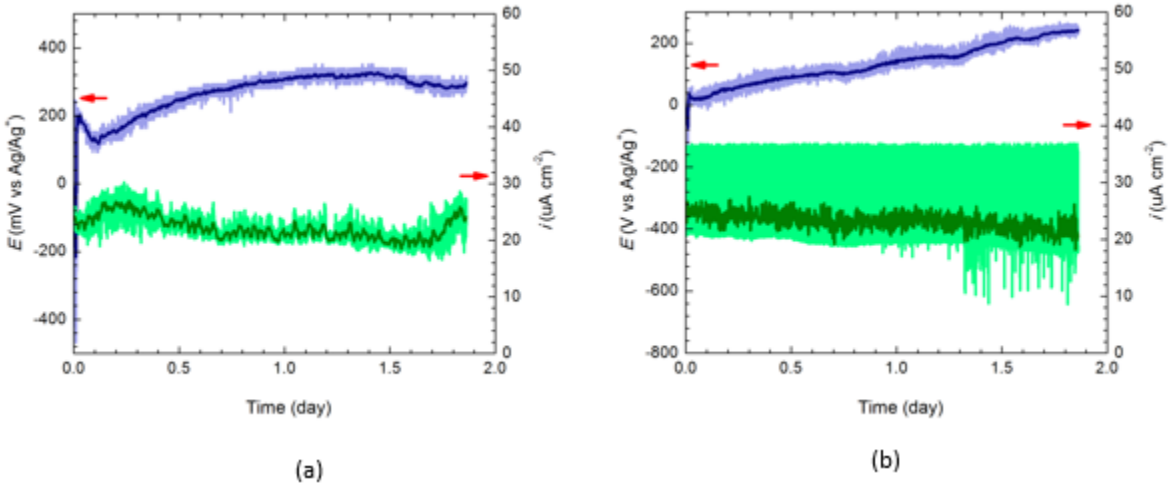

Figure 140 Comparison between corrosion potential and current signals after data smoothing: (a) recorded from wireless communication system, and (b) from Keithley instrument

Conclusions

- Wireless electrochemical potential and current noise signals from a simulated coal ash hot corrosion process were concurrently transmitted and recorded.
- Validation of lab-scale results was successfully performed with real time USC boiler systems in WRI. The resulting conditioned electrochemical noise signals from the sensor clearly distinguished the coal ash hot corrosion potential and its reaction kinetics. A good consistency was observed between lab and pilot scale results.

3.0 Conclusions

- The project demonstrated an application of a novel self-powered wireless high temperature electrochemical sensor for in-situ corrosion monitoring to provide a clearer picture of the hot coal ash corrosion degradation in next generation coal-based power systems.
- The sensor was specially designed to utilize the response of several electrochemical measurements from a single sensor. It was based on a five-electrode system (three identical working electrodes (WE1, WE2 and WE3), one reference electrode (RE) and one counter electrode (CE)).
- The developed sensor was applied to investigate uniform and localized under-coal ash deposit corrosion behavior of Inconel 740 superalloy in different synthetic coal ash environments.
- The characteristic potential noise signatures distinguished the oxidation and sulfidation stages of coal ash hot corrosion process. The characteristic current noise signatures can indicate the severity of corrosion attack.
- The quantitative determination of the corrosion rates via the electrochemical noise technique was proposed and there was a good correlation between the metal loss values from the EN test data and those from the weight loss test data and the corroded surface analysis.
- Wireless electrochemical potential and current noise signals from a coal ash hot corrosion process were concurrently transmitted and recorded. The Savitzky-Golay least square polynomial smoothing was proposed to extract the real noise from the raw electrochemical noise signal of the nonstationary coal ash hot corrosion process. A computer interface and data acquisition software was used to calculate instantaneous corrosion rates from electrochemical current signals.
- Analysis of electrochemical noise signals by power spectral density (PSD) was applied to coal ash hot corrosion study. PSD plots using FFT and MEM gave more information for mechanism of the oxidation and sulfidation processes.
- Validation of lab-scale results was successfully performed with real time USC boiler systems in WRI. The resulting conditioned electrochemical noise signals from the sensor can clearly distinguish the coal ash hot corrosion potential and its reaction kinetics. A good consistency was observed between lab and pilot scale results.
- The technology is at a stage where companies have expressed interest in the technology. Communications have occurred with two companies interested in the technology but more effort needs to be done to commercialize the technology.
- The challenges and lessons learned from the project are: more communication with the final users/utilities to incorporate their needs and concerns in terms of operation, cost, maintenance in the final sensor design development and deployment.
- Why was this a good investment – because utilities understand that corrosion is a major issue in the development and operation of coal-fired power plant, but due to complexity of the physical/chemical process of different types of corrosion, it is difficult for private companies to invest in this area before fundamental research and early-stage development is done through government-funded research.

4.0 Future Work

The future work of the sensor system development should focus on the following:

- Development sensors that can detect localized corrosion. As indicated in this report, our current sensor can indicated the occurrence of localized corrosion by “localized index”, but it cannot provide real-time information on the initiation and development of such behavior. While it is important to monitor the general corrosion kinetics like what our current sensor can do, it is necessary to develop the sensors that can provide real-time monitoring on the localized corrosion.
- Development of sensors that are more cost effective and robust to easily be incorporated into a utility’s operation
- Demonstration of the simultaneous transmission of both the mV signal (between a working electrode and reference electrode) and the μA signal (working electrodes).
- Investigation of system modifications to mitigate the signal losses from the interface of the sensor and the signal converter.
- Development of a computer interface and data acquisition software to calculate instantaneous corrosion rates from electrochemical current signals.

5.0 Products Produced

1. Naing Naing Aung, Xingbo. Liu, High Temperature Electrochemical Sensor for In Situ Monitoring of Hot corrosion, Corros. Sci., 65, 1 (2012).
2. Naing Naing Aung, Xingbo Liu, Effect of SO_2 in Flue Gas on Coal Ash Hot Corrosion of Inconel 740 alloy-A High Temperature Electrochemical Sensor Study, Corros. Sci., 76, 390 (2013).
3. Naing Naing Aung, Xingbo Liu, Effect of Temperature on Coal Ash Hot Corrosion Resistance of Inconel 740 Superalloy, Corros. Sci., 82, 227 (2014).
4. Naing Naing Aung, Edward Crowe, Xingbo Liu, Development of Self-Powered Wireless-Ready High Temperature Electrochemical Sensor for In Situ Corrosion Monitoring in Coal-Fired Power Plant, ISA Trans. 55 (2015) 188-194.
5. Naing Naing Aung, Xingbo Liu, In Situ Monitoring Coal Ash Hot Corrosion using the Combined High Temperature Electrochemical Sensor with Electrochemical Noise Analysis Method, Corros. Sci (under review).
6. Naing Naing Aung, Xingbo Liu, Study of under-coal ash deposit corrosion of Inconel 740 alloy using high temperature electrochemical sensor, CORROSION (under review).